THE ROLE OF CHARGE REDISTRIBUTION IN THE SELF-DISCHARGE OF ELECTROCHEMICAL CAPACITOR ELECTRODES

by

Jennifer Marie Black

Submitted in partial fulfilment of the requirements
for the degree of Doctor of Philosophy

at

Dalhousie University
Halifax, Nova Scotia
December 2010

DALHOUSIE UNIVERSITY

DEPARTMENT OF CHEMISTRY

The undersigned hereby certify that they have read and recommend to the Faculty of Graduate Studies for acceptance a thesis entitled "The Role of Charge Redistribution in the Self-discharge of Electrochemical Capacitor Electrodes" by Jennifer Marie Black in partial fulfillment of the requirements for the degree of Doctor of Philosophy.

Dated: December 8, 2010

External Examiner: ___________________________________

Research Supervisor: ___________________________________

Examining Committee: ___________________________________

____

____

Departmental Representative: _____________________________

DALHOUSIE UNIVERSITY

DATE: December 8th, 2010

AUTHOR: Jennifer Marie Black

TITLE: The Role of Charge Redistribution in the Self-discharge of Electrochemical Capacitor Electrodes

DEPARTMENT OR SCHOOL: Chemistry

DEGREE: PhD CONVOCATION: May YEAR: 2011

Permission is herewith granted to Dalhousie University to circulate and to have copied for non-commercial purposes, at its discretion, the above title upon the request of individuals or institutions. I understand that my thesis will be electronically available to the public.

The author reserves other publication rights, and neither the thesis nor extensive extracts from it may be printed or otherwise reproduced without the author's written permission.

The author attests that permission has been obtained for the use of any copyrighted material appearing in the thesis (other than the brief excerpts requiring only proper acknowledgement in scholarly writing), and that all such use is clearly acknowledged.

____

Signature of Author

TABLE OF CONTENTS

LIST OF TABLES

LIST OF FIGURES

ABSTRACT

This work examines the role of charge redistribution in the self-discharge of electrochemical capacitor electrodes. Electrochemical capacitors are charge storage devices which have high power capability and a long cycle life, but have a low energy density compared to other devices, coupled with a high rate of self-discharge which further diminishes the available energy. The mechanisms of self-discharge in electrochemical capacitors are poorly understood, and it is important to gain a better understanding of the electrode processes which lead to self-discharge, in order to minimize self-discharge and enhance electrochemical capacitor performance.

To learn more about charge redistribution and its role in the self-discharge of electrochemical capacitors, multiple self-discharge experiments were performed on carbons with various surface areas/pore structures and in various electrolytes. Charge redistribution was also examined in a model pore (a transmission line circuit based on de Levie's model of a porous electrode) and results from this model were compared to the self-discharge of a high surface-area carbon.

Results demonstrate that charge redistribution is a major component of the self-discharge in high surface-area carbons. Results also indicate that charge redistribution requires a much longer time than previously thought (tens of hours rather than minutes) which further highlights the importance of charge redistribution during self-discharge. Therefore when performing mechanistic studies of self-discharge in electrochemical capacitors, it is important that effects of charge redistribution are not neglected.

The self-discharge profiles of various pore shapes were also examined using the model pore, and results emphasize the superiority of cone and cylindrically shaped pores, and the disadvantages of restrictive pore mouths and bottlenecks for high power applications.

LIST OF ABBREVIATIONS AND SYMBOLS USED

°C	degrees Celsius
α	symmetry parameter
Å	angstrom
δV	voltage difference
ε	dielectric constant of electrolyte
μA	microamp
μF	microfarad
μHz	microhertz
μm	micrometer
Ω	ohm
ρ	resistivity
τ	integration constant
ϕ	phase shift
ω	frequency
a.c.	alternating current
atm	atmosphere
A	amp
A	pre-exponential factor (Section 2.1), electrode surface area (Sections 2.3 and 2.7), cross-sectional area (Section 2.4), amplifier gain (Section 2.11)
AC	activation-control
AN	acetonitrile
BET	Brauner-Emmet-Teller
BN	bottleneck
C	coulomb
C	capacitance
CE	counter electrode
cm	centimeter
c_0	initial concentration
$\mathrm{CR}_{\mathrm{down}}$	charge redistribution down the pore
$\mathrm{CR}_{\mathrm{up}}$	charge redistribution up the pore
CV	cyclic voltammogram
d	distance between electrolyte ion and electrode surface

D	diffusion coefficient
DFT	density functional theory
e	sinusoidal potential
E	energy (Section 2.3), voltage magnitude (Section 2.11)
E_a	activation energy
EC	electrochemical capacitor
E_o	equilibrium potential
ESR	equivalent series resistance
F	farad
F	Faraday constant (96 485 C mol^{-1})
g	gram
G	Gibbs energy
GCPL	galvanostatic cycling with potential limitation
h	hour
Hz	hertz
l	length
i	sinusoidal current
i_{net}	electrode current
i_o	exchange current density
I	current magnitude
ID	inverted diamond
IR	Ohmic drop
J	joule
k	rate constant
kg	kilogram
kHz	kilohertz
kΩ	kiloohm
K	kelvin
mA	milliamp
mg	milligram
min	minute
mL	milliliter
mm	millimeter
mol	mole

mV	millivolt
MΩ	megaohm
M	molar
n	number of electrons
n	number of capacitors
nm	nanometer
Pa	pascal
PC	propylene carbonate
PFA	poly(fluoroalkoxy)
PTFE	poly(tetrafluoroethylene)
PZC	potential of zero charge
r	radius
$\mathrm{r_{bottleneck}}$	radius of bottleneck
$\mathrm{r_{mouth}}$	radius of pore mouth
R	resistance, gas constant (8.314472 J K^{-1} mol^{-1})
RE	reference electrode
RE1 - 8	capacitor 1 - 8 in transmission line circuit
R_s	equivalent series resistance
$\mathrm{R_s}$	resistor 1 in transmission line circuit
s	second
SA	surface area
SEM	scanning electron microscopy
SHE	standard hydrogen electrode
t	time
T	temperature
TEM	transmission electron microscopy
V	volt
V	voltage
V_-	input voltage (-) operational amplifier
V_+	input voltage (+) operational amplifier
V_i	initial voltage
V_{out}	output voltage, operational amplifier
V_t	voltage at time t
W	watt

WE	working electrode
z	charge
$Z(\omega)$	impedance
Z_{im}	imaginary impedance
Z_{re}	real impedance

ACKNOWLEDGEMENTS

First and foremost, I would like to express my sincere gratitude to my supervisor, Dr. Heather Andreas. It has been an honour to be her first Ph.D. student. Her enthusiasm, patience, humour, kindness, and vast knowledge have made my Ph.D. experience both educational and enjoyable. I simply could not imagine a better or friendlier supervisor.

I also extend thanks to the members of my supervisory committee, Dr. Russell Boyd, Dr. Mary Anne White and Dr. Peng Zhang for their helpful suggestions and feedback over the years. Thanks to Dr. Peter Pickup from Memorial University of Newfoundland for taking the time and effort to participate in my defence as the external examiner.

Many people in the Department of Chemistry have contributed to my work. Thanks to Brian Millier for building several electrochemical instruments and electronic devices (including the transmission line circuits used extensively in this research), and for the numerous enlightening discussions. I would like to thank glassblower Juergen Mueller for creating and helping design electrochemical cells and other glassware used in my research. Thanks to machinists Mike Boutilier and Rick Conrad for their input in many aspects of this work, especially the construction and development of the thin layer cell. Thanks to the office staff, particularly Giselle Andrews who has been extremely helpful, patient, and kind.

Thanks to Dr. Jeff Dahn in the Physics Department for use of BET equipment, and to Dr. David Stevens and Xuemei Zhao for their assistance in using those instruments. Thanks to Patricia Scallion of the Institute for Research in Materials for help with the SEM images, along with Dr. Ping Li of the Department of Biology for his assistance with TEM images.

I would like to extend a special thanks to current and former members of the Andreas Group for all of their help and support through the years, and for making the Andreas Lab an enjoyable working atmosphere: Alicia Oickle, Zac Cormier, Sarah Goertzen, and Michelle Everist. Thanks to summer students Rhonda Stoddard, who contributed extensively to the electrolyte project, and also to Jeff Wagner who helped with the iron self-discharge experiments.

Lastly, I wish to thank my friends and family for their support during my graduate degree. Most importantly I would like to thank my parents, Brian and Janice, for providing a loving environment, encouragement, and emotional and financial support throughout the years. None of this would be possible without them, and it is to them I dedicate this thesis.

Chapter 1

INTRODUCTION

Electrochemical capacitors (ECs) are charge storage devices that can store charge in the double-layer of an electrode/electrolyte interphase, or in Faradaic reactions as pseudocapacitance.[1] Double-layer ECs typically utilize high surface-area electrodes (often carbon which may have a BET surface area of up to 2500 m^2 g^{-1}). High surface area is necessary since the charge is stored in the electrode/electrolyte boundary region, and a higher surface area results in more charge storage. By necessity, this requires very small pores in the electrodes, and these small, often very tortuous pores, lead to significant diffusion and migration limitations in the pores during charging/discharging.[2]

A mathematical evaluation of the potential and current distribution in porous electrodes was previously given by de Levie, who showed that the electrode processes do not proceed evenly throughout the thickness of a porous electrode, largely due to the *IR* drop in the solution within the pores, resulting in faster electrode processes at the mouth of the pore, closer to the counter electrode, versus those which occur at the base of the pore.[2] During charging or discharging of these highly porous electrodes the potential at the tip of the pore (closest to the counter electrode) changes more quickly than the potential at the base of the pore (farthest from the counter electrode) due to the added solution resistance in the pore.[2] This behaviour can be modeled with a transmission line consisting of resistors (which model the solution resistance) and capacitors (which model the double-layer capacitance).[2]

As a result of this pore effect and its transmission line characteristics, after incomplete charging (discharging) of an EC electrode there is a distribution of potentials in the pores of the electrode. Upon switching the system to open-circuit configuration there is a redistribution of charge in the pores until all parts of the electrode surface are at an equal potential. In other words, after charging of a porous electrode the potential at the pore tip falls (since the potential here is the highest) and the potential at the pore base climbs, until the entire pore is at an equal potential.[3] Because the potential at the tip of the pore, where the potential is measured, falls during this charge redistribution, this may appear as a rapid self-discharge.

Self-discharge is the spontaneous decline in voltage with time of a charged EC left on open circuit. When a charged EC is placed on open circuit there is no external circuit through which electrons may pass and discharge the cell, and therefore self-discharge must take place through coupled anodic and cathodic processes.[4] Because during self-discharge there is a loss of voltage over time, the amount of energy available in the system decreases. Whether or not the self-discharge is of practical importance depends on the application of the EC.[4] For load-leveling applications, or in bridging short-term power outages, it may not be overly significant since recharge is imminent. However, in cases where the EC is designed for accumulation and storage of energy or where there are appreciable periods of time before recharge (*e.g.* solar cells) self-discharge behaviour is of major consequence.

Conway *et al.* proposed three mechanisms through which self-discharge may occur, and derived models which describe the predicted self-discharge profile for each mechanism.[5] The first mechanism describes an activation-controlled Faradaic process, where the decline of voltage (V or V_t) versus log t would give a straight line.[4, 5] The second mechanism is a diffusion-controlled Faradaic process where the potential would decline with $t^{1/2}$.[4] The final mechanism is due to an internal Ohmic leakage or a 'short circuit' due to faulty construction. Here a plot of ln V_t versus t would give a linear relationship.[4]

Since each self-discharge mechanism results in a distinguishable potential profile, Conway *et al.* suggested that examining the potential profile of an experimental system may help to elucidate the mechanism of self-discharge.[5] However, due to the uneven charging of high surface-area electrodes, such as those used in double-layer capacitors, when the system is placed on open circuit after charging, charge redistribution takes place, resulting in a potential loss, in addition to any loss in potential due to Faradaic self-discharge mechanisms. Thus, charge redistribution may then alter/mask the self-discharge profile from what is expected based on the Conway mechanisms, which were derived for planar electrodes, rendering the model ineffective for mechanistic studies.[4, 5]

The goal of this project was to gain a full understanding of charge redistribution and to determine how it influences self-discharge of ECs and other systems based on the charging of porous electrodes. To do this various self-discharge experiments were performed on different carbon samples to examine the effects of carbon surface area/pore structure on charge redistribution (Chapter 4). The presence of charge redistribution in high surface-area carbons was tested by performing self-discharge experiments at various charging rates (or different potential hold times), and from different initial charging potentials (Chapters 4). A hardware transmission line circuit was also used as a model pore to further study charge redistribution, as this setup allows for a better understanding of processes taking place throughout the entire length of the model pore, rather than only the mouth or base of the pore (Chapter 4). Using the transmission line pore model, the profile of a porous electrode undergoing both charge redistribution and an activation-controlled Faradaic self-discharge process was predicted and compared to self-discharge in a high surface-area carbon (Chapter 5). In addition, the transmission line model was used to examine the effect of pore shape on charge redistribution (Chapter 6), and electrochemical impedance spectroscopy (Chapter 7). Self-discharge profiles of high and low surface-area carbons also were examined in various electrolytes to examine the effect of electrolyte ions on self-discharge and determine the role of charge redistribution during self-discharge of a high surface-area carbon (Chapter 8). Finally, a thin layer cell was designed and constructed for the purpose of studying charge redistribution in a model pore (Chapter 9), however further work on this project is required.

Chapter 2

BACKGROUND

2.1 Batteries, Fuel Cells, and Electrochemical Capacitors

The majority of energy production today relies on the combustion of fossil fuels, a non-renewable energy source.[6] The burning of fossil fuels releases large amounts of carbon dioxide, a greenhouse gas, into the atmosphere and is a main contributor to global warming.[7, 8] It is therefore important to develop alternate energy sources which are more sustainable and environmentally friendly, and combine these sources with the ability to store available charge and retrieve that stored charge when needed.[9] Electrochemical energy storage is one alternative, with batteries, fuel cells, and electrochemical capacitors (ECs) as systems for electrochemical energy storage and conversion.[9] ECs have attracted attention from the perspective of the prevention of global warming as the energy outputs of both photovoltaic and wind power generation can be stored in ECs and used efficiently, and neither technology exhausts carbon dioxide.[10]

Although the energy storage and conversion mechanisms for batteries, fuel cells, and ECs are different, there are similarities between these systems.[9] All three devices consist of two electrodes (electronic conductors) in contact with an electrolyte (ionic conductor, electronic insulator), and the energy-providing processes take place at the electrode/electrolyte interfaces.[9] In both batteries and fuel cells electrical energy is generated by conversion of chemical energy via redox reactions.[9] The difference between batteries and fuel cells is that in batteries, the energy storage and conversion takes place in the same compartment, making batteries closed systems. Here, the anode and cathode play an active role in redox reactions, and the electrodes react and change as the battery is charged or discharged. In fuel cells the anode and cathode are catalytic, and the active masses undergoing the redox reaction are delivered from outside the cell, (*e.g.* fuel in the form of gas or liquid, and oxygen from a tank or air) and fuel cells are thus open systems.[9]

Conversely, ECs (also called 'double-layer capacitors', 'supercapacitors', 'ultracapacitors', and 'power capacitors' [9, 11]) store electrical energy in an electrochemical double-layer formed at an electrode/electrolyte interface (Figure 2.1). When an electrode is placed into an electrolyte solution, there is a spontaneous organization of charges at the surface of the electrode, and positive or negative ionic charges within the electrolyte accumulate at the surface of the electrode to compensate for the opposite electronic charge at the surface of the electrode. This organization of charges creates the double-layer, with one layer of charge on the electrode surface, and the other layer in the electrolyte. The double-layer can be used to store charge by adding charges to the electrode (with concomitant balancing of the charge by electrolyte ions) during charging, and when a load is added to the system, the double-layer spontaneously discharges, resulting in parallel movement of electrons in the external wire. The characteristics of the double-layer depend on the electrode surface structure, the composition of the electrolyte, and the potential field between the charges at the interface. Typically ECs which rely on the double-layer are composed of two high surface-area carbon electrodes. This arrangement, where both electrodes are the same material is referred to as a symmetric capacitor, while asymmetric capacitors refer to capacitors that combine a carbon electrode with a battery or redox electrode.[9]

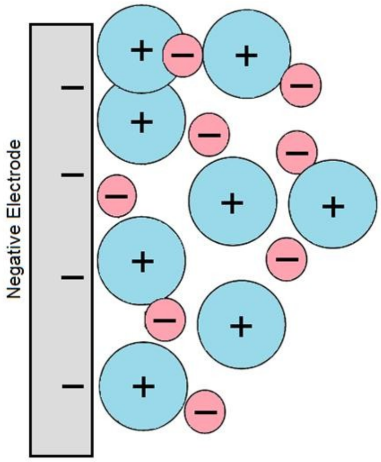

Figure 2.1: Schematic of a double-layer formed at electrode/electrolyte interface. Modeled after figure in reference 8.

A second type of EC is based on surface redox processes, often at transition metal oxide films.[12, 13] Unlike the previous case, this type of capacitance is Faradaic in origin, and involves the passage of charge across the double-layer. This type of EC stores charge indirectly through Faradaic chemical processes, but its electrical behaviour is like that of a capacitor, in that it is highly reversible, and is therefore called pseudocapacitance.[1, 13]

Cyclic voltammograms (CVs) of both capacitive and pseudocapacitive materials have an almost mirror image shape across the zero current axis, and this is related to the reversibility of the reactions taking place. Electrochemical reversibility is when the electron transfer step is very fast, allowing for an equilibrium situation to be obtained at each potential. In this circumstance, switching the direction of the potential sweep causes a reversal in the direction of the current, but no change in the magnitude.[1]

Of the electrochemical energy systems described above, fuel cells are considered to be high energy systems, whereas ECs are considered to be high power systems.[9, 14] Batteries have intermediate power and energy characteristics.[9] However, it is important to note that no single electrochemical power source can match the characteristics of the internal combustion engine, which is able to achieve both high power density and high energy density.[9] Electrochemical systems may be combined in order to achieve an overall high power density and high energy density. In these hybrid systems, the ECs would provide high power, while the batteries or fuel cells would deliver high energy.[9]

Energy is described as the ability to do work, while power is the rate at which work is done. Using an electric vehicle as an example, the energy determines how far you can go, while power determines how fast you can go. The energy content of electrochemical systems are often compared in terms of specific energy, also called gravimetric energy (watt hours per kilogram) and energy density, also called gravimetric energy (watt hours per liter). The rate capability is expressed as specific power (watt per kilogram) and power density (watts per liter). A Ragone plot is shown (Figure 2.2) which compares the energy and power characteristics of various systems, and a comparison of various properties of batteries and electrochemical capacitors is shown in Table 1.

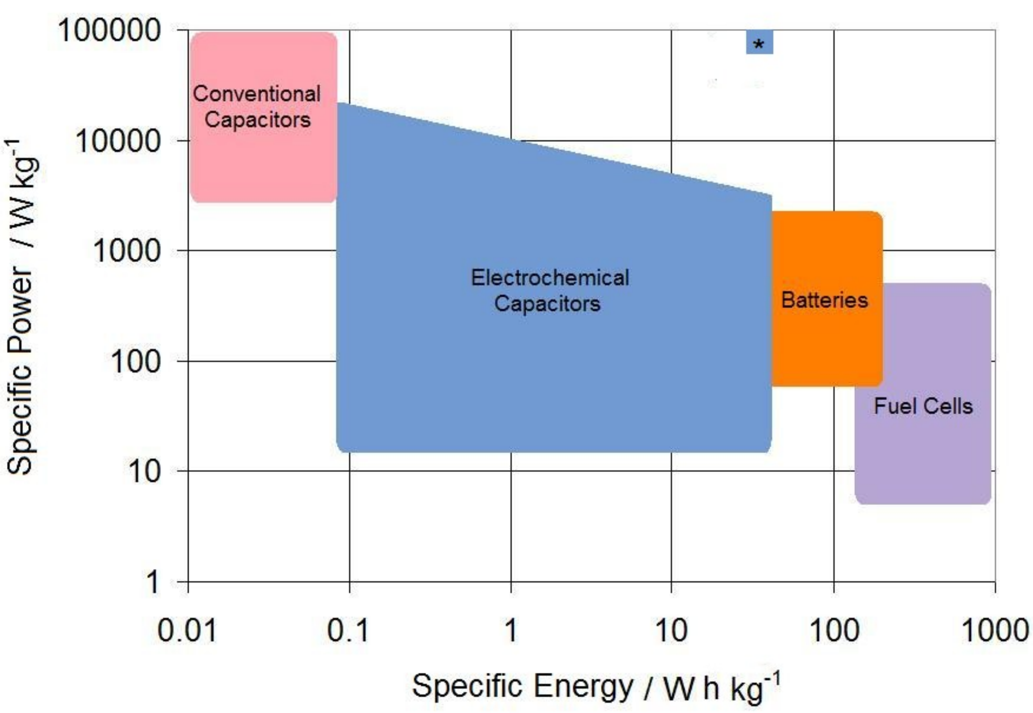

Figure 2.2: Ragone plot for various electrochemical systems. Modeled after figure from reference 9 and data taken from reference 15 and 16. *ECs using vertically aligned carbon nanotube technology.[16]

Table 1: Comparison of battery and electrochemical capacitor characteristics.[*]

	Pb-Acid	Ni-Cd	Li-Ion	ECs
Voltage (V)	2	1.2 - 1.6	3.7	1 - 3
Energy (W h kg^{-1})	30	15 - 150	80 - 150	5 (60[†])
Power (W kg^{-1})	180	50 - 1000	500 - 2000	10 000 (100 000[†])
Efficiency	85 - 90%	65 - 80%	90 - 100%	85 - 98%
Cycle life	1500	3000	1500	>500 000
Self-discharge rate[‡]	2%	10%	5%	5 - 60%[§]

---

[*] Data taken from reference 15.

[†] Electrochemical capacitors using vertically aligned single wall carbon nanotube technology.

[‡] Self-discharge rate defined as percentage loss of nominal energy per month.

[§] Loss in electrochemical capacitor voltage for a two week period taken from reference 16.

Table 1 shows that the specific power of ECs is high compared to batteries. It is worth noting that some Li-ion batteries are able to achieve a specific power as high as 2000 W kg^{-1}. In the case of ECs utilizing vertically aligned single wall carbon nanotubes a specific power of 100 000 W kg^{-1} has been achieved.[16] The reason ECs display high power compared to batteries stems from a different mechanism of energy storage. Batteries store energy by redox reactions in the bulk electrode, which allow them to achieve high energies, but these reactions have slow kinetics. In double-layer ECs there is an absence of charge transfer, and the transport of ions in the solution is quick, leading to a higher rate capability.[9, 18, 19] The double-layer forms and relaxes almost instantaneously, with a time of formation of 10^{-8} s, while the time constant for a redox reaction is much slower, in the range of 10^{-2} to 10^{-4} s. The short time constant of the EC is the reason for the high power density.[9]

Batteries, however, have higher specific energies, with Li-ion batteries achieving specific energies as high as 150 W h kg^{-1}, while typically ECs have specific energies of *ca.* 5 W h kg^{-1}, with a maximum specific energy of 60 W h kg^{-1} achieved when using vertically aligned single wall carbon nanotubes as the electrode material.[16] In the double-layer only 0.18 electrons per atom can be stored (calculated based on an average charge density of 30 μF cm^{-2} and an atom density of 10^{15} cm^{-2} at a smooth electrode surface) while redox reactions in batteries usually involve one or two electrons per atom.[1] Thus EC charge storage involves only 10 – 20 % of that involved with battery materials, per atom of surface area, which is the basis of the lower energy of these systems.[1]

The charging and discharging processes in ECs are highly reversible, and do not require phase changes. In batteries, on the other hand, phase changes do take place, and fast charging and discharging require rapid phase changes, which may cause structural changes leading to failure modes and reduced cycle life. As a result ECs have been shown to reach over 500 000 cycles, while batteries can usually only reach a few thousand cycles.[9, 15, 19-21] Although the cycle life of ECs is very long, they also experience degradation processes, especially during overcharge and overdischarge.[20]

Other advantages of ECs include large possible temperature and voltage ranges.[20, 22] Particularly at low temperatures ECs outperform batteries. Since batteries rely on redox reactions to produce current, and as can be seen from the Arrhenius equation below, the lower the temperature, the lower the rate of the reaction:

$$k = Ae^{\frac{-E_a}{RT}} \tag{1}$$

where A is the pre-exponential factor, E_a the activation energy, R the gas constant (8.314472 J K^{-1} mol^{-1}), T the temperature, and k the rate constant. ECs meanwhile do not rely on chemical reactions, only on reorganization of charges, which has less dependence on temperature.[22] Some configurations of ECs also have the advantage of being free from toxic materials.[11, 21, 22] Unlike a lead-based battery, the electrode material in ECs is often carbon, which is superior in terms of environmental protection.[10]

Of the electrochemical energy storage systems, batteries have found, by far, the most application markets. Fuel cells are being considered for a number of applications including transportation (*e.g.* bus, passenger car) uninterrupted power supply, and portable electronic equipment, however a number of issues must be addressed before fuel cells can be fully commercialized, including manufacturing costs, and fuel generation and distribution.[23, 24]

Although the concept of ECs has been known for many years, as the first patents date back to 1957 where a capacitor based on porous carbon was described by Becker, only over the past fifteen to twenty years have efforts toward practical commercialization taken place.[11, 25, 26] A number of applications of ECs are discussed below.

2.2 Applications of ECs

The application of ECs has been limited in the past due to their large equivalent series resistance (*ESR*).[22] Equivalent series resistance can be thought of as a series resistor whose value is equal to the sum of all of the resistances of the components of the capacitor including the resistance of the electrolyte and any contact resistances. The current in the capacitor has to pass through this amount of resistance when the system is in use and a high *ESR* has a major influence on the power performance; this restricts the rate at which the capacitance can be charged or discharged.[1] More recently ECs have been developed with a large capacitance, and low *ESR*.[27] ECs display high power density, and long cycle life, making them useful in many applications.[10, 27, 28] The energy density and power density of an EC depend on its application, for example the discharge time may vary from milliseconds for a camera flash to hours for an alarm clock back-up.[29]

For many years now, ECs have been incorporated into various electronic products (*e.g.* clocks, computers) where they serve as a memory back-up, so that an interruption in the power supply does not result in a loss of stored information.[30] In these conditions, there is another power source which normally supplies the load, and the EC takes over during times where the main power source is disconnected.[11, 31] This back-up power may be provided for hours/weeks (video recorders for back-up of TV channel settings and clock time), hours/days (car audio systems for back-up of radio station memory and taxi fare programs when the car battery is disconnected), minutes/hours (alarm clocks, coffee machines during times of temporary power outage), and seconds/minutes (cameras, calculators, cell phones and pagers during replacement of the batteries).[11] Batteries are an alternative to ECs in this type of application, however, the cost of an EC is comparable, and sometimes lower than the cost of a rechargeable battery for this application. In addition, the lifetime of batteries is not as long as ECs, and they require regular replacement.[11, 30]

Other applications use ECs as the main power source in portable electronic equipment with only modest energy demands. Batteries are often employed for this type of application; however the longer recharge times for batteries can be a disadvantage.[30] For example, ECs have been used in an electric screwdriver, which could be fully charged in only 90 s.[32] State of the art batteries, on the other hand, typically require a minimum charging time of ten minutes.[32] Although the EC would require more frequent charging than a battery (as a result of the lower energy of ECs), ECs are attractive for this type of application in which the device is used infrequently, and for typically short periods of time.[32]

ECs are also used as intermittent power sources. For example, during the day energy can be provided by solar cells, which also charge the EC, and the EC delivers the power during the night.[11] A solar watch is one illustration where the EC can power the watch for several days from one charge, and the watch would not need a change in power supply during its lifetime. Other applications of this type include solar lanterns, lighting of time tables at bus stops, and the illumination of parking meters.[11] Batteries used in solar cell applications must be replaced every three to seven years since the continuous cycling results in a reduced lifetime.[30] ECs used for the same application only need to be replaced every 20 years, approximately the lifetime of the solar cells themselves, reducing the cost associated with maintenance of the system.[30] ECs also have the advantage of being able to operate over a wide range of temperatures, which is important for remote stations which are located in cold climates. Batteries would have to be maintained close to room temperature, increasing the energy consumption, and cost.[30]

ECs have gained much of their recognition in the context of hybrid electric vehicles, which can be operated with less, or zero, toxic gas emission.[9, 12, 30, 33] ECs are designed to supplement batteries or fuel cells, by providing the necessary power for acceleration. In systems where the EC is combined with a battery, the lifetime of the battery may be substantially increased, as the EC will take over during times of overload.[13, 20] Overload refers to periods of time requiring high power (such as accelerating or uphill driving) which in turn leads to high currents, and batteries operated under such situations have the tendency to fail more quickly.[34] One problem with electric vehicles is their limited driving range, due to the low energy density of batteries and ECs compared to the internal combustion engine. This has led to the development of vehicles which combine a fuel efficient engine with either a battery or EC and an electric drive train. One problem with ECs is that although they can provide the fast charging and discharging necessary in electric vehicles, they provide a lower energy and higher self-discharge rate when compared to batteries (Table 1), which prevent ECs from simply replacing batteries.[9, 19]

One application very suitable for ECs is energy harvesting, wherein regenerative stopping energy is captured, stored, and reused. Applications include diesel electric hybrid vehicles with frequent start/stops such as city transit buses and trash pick-up trucks.[32] The brake energy can be quickly recovered to be stored in the EC and released during periods of large power requirements.[20, 30] When ECs are used in hybrid-applications, regenerative braking can reduce fuel consumption by *ca.* 15%.[30] Another energy harvesting application where ECs have found use is in gantry cranes, which are used to load and unload containers at seaports. In this application the EC is used to capture and deliver energy during the repetitive up and down movement of the heavy shipping containers.[32]

To widen the scope of applications for ECs efforts must be made to increase the energy density and lower the cost, while maintaining the high cycle life and power densities unobtainable with batteries.[32]

2.3 Energy and Power of ECs

Increasing the energy density of ECs is important for their commercialization. The energy, *E,* increases with capacitance according to the equation:

$$E = \frac{1}{2} C V^2 \tag{2}$$

where *C* represents the capacitance, and *V* the operating voltage. An improvement in energy can therefore be achieved by either an increase in capacitance, or an increase in the operating voltage.[12] The large capacitance, *C*, and hence energy storage potential in double-layer capacitors is due to the small separation (*ca.* 1 nm) of electrolyte ions and the carbon, as well as the high surface area of the carbon:

$$C = \varepsilon \frac{A}{d} \tag{3}$$

where A is the electrode surface area accessible to electrolyte ions, ε the dielectric constant of the electrolyte, and d is the separation.[35] An increase in the capacitor voltage also causes a significant enhancement in power, P:

$$P = \frac{V^2}{4R} \tag{4}$$

where R represents the resistance. An increase in the operating voltage then greatly improves both the power and energy density.[36]

2.4 Electrode Materials

The three main types of electrode materials used in ECs are transition metal oxides, conductive polymers, and most commonly, carbon. Carbon is chosen for a number of reasons, including its large possible surface area (2500 m^2 g^{-1}), easy processibility, high electronic conductivity, and low cost. Carbons with large specific surface areas are available as powders, woven cloths, felts, or fibers.[9-11, 36-38] Carbon electrodes are chemically stable in many different solutions, and at a wide range of temperatures.[36]

2.4.1 Carbons

Charge storage on carbon electrodes is mainly electrostatic, however, there can be a contribution from pseudocapacitance, due to Faradaic redox processes at surface functional groups present on carbon. This can then lead to higher capacitance values than is expected based solely on the surface area.[11, 37, 39]

Activated carbons and activated carbon fibers are commonly employed as electrode materials in ECs and are prepared by either physical, or chemical (*e.g.* KOH, NaOH) activation of a carbon precursor (*e.g.* bituminous coal, coconut shell, corncob).[25, 40] Activated carbons typically have surface areas up to 2500 m^2 g^{-1}, and in some cases as high as 3100 m^2 g^{-1}, leading to a high gravimetric capacitance.[41] The porosity is somewhat controllable depending on the type of precursor and the activation method. Parameters of the activation process including temperature, time, and type of activating agent significantly affect the porosity of the resulting carbon. The porous structure of the carbon has a large influence on the electrochemical behaviour of the EC.[36]

Theoretically, the higher the surface area of the carbon, the higher the specific capacitance.[14, 31] However, low values of capacitance are observed for carbons with very high surface areas (2500 - 3000 m^2 g^{-1}), which infers that not all the pores are effective in the charge accumulation. Pore sizes can be grouped into four classes: ultramicropores, < 0.7 nm; micropores, 0.7 to 2 nm; mesopores, 2 to 50 nm, and macropores, > 50 nm.[35, 42] The micropores are responsible for the high surface area, and in turn the capacitance, while the mesopores are needed for the rapid transportation of ions to the bulk of the material.[36, 43] The micropores are essential in the formation of the double-layer, however the pores must be accessible to the electrolyte in order to be functional.[42, 44] A pore network with larger pores provides a less resistive pathway for ions, indicating that materials with more large pores should be capable of delivering high power, since the resistance, R, is smaller (Equation 4). The lower resistance associated with larger diameter pores is apparent as the resistance, R, is inversely proportional to the cross-sectional area, A, of the pore:

$$R = \rho \frac{l}{A} \tag{5}$$

where l is the length, and ρ is the electrolyte resistivity.

One problem with high mesopore volume, is the resulting lower density of the material, and therefore a diminished volumetric energy, or energy density. Large volumetric energies are important as there is a trend toward miniaturization and consumers are demanding products which are smaller and smaller (*e.g.* cell phones, cameras). There is then a trade-off between specific surface area and pore size to achieve either high energy density or high power density.[14]

An issue with activated carbons is the difficulty in controlling the pore size and the pore size distribution. Activated carbons contain a large number of micropores and ultramicropores, which may be too small to allow penetration of the electrolyte.[35] The non-wetting of the pores leaves a portion of the electrode which cannot take part in the charging or discharging process, resulting in dead volume. In addition to this, the pore structures of activated carbons are very tortuous, and the pores are randomly connected, making the ion transport difficult.[35]

Microporous carbons with very small pores, and small pore size distributions have also been prepared through heat treatment of various metal carbides in a flow of Cl_2. The pore structure of carbide-derived carbons depends on the precursor used, as well as the treatment temperatures, and surface areas can reach as high as 2000 $m^2 g^{-1}$.[41]

Another way to increase the surface area of carbon fibers is through exfoliation. Carbon fibers which have been exfoliated - by rapid heating of their intercalation compounds formed in nitric or formic acid - result in single carbon fibers splitting into a number of thin filaments.[45] This exfoliation process generates carbon fibers with surface areas of *ca.* 300 $m^2 g^{-1}$. However the capacitance of these exfoliated carbon fibers in 1 M H_2SO_4 is quite high at *ca.* 120 F g^{-1} compared to the capacitance of an activated carbon fiber of surface area *ca.* 2000 $m^2 g^{-1}$ of *ca.* 140 F g^{-1}.[45] Comparing the capacitance per surface area, the exfoliated carbon fiber has an extremely high capacitance, *ca.* 0.4 F m^{-2}, compared to the activated carbon fiber, *ca.* 0.07 F m^{-2}. Exfoliated carbon fibers have been shown to have more crystallinity than activated carbon fibers, and results suggest that the degree of crystallization or graphitization is an important factor in determining capacitance, as well as surface area.[45] In 18 M H_2SO_4 the capacitance of exfoliated carbon fibers was found to be as high as 550 F g^{-1}. It has been suggested that the high capacitance is from contributions of pseudocapacitance due to intercalation of H_2SO_4 molecules into graphite, in addition to the double-layer capacitance.[41]

In order to improve the electrochemical performance of ECs, optimal porous characteristics need to be determined, and this has created interest in carbon materials with a well tailored porous structure.[33] Synthesis of carbons with a well defined porosity is very difficult using the classical methods.[44] One method for preparing carbons with controllable pore sizes is the template method, however it is a relatively expensive technique.[36]

Carbons having a well controlled pore structure can be obtained using hard and soft templating techniques. Hard-template techniques involve the use of presynthesized templates which act as a mould into which the carbon precursor is impregnated. The space occupied by the template becomes the pores of the carbon material, while the pores of the template become the carbon framework. Recently, the use of soft templating techniques have also been used to generate nanostructures through the self assembly of organic molecules, however, these techniques are still in the early stages of development and synthesizing carbons using the soft templating technique can be difficult.[46]

Carbons have been templated using mesoporous silicas, producing carbons with three dimensionally ordered mesopores. This type of templated carbon can have surface areas up to 2200 m^2 g^{-1}.[41] Using typical activation processes, micropores can also be introduced into these carbons to further increase surface area.[41]

Microporous carbons have also been prepared using various types of zeolite as a template, denoted as zeolite-templated carbons, with BET surface areas over 3000 m^2 g^{-1}.[41] The pores of the carbon are adopted from the zeolite channels, resulting in micropores which are homogenous in size and morphology. These types of carbons have been shown to have high capacitances and rate performances.[41] The high rate performance is attributed to the well ordered three dimensional micropores, allowing for rapid ion transport.[41]

Aside from surface area and pore size, pore geometry is an important factor determining the charge and discharge characteristics of the EC. The effect of pore shape on the electrochemical impedance of porous electrodes has been evaluated using different mathematical models, as well as examined experimentally on various pore geometries, and the geometry was shown to be a significant factor in determining the power capability.[7, 47-51] Many different pore geometries have been obtained using the hard templating techniques, including cylindrical pores, spherical pores, and pores between nanocarbon wires.[14, 46, 52, 53]

The effect of pore size on the performance of ECs has been examined using electrode materials with well known pore structures: these electrode materials include carbide derived carbons which have a very narrow pore size distribution, as well as templated carbons engineered with a specific well known pore structure. Chmiola and co-workers discussed three possibilities relating ion and pore size.[35] In the first scenario the pore size is greater than twice the size of the solvated ions, allowing ions to line up along both pore walls, and leading to a high capacitance.[35] When the pore size drops to less than twice the solvated ion the capacitance is reduced as the ions can no longer line up along both adjacent walls of the pore. Upon further reduction of the pores size, to less than that of the solvated ion, the solvation shell surrounding the ion must distort in order access the pore, and an increased capacitance arises as the ion is now able to closer approach the pore wall, reducing d in Equation 3.[35]

Recently carbon nanomaterials, such as graphene and carbon nanotubes, have received a lot of attention as electrode materials for ECs, due to their low electrical resistivity (*ca.* 10^{-6} Ω cm).[54] Graphene is a single layer of carbon atoms arranged hexagonally, and a single graphene sheet can have a surface area over 2500 m^2 g^{-1}.[54] Studies have shown that the specific capacitance of graphene in aqueous electrolytes can reach 135 F g^{-1}.[55] Graphene was first isolated by micromechanical cleavage from bulk graphite, capable of producing graphene sheets *ca.* 100 μm in size.[56] Since then other methods of synthesizing graphene sheets include chemical vapour deposition, and unzipping of carbon nanotubes.[55] However, owing to the difficulty in producing large amounts of high quality graphene, graphene is yet to be used in real applications.[55]

Another promising material for ECs is carbon nanotubes, due to both their high surface area and electrical conductivity.[41] Single wall carbon nanotubes with BET surface areas of *ca.* 2000 m^2 g^{-1} have been synthesized.[41] Using single wall carbon nanotube technology, remarkably high power densities of *ca.* 100 000 W kg^{-1} have been achieved.[17]

2.4.2 Transition Metal Oxides

Transition metal oxides are attractive materials for use in ECs due to their high capacitance, and low resistance, leading to high power density.[57] The most common pseudocapacitive types of ECs are based on ruthenium dioxide, due to its high specific capacitance (720 F g^{-1} [57]). These systems are also highly reversible, however the high cost of these materials makes them less than ideal for many commercial applications, so research has been directed to finding oxides of cheaper transition metals that can exhibit pseudocapacitive behaviour, (*e.g.* MnO_2[57]) as well as studying pseudocapacitive conducting polymers.[11, 39]

2.4.3 Conductive Polymers

Like transition metal oxides, conductive polymers can also exhibit pseudocapacitive behaviour due to reversible oxidation and reduction processes related to the π-conjugated polymer chains. An EC using the electroactive polymer, polyanaline, achieved a power density of 2 kW kg^{-1} and an energy density of 10 W h kg^{-1}, approximately double the energy density of an EC utilizing activated carbon.[58] Other advantages of conductive polymers are that they are light weight, cheap, and relatively easy to manufacture. However, the swelling and shrinking of these polymers during charge or discharge is a problem, as it leads to degradation during cycling, reducing their lifetime.[57]

2.5 Carbon Surface Functionalities/Heteroatoms

Carbon materials may contain functional groups and foreign elements within their structure or upon their surfaces to varying degrees, depending on the type of precursor and/or the preparation conditions. The most common of these groups are carboxyl, carboxylic anhydrides, lactones, lactols and hydroxyl groups.[59] The functional groups can enhance the performance of the EC in two ways: increasing the capacitance due to a pseudocapacitive contribution, or increasing the wettability of the carbon, allowing the electrolyte to fill the pores more completely and reducing any dead volume.[20, 25, 36] The additional pseudocapacitance results from the functional groups on the surface undergoing reversible oxidization and reduction. Pseudocapacitance induced by oxygen functionalities is the most common, and the amount of oxygen functionalization depends on the precursor as well as the method of surface preparation.[36] It is possible that the functional groups on the carbon surface which are able to undergo oxidation and reduction reactions are involved in self-discharge of ECs.

2.5.1 Oxygen-containing Carbon

A number of oxygen-containing functional groups are present in activated carbons, as they are introduced during the activation process.[41] Oxygen-containing groups can be undesirable in ECs using organic electrolytes due to their instability at high voltage, and significant effort and expense is put forth to remove oxygen for these applications.[41] However, in aqueous electrolytes oxygen-containing groups can be advantageous, as they can contribute to the overall capacitance through pseudocapacitive reactions.[41]

The oxygen-containing surface groups present on carbon may be separated into acidic or basic functionalities. Acidic groups include carboxyl groups, lactones, phenol and lactol groups, and basic groups include chromene structures, diketone or quinone groups, and pyrone-type groups (Figure 2.3).[36, 60] Acidic reactions have been associated with oxide structures, which are part of the chemisorbed oxygen seen on all carbon surfaces which have been exposed to air.[59]

It is not yet clear whether the oxide structures are also responsible for the basic reactions shown by some carbon surfaces, as two different contributors to the carbon basicity can be taken into account: the surface functionalities of electron donating character (as listed above) and π-electrons present on the basal planes.[60, 61]

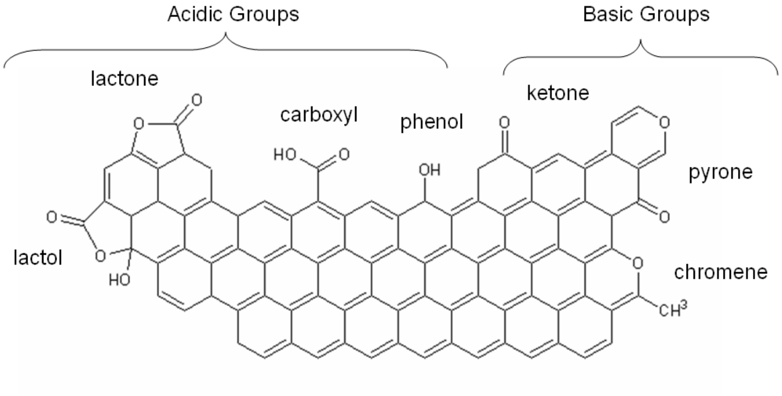

Figure 2.3: Acidic and basic carbon surface functionalities. Modeled after figure from reference 60.

2.5.2 Nitrogen-containing Carbon

Nitrogen-containing carbons have also been shown to exhibit large capacitance values (160 – 180 F g^{-1}), despite having low surface areas (880 m^2 g^{-1}).[62] The increased capacitance in nitrogen-containing carbons is attributed to Faradaic reactions of the nitrogen-containing functional groups, as with the case of oxygen-containing functional groups.[41] However, in many nitrogen-containing carbons, the nitrogen content alone is not enough to explain the high capacitance, and improvements in capacitance are also attributed to other factors, such as enhancing the wettability of the carbon.[41]

2.6 Electrolyte

The voltage of an EC is restricted by the decomposition potential window of the electrolyte. In aqueous electrolytes, the practical cell voltage for commercial systems is limited to *ca.* 1 V as water begins to break down at higher potentials (1.23 V vs. SHE) and at lower potentials (0.0 V vs. SHE).[9, 11, 12, 20] Organic electrolytes, such as propylene carbonate (PC) or acetonitrile (AN) have the advantage of a higher achievable cell voltage, typically around 2.3 V.[11, 20] The increase in voltage significantly increases the energy density, as energy is proportional to the square of the voltage (refer to Equation 2). For an EC consisting of two carbon electrodes in aqueous electrolytes, with a cell voltage of about 1 V, a specific energy of about 3.5 W h kg^{-1} of active mass can be achieved. Using organic electrolytes, the increase in cell voltage to 2.3 V leads to an increase of specific energy to about 18 W h kg^{-1} of active mass.[11] The decomposition voltage of the organic electrolyte is also affected by the water content. Extreme purification procedures are required to allow the voltage to be increased to 3 V or higher, however this increases the cost of the electrolyte.[11, 12]

The drawbacks of using organic electrolytes are their high cost (compared to aqueous electrolytes), high corrosion activity, low dielectric constant, and low conductivity.[63] In addition to this, ECs containing organic electrolyte often require extra packaging for isolation, as they may be harmful to the environment or potential users.

The capacitance values of carbon electrodes in aqueous electrolytes are generally in the range of 100 to 200 F g^{-1}, and 50 to 150 F g^{-1} in organic media.[36] The larger capacitances in aqueous electrolytes are partly due to the higher dielectric constant and to the smaller size of solvated ions, which are more easily able to access smaller pores increasing the effective surface area (thus, capacitance) and can get closer to the pore wall, resulting in smaller d (Equation 3).[13, 35]

Another reason for the reduced capacitance in organic electrolytes is because the contribution from functional groups is significantly reduced in organic electrolytes vs. that seen in acidic media, because there are no protons available in the traditionally used organic electrolytes such as PC and AN (Figure 2.4). In organic electrolytes the CV of carbon approaches the rectangular shape expected for an ideal capacitor, while in aqueous electrolytes peaks appear in the CV around 0.6 V vs. SHE, which indicate the participation of redox reactions.[59] These peaks have been identified as the oxidation and reduction of quinone groups (Figure 2.5).[64, 65] The pseudocapacitive peaks are generally only seen in aqueous electrolytes because the protons necessary for this reaction are not present for the typically used organic electrolytes.[11] The quinone groups are responsible for a significant amount of the total capacitance, and this may be due to the fact that this redox reaction allows for the storage of one electron per oxygen atom, as opposed to the 0.18 electrons stored per carbon atom.[1]

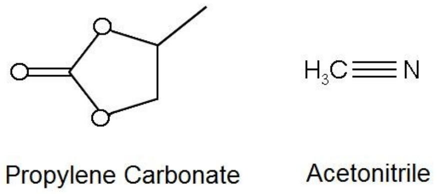

Figure 2.4: Chemical structure of propylene carbonate (PC) and acetonitrile (AN).

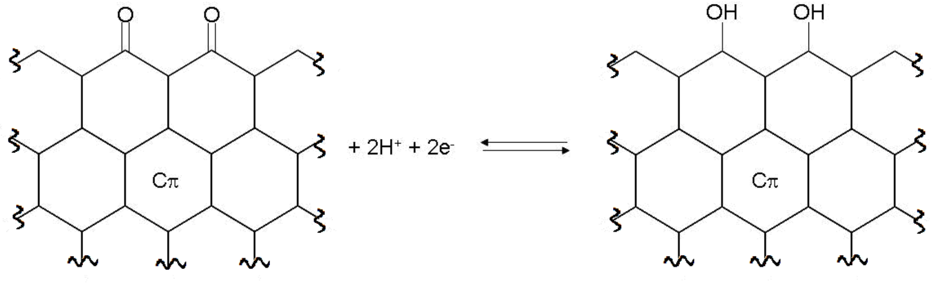

Figure 2.5: Reduction/oxidation of a quinone to a hydroquinone on the edge of a graphene sheet.

The capacitance of an EC with a non-aqueous electrolyte increases with decreasing size of the ions: BF_4^- > PF_6^- > Et_4N^+ [20, 36] (4.74 Å,[66] 4.08 Å,[67] and 2.78 Å,[68] respectively). One solution for optimizing the performance of an EC in organic electrolyte is to adapt the pores of the carbon to the size of the ions. This could involve using different carbons for the anode and cathode, as the ionic radii of the anions and cations are different.[36] Recall, however, that although the capacitance per surface area is smaller in the organic electrolytes, the practical voltage window is larger, so a higher energy density is possible (Equation 2).

Organic electrolytes have a higher resistivity than do aqueous ones, typically by a factor of 50. This higher resistance then reduces the power available, as the two are inversely related (Equation 4). Thus, the power available from an EC using an organic electrolyte is typically smaller than that available from an EC using an aqueous electrolyte.[11] The electrolyte chosen for an EC depends on the application. Organic media may be used if a higher energy density is required, and acidic media may be used in situations requiring higher power.[11]

A third type of electrolyte, ionic liquids, allows for a further increase in the practical capacitor voltage, up to *ca.* 5.5 V.[63, 69] Ionic liquids are thermally stable salts made up of a bulky organic cation combined with an anion.[63] Ionic liquids are generally liquid at room temperature, and have negligible vapour pressure.[63] The properties of ionic liquids strongly depend on the type of cation and anion. Common ionic liquids are based on imidazolium, pyridinium, and quaternary ammonium salts.[63] One problem with ionic liquids is that they are often characterized by a high viscosity, which complicates wetting of the carbon, especially in micropores.[63] This means that even though they permit an increase in the operating voltage, their high viscosity and lower conductivity lead to slightly reduced power performance per electrode surface area.[63] One way to overcome the viscosity problem is to operate the EC at a higher temperature, thereby increasing the conductivity, which leads to an increase in capacitance. The absence of solvent means that the dimensions of the ions can be more accurately determined, and therefore the effect of ion size can also be studied.[70] A major drawback to the use of ionic liquids is that they are very expensive.[36]

2.7 Self-discharge

When a charged capacitor or battery is left on open circuit, there is a thermodynamic driving force for its 'self-discharge' or the decline of voltage with time. This arises because in the charged state, batteries and supercapacitors are in a state of higher Gibbs energy, *G*, than in their discharged state, so there is a thermodynamic driving force for the spontaneous decline of *G* with time.[4] This situation is comparable to a reaction between chemical compounds (high Gibbs energy), which, when mixed, proceed to produce products (lower Gibbs energy) at a rate dependent on the kinetics and mechanism of the reactions involved.[4] In ECs this loss of charge over time is greater than with batteries (Table 1). The self-discharge rates vary depending on the chemistry and electrochemistry of the system, and this limits the performance, application, and reliability of ECs.

The rate of self-discharge is determined by the mechanisms of the processes by which the self-discharge takes place. When a charged EC is in open-circuit configuration there is no external circuit through which electrons may pass and discharge the cell. Self-discharge must then take place through coupled anodic and cathodic processes passing parasitic currents, and this current is normally of a Faradaic nature.[4] There are three mechanisms through which self-discharge is proposed to occur.[5, 12]

The first is an activation-controlled Faradaic process, which can occur when a capacitor has been charged beyond the decomposition potential limit of the electrolyte, or with reactions of carbon surface functionalities, *etc.* Here the decline of voltage versus log *t*, would give a straight line:[4, 5]

$$V_i - V_t = \frac{-RT}{\alpha F}\left[\ln\frac{\alpha F i_0 t}{RTC} + \alpha F C\tau\right] \tag{6}$$

where V_t is the potential at time t, V_i is the initial potential, R the universal gas constant (8.314472 J K^{-1} mol^{-1}), T the temperature, α a symmetry parameter, F the Faraday constant (96 485 C mol^{-1}), i_0 the exchange current density, C the capacitance, and τ an integration constant.

The second is a diffusion-controlled Faradaic process that may occur if the electrolyte contains impurities (or if the electrode material contains impurities that may dissolve into the electrolyte) that are oxidizable or reducible within the potential window, and the transport of these species to the electrode surface is the rate determining step. Here the potential would decline with $t^{½}$:[4, 5]

$$V_i - V_t = \frac{2zFAD^{1/2}c_o}{C\pi^{1/2}}t^{1/2} \tag{7}$$

where V_t is the potential at time t, V_i is the initial potential, A the electrode surface area D is the diffusion coefficient of the redox species, z, the charge, and c_o the initial concentration.

The last mechanism is due to the energy storage device having internal Ohmic leakage pathways, or a ‘short circuit’ due to faulty construction. Here a plot of ln V_t versus t would give a linear relationship:[4, 5]

$$\ln V_t = \ln V_i - \frac{t}{RC} \tag{8}$$

where R is an Ohmic load resistance.

As each mechanism outlined above is easily distinguishable, one can use these equations to identify a self-discharge mechanism after recording the time dependent voltage of an electrode on open circuit.[4, 5]

The mechanism and rate of the self-discharge of ECs have considerable effect on the energy, capacity, and operation parameters, and often result in a decrease in their cycle life.[4] Self-discharge is most detrimental in applications where the EC is being used for long term storage. Some self-discharge is acceptable in certain applications where there are short time periods between charge and discharge. However, in cases where the EC is designed for accumulation and storage of energy or where there are appreciable periods of time between charge and discharge (*e.g.* solar cells) self-discharge behaviour is of major consequence. As the self-discharge of ECs brings about a loss of energy, it is advantageous to minimize this value.

The most widespread impurities found in activated carbon materials are Fe and Mn, and their presence may have a considerable effect on energy, capacity, and self-discharge of an EC.[71] These impurities can dissolve into solution, and cause an increase in the self-discharge value, as well as decreasing the energy and Coulombic efficiency. They may also decrease the overpotential of evolution of hydrogen and oxygen at the negative and positive electrodes respectively, limiting the operating voltage of the capacitor.[71]

2.8 Porous Electrodes and Penetration Depth

Electrochemistry is generally thought of as occurring at the surface of a planar electrode, and is seen as a two-dimensional process. However, porous electrodes are essentially three dimensional, and the electrode process (Faradaic reaction or double-layer charging/discharging) takes place within a volume, rather than at a plane, and the electrochemistry is then quasi-three-dimensional. The electrode process does not proceed evenly throughout the thickness of the electrode. It is faster on parts located closer to the counter electrode.[72] This is largely due to the *IR* drop in the solution within the pores. In other words, the external surface of the electrode charges/discharges faster than the surfaces within the pores.[73] If one imposes potentiostatic or galvanostatic conditions at the orifice of a pore, the potential or current deep within the pore changes more sluggishly than at the pore mouth. The fraction of the pore effectively playing a part in the charging process is referred to as the penetration depth.[2] The penetration depth increases with time in potentiostatic or galvanostatic measurements, and increases with decreasing frequency in alternating voltage or alternating current techniques. So after a very short time or at very high frequencies, one is essentially measuring the capacitance of the external electrode surface, as the pores are unable to follow the variations in potential or current.[2] After a certain lapse of time, or at lower frequencies, the influence of the pores becomes relatively important, as the inner electrode surface is usually very large in comparison to the outer one.[2]

Because of this distributive characteristic of porous electrodes, the energy density of an EC decreases with increasing power density. The useable energy in ECs diminishes as it is extracted at higher rates. It is therefore important to understand these distributed characteristics in order to maximize the energy density at desired power densities.[29]

2.9 Charge Redistribution

During charging of a porous electrode, the potential at the mouth of the pore climbs more quickly than at points located further down the pore. As a result, when the electrode is charged, and then switched to open circuit there is a distribution of potentials along the electrode surface. These potentials equalize, or in other words the charge redistributes over the electrode surface until all points are at an equal potential (Figure 2.6). This means that charges present in the outer electrode surface migrate toward the inner part of the electrode surface in order to even the potential gradient. Because the voltage of the electrode is measured at the external electrode surface, this charge redistribution results in a loss in potential upon switching to open circuit which adds to the potential loss due to other self-discharge processes at the electrode surface, increasing the overall self-discharge. During charge redistribution there is no loss of charge on the electrode, only a rearrangement of charges, but because the electrode potential is measured at the external electrode surface, this charge redistribution results in a potential loss on open circuit. This loss in potential due to charge redistribution is undesirable, as it reduces the amount of energy available, as the energy is proportional to the square of the voltage (Equation 2).

Charge redistribution can also take place in the same way after discharging a porous electrode. In this situation the surface area at the pore mouth is discharged more quickly than surface area deep within the pores, and upon switching to open circuit charge would move toward the pore mouth to even the potential distribution created during discharge.

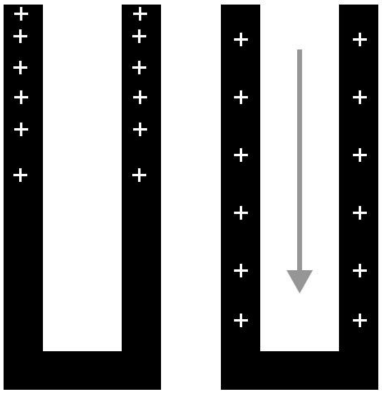

Figure 2.6: Schematic of (left) charge placed on a pore during charging and (right) charge redistribution on open circuit.

2.10 Pore Models

It was shown by de Levie that a transmission line equivalent circuit (Figure 2.7) could simulate the distributed characteristics in a pore.[2] In de Levie's transmission line model, the equivalent circuit of a pore is approximated by a line of resistive elements, *R*, and capacitive elements, *C*.[2] The resistors along the top of the circuit model the electrolyte resistance down the pore, the capacitors represent the double-layer capacitance at the electrode/electrolyte interface, and the electrode itself is assumed to have no resistance and is represented by the bottom half of the circuit.[13]

It was later showed by Hinman *et al*. that a thin layer cell can be described by the same equivalent circuit (Figure 2.8).[74] As with the de Levie model, the resistors represent the solution resistance. In this model the electrode/electrolyte interface is represented by an impedance, which models both the double-layer charging, using the capacitor, and a Faradaic reaction occurring at the interface, modeled by a resistor. In situations where there are no Faradaic reactions present, the resistance can be ignored, and the impedance is equivalent to the double-layer capacitance (Figure 2.8). This suggests that a thin layer cell may act as a good model to study the electrochemical behaviour of a pore.[74]

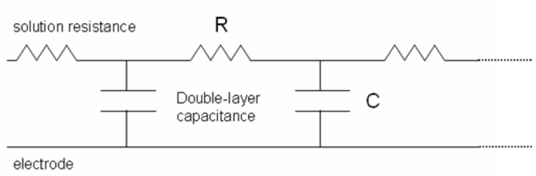

Figure 2.7: Section of de Levie's equivalent circuit of a pore. Modeled after figure from reference 2.

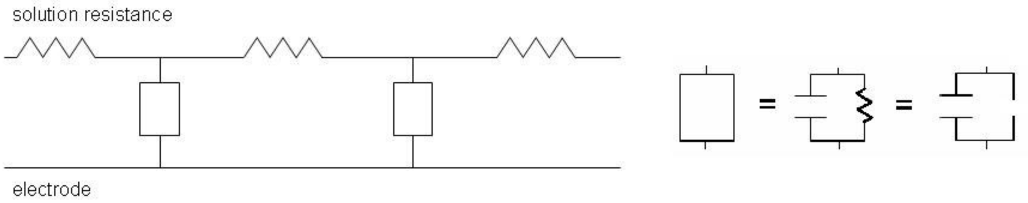

Figure 2.8: Model for potential distribution at thin layer cells. Modeled after figure from reference 74.

In a thin layer cell the electrolyte is confined within a thin layer (*ca.* 2-50 μm) at the working electrode surface. The reference electrode and counter electrode are placed near one end of the working electrode surface, and the thin layer of electrolyte lies over all of the electrodes. In the thin layer cell setup the current flowing between the working electrode and the counter electrode traverses the length of the thin solution layer. This introduces Ohmic potential differences along the length of the cell, as current flowing from the counter electrode to a point A, near the counter, encounters less resistance than current flowing to some point B, more distant from the counter electrode. The result is then a higher current density at A than at B, meaning the supply of reactants is altered more rapidly at A than at B (Figure 2.9).[72]

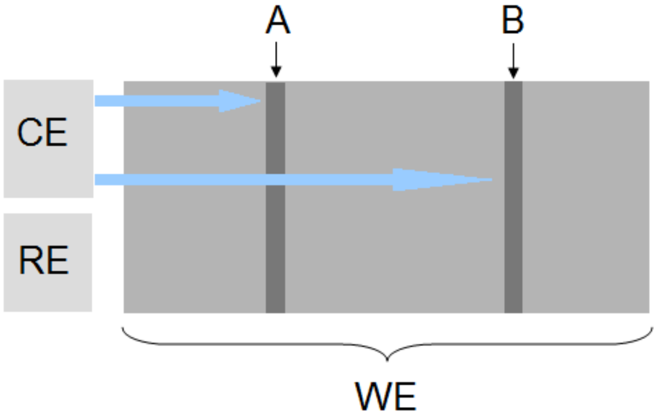

Figure 2.9: Schematic of a thin layer cell. Current traveling to point B on WE has to travel further, and therefore encounters more resistance than current traveling to point A.

This situation is similar to the situation within a pore of a porous electrode. The pores within a carbon-cloth electrode, however, generally have dimensions in the 1 - 10 nm range which are considerably smaller than solution layers found in thin layer cells. As can be seen from Equation 5, it is not simply the cross-sectional area, A, that is important to the value of the resistance, R, but rather the ratio of the length, l, to the area, since the length of the solution layer in a thin layer cell is very long compared to the cross-sectional area of the electrolyte, the ratio remains comparable to the ratio of length and cross-sectional area in a pore.

Posey and Morozumi used a mathematical model based on a one-dimensional porous electrode to determine potentials at various points down the electrode and at various times during galvanostatic charging experiments.[75] In their mathematical model a number of assumptions were made, including the absence of Faradaic reactions.[75] They were able to show that during a galvanostatic charging experiment, the potential at parts of the electrode located closer to the counter electrode was able to climb more quickly than in parts of the electrode further away.[75] While this modeling provides an approximation of voltage transients for real systems, the fact that real porous electrodes have many complicating parameters means the voltage transients predicted by these equations may not be in agreement with experimental results.

Yaniv and Soffer used an experimental arrangement where, by using separate reference electrodes at the front and rear side of a porous carbon electrode, they were able to record potential transients on either side of a porous carbon electrode during constant current charging/discharging.[73] A schematic of the setup used in shown in Figure 2.10.[73] The electrolyte used was 0.10 M NaCl. They compared the experimental data to mathematical data calculated for a theoretical porous electrode, flooded with electrolyte, in a tube of constant cross section, where the two ends of the tube were in contact with separate solutions of the same composition and the counter electrode is situated on one side of the porous electrode.[73] The *IR* drop for the rear side reference electrode was negligible compared to the *IR* drop for the front side reference electrode since the rear side reference electrode is screened from the *IR* drop by the porous electrode. Because of this their experimental and theoretical data from the front side of the electrode deviate significantly from one another, while the data collected with the rear side reference electrode agrees very well with the theoretical calculations.[73]

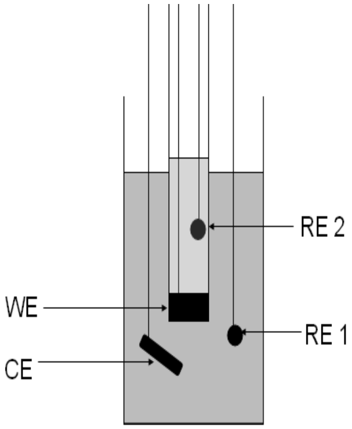

Figure 2.10: Schematic of the experimental setup used by Yaniv and Soffer. Modeled after figure from reference 73.

The Conway group used a RC-element hardware circuit to model the behaviour of a porous electrode based on the transmission line model proposed by de Levie (Figure 2.11).[76] In this hardware circuit the current and potential can be measured at each of the five connections down the circuit. Knowledge of the processes taking place along the entire length of the electrode can then be gained, rather than just looking at the behaviour at the front and rear of the electrode.[76]

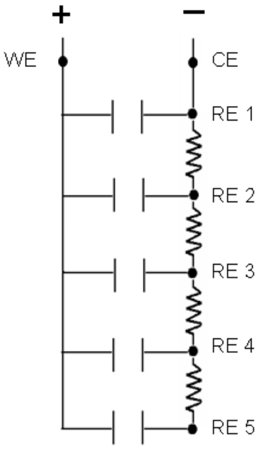

Figure 2.11: Schematic of transmission line hardware circuit. Modeled after figure from reference 76.

2.11 Electrochemical Measurements

2.11.1 Potentiostat

A potentiostat is used to control the potential applied to a working electrode relative to the potential of a reference electrode. A reference electrode is one which has a stable potential versus the potential of the standard hydrogen electrode (SHE). A SHE consists of a platinised Pt wire or mesh in a 1 M acidic solution, with H_2 gas bubbled through the solution. The SHE is based on of the reversible reaction: $2H^+ + 2e^- \leftrightarrows H_2$, and the potential of this reaction at standard conditions (1 M H^+, $\rho_{H_2} = 1$ atm) is by definition 0 V. However, when current is passed through a reference electrode, the electrode becomes polarized, altering the potential of the reference electrode. For this reason, it is important that only a small amount of current is passed through the reference electrode, in order for it to maintain a stable potential. Consequently, a third electrode is introduced, a counter or auxiliary electrode, which can supply current to the working electrode.

A simplified schematic of a potentiostat's electronics are shown in Figure 2.12. In a true potentiostat the circuitry is much more complex than described here. A principal component of the potentiostat is the operation amplifier. An operation amplifier has two inputs, V_+ and V_-, with high impedance, and one output of low impedance, $V_{out} = A\delta V$, where δV is the difference between the two input voltages, and A is the amplifier gain.[77] Typically, in a three electrode potentiostat, the working electrode is held at ground, and a potential is applied between this ground and one input of an operational amplifier, with the second input being connected to the reference electrode. Because of the high input impedance of the operational amplifier, the potential can be measured with only minimal amounts of current being drawn, such that the potential of the reference electrode is unaltered. The output of the amplifier is connected to the counter electrode, and due to the low resistance the current is allowed to flow freely between the counter and working electrodes.[78] Using a potentiostat, the working electrode can be set to a chosen potential by passing anodic or cathodic current through the counter electrode until the desired working electrode potential is reached.[79]

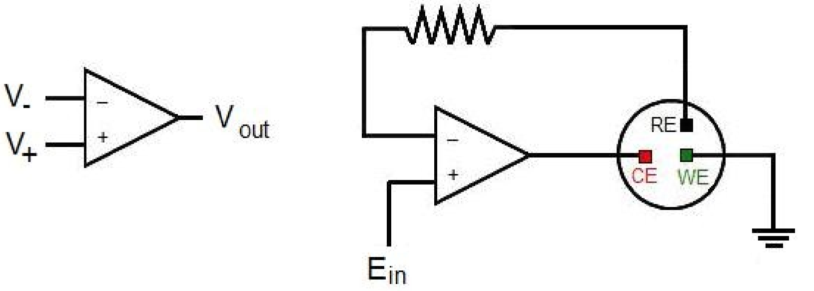

Figure 2.12: Schematic of an operational amplifier (left) and simplified version of a potentiostat (right).

2.11.2 Electrochemical Impedance Spectroscopy

In electrochemical impedance spectroscopy experiments, a sinusoidal potential, *e*, of small magnitude, *E*, typically 5 or 10 mV, is applied to a working electrode at various frequencies, *ω*, and the resulting sinusoidal current, *i*, is measured (Figure 2.13), which is of the same frequency but may be shifted in phase as:[80]

$$e = E\sin(\omega t) \tag{9}$$

$$i = I\sin(\omega t + \phi) \tag{10}$$

where I is the magnitude of the current oscillation, and ϕ is the phase shift.

Impedance, in general, is an opposition of alternating current, and can cause a phase shift between the potential and current. Both the phase shift, and the magnitude of the current are correlated to the resistive and capacitive components in the system.[80]

If a sinusoidal potential is applied across a pure resistor, R, the resulting current - according to Ohm's law - is in phase with the potential, and the phase angle is zero:[80]

$$i = \frac{e}{R}\sin(\omega t) \ . \tag{11}$$

For a pure capacitor, C, on the other hand, the phase angle is $\pi/2$ (Equation 12), and for more complicated circuits, intermediate phase angles are seen:[80]

$$i = \omega CE\cos(\omega t) = \omega CE\sin(\omega t + \pi/2) \ . \tag{12}$$

The impedance, Z(ω), is often represented in complex notation as:

$$Z(\omega) = Z_{\mathrm{Re}} - jZ_{\mathrm{Im}} \tag{13}$$

where $j = \sqrt{-1}$. Although the impedance is separated into real and imaginary components, Z_{Re} and Z_{Im}, both of these are real in the sense that they can be measured by phase angle.[80]

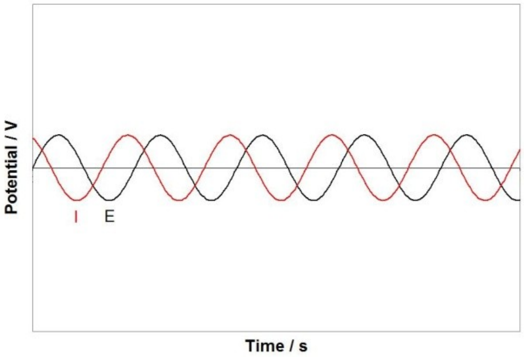

Figure 2.13: Potential and current profiles during an electrochemical impedance spectroscopy experiment.

Electrochemical impedance spectroscopy data can be displayed in a number of ways, however only a couple examples are discussed here, as a full explanation of electrochemical impedance spectroscopy is beyond the scope of this work. Electrochemical impedance spectroscopy can provide information on the frequency response of porous electrodes, or in other words the variation of the capacitive and resistive components of a system with the frequency of an applied alternating voltage. At very low frequencies (analogous to slow charging rates), there is a large penetration depth and the entire capacitance of the system is accessed. However, at higher frequencies (analogous to faster charging rates), the alternating signal does not penetrate the entire depth of the pores, resulting in some surface area deep within pores not participating in the charging/discharging process, which reduces the both the capacitance and the resistance, as the additional surface area is only accessed through additional solution resistance.

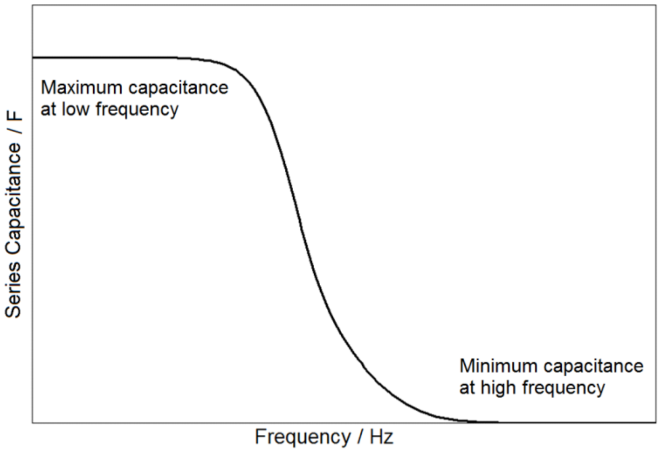

Figure 2.14: Relationship between capacitance and frequency of a porous electrode.

A Nyquist plot displays Z_{Re} versus $-Z_{Im}$, and each point on the Nyquist plot corresponds to a different frequency. An ideal capacitor is represented in the Nyquist plot as a vertical line (Figure 2.15). In porous electrodes, the penetration depth of the alternating signal increases as the frequency decreases which means that different surface areas area accessed at different frequencies. At very low frequencies the Nyquist profile of a porous electrode approaches that of an ideal capacitor, and Z_{Re} reaches a limiting value.

Electrochemical impedance data for various pore geometries have previously been calculated mathematically, and the electrochemical impedance profile was shown to be dependent on pore geometry.[7, 47] Eloot *et al.* demonstrated that the value of Z_{Re} is due to the resistance of the electrolyte within the pore, and found that a small pore radius at the pore mouth increases Z_{Re} more than the same pore radius at the pore base, due to a dampening of the a.c. signal down the pore.[7] For this reason, a narrowing pore would result in a smaller limiting value of Z_{Re} , $Z_{Re} < 1/3$ of the total electrolyte resistance than, would a pore which is broadening, Z_{Re} > 1/3 of the total electrolyte resistance, and for cylindrical pores the limiting value of Z_{Re} is 1/3 of the total electrolyte resistance.[7]

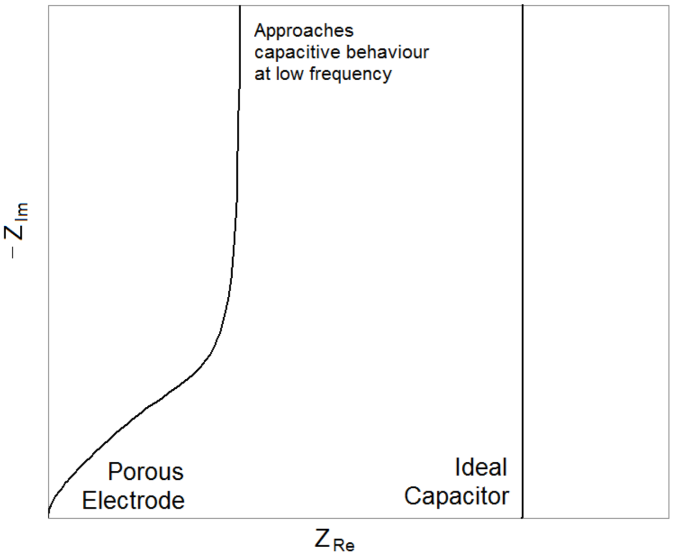

Figure 2.15: Nyquist plot for an ideal capacitor, and a curve representing a porous electrode.

Chapter 3

EXPERIMENTAL METHODS

3.1 Cell, Electrodes, and Electrolytes

Working electrodes were composed of either *ca.* a 10 mg piece of Spectracarb 2225 carbon cloth **(**Engineered Fibers Technology) or *ca.* 100 mg of one of the following carbon powders: Black Pearls 2000 (Cabot Corp.), glassy carbon powder (Sigma-Aldrich), graphite carbon powder (Sigma-Aldrich), or mesoporous carbon powder (Sigma-Aldrich, average pore diameter = 10 nm ± 1 nm), mounted in a Teflon Swagelok system (PFA tube fitting) with either a Pt disc or mesh current collector, or an ionically insulating, electronically conducting current collector (supplied by Axion Power International Inc.) and electrical contact to a Pt wire, sealed in glass tubing. Carbon powders were held in the Swagelok fitting by placing two layers of KimWipe lab tissue (Kimtech) on the bottom of the Swagelok. Counter electrodes were fabricated from the Spectracarb 2225 carbon cloth, wrapped with Pt wire for electrical contact. A standard hydrogen electrode (SHE) was used as a reference electrode when using acidic electrolytes, and a Ag/AgCl electrode was used as a reference electrode in neutral electrolytes. All potentials in electrochemical cells discussed in the document are referenced to the SHE, unless otherwise noted.

Experiments were performed in a three-compartment, three-electrode glass cell filled with a 1 M solution of H_2SO_4 (Sigma-Aldrich, 99.999% pure), HCl (Sigma-Aldrich, 99.999% pure, metal basis), NaCl (Sigma-Aldrich, 99.999% pure, metals basis), KCl (Sigma-Aldrich, 99.999% pure, metals basis), $CaCl_2$•$2H_2O$ (Sigma-Aldrich, minimum 99.0% pure), or $MgCl_2$ (BDH Chemicals, 98% pure) in 18 MΩ water. The reference compartment was separated from the working electrode compartment via a Luggin capillary. Nitrogen was bubbled through the working and counter electrode compartments prior to and during experiments to remove O_2 from the electrolyte.

3.2 Transmission Line Circuit

A hardware transmission line circuit was used as a model pore, based on the de Levie transmission line model for charging and discharging of a porous electrode.[2] A schematic of the transmission line circuit used in this work is shown in Figure 3.1. It consists of eight parallel sections, with each section being composed of a resistor and capacitor in series. The resistors model the solution resistance in the pore which leads to the potential drop down the pore during charging/discharging (based on Ohm's law). The capacitors model the capacitance of the double-layer at the electrode/electrolyte interface. Two equivalent hardware circuits were used in this research. In the first circuit the resistance could be set between 0 and 100 kΩ in 10 kΩ increments, or could be set to an infinite resistance. In the second circuit the value of the resistance can be set to a value between 0 and 300 kΩ in 0.10 kΩ increments, or may be set to an infinite resistance. Each capacitor was made up of a parallel combination of ten 10 μF/6.3 V multilayer ceramic chip capacitors, for a nominal capacitance of 100 μF. The capacitors in the hardware circuit could be shorted out (connected to ground) and were brought to a zero charge state (0 V) prior to each experiment.

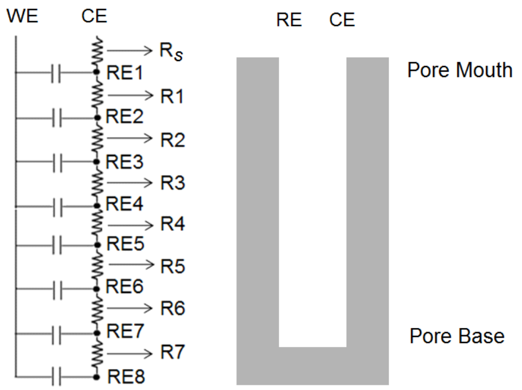

Figure 3.1: Schematic of hardware circuit based on de Levie's transmission line model[2] (left) and an EC electrode pore (right).

3.2.1 Activation-Controlled Discharge

The current, i_{net}, at an electrode in the presence of an activation-controlled reaction varies with the electrode potential, E, according to the Butler-Volmer equation:[79]

$$i_{net} = i_0 \left[\exp\left(\frac{((1-\alpha)nF(E-E_0))}{RT} \right) - \exp\left(\frac{-\alpha nF(E-E_0)}{RT} \right) \right] \qquad (14)$$

where i_0 is the exchange current density, α a symmetry parameter, n is the number of electrons involved in the reaction, F is Faraday's constant (96 485 C mol^{-1}), E is the electrode potential, E_o is equilibrium potential of the reaction, R is the universal gas constant (8.314472 J K^{-1} mol^{-1}), and T is the temperature. An experiment modeling an activation-controlled Faradaic discharge was created using EC-Lab software (v.9.55 – Bio-Logic) and a 100-step galvanostatic cycling with potential limitation (GCPL) technique. This technique allows the user to draw a constant current until the system reaches a given potential limit, upon which a new constant current is drawn until the next potential limit is reached. For example, after ramping the potential to 1.0 V, the instrument draws 6.484 μA of current until the potential drops to 0.998 V, at which time the instrument draws 6.237 μA of current until the potential drops to 0.996 V, and so on. The experiment was set to model a one-electron reaction with an equilibrium potential of 0.75 V, an exchange current density of 5×10^{-8} A cm^{-2}, a symmetry parameter of 0.5, at a temperature of 298 K. Because the multi-potentiostat is unable to draw currents below 0.1 μA the activation-controlled discharge can only be modeled down to an overpotential of 50 mV, below which the value of the current required, as calculated from the Butler-Volmer equation, is at a lower value than the multi-potentiostat is capable of drawing. The maximum current that could be drawn from the transmission line circuit was *ca.* 7 μA, as higher current than this would discharge the capacitors too rapidly, meaning that capacitor 1 would be completely discharged to 0.75 V before charge redistribution had begun. Given the i_0 used in this model, a 250 mV overpotential was the maximum used. The activation-controlled discharge was set to occur on capacitor 1 of the hardware circuit (RE1, Figure 3.1), which represents the pore tip.

3.2.2 Modeling Various Pore Geometries

Since the electrolyte resistance within a pore is inversely related to the cross-sectional area of the pore, a higher resistance in the hardware transmission line models a smaller pore cross-sectional area. To model various pore geometries using the hardware circuit, the values of the resistors were varied according to this relationship. For example, a cylindrical pore, which has the same cross-sectional area along the entire pore length, is represented in the hardware circuit with all resistors set to a common value. A cone shaped pore on the other hand, with a decreasing cross-sectional area down the pore is represented in the hardware circuit by having an increased value of resistance down the circuit (Figure 3.2).

To calculate the various pore shapes, the pore was divided into seven sections of equal surface area, as the surface area is directly related to the capacitance and each section of the hardware circuit contains a fixed capacitance. Although the circuit contains eight capacitors, the first capacitor corresponds to the external surface area of the electrode surface (outside of the pore), as the first resistor in the circuit (R_s, Figure 3.2) is set to 0. Each of the seven sections is assumed to be cylindrical in shape with varying dimensions of the length and cross-sectional areas depending on the value of the resistance. The resistance, R, relates to the length, l, and cross-sectional area, A, according to the equation 5. The resistivity is assumed to be constant. The cross-sectional area and surface area, SA, are related to the pore radius, r, and length according to:

$$A = \pi r^2 \tag{15}$$

$$SA = 2\pi r l \tag{16}$$

Combining the above equations, and assuming a constant ρ (set to 1) maintaining a constant surface area, the radius and length of each pore section was calculated from the following relationships:

$$R = \frac{1}{2\pi^2 r^3} = 4\pi l^3 \tag{17}$$

The resistances used to model each of these pore shapes are shown Appendix B4. Because there is a fixed capacitance in each section of the hardware circuit, and therefore a fixed surface area, a high resistance results in a long, narrow pore section, while a lower resistance results in a short wide section. This makes it more difficult to model pore shapes accurately.

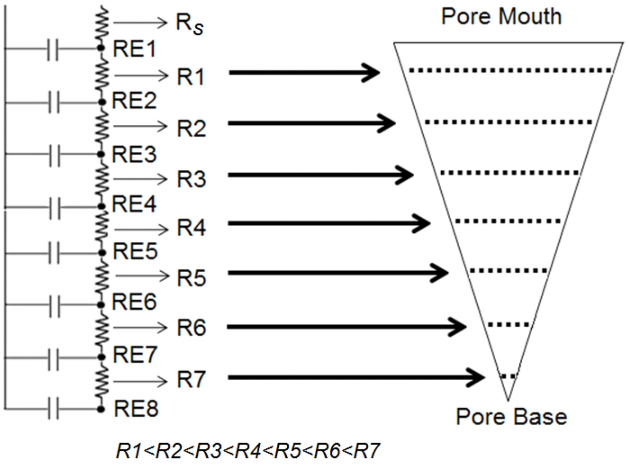

Figure 3.2: Schematic of the transmission line hardware circuit (left) and the relationship between pore cross-sectional area and the resistance used to model that area.

3.3 Electrochemical Measurements

3.3.1 Instrument

All electrochemical measurements were performed using a Bio-Logic VMP3 multi-potentiostat. Data were collected using EC-Lab software. The experiments were conducted at 22 ± 3 °C.

3.3.2 Procedure to Reach Steady State

Spectracarb 2225 carbon-cloth working electrodes were cycled between 0.0 and 1.0 V vs. SHE in 1 M H_2SO_4 using a sweep rate of 1 mV s^{-1} for one week (*ca.* 350 cycles) prior to self-discharge measurements in order to bring the electrodes to a steady state whereupon no further changes in the shape or size of the CVs were seen. The 0.0 and 1.0 V potential limits were used since at potentials outside of these limits, undesirable, irreversible Faradaic reactions occur which destroy the carbon-cloth electrode. This cycling was then followed by a soak in 18 MΩ for at least one week before performing further experiments in an electrolyte other than H_2SO_4.

3.3.3 Self-Discharge Measurements

Self-discharge experiments were performed on carbon electrodes by first ramping the potential of the working electrode from 0.5 V to the desired initial potential (ranging from 0.0 to 1.0 V) at various ramp rates (between 0.05 and 50 mV s^{-1}), then holding at this potential for a given amount of time (0 s – 75 hours). The system was then switched into open-circuit configuration and the potential of the working electrode was monitored over time. Open-circuit potentials were recorded for 2 – 30 hours. During open-circuit measurements there is a very high resistance to current flow (10^{12} Ω) which allows only a miniscule amount of current to pass in order to determine the potential. The instrument measures the potential 200 000 times per second, and data were recorded at different times depending on the experiment.

For self-discharge experiments in the presence of Fe, the potential of the working electrode was ramped from 0.0 to 1.0 V at 1 mV s^{-1}, and the potential was held at 1.0 V for 30 s. During the 30 s hold, 10.0 mL of 1 M Fe^{2+}/Fe^{3+} ($FeSO_4$•$7H_2O$, Sigma-Aldrich and $NH_4Fe(SO_4)_2$•$12H_2O$, Sigma-Aldrich), in 1 M H_2SO_4 was added to the cell containing 90.0 mL of 1 M H_2SO_4, resulting in a Fe^{2+}/Fe^{3+} concentration of 0.1 M. The electrolyte was stirred using a magnetic stirrer. After holding the potential of the working electrode at 1.0 V for 30 s, the system was then switched to open circuit and the potential was recorded over time.

A similar procedure was used for the transmission line circuit, except in this setup capacitor 1 (RE1) was charged from 0.0 V to a chosen final potential (ranging from 0.1 to 1.0 V) at various ramp rates (between 0.05 and 50 mV s^{-1}) and then held for the desired time (0 s – 120 min). The circuit was then opened and the voltages of all eight capacitors of the transmission line circuit (RE1 - 8) were recorded with time. For experiments utilizing an activation-controlled discharge the ramp and hold steps were followed by the activation-controlled discharge experiment on capacitor 1 (RE1) of the hardware circuit, while the potentials of the other seven capacitors (RE2 - 8) were recorded with time. To do this the working electrode (WE) leads of the multi-potentiostat were linked together and connected to the WE point on the hardware circuit (as shown by WE in the schematic in Figure 3.2). Similarly, the counter electrode (CE) leads were connected to the CE point. The reference electrode (RE) leads of each of eight channels were connected to points RE1 - 8 of the hardware circuit.

When examining charge redistribution up the hardware circuit (toward RE1) , capacitor 1 (RE1) was charged from 0.0 to 1.0 V, and held at 1.0 V until all capacitors reached the desired 1.0 V. The potential of capacitor 1 was then stepped to 0.0 V, and the potential of all capacitors were monitored over time.

3.3.4 Cyclic Voltammetry

Two cyclic voltammetry cycles were run prior to, and following each self-discharge experiment. For Spectracarb 2225 carbon cloth, Black Pearls 2000 carbon powder, and mesoporous carbon powder, cyclic voltammograms (CVs) were run at a sweep rate of 1 mV s^{-1} between 0.0 and 1.0 V vs. SHE. For graphite and glassy carbon powders, CVs were run at a sweep rate of 1 mV s^{-1} between 0.4 and 1.3 V, since at potentials below 0.4 V a large reduction wave is present in the CV.

Additional cyclic voltammetry cycles were performed on graphite carbon powder between potentials of 0.4 and 1.3 V at sweep rates between 1 and 500 mV s^{-1}, and also at 1 mV s^{-1} between potentials of 0.0 and 1.0 V.

3.3.5 Electrochemical Impedance Spectroscopy (EIS)

Electrochemical impedance spectroscopy (EIS) was run on Spectracarb 2225 carbon cloth and graphite carbon powder in 1 M H_2SO_4 at a potential of 0.75 V, with a peak amplitude of 5 mV, between frequencies of 200 kHz and 300 μHz. EIS experiments were also run on the transmission line circuit by connecting the working electrode lead of the potentiostat to WE of the hardware circuit, and the counter and reference electrode leads were connected to CE of the hardware circuit. EIS experiments were run at 0.0 V with a peak amplitude of 5 mV, between frequencies of 200 kHz and 300 μHz.

Electrochemical impedance data of different pore shapes were simulated using the Z-Sim function in EC-Lab software. The equivalent circuits used to simulate the data were based on the hardware transmission line circuit used in this work and consisted of eight sections of resistors and capacitors, as well as an expanded model consisting of 22 sections of resistors and capacitors (Figure 3.3). To model various pore geometries for simulated data the values of the resistors in the equivalent circuit were varied in the same way described in Section 3.2.2. The resistances used for each pore geometry are shown in Appendix B4. The total circuit capacitance for simulated data was kept constant at 800 μF. Data were simulated between frequencies of 200 kHz and 1 μHz.

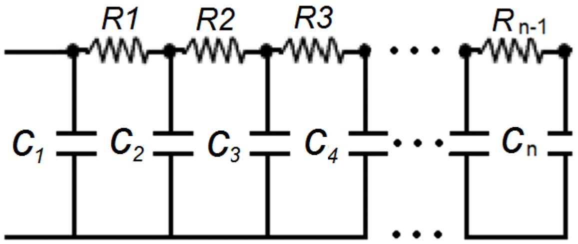

Figure 3.3: Equivalent circuit used to simulate impedance data, where *n* represents the number of capacitors, and was either 8 or 22.

3.4 Characterization Techniques

3.4.1 Brauner-Emmet-Teller (BET) Surface Area Measurements

Nitrogen isotherms of a 0.1866 g sample of Spectracarb 2225 carbon cloth, and a 0.515 g sample of mesoporous carbon powder were determined using a Micrometrics ASAP 2010, Folio Instruments, Inc. (Department of Physics, Dalhousie University). Samples were degassed at 200 °C for 24 hours. Surface area was determined using the BET method. The pore size distribution was calculated with the program DFT plus, using slit shaped pores and nonlocal density functional theory (DFT).

BET surface area measurements on mesoporous (0.175 g), graphite (0.158 g), and glassy (0.283 g) carbon powders were performed using a Micrometrics Flowsorb II 2300, Folio Instruments Inc. (Department of Physics, Dalhousie University).

3.4.2 Scanning Electron Microscopy (SEM)

SEM images of Spectracarb 2225 carbon cloth, mesoporous carbon powder, glassy carbon powder, and graphite carbon powder were collected using a Hitachi S-4700 SEM (Dalhousie University). Carbon samples were attached to the sample holder using double-sided conductive carbon tape, and images were taken at a pressure of 2×10^{-7} Pa.

3.4.3 Transmission Electron Microscopy (TEM)

TEM images of Spectracarb 2225 carbon cloth were collected by Dr. Ping Li using a Phillips FEI Tecnai 12 transmission electron microscope, at an operating voltage of 80 kV (Department of Biology, Dalhousie University). Samples were prepared by first embedding the carbon cloth into an epoxy resin, and 100 nm slices were obtained for imaging.

3.5 Thin Layer Cell

3.5.1 Cell Design and Construction

The thin layer cell design was adopted from the design used in reference 81. The first thin layer cell setup is shown in Figure 3.4a. It consisted of either one glassy carbon working electrode (SPI Supplies - 4 cm x 2.5 cm x 0.6 cm), or eight separate glassy carbon working electrodes (SPI Supplies - 0.4 cm x 2.5 cm x 0.6 cm) embedded in an epoxy resin (4.0 x 2.5 x 0.6 mm, Figure 3.5). The glassy carbon plates obtained from SPI were 5 cm x 5 cm with a thickness of either 3 or 6 mm, and were cut to the appropriate size using a handheld rotary tool with a diamond blade. Each working electrode is in contact with an aluminum current collector (0.5 cm x 2.5 cm x 1.9 cm, Figure 3.5), separated from one another by a piece of weigh paper. The working electrodes and current collectors were sandwiched between two PTFE blocks (Block A and B, 1.75 x 2.5 x 2.0 cm, Figure 3.6) held within a PTFE casing (9.0 x 5.5 x 4.0 cm, Figure 3.7). A bolt is then run through both blocks and the current collectors and tightened using a nut, with PTFE spacers placed between the PTFE blocks and the nut/bolt. One PTFE block has recessed spaces to hold the counter and reference electrodes, as well as an inlet for adding electrolyte to the cell. The counter electrode was a Pt mesh (1 cm x 1 cm, Figure 3.5). The reference electrode was either a Pt mesh pseudo-reference or a Ag/AgCl reference electrode. The second PTFE block contains a large recess which provides the option of using a larger counter electrode. There is also a large inlet which could possibly be coupled with an external reference electrode (*e.g.* SHE), and a second inlet for adding electrolyte to the cell.

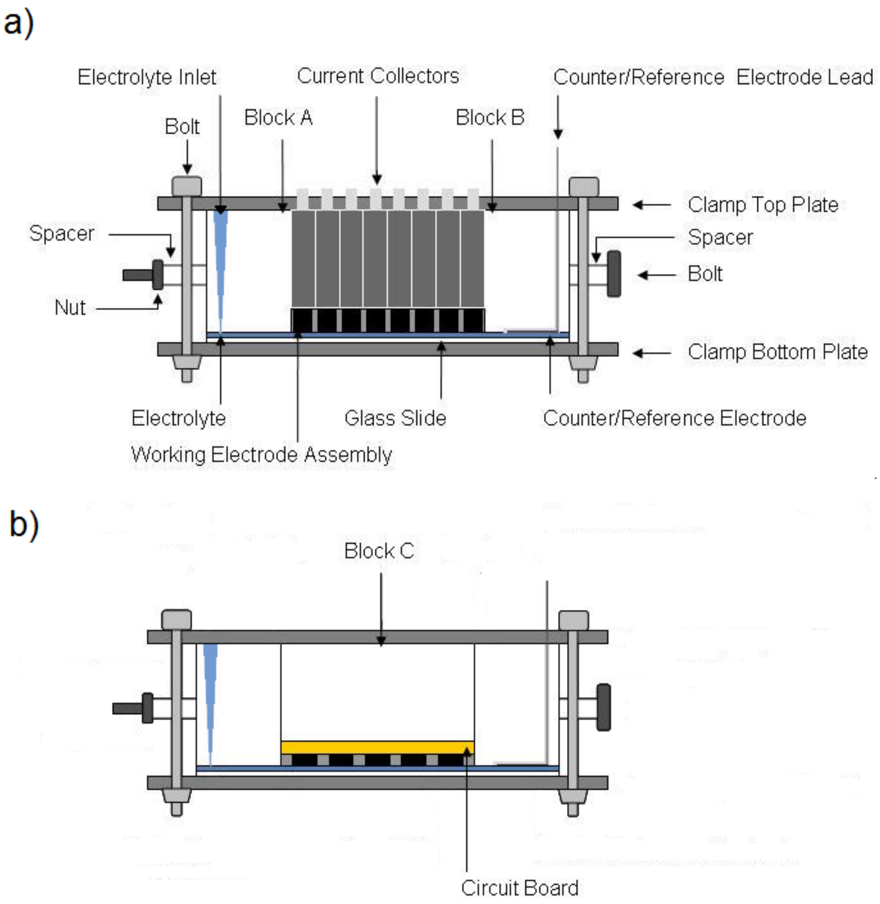

Figure 3.4: a) Schematic of first thin layer cell setup (side view). b) Updated thin layer cell setup where current collectors are replaced by circuit board and Block C, and a different working electrode assembly is used, with same labels as a).

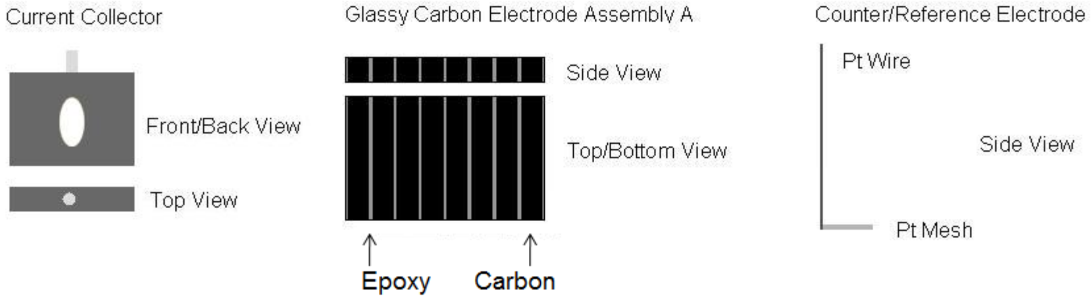

Figure 3.5: Schematic of aluminum current collector, assembly of eight glassy carbon working electrodes embedded in an epoxy resin, and the Pt counter and reference electrode.

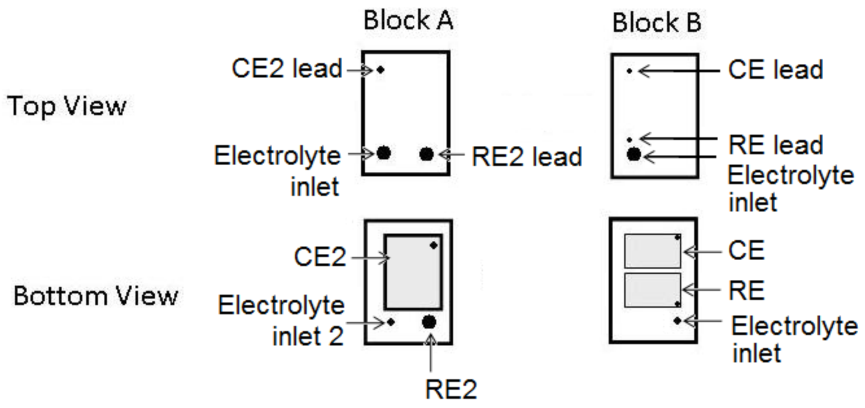

Figure 3.6: Schematic of PTFE block A and B.

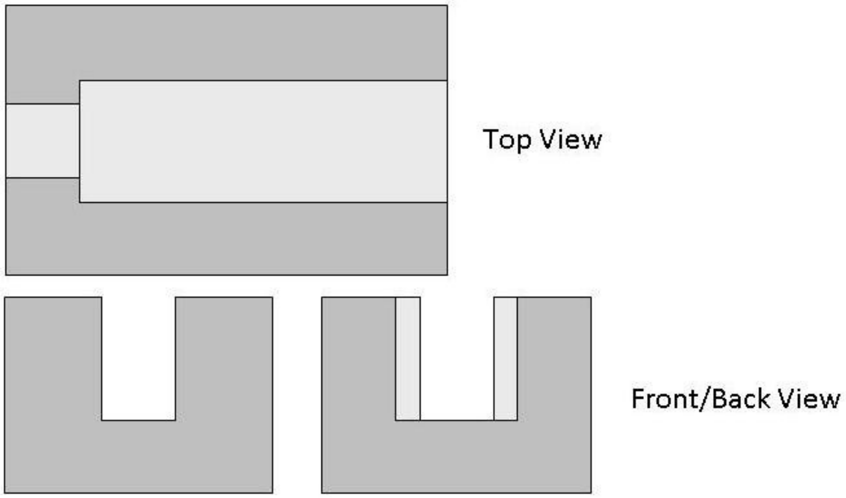

Figure 3.7: Schematic of casing used to assemble the thin layer cell.

When all components were joined together (Figure 3.8), the assembly was then removed from the casing, and placed on a glass microscope slide with a PTFE gasket (12.5, 25, 50, 125, 187.5 μm thickness, American Durafilm) separating the glass slide from the electrodes. The glass slide sits in a recess in the bottom aluminum plate (9.5 cm x 4.5 cm x 0.2 cm, Figure 3.9), which contains an opening such that the working electrodes are visible through the glass slide. This provides the option of running spectroscopic experiments *in situ*. The top clamp plate (9.5 x 4.5 x 0.2, Figure 3.9) was then placed on top, and four nuts and bolts were used to tighten the top and bottom plates together.

Later, this design was updated to replace the aluminum current collectors with a circuit board (3.0 x 2.5 x 0.1 cm, Figure 3.10). Because the circuit board could accommodate only five working electrodes, a new working electrode assembly with five glassy carbon electrodes (0.5 x 2.5 x 0.3 cm) was constructed (Figure 3.10), and an additional PTFE block (Block C, 4.0 x 2.5 x 2.0, Figure 3.10) was placed atop the circuit board. This setup is shown in Figure 3.4b.

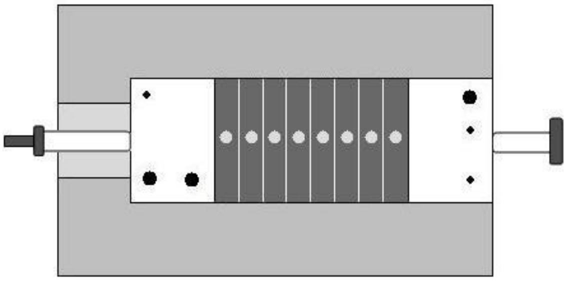

Figure 3.8: Schematic of casing with electrode assembly.

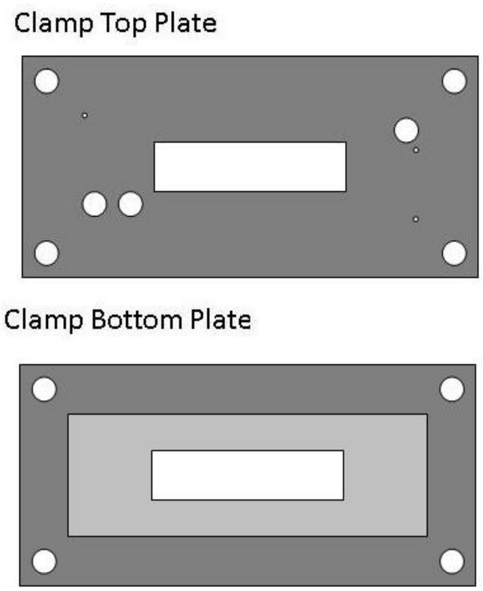

Figure 3.9: Schematic of aluminum plates used to hold thin layer cell together.

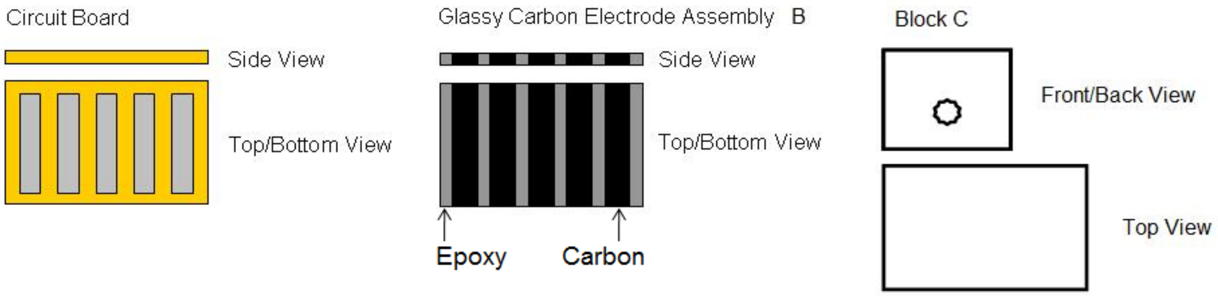

Figure 3.10: Schematic of circuit board, working electrode assembly B, and PTFE block C.

3.5.2 Electrochemical Experiments

Initial thin layer cell experiments were performed on a single glassy carbon working electrode placed in lieu of the working electrode assembly in Figure 3.4a. With this one-piece working electrode, either the eight current collectors shown in Figure 3.4a were used or a solid block current collector was placed in the position occupied by the multiple current collectors in Figure 3.4. For these experiments the working electrode lead for the potentiostat was connected to a post on the current collector, providing electrical contact with the working electrode. The reference and counter electrode leads were connected to the reference and counter electrodes, respectively. The electrolytes used in the cell were aqueous H_2SO_4 or NaCl solutions (0.01 – 1 M).

Thin layer cell experiments were also performed with multiple working electrodes, with a circuit board providing electrical contact to each working electrode independently. The circuit board is connected to a box which houses five separate posts, one for each working electrode, to which the potentiostat's working electrode leads were connected. The box for the circuit board also contains a switch which allows the five electrodes to be either electrically connected or separated. The counter and reference leads for each of the five channels were then connected to one another and connected to the counter and reference electrodes, respectively.

Cyclic voltammetry experiments were run in the thin layer cell at a sweep rate of 1 mV s^{-1} in various potential windows to determine the optimal potential window to run experiments using the thin layer cell. CVs were also used to determine if the electrolyte was leaking from the cell.

Self-discharge experiments were performed on the thin layer cell in which the potential of electrode 1 was ramped from 0.0 to 1.0 V at 1 mV s^{-1} (while either electrodes 1 - 5 were electrically connected, or separate from one another). After the potential ramp, the system was switched to open circuit, and the potentials of electrodes 1 - 5 were monitored over time.

Chapter 4

EFFECT OF CARBON SURFACE AREA AND CHARGING PARAMETERS ON SELF-DISCHARGE AND CHARGE REDISTRIBUTION

Part of this work was published as *"Effects of charge redistribution on self-discharge of electrochemical capacitors", Jennifer Black and Heather A. Andreas, Electrochimica Acta, 54 (13), 2009, 3568-3574.* All data examining the effect of different carbon surface areas and electrolytes are previously unpublished.

4.1 Introduction

This chapter examines various self-discharge profiles of a number of different carbons of varying surface area, including Spectracarb 2225 carbon cloth (*ca.* 2100 m^2 g^{-1}), Black Pearls 2000 carbon powder (*ca.* 1500 m^2 g^{-1}), mesoporous carbon powder (*ca.* 300 m^2 g^{-1}), graphite carbon powder (*ca.* 3 m^2 g^{-1}), and glassy carbon powder (*ca.* 1 m^2 g^{-1}). The high surface-area carbons (Spectracarb 2225 carbon cloth, Black Pearls 2000 carbon powder), which have high porosity, are expected to suffer from porous electrode effects, *i.e.* external surface area charges and discharges more quickly than surface area deep within the pores, due to the *IR* drop through the solution in the pores. Therefore, after charging, the potential of the external surface area is higher than the potential deep within the pores, and on open circuit charge redistribution takes place, such that the potential at the external surface decreases, as the potential at the base of the pores climbs in order to equalize the potential distribution. Although during charge redistribution there is no loss of charge on the electrode, and rather a rearrangement of charges, because the electrode potential is measured at the external electrode surface, this charge redistribution results in a potential loss on open circuit, which may look like a loss in potential due to a Faradaic reaction at the electrode surface which discharges the electrode. To determine the effect of charge redistribution on self-discharge, a number of self-discharge experiments were performed with various potential ramp rates, hold times, and initial charging potentials, as well as an examination of the self-discharge which results purely from charge redistribution using a transmission line model.

4.2 Results and Discussion

4.2.1 Cycling to Steady State

Figure 4.1 shows various CV cycles of a Spectracarb 2225 carbon-cloth electrode while being electrochemically cycled to steady state, and it is obvious from this figure that there is a significant change in the shape of the CV over time. During this cycling program there is development of a surface functionality on the surface of the carbon, evidenced by oxidation and reduction peaks at *ca.* 0.5 V (Figure 4.1). This surface functionality is believed to be a quinone group.[65, 82] The quinone groups contribute a pseudocapacitive Faradaic current at 0.5 V in the CV profile, via the redox reaction shown in Figure 2.5. So, as these groups develop, the shape/size of the CV changes (as seen in Figure 4.1). After no further changes in the shape/size of the CV are seen it can be assumed that the quinone groups are fully developed and the electrochemistry of the electrode is no longer changing. This takes approximately 350 cycles when cycling at a sweep rate of 1 mV s^{-1} (*ca.* one week). A sweep rate of 1 mV s^{-1} was chosen as it is relatively slow, allowing quinone groups to develop over the majority of the electrode surface (surface area accessed at a sweep rate of 1 mV s^{-1}). By bringing the electrodes to steady state prior to any testing it can be ensured that changes in the self-discharge profile and CV are not due to the development of the quinone groups, but are rather due to the self-discharge processes under study.

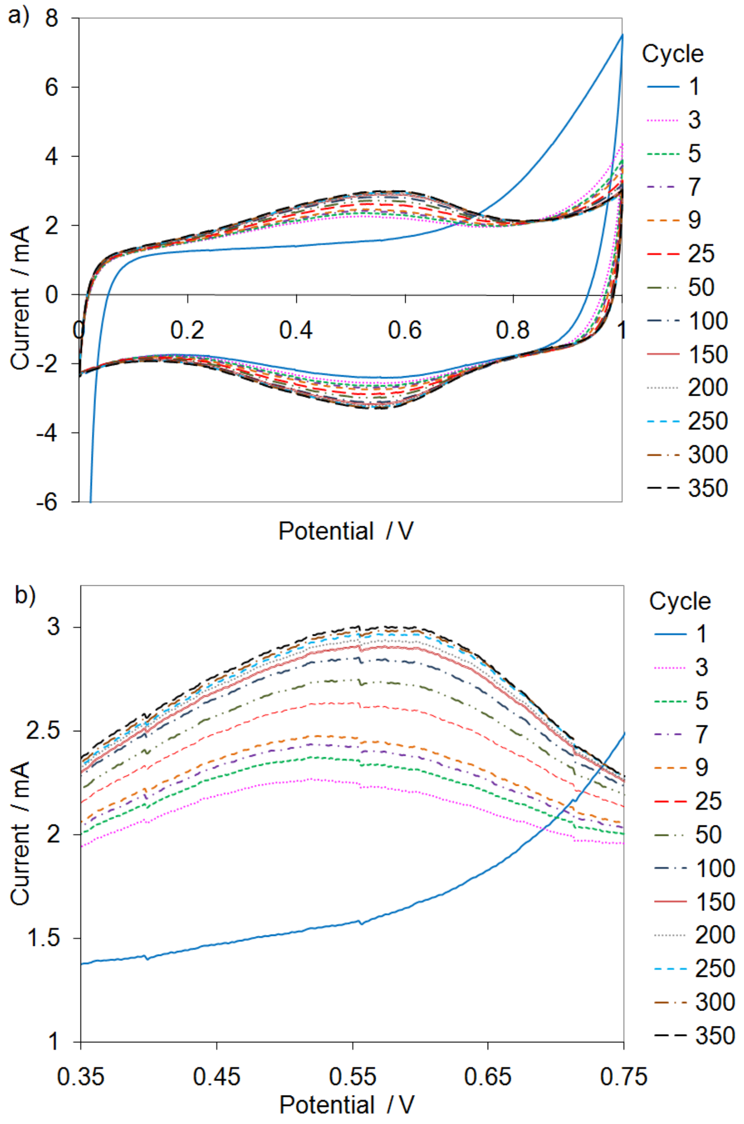

Figure 4.1: a) Various cycles of CV for a Spectracarb 2225 carbon-cloth electrode (9.1 mg, in 1 M H_2SO_4, with sweep rate 1 mV s^{-1}) approaching steady state and b) close-up of oxidation peak at *ca.* 0.5 V.

4.2.2 Examining Charge Redistribution Using a Hold Step in the Charging Process of Carbon Electrodes

4.2.2.1 Spectracarb 2225 Carbon Cloth

In order to detect the presence and degree of charge redistribution in the porous carbon, the potential of the working electrode was held at the desired initial potential for some period of time before the system was switched to open circuit. A very long hold step allows time for the entire electrode surface to reach the desired potential, minimizing any potential gradient developed in the pores during charging. Therefore, when the system is switched to open circuit no charge redistribution is necessary to equalize the potential on the electrode surface.

Figure 4.2a shows that for an electrode charged to 1.0 V, as the length of the hold step increases there is less potential drop over time, indicating a reduction in the self-discharge, which may be due to a decrease in charge redistribution. This is expected for a self-discharge process due to charge redistribution, since as the electrode is held at a constant potential, more time is available to allow the inner surface of the carbon to reach the desired potential. Therefore when the system is switched to open circuit, less charge movement is required to even the potential within the pores. These data is consistent with charge redistribution occurring in the porous electrodes, which is not unexpected given the porosity of the Spectracarb 2225 carbon-cloth electrode.

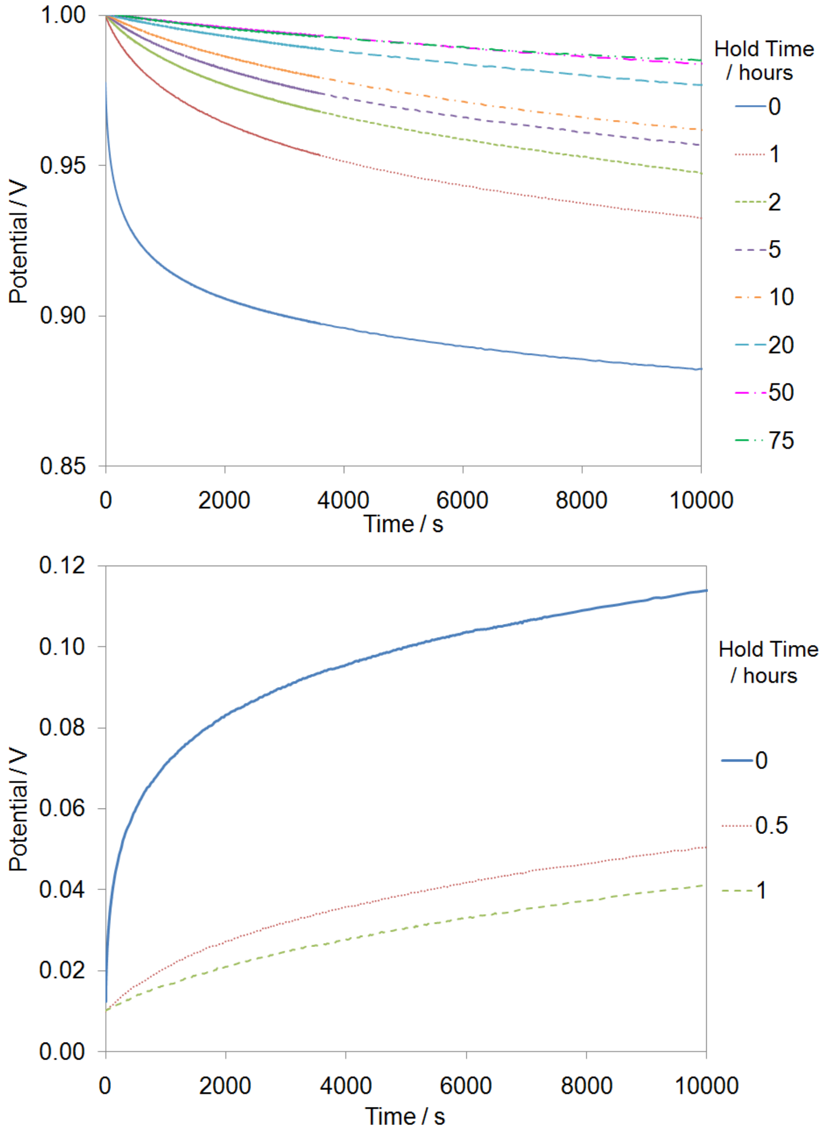

Figure 4.2: Self-discharge profile of a 9.1 mg Spectracarb 2225 carbon-cloth electrode in 1M H_2SO_4 with various hold times for an electrode charged from 0.5 V to (a) 1.0 V and (b) 0.0 V at 1 mV s^{-1}.

A major reduction in self-discharge is seen after a hold time of one hour, and as the length of the hold time increases beyond one hour, the decrease in self-discharge is less noticeable. The major reduction in self-discharge with a one hour hold time may suggest that a large part of the potential loss on open circuit, or a large part of the overall self-discharge experienced with this carbon is due to charge redistribution. As the hold time increases the curves start to approach one another. This is important because as the effect of charge redistribution is removed the curves should fall on top of one another, and since the curves approach one another as the hold time increases, this supports the idea that the effect of charge redistribution is diminished with the addition of the hold step. Nevertheless, even after very long hold times (> 50 hours) the self-discharge profile is still changing, consistent with the continued existence of charge redistribution (*cf.* 75 hour hold in Figure 4.2a).

Figure 4.2b shows the self-discharge profiles for the Spectracarb 2225 carbon cloth after various hold times at 0.0 V. A major reduction in the self-discharge is seen after 30 minutes of hold time, with a further decrease in self-discharge after a one hour hold time, consistent with a reduction in charge redistribution effects with increasing hold times. The hold time required to for the self-discharge profiles from 1 V to overlap is very long, and may suggest that the cumulative solution resistance in the pores is very high. Given that the electrolyte used was 1 M H_2SO_4 (high concentration of highly mobile protons in the pores), the incremental solution resistance should be relatively low. However, due to the large ratio of the length to cross-sectional area of the pores (meaning they are long and narrow) the cumulative solution resistance is quite high. This correlates nicely with the highly porous nature of the carbon, which gives it its very high surface area, as seen from SEM images (Figure 4.3) as well as the very narrow pores (< 2.5 nm) suggested by density functional theory (DFT) calculations on BET measurements (Figure 4.4).

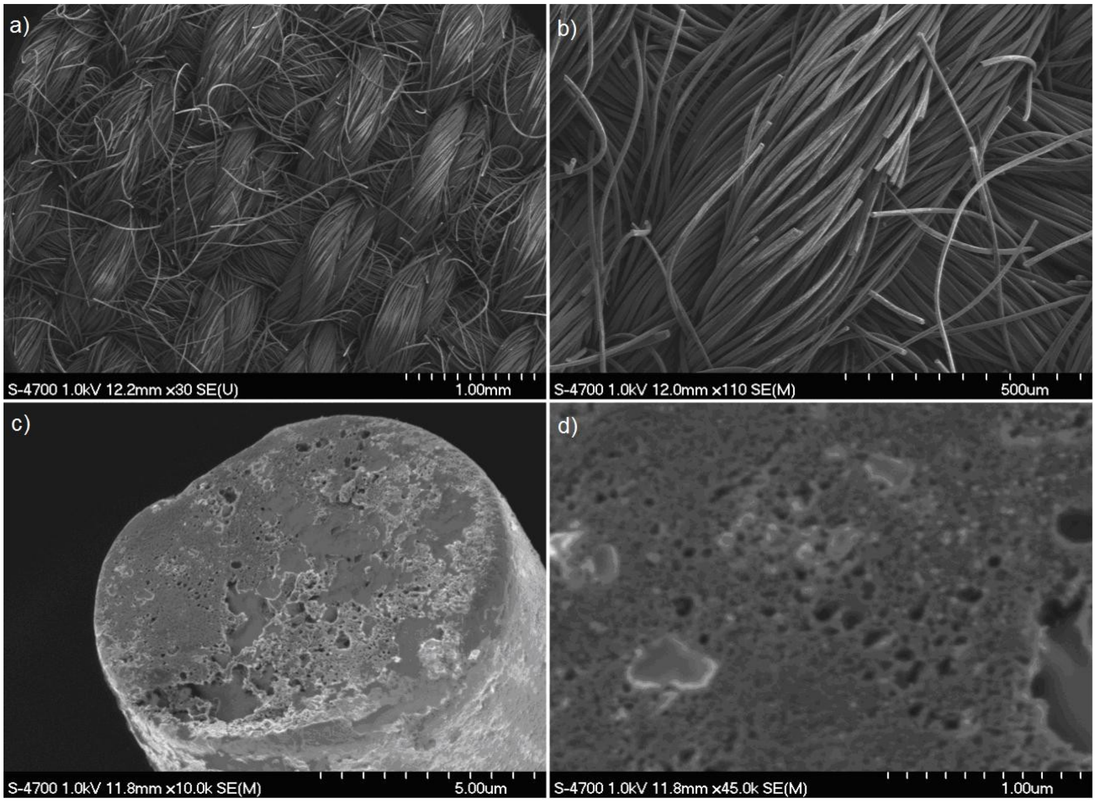

Figure 4.3: SEM images of Spectracarb 2225 carbon cloth.

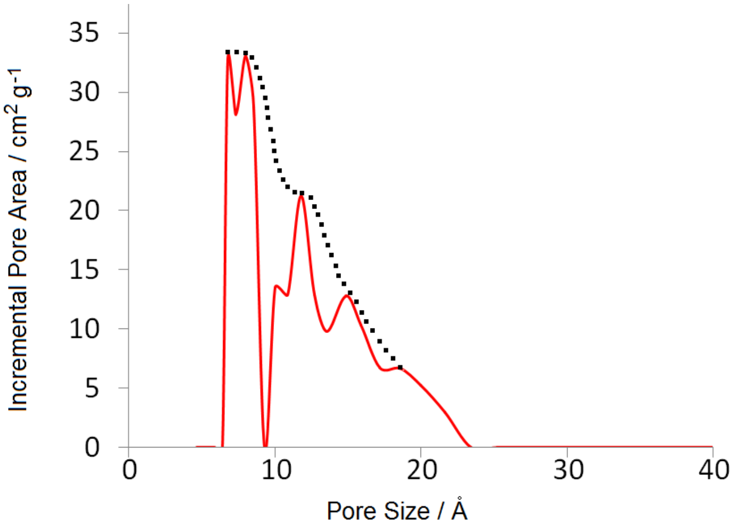

Figure 4.4: DFT calculation of pore size distribution based on BET nitrogen adsorption isotherm of 0.1866 g sample of Spectracarb 2225 carbon cloth (red, solid). Also provided is a more realistic estimation of the pore size distribution curve, wherein the sharp drops, which are often an artefact of the DFT calculations, were removed (black, dashed).

TEM images of Spectracarb 2225 carbon cloth were also collected in hopes of obtaining further information on the pore structure. Figure 4.5 shows TEM images at the maximum magnification of the instrument. Unfortunately, the images are not very clear, and individual pores are not seen, therefore no useful information is gained from TEM images.

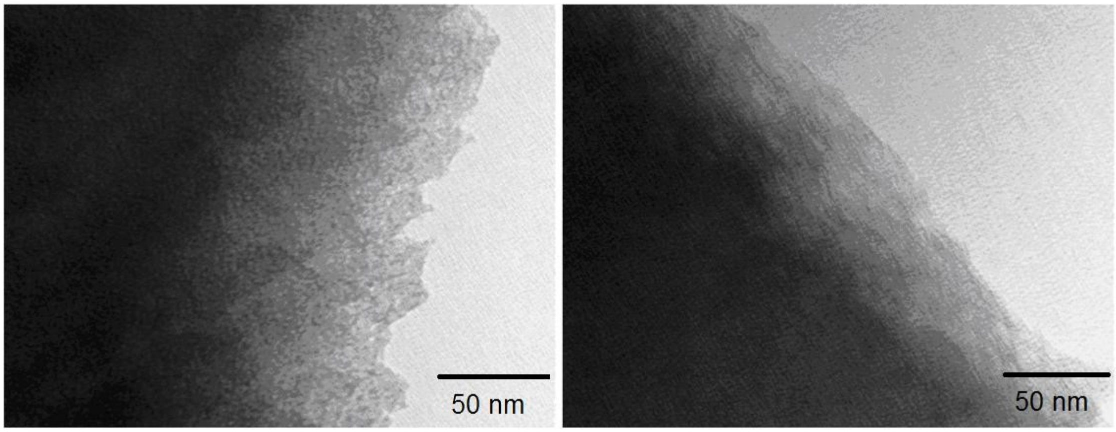

Figure 4.5: TEM images of a 100 nm cross-section of Spectracarb 2225 carbon cloth.

Alternatively, it is also possible that the reduction of self-discharge due to an increase in hold time at 1 V is not due to a decrease in charge redistribution effects, but rather to some change within the system, such as the electrode surface. For example, if during the hold step at 1 V, Faradaic reactions involving carbon surface functionalities present on the electrode surface were taking place, an increase in the hold time would simply provide more time for these reactions to occur. It is possible that part or all of the potential loss on open circuit is due to Faradaic reactions of carbon surface functionalities, and by reacting more of these groups during the charging and hold step there are less sites available to react during the open-circuit measurements, resulting in a decreased self-discharge.

Figure 4.6 shows the CVs obtained after each self-discharge experiment with hold times. The size/shape of the CV changes over time, after exposure to increasingly longer hold steps during self-discharge experiments. The anodic current below 0.5 V remains essentially constant, however between potentials of *ca.* 0.5 and 1.0 V the anodic current increases with hold time (the cathodic current changes essentially throughout the whole potential window). The anodic current being reproducible at lower potentials suggests that the increase in CV size is not due to an increased accessible surface area, as this should increase the current at all potentials, but rather to a change of electroactive carbon surface functionalities. In other words, during the long hold steps used for the self-discharge experiments, additional surface functionalities are formed which are able to perform oxidation and reduction reactions during subsequent CVs, increasing the current due to pseudocapacitance. Therefore, it is unclear whether the reduction in self-discharge with increasing hold time is due to a reduction in charge redistribution effects, or to changes in the carbon surface functionalities.

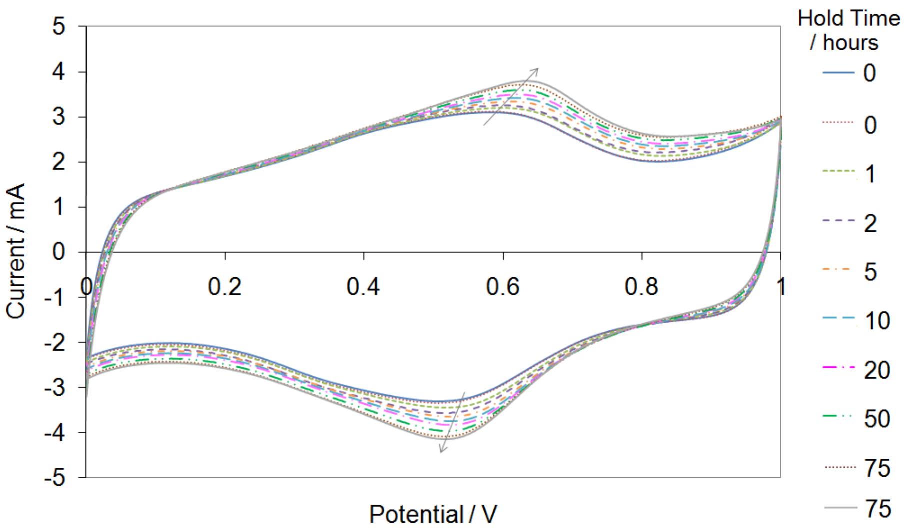

Figure 4.6: CV cycles of a 9.1 mg Spectracarb 2225 carbon-cloth electrode obtained after self-discharge experiments with various hold times at 1.0 V.

Since Faradaic reactions involving carbon surface functionalities (such as the oxidation/reduction of quinone groups) often require protons, similar experiments were performed in a neutral electrolyte, 1 M NaCl. Hopefully, in this way, the change of the self-discharge profile with hold time can be attributed to changes in the amount of charge redistribution, rather than changes in functional groups on the carbon surface. Figure 4.7a shows the self-discharge profiles of Spectracarb 2225 carbon cloth in 1 M NaCl after various hold times. As with the H_2SO_4 electrolyte, there is a decrease in the amount of self-discharge as the length of the hold step increases. Figure 4.7b displays the CVs obtained after each self-discharge experiment, and there are only small changes in the CV after exposure to long hold steps. This suggests that in neutral electrolytes during the hold step at 1 V there are no irreversible Faradaic reactions which alter the size/shape of the CV, as in acidic electrolytes. However, it is still possible that during the hold step a Faradaic reaction occurs at the electrode surface, possibly using up reactants, and therefore leaving less available to react during self-discharge. The reduction in self-discharge with hold time also correlates with what is expected for self-discharge due to charge redistribution. It is then possible that the reduction in self-discharge with increasing hold time may be due to either a depletion of a species involved in self-discharge, or to a reduction of charge redistribution effects.

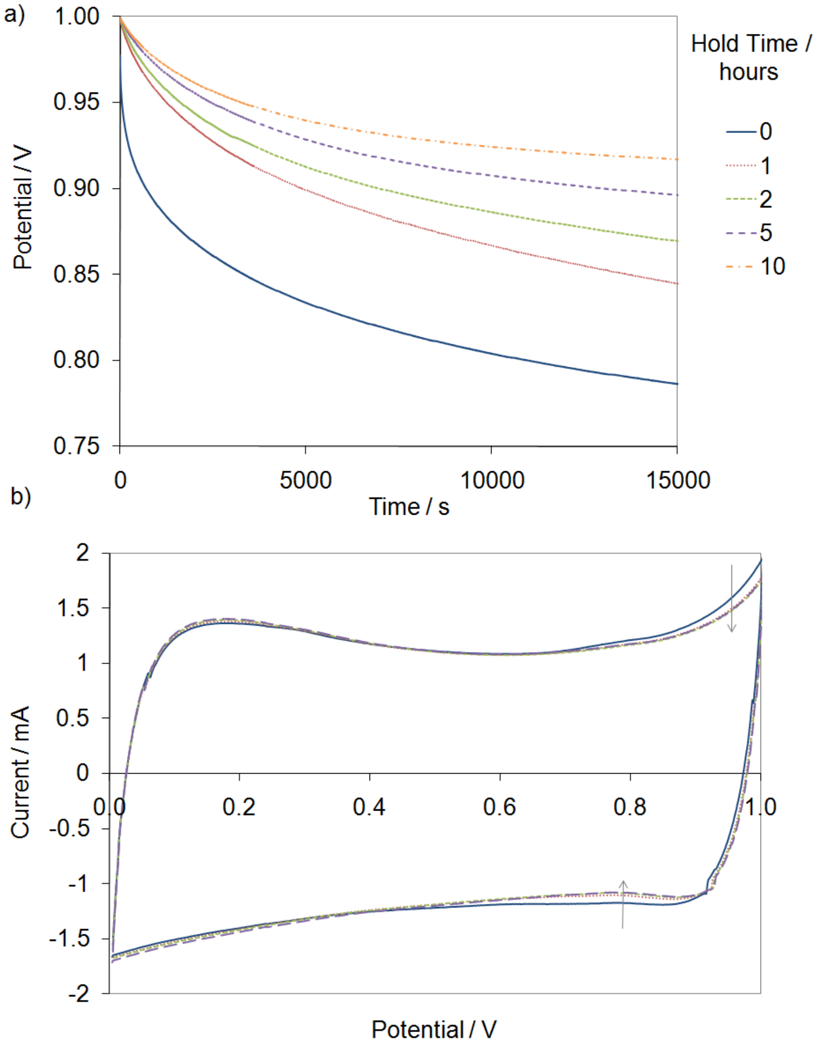

Figure 4.7: a) Self-discharge profiles of a 7.4 mg Spectracarb 2225 carbon-cloth electrode in 1 M NaCl after ramping from 0.5 to 1.0 V at 1 mV s^{-1} and holding at 1.0 V for 0 - 10 hours. b) CVs collected between each self-discharge experiment.

4.2.2.2 Carbon Powders

Self-discharge experiments with various hold times were also performed on various carbon powders to determine the extent to which charge redistribution affects the self-discharge profiles of the different carbon samples of various surface areas and pore structures. Four carbon powders were examined: Black Pearls 2000 carbon powder, mesoporous carbon powder, glassy carbon powder, and graphite carbon powder.

Figure 4.8a shows the self-discharge profiles of Black Pearls 2000 carbon powder in 1 M H_2SO_4 after charging to and holding at 1.0 V for various lengths of time. Results are similar to those obtained with Spectracarb 2225 carbon cloth in that there is a decrease in self-discharge with increasing hold time, consistent with charge redistribution being responsible for part of the potential loss during self-discharge. This is not surprising as Black Pearls 2000 is a high surface-area carbon (BET surface area of *ca.* 1500 m^2 g^{-1} [83]), and therefore charge redistribution is expected to be significant. With no hold time the potential of the Black Pearls 2000 rapidly drops to below 0.7 V in *ca.* 500 s, which is a significant loss in potential, and as the hold time is increased, there is a decrease in self-discharge, up to 20 hours of hold time. After 20 hours of hold time the self-discharge profiles begin to approach one another, possibly suggesting that the effects of charge redistribution have been essentially removed. This hold time is less than the hold time required for the self-discharge profiles of Spectracarb 2225 carbon cloth to overlap. The apparent correlation between the surface area and the amount of hold time required to get self-discharge to overlap is consistent with charge redistribution being a significant contributing factor to self-discharge.

Alternatively, it is also possible that the reduction in self-discharge with increasing hold times is due to a depletion of a species involved in self-discharge during the long hold time, as discussed in Section 4.2.2.1, and this possibility is further discussed below.

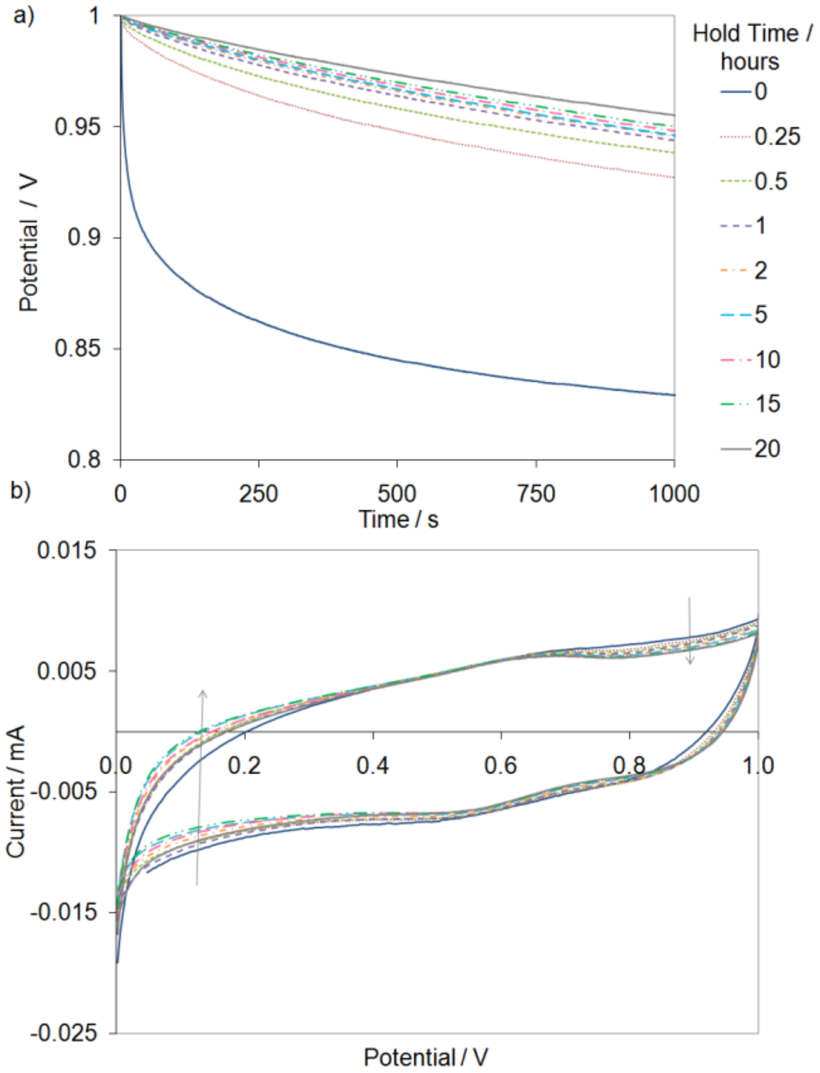

Figure 4.8: a) Self-discharge profile of a 30 mg Black Pearls 2000 carbon powder electrode in 1 M H_2SO_4 after charging from 0.5 to 1.0 V at 1 mV s^{-1}, with various hold times at 1 V. b) CVs at a sweep rate of 1 mV s^{-1}collected between each self-discharge experiment.

Figure 4.8b shows the CVs of Black Pearls 2000 carbon powder collected between each self-discharge experiment. The CVs contain a reduction wave at potentials below *ca.* 0.5 V, and the peaks found in Spectracarb 2225 carbon cloth, centered at *ca.* 0.5 V (attributed to oxidation/reduction of quinone groups) appear to be absent. The reduction wave decreases over time after each self-discharge experiment, suggesting that the system is altered over time (*e.g.* carbon surface functionalities). There is also a reduction of the anodic current close to 1 V with increasing hold time, contrary to results obtained with the Spectracarb 2225 carbon cloth where there was an increased anodic current near 1 V with increasing hold time. It is possible that changes in the self-discharge profile with various hold times are related to a depletion of a self-discharge species during the hold time, however, assuming the same self-discharge mechanism occurs on both the Spectracarb 2225 carbon cloth and the Black Pearls 2000 carbon powder, a correlation between the trend in the anodic current after exposure to long hold steps and the amount of self-discharge would be expected. Instead, a reduction in self-discharge is seen with both increasing (in the case of Spectracarb 2225 carbon cloth) and decreasing (Black Pearls 2000 carbon powder) anodic current near 1 V, which suggests that the reduction in self-discharge is related to charge redistribution effects, and not to an activation-controlled Faradaic self-discharge mechanism.

The self-discharge profiles of two low surface-area carbons were also examined: glassy carbon powder, and graphite carbon powder. Since these carbons have low surface area, and therefore contain very few pores, charge redistribution is not expected to play a major role during self-discharge for these carbons. Figure 4.9a shows the self-discharge profiles for glassy carbon powder in 1 M H_2SO_4 after various hold times. As with the previous carbons, there is a reduction in self-discharge with an increase in hold time; however, for the glassy carbon powder, after only 4-5 hours of hold time the self-discharge profiles begin to overlap, and the overall reduction in self-discharge is small compared to the larger surface-area carbons (Spectracarb 2225, Black Pearls 2000).

Figure 4.10 shows SEM images of the glassy carbon powder at different magnifications. It can be seen from the lower magnification (Figure 4.10a) image that the glassy carbon powder consists of 2-5 μm spherical carbon particles, which upon further magnification are seen to have very smooth surfaces which contain no pores. The surface area of this carbon obtained by BET measurements is 1 m^2 g^{-1}, which corresponds nicely to what is seen in the SEM images. Due to the absence of pores in this carbon, charge redistribution is not expected to significantly contribute to self-discharge, and a decrease in self-discharge with an increase in hold time was a surprising result for this carbon.

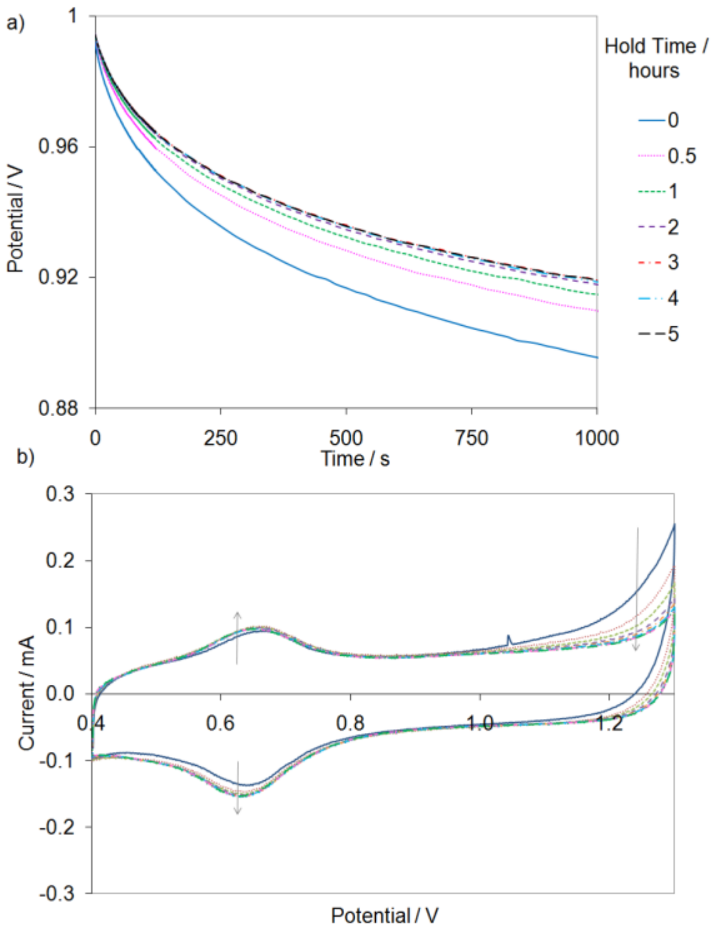

Figure 4.9: a) Self-discharge profile of a 0.1816 g glassy carbon powder electrode in 1 M H_2SO_4 after charging from 0.5 to 1.0 V at 1 mV s^{-1}, with various hold times. b) CVs at a sweep rate of 1 mV s^{-1} collected between each self-discharge experiment.

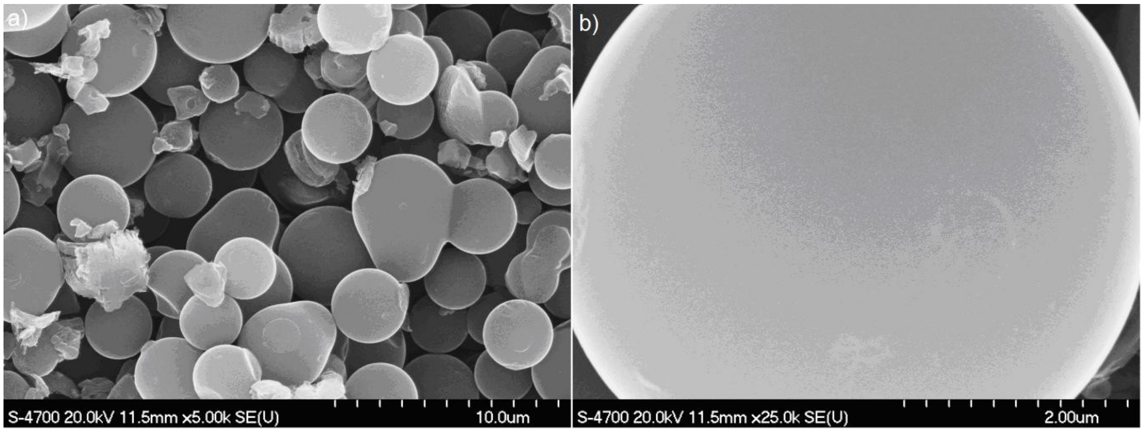

Figure 4.10: SEM images of glassy carbon powder.

Figure 4.9b shows CVs for glassy carbon powder obtained after each self-discharge experiment. The CVs contain a set of peaks centered at *ca.* 0.65 V, as well as an oxidation peak above *ca.* 1 V. There is a decrease in the oxidation peak above 1 V with time, accompanied by a slight increase in the peaks centered at *ca.* 0.65 V, suggesting the carbon surface is altered over time. Therefore, the small changes in the self-discharge profiles for glassy carbon powder with increasing hold times may be a result of alterations of the carbon surface, rather than a reduction of charge redistribution. This is consistent with charge redistribution not being a significant contributor to self-discharge in non-porous carbons.

Figure 4.11a shows the self-discharge profiles after various hold times for graphite carbon powder, and Figure 4.11b shows the CVs collected after each self-discharge experiment. Graphite carbon powder is a low surface-area carbon (BET surface area – 3 m^2 g^{-1}). The CVs for graphite carbon powder, like the glassy carbon powder, contain peaks centered at *ca.* 0.65 V. However, the CVs for the graphite carbon powder are more reproducible over time, with only a slight reduction in the anodic current at potentials above *ca.* 1 V, and no significant changes in the peaks centered at 0.65 V. This suggests that the surface of the graphite remains essentially unchanged over time. Trends in the self-discharge profiles for graphite carbon powder were similar to results obtained with the glassy carbon powder, with a slight decrease in self-discharge with increasing hold times up to *ca.* 4 hours, at which point the self-discharge profiles overlap.

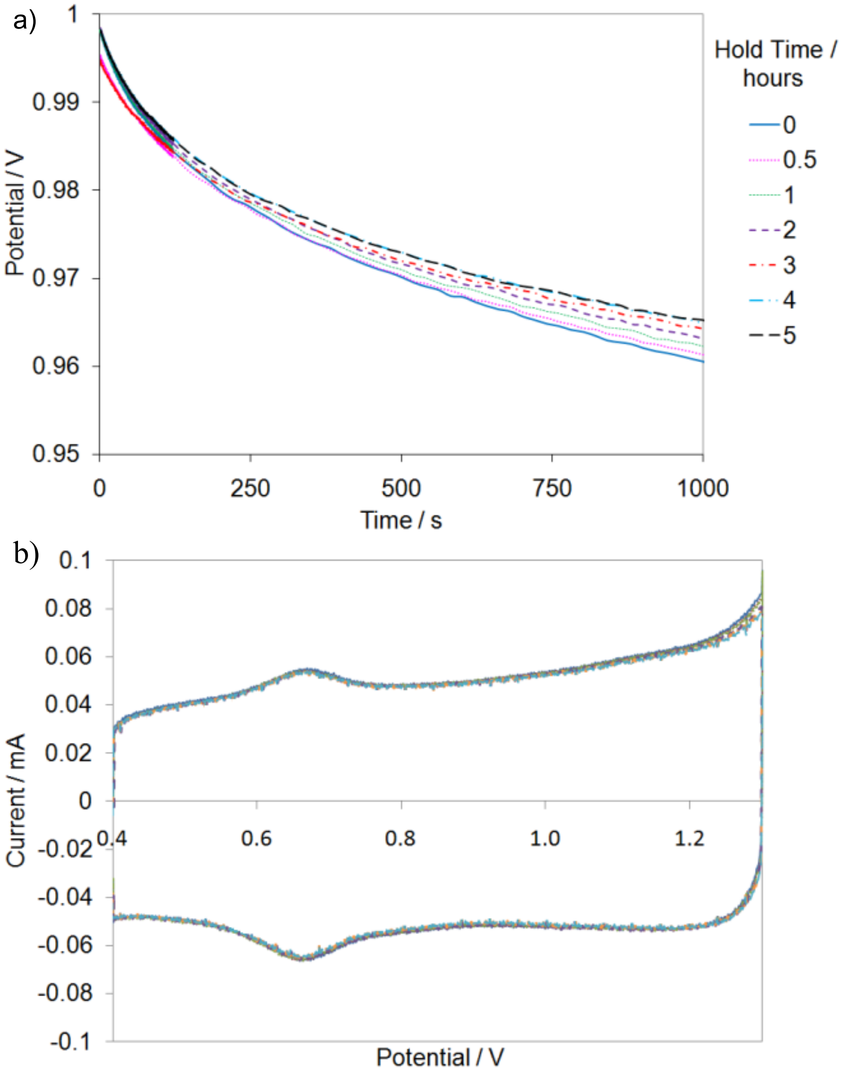

Figure 4.11: a) Self-discharge profile of a 0.2209 g graphite carbon powder electrode in 1 M H_2SO_4 after charging from 0.5 to 1.0 V at 1 mV s^{-1}, with various hold times. b) CVs at a sweep rate of 1 mV s^{-1} collected between each self-discharge experiment.

Figure 4.12 shows SEM images of graphite carbon powder which is made up of irregular shaped carbon particles 10 – 100 µm in size. At higher magnifications it can be seen that the particles consist of multiple graphene sheets, which have a fairly smooth surface, with no pores visible by SEM. Charge redistribution is therefore not expected to contribute significantly to self-discharge in this carbon. Given the low surface area, as well as the stability of the CVs over time, the decrease in self-discharge with increasing hold time for graphite carbon powder is a surprising result, as it cannot be easily explained by changes in surface functionalities or charge redistribution. However, it is possible that during the potential hold step at 1 V species involved in the self-discharge are depleted, resulting in less self-discharge with longer hold times. Also, graphite carbon powder is known to contain intra-granular pores (normally micropores or mesopores[84]) which may cause a small amount of charge redistribution after charging.

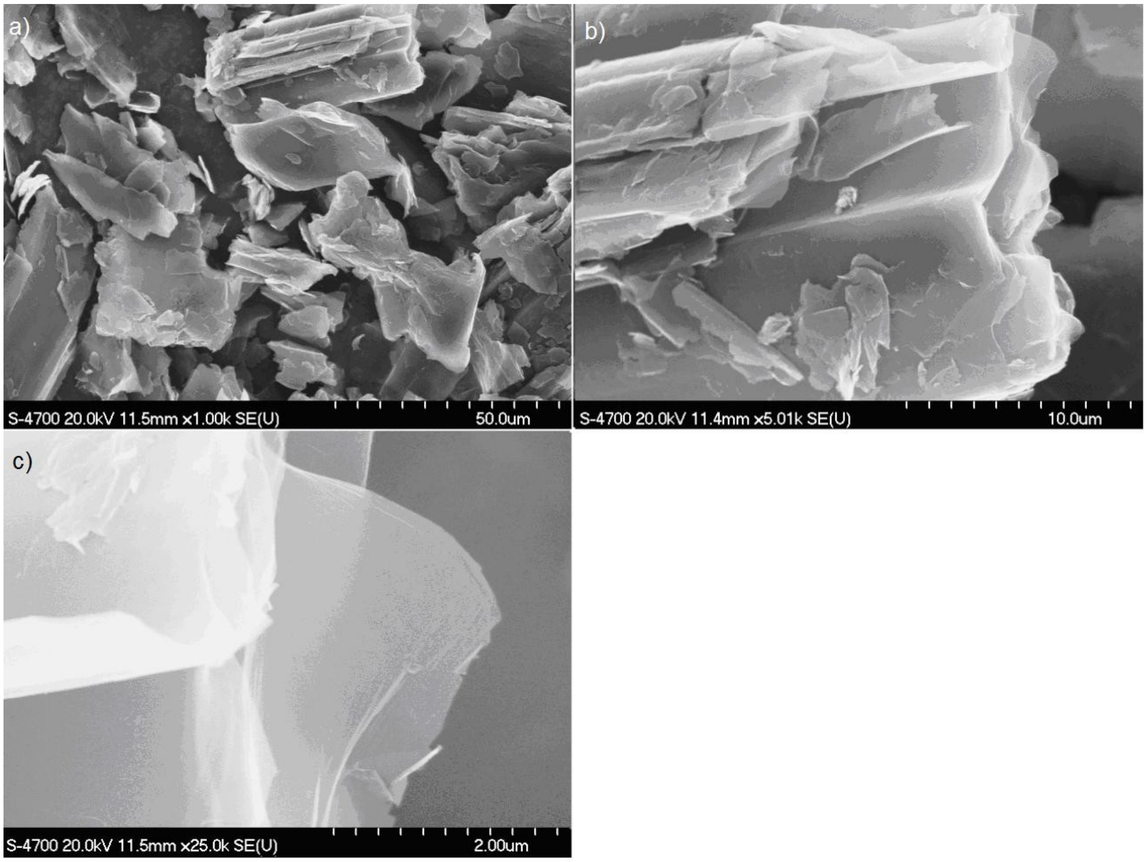

Figure 4.12: SEM images of graphite carbon powder.

Self-discharge experiments were also performed on a mesoporous carbon powder, which has a mid range surface area (BET surface area of *ca.* 300 m^2 g^{-1}). Figure 4.13a shows the self-discharge profiles of mesoporous carbon powder after various hold times.

Unlike the results obtained for the previous carbons, there is no real trend in the self-discharge profiles with hold time, and the hold time seems to have little effect on the self-discharge profile.

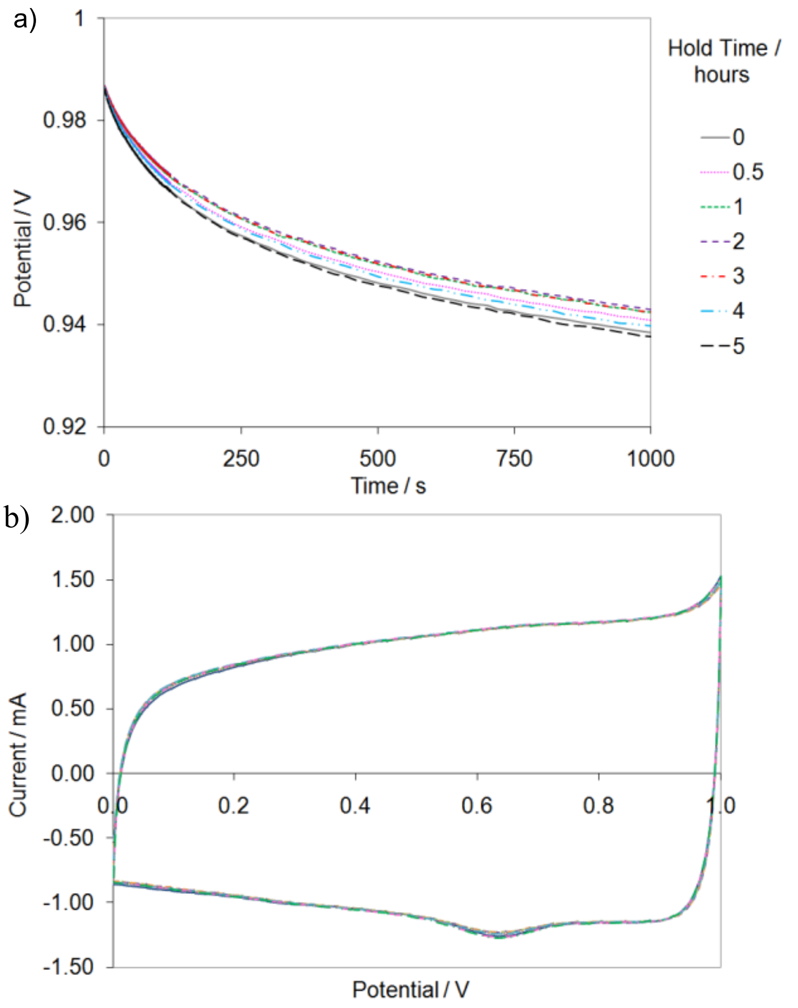

Figure 4.13: Self-discharge profile of a 0.0855 g mesoporous carbon powder electrode in 1 M H_2SO_4 after charging from 0.5 to 1.0 V at 1 mV s^{-1}, with various hold times. b) CVs at a sweep rate of 1 mV s^{-1}collected between each self-discharge experiment.

Figure 4.13b shows the CVs for mesoporous carbon powder collected after each self-discharge experiment. The CVs contain an oxidation peak above potentials of *ca.* 0.9 V, accompanied by a reduction peak at *ca.* 0.65 V. Both peaks decrease slightly over time, after each self-discharge experiment, but overall the CVs are very reproducible over time.

Figure 4.14 shows the SEM images of mesoporous carbon powder. The particle size for the mesoporous carbon powder is *ca.* 50 µm (Figure 4.14a). At higher magnifications it can be seen that the particles have a rough texture with large pores visible by SEM (Figure 4.14b and c).

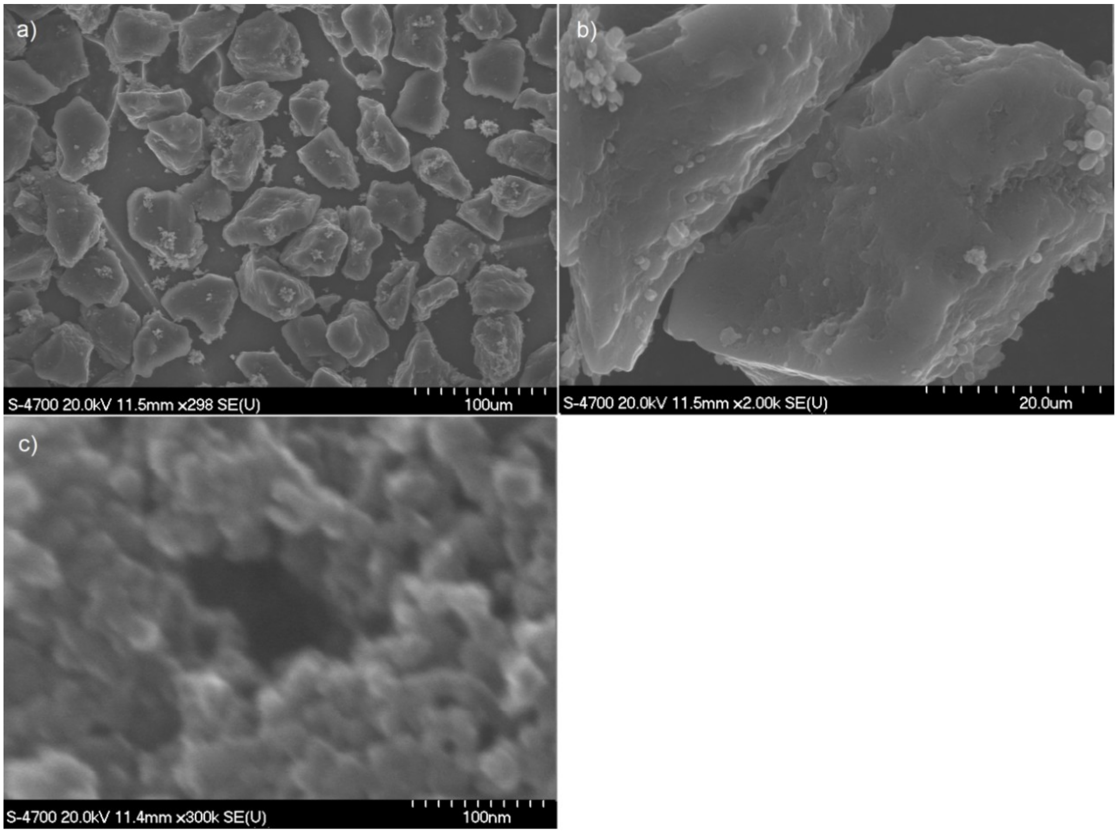

Figure 4.14: SEM images of mesoporous carbon powder.

Figure 4.15 shows the pore size distribution of mesoporous carbon powder calculated using DFT from BET nitrogen adsorption isotherms. The calculations predict a number of pores with an average diameter of *ca.* 5 – 25 nm, consistent with the average pore size given by the manufacturer (10 nm ± 1 nm). However, the DFT calculations also predict a large number of pores with a diameter of *ca.* 1 nm.

Because the mesoporous carbon powder contains very small pores (according to DFT calculations), it is expected to suffer from porous electrode effects, and therefore charge redistribution. However, it is possible that the surface area within the very small pores is inaccessible, and only the surface area within the larger pores is electroactive. This is one possible explanation why there is no correlation between the self-discharge profile and hold times for this carbon. If only the larger pores participate in charging, it is reasonable that the surface area is fully charged at the charging rate of 1 mV s^{-1} used in this study, and additional hold steps are not required to remove charge redistribution effects.

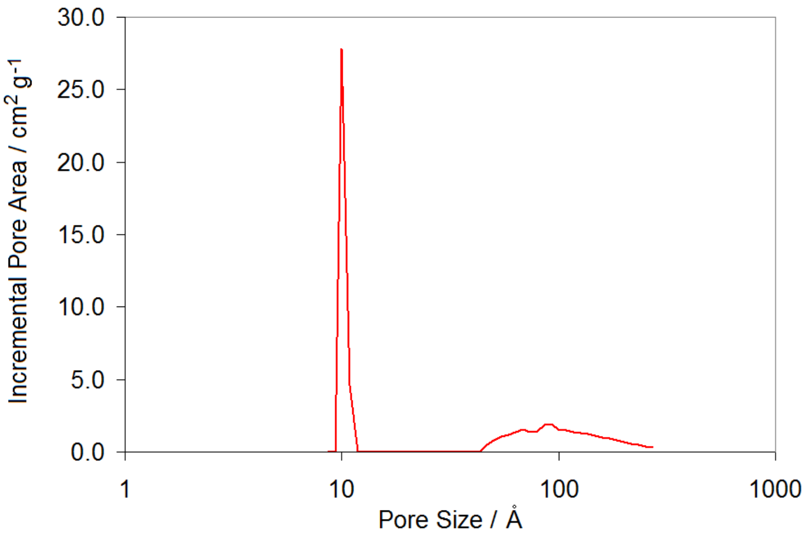

Figure 4.15: DFT calculation of pore size distribution based on BET nitrogen adsorption isotherm of a 0.5150 g sample of mesoporous carbon powder.

4.2.3 Examining Charge Redistribution Using a Hold Step in Hardware Circuit

The distributed potential within a pore which results from charging/discharging, and leads to charge redistribution, can be modeled with a transmission line circuit (as shown in Figure 3.1). Thus, a hardware transmission line circuit is used to study charge redistribution and the self-discharge profile it produces, as well as the effects of hold steps on the resulting self-discharge profile.

The capacitor at the top of the circuit (RE1) represents the behaviour at the mouth of the pore, while capacitors further down the circuit represent the behaviour further down the pore. Figure 4.16a shows that during charging of the hardware circuit the potential at RE1 climbed more quickly than the potential at RE2, and so on, due to the added resistance down the length of the circuit. At the end of the charging process the terminals at the "pore mouth" (*e.g.* RE1 and 2) were at significantly higher potentials than those at the "pore base" (*e.g.* RE7 and 8). This distribution of potentials leads to charge redistribution on open circuit, shown in Figure 4.16b, where the potential of the capacitors near the top of the circuit fell, while the potential of capacitors near the back of the circuit climbed until all potentials had equalized, requiring approximately 150 s.

Since the potential measured at a porous working electrode is the potential present at the pore mouth, or outer surface area of the electrode, charge redistribution results in a loss of potential on open circuit for a positively charged electrode. It is important to point out, however, that this potential loss is not due to a loss of charge on the electrode, but is rather a rearrangement of the charges within the electrode. This loss in potential may then look like a potential loss due to a Faradaic reaction at the electrode surface discharging the electrode. However, Figure 4.16c shows that if a hold step is added after the charge, the potential of terminals RE2-8 climb toward the desired 1.0 V during this hold step, and for long enough hold times (*ca.* 600 s) all terminals reach 1.0 V. When this condition has been achieved (all the capacitors at the desired potential), there are no charge redistribution effects, as there is no longer a potential gradient to drive charge redistribution.

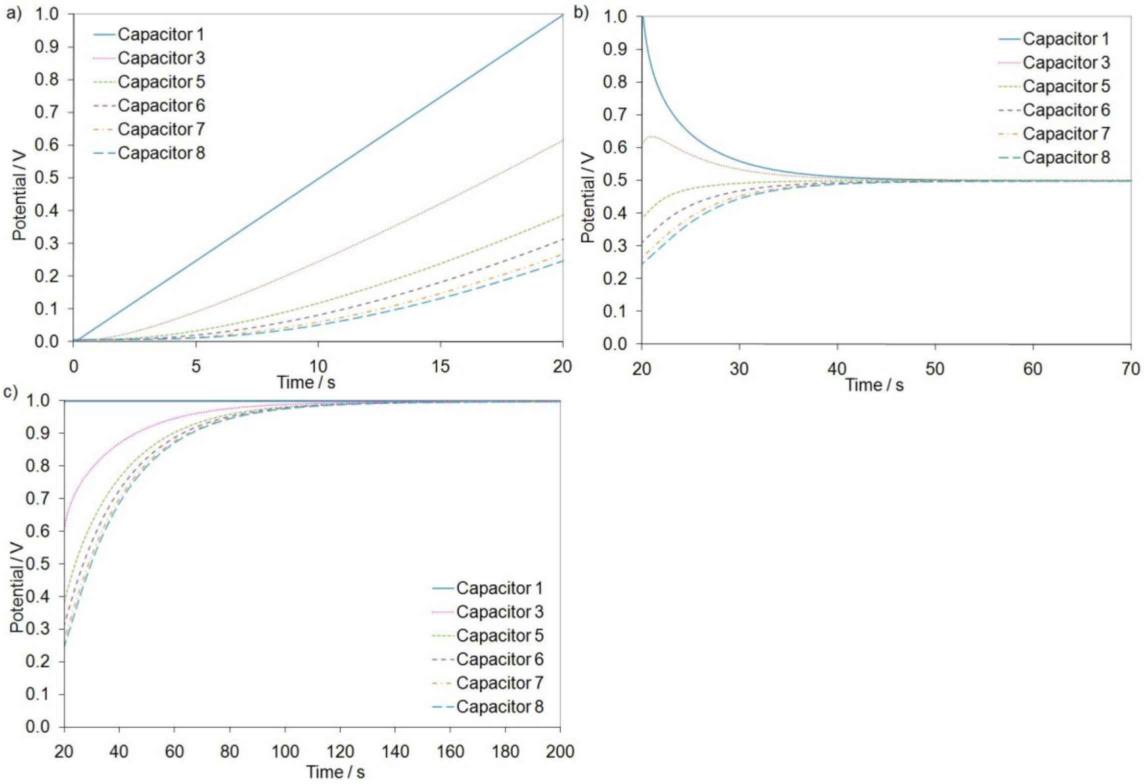

Figure 4.16: Data taken from the hardware transmission line circuit at various positions down the transmission line circuit during a) charging, b) self-discharge with no hold, and c) a hold step. In each case, the resistances were set to 50 kΩ and the voltage of the first capacitor was ramped from 0.0 V to 1.0 V at 50 mV s^{-1}.

Figure 4.17 shows that as the length of the hold step increased, capacitor 1 (RE1), or the "pore mouth", undergoes less self-discharge due to charge redistribution throughout the circuit, resulting in higher equalization potentials. Thus, the addition of a hold step in the charging profile may act as both a diagnostic for the presence of charge redistribution and as a means for minimizing charge redistribution in porous electrodes.

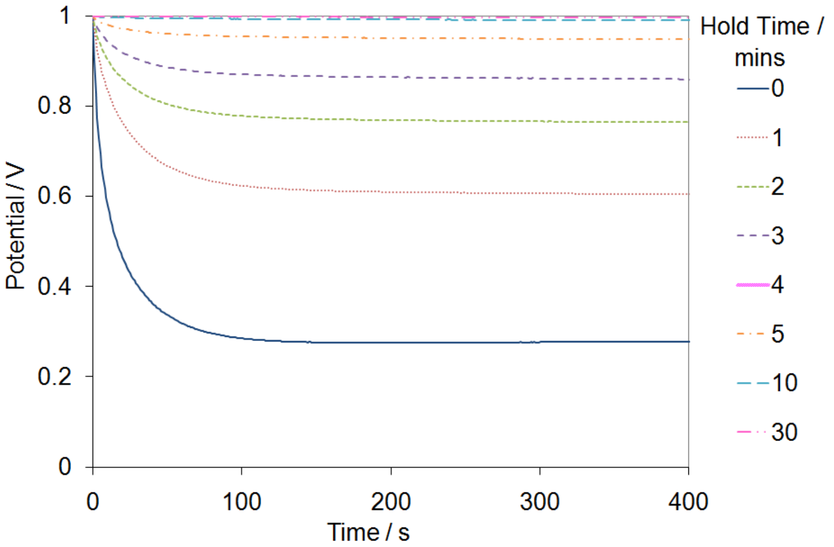

Figure 4.17: Self-discharge profile of capacitor 1 (RE1) of hardware transmission line circuit after ramping the potential of capacitor 1 at 50 mV s^{-1} from 0.0 to 1.0 V with various hold times. All resistors were set to a value of 50 kΩ.

Due to the distributive properties of the hardware circuit, a potential gradient is formed during charging similar to the situation within a pore, and as such this circuit is used to model charge redistribution within a pore. So far the data obtained using the hardware circuit agrees with the data collected on the high-surface-area carbons, suggesting that this transmission line model may in fact be a satisfactory model for porous electrodes.

In a typical porous electrode system, it is difficult, if not impossible, to determine when charge redistribution is complete (*i.e.* the time required to reach the equalization potential). Data obtained with the hardware circuit suggests that the time required for charge redistribution to complete on open circuit (the completion time is defined as the time at which there is a difference of < 5 mV between potential at RE1 and RE8) is shorter than the hold time required for the whole system to reach the full charging potential (defined as the time at which there is a difference of < 5 mV between potential at RE1 and RE8) (Table 2). Due to the scale this small difference in potential is difficult to see in Figure 4.16b and Figure 4.16c.

That the time required for charge redistribution is shorter than the hold time required for the whole system to reach full charge can be justified in terms of the total amount of charge present in the system. When all the capacitors in the circuit have reached 1.0 V, there is more total charge in the system than the case where only the first capacitor has been brought to 1.0 V, and the remaining capacitors are at some potential lower than this. Since there is less charge present during charge redistribution, less time is required for the charge to redistribute. The hold time required to reach full charge increases more quickly than the charge redistribution time with increasing resistance, resulting in an increasing ratio with increasing resistance. The ratio obtained for resistances used in this study (10 – 300 kΩ) ranged between 4.4 and 9.7, and suggests that a system requiring a hold time of tens of hours would likely require a charge redistribution time of hours, rather than seconds.

Previously, Conway *et al.* predicted that the charge redistribution in the Spectracarb carbon cloth required 100 s to complete charge redistribution.[3, 5] The data from the hardware circuit suggest that a solution resistance of 50 kΩ, which only requires 600 s to remove charge redistribution completely, requires approximately 150 s to complete charge redistribution. Results from Section 4.2.2 showed that the hold time necessary to remove the effects of charge redistribution were very long (> 50 hours), which when combined with the results here, suggest that the charge redistribution time is much longer than previously assumed.

Table 2: The hold time required to reach full charge and the time required for charge redistribution for transmission line circuits of various resistances.[*]

Resistance (kΩ)	Hold Time to Full Charge (s)	Charge Redistribution Time (s)	Ratio
10	150	34	4.4
20	315	70	4.5
30	480	102	4.7
40	640	134	4.8
50	810	170	4.8
60	880	196	4.5
70	1060	234	4.5
80	1230	255	4.8
90	1580	306	5.2
100	2030	330	6.2
200	5600	665	8.7
300	7500	820	9.7

Conway *et al.* suggested that charge redistribution for carbon-cloth electrodes takes place in the first approximately 100 s of self-discharge, and that after this time the potential loss is due to an activation controlled self-discharge mechanism.[3, 5] The results from the transmission line model suggest that the charge redistribution in fact continues well into the region of self-discharge time the Conway model predicts is activation controlled, and suggests that the self-discharge profile seen in these porous systems is not purely activation controlled, if at all. Because the time required for charge redistribution is so long, the role of charge redistribution in self-discharge profile of carbon-cloth electrodes should not be ignored, as charge redistribution may play a major role in the overall potential loss during self-discharge.

---

[*] Data for this table are available in Appendix B1

4.2.4 Examining Self-discharge Using Various Potential Ramp Rates in Carbon Cloth

Similar to the case of adding a potential hold step, using a slower ramp rate allows more time for charge to reach further into the pores, diminishing the charge redistribution effect, and therefore self-discharge upon switching to open circuit. Self-discharge experiments with various potential ramp rates were also performed on carbon-cloth working electrodes.

Figure 4.18a shows a typical set of data collected with carbon cloth charged at different ramp rates. The data in Figure 4.18 show that the higher the ramp rate, the more significant the self-discharge rate, as expected. For the 0.05 and 0.1 mV s^{-1} ramp rates the self-discharge curves are very similar, indicating that ramp rates this low allow for the effects of charge redistribution to essentially be removed. Ramp rates which are significantly higher than 1 mV s^{-1} have a drastic effect on the degree of the self-discharge, demonstrating that when charging the surface up quickly there is not enough time to allow for the charges to reach the base of the pores. These results are consistent with what is expected for charge redistribution being responsible for self-discharge. However, a lower ramp rate means that the electrode is charged over a longer period of time, and it is possible that during a slower charge there is depletion of a species involved in self-discharge, such that a lower ramp rate results in a more depleted species, and therefore less self-discharge.

In Figure 4.18 each run consisted of a potential ramp from 0.0 to 1.0 V at various ramp rates (0.05 – 50 mV s^{-1}). With each curve there is an associated instantaneous drop in potential on open circuit related to Ohmic effects. This initial drop in potential describes the potential drop through the solution, V, due to the resistance, R, encountered by ions in the electrolyte as they move through the solution while the current, I, is flowing (as per Ohm's law: $V = IR$). The potentiostat cannot differentiate between the potential drop in the solution and the potential applied to the working electrode (so when asked to supply a 1 V potential, part of that potential is lost as Ohmic effects in solution, and the remainder is what is actually applied to the working electrode). The potential drop is proportional to the potential ramp rate being used, as higher ramp rates result in higher currents and thus, higher ramp rates result in larger instantaneous drops, as evidenced in Figure 4.18 at $t = 0$ s.

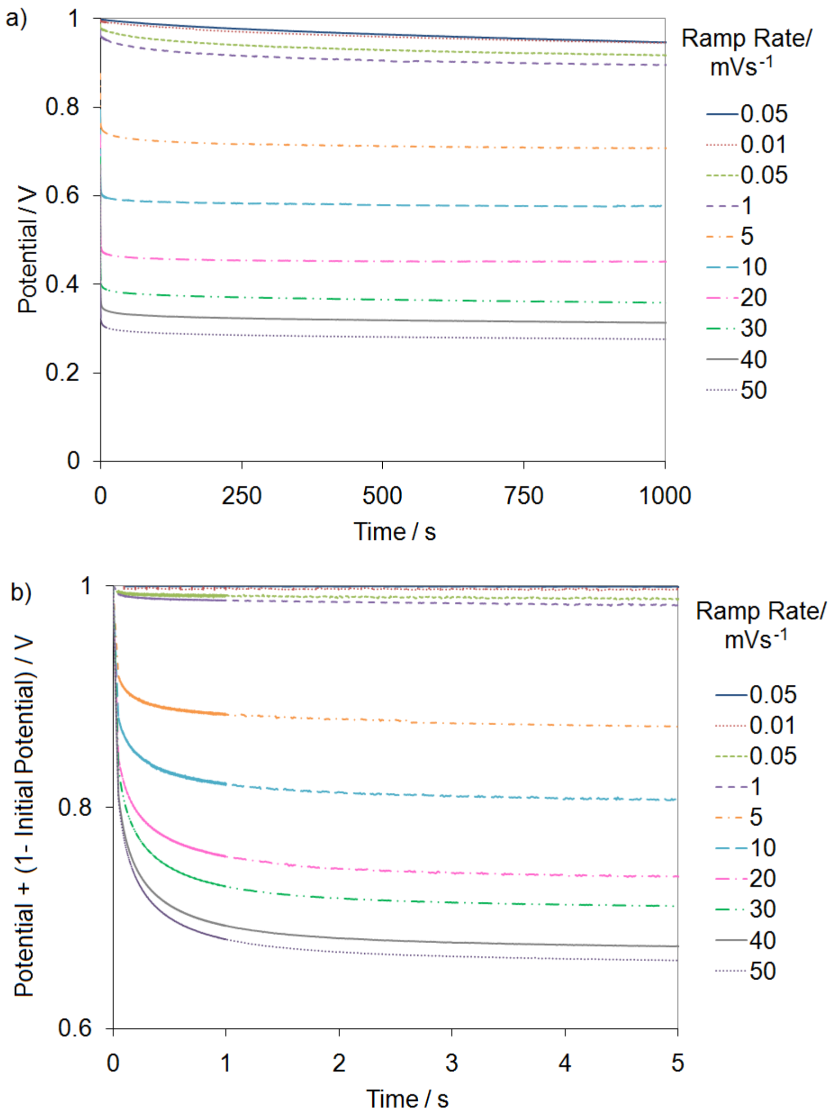

Figure 4.18: Self-discharge data for a 10.2 mg Spectracarb 2225 carbon-cloth electrode in 1 M H_2SO_4. The electrode potential was ramped from 0.0 to 1.0 V at ramp rates of 0.05 to 50 mV s^{-1}. b) Self-discharge data from a) with *IR* drop subtracted out.

Figure 4.18b shows the same data plotted in Figure 4.18a with the *IR* drop removed for easier comparison (the *IR* drop was taken as the drop in potential from the initial charging potential to the first potential measurement upon switching to open circuit). At very low ramp rates (0.05 and 0.1 mV s^{-1}) the profiles overlap as the effects of charge redistribution are essentially removed. As the ramp rate increases, the potential loss on open circuit also increases.

Self-discharge data collected on carbon-cloth electrodes with different ramp rates matches what is expected for charge redistribution, where larger ramp rates lead to a greater potential distribution within the pores after charging, leading to a greater potential loss on open circuit. The effect of ramp rates on charge redistribution was further examined using a transmission line circuit.

4.2.5 Examining Charge Redistribution Using Various Potential Ramp Rates in Hardware Circuit

Self-discharge experiments with various potential ramp rates were performed on the transmission line circuit by charging the top capacitor from 0.0 to 1.0 V at ramp rates of 0.05 to 50 mV s^{-1}, and allowing the other capacitors to charge naturally. Figure 4.19a shows the potentials for all capacitors, RE1-RE8, in the circuit when RE1 is charged at a ramp rate of 0.05 mV s^{-1}. For the case of the low ramp rate the potential at each capacitor is equal throughout the duration of the experiment. The slow ramp rate of 0.05 mV s^{-1} allows sufficient time for the charge to reach down the length of the circuit, and thus all of the capacitors can reach the desired potential easily. Conversely, for the experiments where a 50 mV s^{-1} ramp rate is used (Figure 4.19b), it is obvious that the potential of the capacitors toward the base of the circuit (RE6-RE8) lags behind during charging.

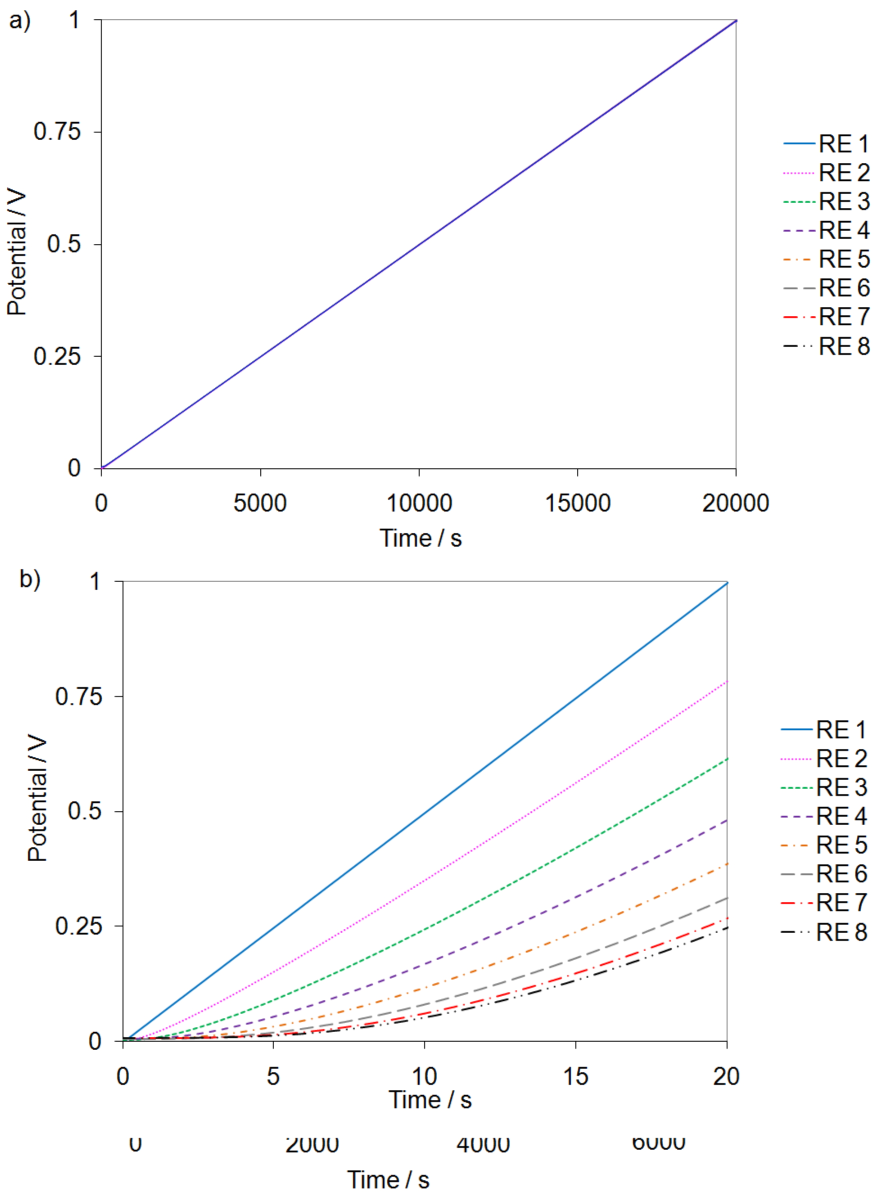

Figure 4.19: Charging data from the hardware circuit. All resistors were set to a value of 10 kΩ. The voltage of the first capacitor was ramped from 0.0 to 1.0 V at a) 0.05 mV s^{-1}, and b) 50 mV s^{-1}.

With ramp rates of 1 mV s^{-1} or higher the effects of charge redistribution start to become evident. Figure 4.20a-f show the data during charge redistribution for the circuit charged at ramp rates between 1 and 50 mV s^{-1}, and as the ramp rate gets higher the effects of charge redistribution become more apparent. In each case, as the system is switched to open circuit at *t* = 0 s, the capacitors closer to the top of the circuit (*e.g.* RE1) have potentials higher than those closer to the back (*e.g.* RE8). This is due to the distributed resistance down the length of the circuit. As a result, once the system is switched to open circuit the potentials at the front of the circuit begin to drop, and the potentials at the back of the circuit begin to climb until the potentials at all capacitors are equal. The equalization of potentials occurs within approximately 30 seconds after opening the circuit when all resistance values are set to 10 kΩ. The time required for the potentials to equalize depends on the resistances used in the circuit, as evidenced in Table 2.

In the mid-section of the circuit (RE2-RE4) a peak can be seen in the voltage-time profile when high ramp rates are used (Figure 4.20e and f). This may be due to the fact that during the initial moments on open circuit the charge is drawn toward the back part of the circuit, as this lies at a lower potential than the front part of the circuit. This charge must travel through the mid-section of the circuit before reaching the back, resulting in a peak corresponding to the extra charge present in this section during charge redistribution. Using the transmission line circuit has made it possible to measure the potentials at various sections of the circuit, at different points down the "model pore", enabling the examination of the potential profile of the mid-section of the pore, which is not possible for porous carbon electrodes.

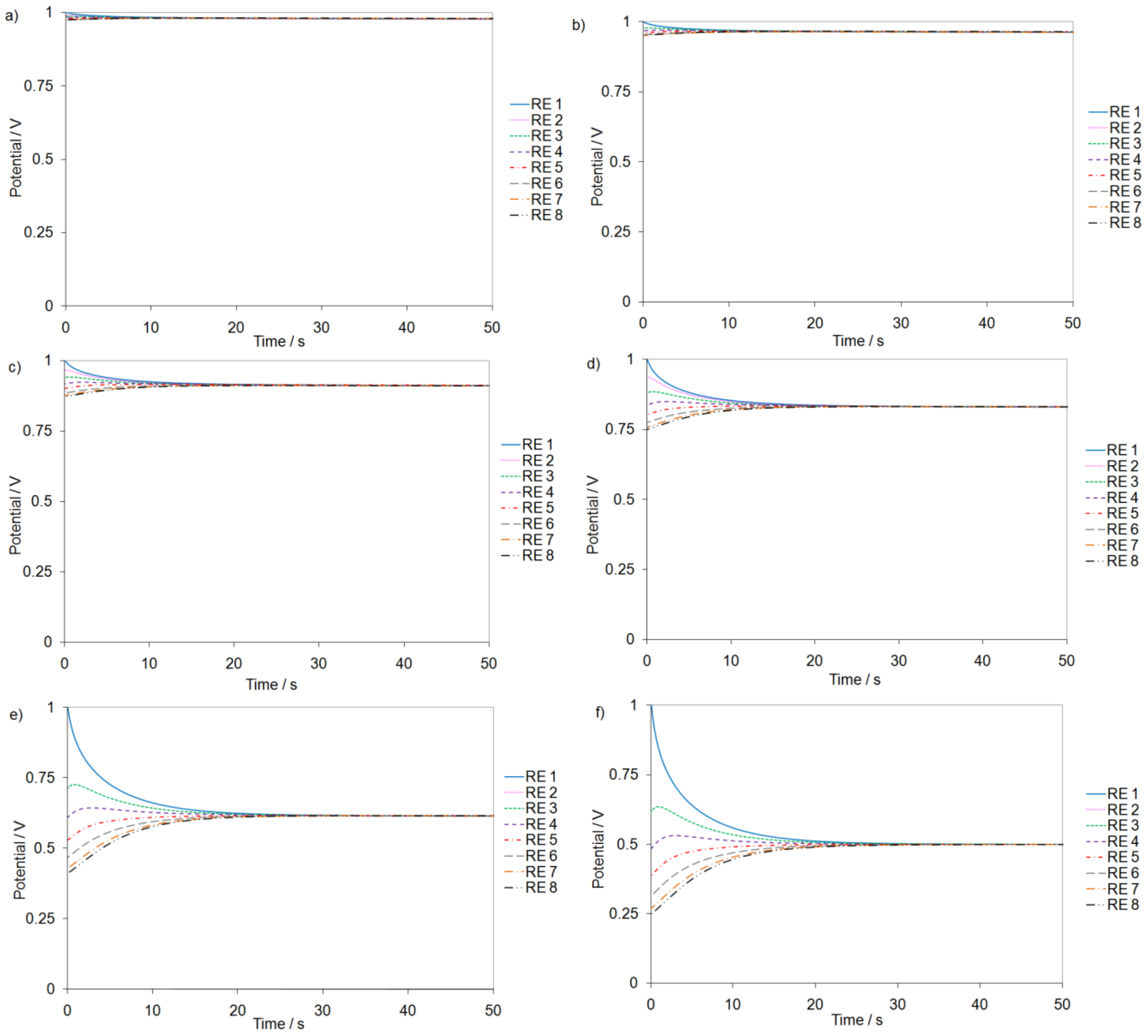

Figure 4.20: Self-discharge data from hardware transmission line circuit. All resistors were set to a value of 10 kΩ. The voltage of the first capacitor was ramped from 0.0 to 1.0 V at a) 1 mV s^{-1}, b) 2 mV s^{-1}, c) 5 mV s^{-1}, d) 10 mV s^{-1}, e) 30 mV s^{-1}, and f) 50 mV s^{-1}, switched to open circuit, and the potentials at all capacitors were recorded with time.

At high ramp rates (> 10 mV s^{-1}, Figure 4.20c-f) the charge redistribution has a significant effect on the degree of the self-discharge and the equilibrium potential. At ramp rates of 1 mV s^{-1} or lower the potential remains above 0.9 V after about an hour of self-discharge. However as the ramp rate is increased to 10 mV s^{-1}, the open-circuit potential drops to about 0.8 V after 30 s. At ramp rates as high as 50 mV s^{-1}, the potential quickly drops to near 0.5 V on open circuit. The data then suggest that the higher the potential ramp rate used, the lower the value of the equalization potential. The value of the equalization potential determines the amount of energy that the EC can provide (Equation 2), and because the energy is dependent on the square of the voltage, a large percentage drop in the voltage of the capacitor has an even more drastic effect on the energy content.

Charge redistribution data collected with the hardware circuit using various ramp rates correlates well with the self-discharge data collected on carbon-cloth electrodes, as there is a decrease in self-discharge with a decrease in ramp rate. The data obtained with the hardware circuit further validates the idea of charge redistribution taking place in the carbon cloth. Also with this setup it is possible to examine in a more meaningful and quantifiable way what is happening throughout the entire length of the circuit (our model pore).

4.2.6 Effect of Initial Charging Potential on Self-discharge Profiles and Comparison to Conway Model

Results obtained so far for various carbon samples, as well as the transmission line circuit, suggest that charge redistribution may be partially responsible for the self-discharge of high surface-area carbons. However, self-discharge profiles are also compared to the Conway model, which predicts the self-discharge profile for an activation-controlled Faradaic self-discharge mechanism. When the self-discharge potential of a Spectracarb 2225 carbon-cloth electrode in H_2SO_4 was plotted versus log t, a plateau was seen (Figure 4.21), such as that predicted by the Conway model [4, 5] (as described in Section 2.7), where the length of time for the plateau corresponds to the integration constant, τ, in the model. After this plateau, the self-discharge potential fell linearly with log t, again corresponding to the expected profile based on the activation control Conway model[4, 5], suggesting that the self-discharge may proceed through an activation-controlled Faradaic mechanism.

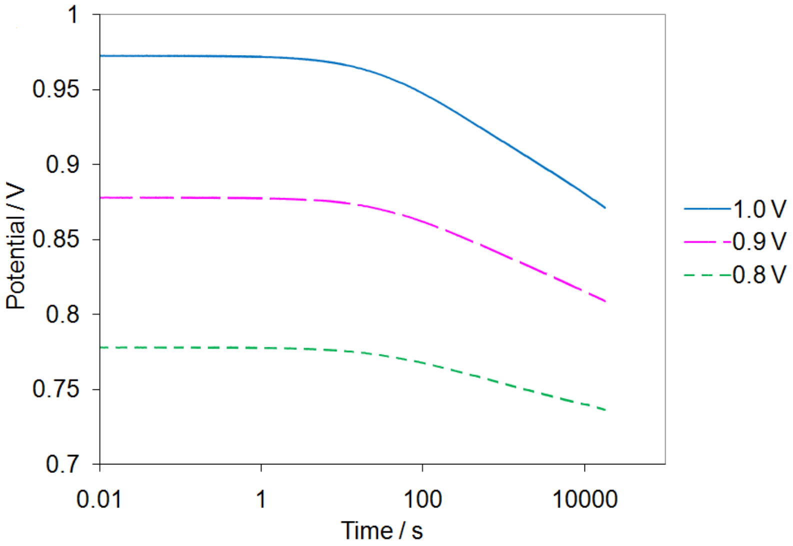

Figure 4.21: Self-discharge profile for a 9.1 mg Spectacarb 2225 carbon-cloth electrode in 1 M H_2SO_4 plotted as a function of log t for various initial charging potentials.

The Conway model predicts that the decline in voltage over log t for an activation-controlled Faradaic mechanism has a slope which is the negative of the tafel slope ($RT/\alpha F$), and thus, the slope should be the same for a given Faradaic self-discharge mechanism. For example, the Conway model predicts that for an activation-controlled Faradaic self-discharge reaction, the slope at each potential should always be the same, independent of the electrode's initial potential. However, when the self-discharge profiles from different initial charging potentials are examined as a function of log t, Figure 4.21 (and those seen by Conway *et al.*), it is seen that there is no correlation between the self-discharge potential and the slope. This is also contrary to that seen for redox electrodes, such as NiOx[4] where the slope is dependent on the self-discharge potential and changes with self-discharge mechanism (as the Tafel slope of the mechanisms change).

Rather, it was seen that when the self-discharge potential was plotted versus log *t* for various initial potentials (Figure 4.21), the slope of the self-discharge curve was dependent upon the initial potential. Figure 4.22 shows a plot of the slope of the self-discharge profile for carbon-cloth electrodes in 1 M H_2SO_4 vs. initial potential. The slope varies linearly with initial charging potential. This is contrary to the Conway model which predicts that the slope of the self-discharge profile, when plotted as a function of log *t*, should be independent of initial charging potential. Therefore, the slope of the self-discharge profile (as plotted vs. log *t*) cannot simply be the negative of the tafel slope of a Faradaic self-discharge reaction and thus, the activation-control model cannot be used to fully explain the shape of this curve. Conway *et al.* suggested that it may be a charge redistribution effect due to the porosity of the electrode which causes this deviation from the model, since the models were developed for planar electrodes, rather than the porous carbon used in this work.[3]

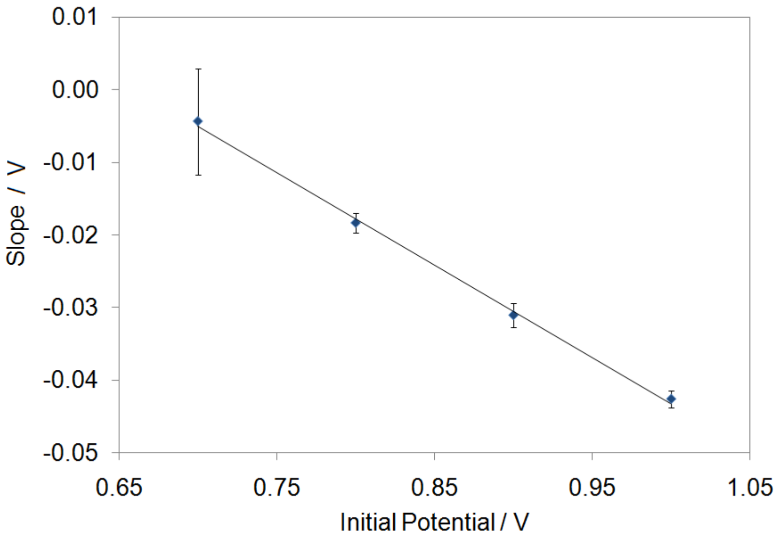

Figure 4.22: Plot of the slope of the linear region of self-discharge profile in log *t* when plotted in s vs. initial potential for Spectracarb 2225 carbon-cloth electrodes in 1 M H_2SO_4.[*]

Self-discharge data collected with carbon-cloth working electrodes indicate that the slope of the self-discharge profile depends on the initial charging potential, contrary to what is expected for an activation-controlled self-discharge mechanism at a planar electrode. To further examine the dependence of the slope on the initial charging potential, experiments were performed on the transmission line circuit at various initial charging potentials.

4.2.7 Effect of Initial Charging Potential on Self-discharge Profiles of Hardware Circuit

Figure 4.23 shows the self-discharge profile of capacitor 1of the hardware circuit (which models the pore mouth) during charge redistribution plotted vs. log *t*. The self-discharge profile falls linearly with log self-discharge time, after some plateau time. This

---

[*] Error bars are one standard deviation for seven electrodes, data are available in Appendix A1.

is the same profile predicted for activation-controlled Faradaic self-discharge mechanism at a planar electrode by Conway *et al*. Thus, the linear fall in potential with log *t* is not characteristic of activation control, and may indeed arise even when only charge redistribution is occurring in the system.

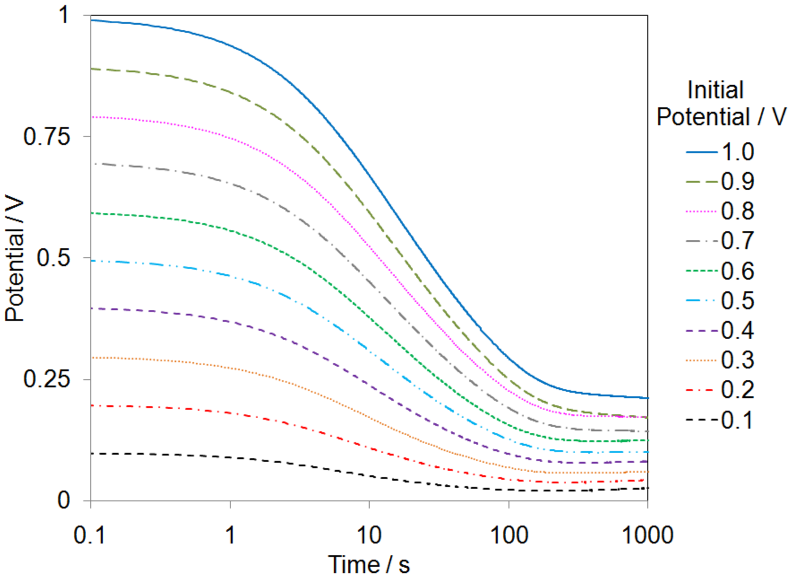

Figure 4.23: Self-discharge profile for capacitor 1 of the transmission line circuit, plotted as a function of log t, for various initial charging potentials. All resistors were set to 50 kΩ and capacitor 1 was charged at a ramp rate of 50 mV s^{-1}.

Conway's assignment of the self-discharge profile of the carbon cloth as being due to an activation-controlled self-discharge mechanism may need to be reconsidered as results shown herein suggest that charge redistribution should not be ignored. It also shows that the Conway model (at least for activation-controlled Faradaic mechanisms) cannot be utilized directly for highly porous electrodes, as the charge redistribution which may take place within these electrodes gives a similar profile as the activation-controlled Faradaic mechanism.

When different initial charging potentials were used on the transmission line circuit, it was found that the slope of the self-discharge profile depends on initial potential (Figure 4.23). Figure 4.24 is a plot of the slope of the self-discharge profile vs. initial potential, and shows that the slope varies linearly with initial potential. Again, this exactly corresponds to what is seen in the Spectracarb 2225 carbon-cloth electrodes (Figure 4.21, Figure 4.22). This is consistent with self-discharge of the porous carbon cloth being due to a very long charge redistribution process in the pores of this carbon.

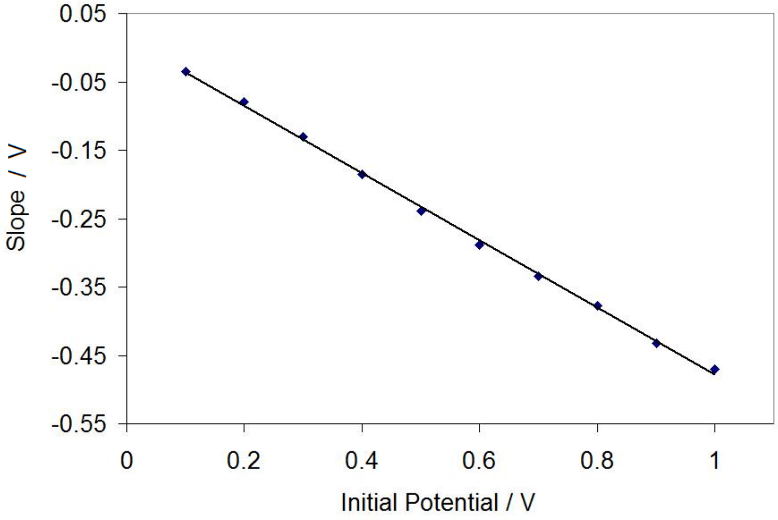

Figure 4.24: Slope of self-discharge profile vs. initial potential for hardware circuit data from Figure 4.23.

Based on the above discussion, it is suggested that the linear log *t* self-discharge profile for the highly porous carbon-cloth material is due to the charge redistribution in the cloth after charging, suggesting that the self-discharge profile for this system is dominated by charge redistribution. Although this profile shape is characteristic of either an activation-controlled Faradaic self-discharge mechanism or a charge redistribution effect, the long charge redistribution times predicted (based on comparison with the transmission line model pore) suggest that up to 10 hours of the self-discharge is due to charge redistribution. Additionally, the effect of the initial charging potential on the self-discharge slope (when plotted as a function of log *t*) conforms to that expected from a charge redistribution effect, rather than an activation-controlled Faradaic process causing self-discharge.

4.3 Conclusions

Self-discharge data obtained with high surface-area carbons (Spectracarb 2225 and Black Pearls 2000) agree with what is expected for charge redistribution, with slower potential ramp rates and longer hold times resulting in a decreased self-discharge, suggesting that charge redistribution is occurring. On the other hand, in self-discharge studies of low surface-area carbons (graphite and glassy carbon powder) and a carbon with larger pore size (mesoporous carbon powder) the addition of a hold step had much less effect on the self-discharge profile, consistent with charge redistribution not being important in these carbons. This further supports that the loss in potential of high surface-area carbons, at least partially, is due to charge redistribution. Thus, the study of charge redistribution in model systems has value for these electrodes as it may help to clarify how the charge redistribution affects self-discharge.

This research has shown that adding a hold step during the charging of the highly porous carbon electrodes used for ECs reduces self-discharge, presumably either due to a reduction in charge redistribution effects, or to depletion of a species involved in self-discharge during the hold step. For Spectracarb 2225 carbon cloth, a very long hold step of more than 50 hours is required before the self-discharge profiles overlap, possibly suggesting that very long hold times are required to minimize charge redistribution. Additionally, results suggest that the charge redistribution step itself may take much longer than anticipated, likely approximately 10 hours, rather than the 100 s predicted previously by Conway *et al.*[3, 5] This was the first study which showed the major effect charge redistribution had on the self-discharge profile of porous electrodes.

It was also shown that the self-discharge profile of a transmission line circuit, having only charge redistribution and no other self-discharge mechanism, results in a linear self-discharge profile when plotted as a function of log *t*. This profile is also what was predicted by Conway *et al.* for an activation-controlled Faradaic self-discharge mechanism. Thus, the Conway model is not diagnostic for an activation-controlled Faradaic reaction in porous electrodes, and the model cannot be applied to porous electrodes unless charge redistribution has been completely removed.

Self-discharge profiles for the carbon cloth showed a dependence on the initial charging potential, while the Conway model predicts no dependence of the slope on initial charging potential. Data collected with the transmission line circuit, where it is known that the potential loss is due only to charge redistribution, showed that the slope varied linearly with the initial charging potential. This is further evidence that charge redistribution is an important cause of the potential loss during self-discharge of the carbon cloth.

Chapter 5

PREDICTION OF THE SELF-DISCHARGE PROFILE OF AN ELECTROCHEMICAL CAPACITOR ELECTRODE UNDERGOING AN ACTIVATION-CONTROLLED FARADAIC SELF-DISCHARGE MECHANISM COMBINED WITH CHARGE REDISTRIBUTION

Part of this work was published as *"Prediction of the self-discharge profile of an electrochemical capacitor electrode in the presence of both activation-controlled discharge and charge redistribution", Jennifer Black and Heather Andreas, Journal of Power Sources, 195(3), 2010, 929-935.* All data, other than the self-discharge experiments in Fe, are published. Some changes have been made to the text.

5.1 Introduction

It was shown in Chapter 4 that the charge redistribution throughout the pore after charging results in a self-discharge profile with a potential plateau followed by a linear region in log *t*. This is the same profile predicted by Conway *et al.* for an activation-controlled Faradaic self-discharge mechanism.[5] The Conway model suggests that an examination of the slope of the self-discharge curve may help in determining the mechanism through which self-discharge takes place. However, as shown previously in porous electrodes, like those often used in ECs, a linear profile in log *t* is not necessarily indicative of an activation-controlled Faradaic discharge mechanism and may rather be due to charge redistribution in the pores of the electrode after charging, or a combination of both effects (Chapter 4).

This chapter examines the potential profile of an EC electrode undergoing an activation-controlled discharge in the presence of charge redistribution within the pores in order to identify the important characteristics of the potential profile. This chapter also examines the effect of higher resistance and longer pores so that this can be used to aid in the identification of the mechanism of self-discharge in experimental systems. To do this, the de Levie transmission line is used as a model pore.[2]

Since the potential at the tip of the pore is highest after charging, any Faradaic reactions are expected to happen preferentially at the tip of the pore, at least until the potential equalizes via charge redistribution. For this reason, in this work the potential profile was examined as an activation-controlled discharge was modeled at the pore tip, and charge redistribution was occurring throughout the pores. A transmission line hardware circuit of a model pore was used to first model charge redistribution with no activation-controlled discharge, then an activation-controlled discharge was modeled with no charge redistribution, and finally both charge redistribution and an activation-controlled discharge were combined. The resulting potential profiles for each case are examined.

5.2 Results and Discussion

5.2.1 Modeling Charge Redistribution Only

Charging of the transmission line circuit results in a distribution of potentials down the length of the circuit (modeling the charging in a pore) and upon switching to open-circuit configuration the charge redistributes until all capacitors in the circuit are at a common potential (Chapter 4). In this situation, the majority of the charge is moving down the circuit to charge the capacitors further down the circuit, denoted CR_{down}, which results in a self-discharge profile with a linear region in log *t* with a slope that is related to the initial charging potential (Figure 4.23). Self-discharge profiles of high surface-area, porous carbon-cloth electrodes are similar to this self-discharge profile, suggesting that charge redistribution is likely a significant factor in the self-discharge (Chapter 4). Results from Chapter 4 show that utilizing different charging rates (or hold times after charging) changes the self-discharge profile of the porous carbon-cloth electrodes, as the amount of potential distribution, and therefore charge redistribution depends on the charging rate (hold time) used. These results are consistent with charge redistribution being important during self-discharge. However, a similar result may also be expected for a Faradaic self-discharge mechanism where a species involved in the self-discharge is depleted more during a longer charging period, therefore reducing self-discharge.

Similarly, and not unexpectedly, it can be shown that if the entire circuit (pore) is brought to full charge (1.0 V) and the pore tip (capacitor 1) is stepped to 0.0 V the potential profile of the pore base (capacitor 8) also falls linearly with log *t* as charge redistributes back up the circuit (Figure 5.1). Since in this case the majority of the charge is moving up the pore, this is termed CR_{up}. A comparison of Figure 4.23 and Figure 5.1 shows that regardless of the direction of charge redistribution in the model pore, the resulting potential profile contains linear regions in log *t*.

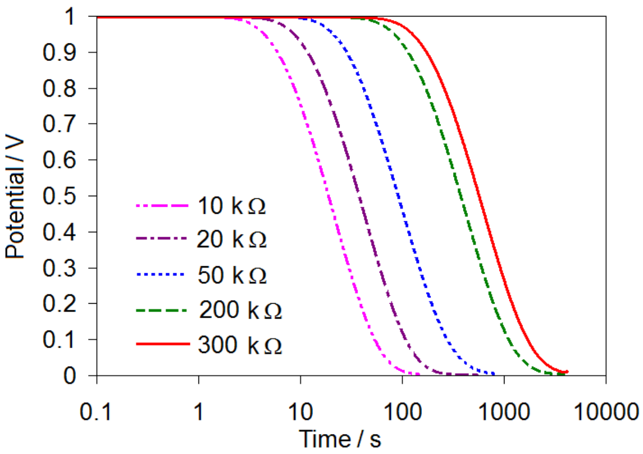

Figure 5.1: Potential profile of capacitor 8 (pore base) of transmission line circuit after all capacitors (1 - 8) were charged to 1.0 V using a ramp rate of 1 mV s^{-1}, and capacitor 1 was stepped to 0.0 V. The different resistances used in the circuit are noted.

5.2.2 Modeling the Activation-Controlled Discharge

The activation-controlled discharge experiment was initially run on only the first capacitor (RE1) of the hardware circuit in order to ensure that the experiment was adequately modeling an activation-controlled reaction. Applying the activation-controlled discharge to only capacitor 1 of the hardware circuit ensures that there is no possibility of charge redistribution, and therefore models an activation controlled discharge taking place at a planar electrode, which is the situation for which the Conway model was developed. In order to run the experiment on capacitor 1 only, R2-R8 of the hardware circuit were set to an infinite resistance, such that they are excluded from the circuit, and only capacitor 1 is involved (R_s was set to 0). Figure 5.2a shows the Butler-Volmer curve from which the activation-controlled discharge experiment was modeled (as described in section 3.2.1) as well as the resulting Butler-Volmer curve obtained experimentally using the 100 step GCPL technique, with very good agreement between the two.

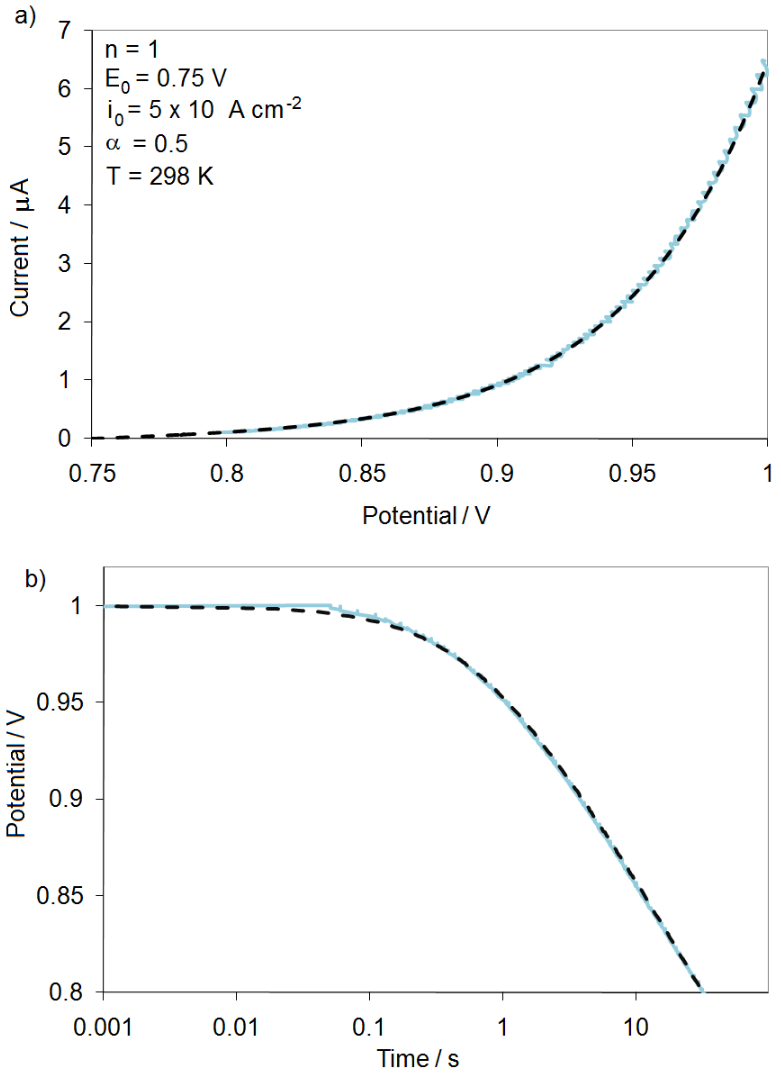

Figure 5.2: Theoretical profile (dark dashed) and experimental profile of capacitor 1 of transmission line circuit (light solid) during activation-controlled discharge plotted as: a) current vs. potential, and b) potential vs. time.

Figure 5.2b shows the potential profile of capacitor 1 in log *t* during the activation-controlled discharge, as well as the theoretical potential profile calculated from Equation 6 using an empirically determined $\tau = 3.3 \times 10^{-4}$ s. Both the experimental and theoretical potential profiles (Figure 5.2b) are linear in log *t*, as expected from the Conway model (Equation 6), with very good agreement between the two, a further indication that the model worked as expected. The slope of the experimental profile (110 mV per decade of time in seconds) agrees well with the slope of the theoretical profile (112 mV per decade of time in seconds). Both slopes are slightly smaller than the predicted value from Equation 6 (118 mV per decade of time, and 51 mV ($RT/\alpha F$) when plotted as ln t), likely due to the non-ideality of the capacitor, as well as some residual influence of the plateau on the slope. Since only capacitor 1 is used there is no charge redistribution in this model, hence the good agreement between the model and the experimental. This confirms that the experiment appropriately models an activation-controlled discharge.

5.2.3 Activation-Control + Charge Redistribution Up the Circuit (AC + CR_{up})

The activation-controlled discharge of the pore tip (capacitor 1) was then run with all capacitors present in the circuit, *i.e.* in the presence of charge redistribution. For simplicity, the experiments were first run with all capacitors in the circuit brought to a full charge of 1.0 V, thereby removing charge redistribution down the circuit (CR_{down}), and having charge redistribution occurring only up the circuit (CR_{up}) from capacitors 2-8 to capacitor 1. Figure 5.3 shows the potential of capacitors 1-8 during an activation-controlled discharge on capacitor 1, after all capacitors in the circuit were brought to a potential of 1.0 V by using a hold time of 15 min (all resistances in the circuit were set to 50 kΩ, Rs was set to 0). At 50 kΩ resistance there is a significant difference in potentials among capacitors 1-8 during charging, and the hold time of 900 s (15 min) after the initial ramp allows all capacitors to reach full charge, removing the effects of charge redistribution down the circuit (CR_{down}). However, there is still be charge redistribution back up the circuit (CR_{up}) induced by the activation-controlled discharge of capacitor 1. This can be seen in Figure 5.3 where the potential of capacitor 1 falls rapidly due to the activation-controlled discharge, followed by a drop in the potential of capacitor 2 (at *ca.* 1 s) as its charge is passed back up to capacitor 1 (as potentials attempted to equalize). Over time, all eight channels eventually began to feed charge back up the circuit. With respect to a real pore, these data suggest that the regions near the pore tip react (begin feeding charge up the circuit) sooner than the regions further down the pore, which is consistent with what was expected based on previous results and on the de Levie model.[2]

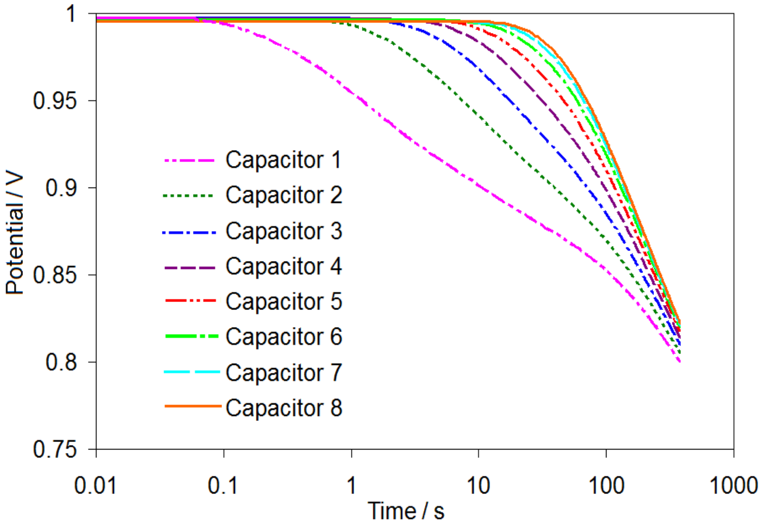

Figure 5.3: Potential of all eight capacitors of transmission line circuit during activation-controlled discharge on capacitor 1 and CR_{up}. Prior to this discharge, all capacitors were brought to 1.0 V using a ramp rate of 1 mV s^{-1},followed by a 15 min hold time. Resistors R2-R8 in the circuit were set to 50 kΩ**,** and R_s was set to 0.

Figure 5.4 shows the potential profile of capacitor 1 of the hardware circuit undergoing both an activation-controlled discharge and charge redistribution up the circuit (AC + CR_{up}). For comparison, the activation-controlled discharge only (AC_{only})

on capacitor 1 is also shown. Several distinct regions are seen in the potential profile of AC + CR_{up}, the first being a curved region, which follows the curve for activation-control, there is then region of mixed control as charge redistribution begins, and finally, charge redistribution diminishes, and in this last region the potential is predominantly determined by the activation-controlled discharge.

In the first region, denoted Region I of Figure 5.4 the curve corresponds almost directly with the curve showing activation-controlled discharge occurring when only capacitor 1 is in the circuit. This suggests that only the first capacitor is instrumental in determining the potential profile for AC + CR_{up} during this region. This occurs because the other capacitors have not yet begun to feed charge back into capacitor 1, since the RC time constant for the circuit (defined as the product of the resistance and capacitance and describes how quickly the system can be charged) prevents charge redistribution from occurring that rapidly. Relating this to a real porous electrode, if an activation-controlled discharge were taking place at the external electrode surface, the potential profile at short times may be predominantly controlled by the activation-controlled Faradaic discharge reaction, as charge redistribution may require more time to initiate. However, due to high electrolyte conductivity (1 M acid), the incremental solution resistance within the pores of the electrode is likely small, meaning that charge redistribution may initiate fairly quickly leading to a short Region I.

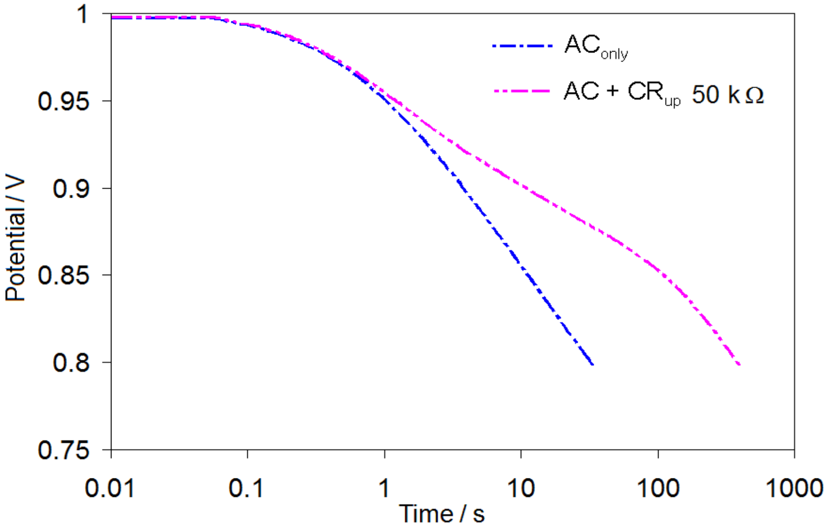

Figure 5.4: Potential profile of capacitor 1 of the hardware circuit during activation-controlled discharge only, as well as activation-controlled discharge with charge redistribution back up the circuit (previously fully charged at 1 mV s^{-1} and held, resistors R2-R8 in the circuit were set to 50 kΩ**,** and R_s was set to 0).

Region I comes to an end as charge redistribution up the circuit initiates. The potential of capacitor 1 decreases as a result of the current drawn from the activation-controlled discharge, causing capacitors 2-8 to begin feeding charge back to capacitor 1, evidenced by the drop in potential for capacitors 2-8 (Figure 5.3). As both charge redistribution and the activation-controlled discharge occur the potential profile is linear in log *t*, and this region is denoted Region II. There is also a curved region between Region I and Region II where charge redistribution has initiated, but has not yet reached its full rate. Because charge redistribution up the circuit is taking place during Region II, some of the charge removed from capacitor 1 due to the activation-controlled discharge is replaced by charge from capacitors 2-8, resulting in a decrease in slope seen in Region II for capacitor 1 (Figure 5.4). This suggests that the slope of the self-discharge profile in porous experimental systems is affected by the presence of charge redistribution, resulting in a slope different than is expected for the purely activation-controlled profile.

Region II is followed by another curved region, as the contributions from charge redistribution diminish, and a second linear region, Region III, where the contributions from charge redistribution are minimal, and the activation-controlled discharge dominates. In Region III, the slope correlates well with the slope obtained for only activation-control with no charge redistribution (Figure 5.4). At this point there was only a small potential difference between capacitors 1-8 (see Figure 5.3), and therefore CR_{up} due to potential distribution had essentially ended, as the charge being fed back into capacitor 1 was minimal. Therefore, in Region III the activation-control is dominating the slope. It is important to note here that for experiments with both activation-control and CR_{up}, the charge redistribution will never truly be over, as the charge removed from capacitor 1 by the activation-controlled discharge is replaced by charge from the capacitors further down the circuit. As a result, the slope may differ from that of the activation-control only profile.

This model suggests that in a real system with an activation-controlled self-discharge occurring on a highly porous electrode, charge redistribution likely affects the slope of the self-discharge curve, as evidenced by the decreased slope in Region II during charge redistribution up the circuit and activation-controlled discharge compared to the slope for activation-control only. This then explains why with high surface-area electrodes there is no relationship between the slope and self-discharge potential, such as that seen with nickel-oxide.[4] The model also suggests that the completion of charge redistribution results in a change of slope, and this change may be used to determine the length of time for charge redistribution in these systems (see Section 5.2.5).

5.2.3.1 Modeling the Effect of Pore Diameter/Electrolyte Conductivity

As the resistance of the circuit increases (which models either a decrease in electrolyte conductivity of an EC electrolyte or a smaller cross-sectional area of pore) the effects of charge redistribution also increase, due the greater potential distribution created during charging. During charging of the circuit with high resistance values, capacitors 2-8 do not climb to as high of a potential as with lower resistances and there is an increased amount of potential distribution among the capacitors (Figure 5.5). Nevertheless, as can be seen in Figure 5.6, Regions I and II (as described above) remain in the self-discharge profile at each different resistance, although Region III is not seen at high resistances, due to experimental limitations described below.

In Region I all curves correspond with one another at short times, regardless of the number of capacitors in the circuit, in this region all systems behave as if only one capacitor is available. For increased resistances the charge moves more slowly through the circuit, as the RC time constant increases, and therefore charge redistribution takes longer and initiates more slowly meaning that Region I (the region where the curve corresponds to AC_{only}) is longer for systems with higher resistances. This is evident in Figure 5.6, as the time of Region I is correlated to the resistance in the circuit, where this region is very short for low resistances (*e.g.* 10 kΩ deviates from AC_{only} at 0.2 s), and very long for high resistances (*e.g.* 200 kΩ deviates from AC_{only} at 2 s). At low resistances, capacitor 2 can very quickly begin to recharge capacitor 1 since only a small resistor hinders this current flow. This suggests that the length and/or presence of Region I in the self-discharge profile of porous EC electrodes may be a gauge to the incremental solution resistance in the system, as a system with a very low incremental solution resistance will exhibit little to no curved Region I, since the current can very easily pass from surface area deeper in the pore up to the pore mouth. Conversely, the significant presence of a curved Region I may suggest a high incremental solution resistance.

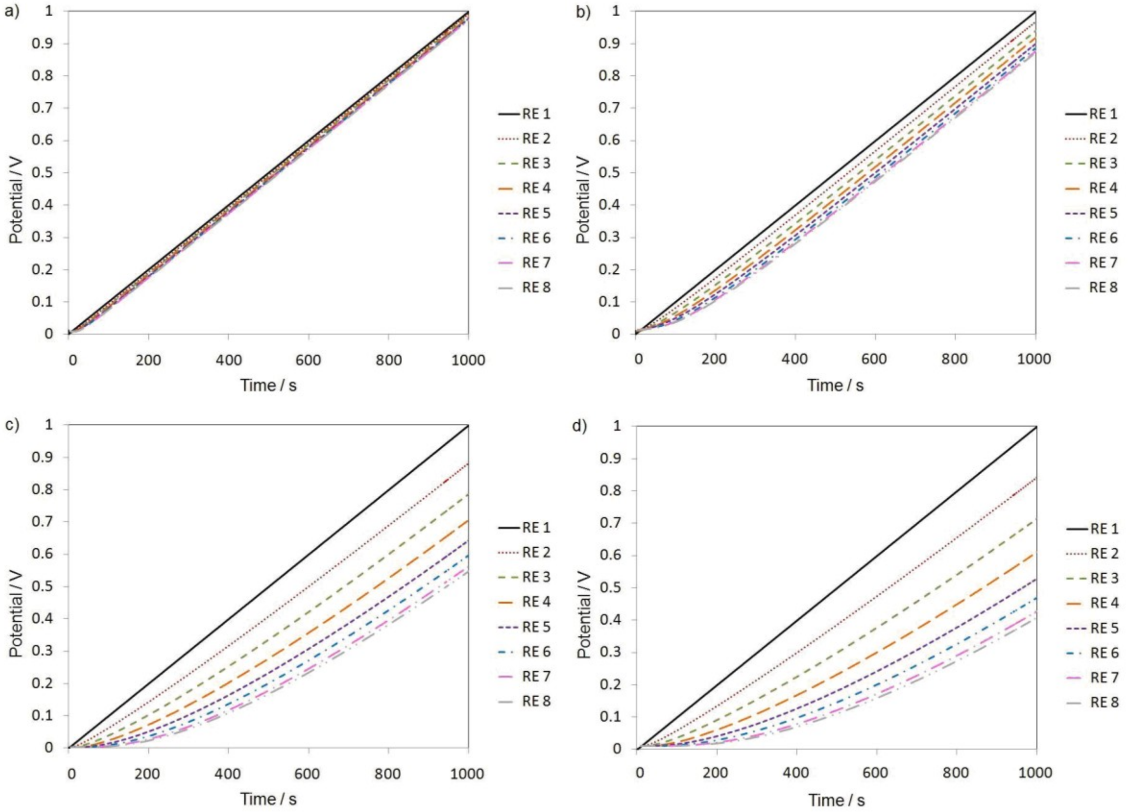

Figure 5.5: Charging data for all capacitors of the hardware circuit at a charging rate of 1 mV s^{-1} and resistances of a) 10 kΩ, b) 50 kΩ, c) 200 kΩ, and d) 300 kΩ.

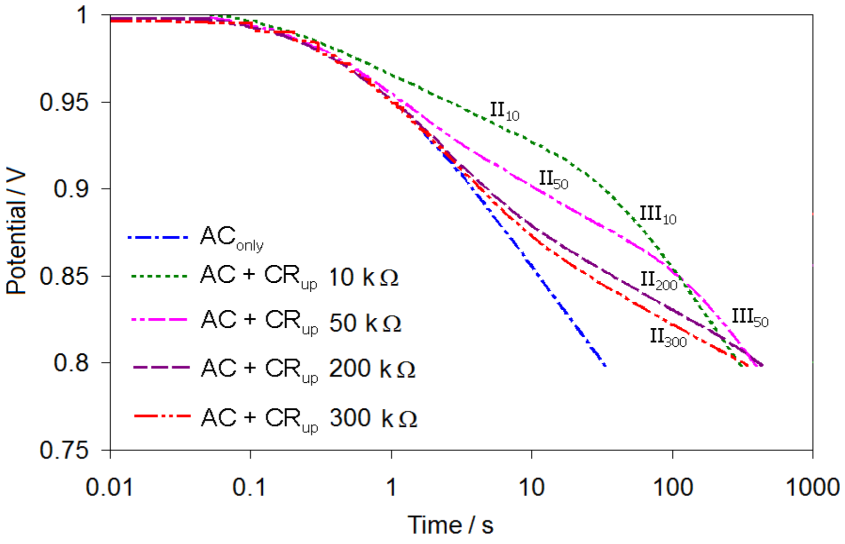

Figure 5.6: Potential profile of capacitor 1 of the transmission line circuit (previously fully charged at 1 mV s^{-1} and held) with activation-controlled discharge and CR_{up} the circuit for different resistances. Labels show Region II and III for each resistance. For comparison the curve for AC_{only} is also shown.[*]

In each circuit, there is a curved region as charge redistribution initiates and before it reaches its full rate. Once the full rate of charge redistribution is established there is a linear region, corresponding to Region II, where the typical linear profile was seen with a shallow slope. This is the region where the rate of self-discharge is under a mixed-control of both an activation-controlled discharge and charge redistribution. At low resistances (*e.g.* 10 kΩ) charge can move quickly through the circuit, meaning that the charge redistribution requires a much shorter time to initiate, *i.e.,* charge can be fed up to capacitor 1 earlier to begin offsetting the current lost through the activation-controlled discharge. This can be seen in Figure 5.6 as the potential remains higher for longer with lower resistance, as charge is quickly and easily passed up the circuit to

---

[*] Data for all channels for 10 and 300 kΩ resistances are shown in Appendix B2. Data for 200 kΩ is not included since data for all capacitors were not collected.

capacitor 1 to keep this capacitor charged. The slope of Region II is independent of resistance (Figure 5.6). This is not unexpected as neither the slope of the AC_{only} nor the charge redistribution only result are dependent on resistance, when plotted as a function of log *t* (see Figure 5.1); however, the slope in normal time plot is smaller for higher resistances because with higher resistances the charge moves more slowly through the circuit. In fact, for high resistances (*e.g.* 200 and 300 kΩ) charge redistribution is much slower and requires the entire activation-controlled discharge time, and there is no region in which the slope is solely under activation-control (no Region III). As is shown in the following section, not only the incremental resistance affects the length of time required for charge redistribution, but also the total resistance.

5.2.4 Activation-Control and Charge Redistribution Down, Up (AC + CR_{down} + CR_{up})

In a real, highly porous electrode system, it is unlikely that the full surface will be completely/fully charged during a commercially viable charging ramp. This is because ECs are typically used in high power applications, and it is therefore required that they be charged and discharged very quickly. Thus, in this case, charge redistribution both up and down the pore (CR_{up} + CR_{down}) is expected to occur. The charge redistribution down the pore occurs as a result of the potential distribution created during charging, while charge redistribution up the pore replaces charge removed by the activation-controlled discharge, as before. To model this more realistic situation, the activation-controlled discharge of the pore tip (capacitor 1) was then run in the presence of charge redistribution both up and down the circuit (CR_{up} + CR_{down}). Here the potential of capacitor 1 was ramped from 0.0 to 1.0 V prior to the activation-controlled discharge, while the potential on capacitors 2-8 remained at some value below 1.0 V due to the added resistance down the circuit. Figure 5.7a shows that similar to the AC + CR_{up} case, three distinct regions are seen in the potential profile of capacitor 1 undergoing an activation-controlled discharge in the presence of charge redistribution both down, and up the circuit (AC + CR_{down} + CR_{up}).

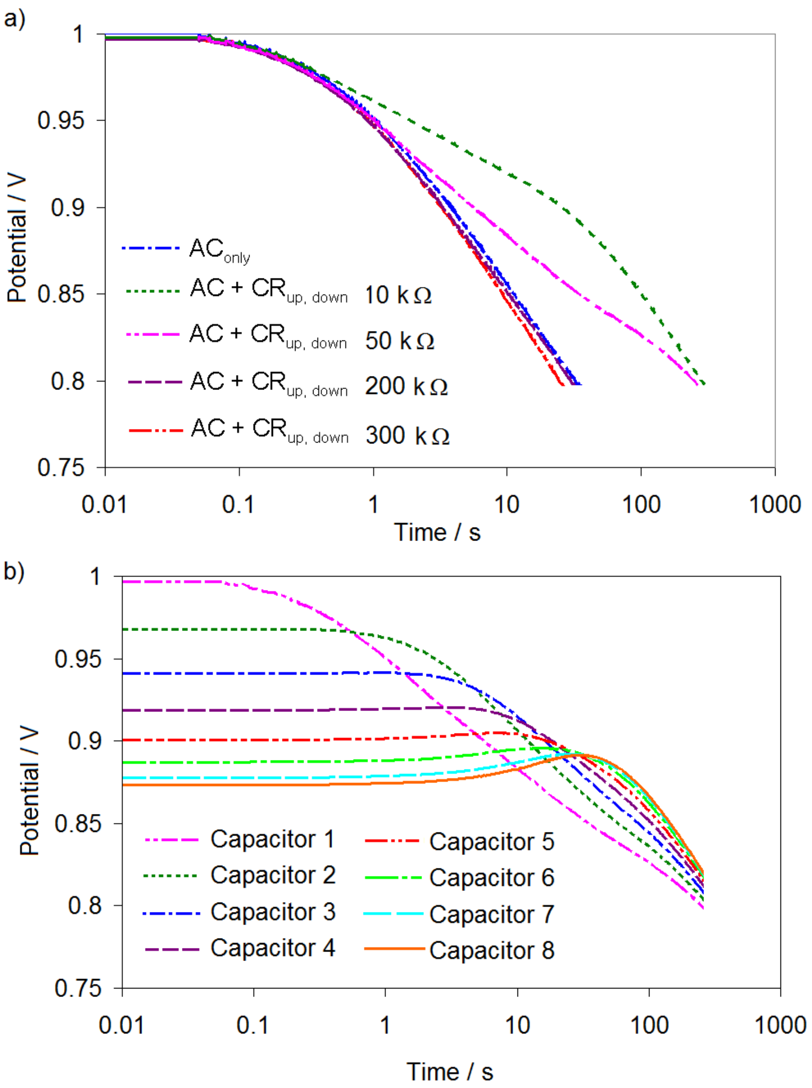

Figure 5.7: a) Potential profile of capacitor 1 of transmission line circuit (charged at 1 mV s^{-1}, no hold time) with activation-control, in the presence of charge redistribution up (CR$_{up}$) and down (CR$_{down}$) the circuit. b) Potential profiles of each capacitor for transmission line circuit using after charging at 1 mV s^{-1}, no hold time. Resistances were set to 50 kΩ for R2-R8, R$_s$ was set to 0.*

Again, the potential profile in Region I is controlled by capacitor 1 as described in Section 5.2.3, and therefore Region I is unaffected by the presence of the additional charge redistribution down the circuit (CR$_{down}$). This is because the RC time constant for

---

* Data for all capacitors for 10, 200 and 300 kΩ resistances are shown in Appendix B2.

the circuit prevents charge redistribution from happening this quickly, and all charge removed from capacitor 1 in Region I was a result of the activation-controlled discharge. This is evident in Figure 5.7b, where the potential of all capacitors 2-8 remained unchanged through this region.

When both CR_{up} and CR_{down} are occurring, Region II depends on both the direction, as well as the amount of charge redistribution, which leads to a more complex profile as seen in Figure 5.7a. For 50 kΩ resistances, the potentials of capacitors 2-8 were significantly lower than 1.0 V (the potential of capacitor 1) after charging, as seen in Figure 5.7b. Because of this, capacitors 2-8 were unable to contribute charge to capacitor 1 until the potential of capacitor 1 dropped to a value below that of capacitors 2-8, meaning there was no charge redistribution up the circuit (CR_{up}) at these short times. However, at *ca.* 1 s, the potential of capacitor 1 fell below that of capacitor 2 (Figure 5.7) resulting in the initiation of CR_{up}, as capacitor 2 began passing charge to capacitor 1. A small amount of charge from capacitor 2 also went into charging capacitor 3 whose potential increased slightly, indicating that CR_{down} had also begun to occur. This CR_{down} is most evident with the potential of capacitor 8 which climbed significantly as charge from the other capacitors was passed down the circuit into capacitor 8. With charge redistribution now occurring in both directions, *i.e.* up and down the circuit (CR_{up} + CR_{down}), Region II is no longer linear as the various processes (activation-control, CR_{up} and CR_{down}) compete.

Figure 5.8 shows the potential profile for the activation-controlled discharge with only charge redistribution up, as well as the activation-controlled discharge with charge redistribution up and down. With charge redistribution both up and down, the amount of charge that capacitors 2-8 contribute to recharging capacitor 1 is less than previously seen with AC + CR_{up}, as the potential of capacitors 2-8 are now lower after charging (whereas with AC+CR_{up} the capacitors were fully charged to 1.0 V). This then results in a slope in Region II which is less than that for AC_{only} but larger than that for activation-control with charge redistribution up only (AC + CR_{up}).

At high resistances (*e.g.* 200 kΩ) there was a very large potential difference developed among capacitors 1-8 during charging (Figure 5.5), and as a result there is a large amount of charge redistributed from capacitor 1 to capacitors 2-8 in Region II. As a result of charge being removed from capacitor 1 due to the activation-controlled discharge as well as from capacitors 2-8 due to charge redistribution down the circuit (CR_{down}), the potential of capacitor 1 dropped very quickly in Region II, and the slope was steeper than for activation-control only. The length of Region II is approximately the same for the curve with activation-control in the presence of only charge redistribution back up the circuit (AC + CR_{up}), compared to having charge redistribution in both directions (AC + CR_{up} + CR_{down}). This indicates that the length of time required for charge redistribution is approximately constant, independent of the direction of charge redistribution.

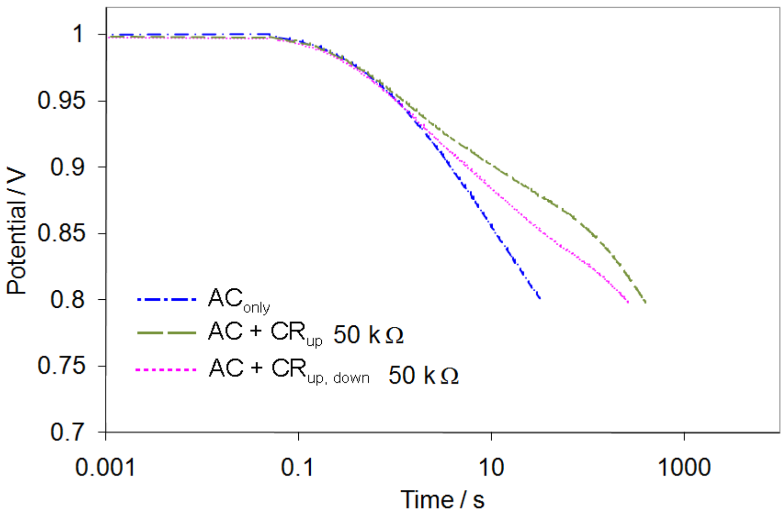

Figure 5.8: Potential profile of capacitor 1 of the transmission line circuit for activation-controlled discharge and CR_{up} (fully charged to 1.0 V and held) and for activation-controlled discharge and $CR_{up,down}$ (charged at 1 mV s^{-1} to 1.0 V, no hold). For comparison the curve for AC_{only} is also shown. R2-R8 were set to 50 kΩ, R_s was set to 0.

5.2.5 Comparison with Self-discharge Profile of Highly Porous Electrodes

5.2.5.1 Self-discharge Profile of Porous Carbon Cloth in 1 M H_2SO_4

Figure 5.9 shows the self-discharge profile of a Spectracarb 2225 carbon-cloth electrode in 1 M H_2SO_4 collected over long times, plotted in log *t*. There is a plateau immediately followed by a relatively linear region. This is similar in shape to the profile evidenced at low resistance (10 kΩ) in Figure 5.6. The absence of a sharply curved Region I suggests that the incremental solution resistance is fairly low which is consistent with the high proton content (*ca.* 1 M) in the electrolyte. A linear region, Region II is seen, between 60 and 30 000 s. This region has a shallow slope, suggesting that charge redistribution is likely occurring possibly coupled with an activation-controlled self-discharge. This is supported by the increase in slope (Region III) at 60 000 s (17 hours) where presumably the charge redistribution ends and the activation-controlled self-discharge reaction discharges the electrode rapidly. These data suggest that charge redistribution takes significantly longer than the 100 s previously suggested,[3] and can therefore not be ignored during mechanistic studies. Given that there is an increase in slope in Region III, this suggests that charge redistribution is occurring during the activation-controlled discharge, and as charge redistribution diminishes the slope increases as charge at the pore mouth is no longer being replaced by charge from deeper within the pore.

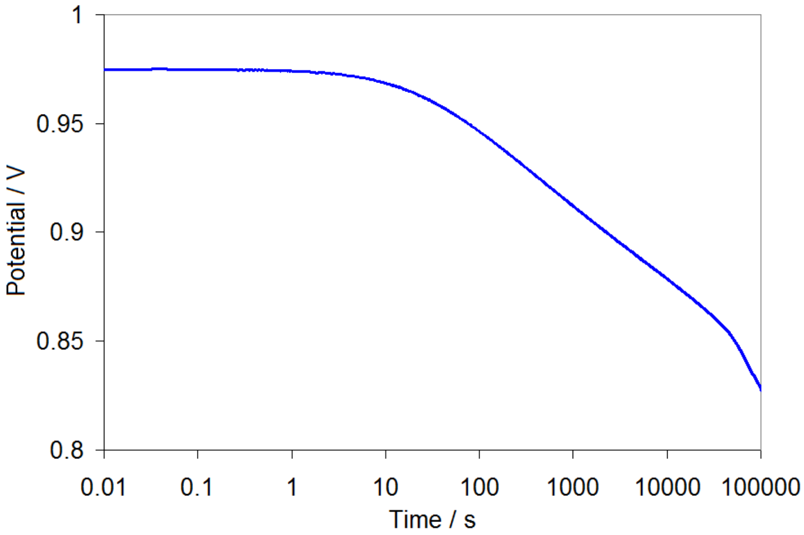

Figure 5.9: Self-discharge profile of a 9.7 mg Spectracarb 2225 carbon-cloth electrode in 1 M H_2SO_4, after charging at 1 mV s^{-1} to 1.0 V.

5.2.5.2 Self-discharge Profile in a 1 M H_2SO_4 Electrolyte Containing 0.1 M $Fe^{2+/3+}$

Self-discharge experiments were also performed on Spectracarb 2225 carbon-cloth electrodes in the presence of high concentrations of Fe ions in an attempt to force an activation-controlled Faradaic reaction at the electrode surface. Fe was chosen because the electrolytes used in ECs may be contaminated with Fe ions, which may cause self-discharge by either oxidation of Fe^{2+} to Fe^{3+} at a positive electrode, or reduction of Fe^{3+}

to Fe^{2+} at a negative electrode.[71, 85] Figure 5.10 shows the self-discharge profile of Spectracarb 2225 carbon cloth from 1.0 V in a 1 M H_2SO_4 electrolyte containing 0.1 M $Fe^{2+/3+}$. At the electrode charged to 1.0 V, Fe^{2+} is oxidized to Fe^{3+} at the electrode surface, reducing the electrode potential over time on open circuit. A high concentration of 0.1 M Fe was chosen since the purpose was to force an activation-controlled Faradaic reaction at the electrode, rather than the reaction being under diffusion-control. The electrolyte was also stirred to minimize diffusion effects. Though only Fe^{2+} is required for this reaction, equimolar concentrations of Fe^{2+} and Fe^{3+} were used to keep the equilibrium potential for the reaction (given by the Nernst equation) approximately constant throughout the experiment.

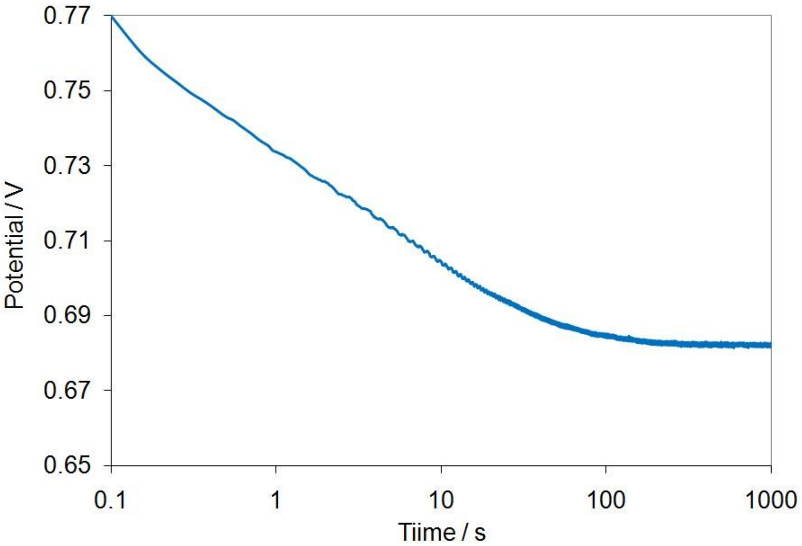

Figure 5.10: Self-discharge profile of a 11.5 mg Spectracarb 2225 carbon-cloth electrode in a 1 M H_2SO_4 electrolyte containing 0.1 M $Fe^{2+/3+}$ after charging at 1 mV s^{-1} from 0.5 to 1.0 V.

Although the electrode was charged to 1.0 V during the charging step, the potential of the electrode was quickly discharged to *ca.* 0.77 V after only 0.1 s of open-circuit measurements. After *ca.* 2 s the potential falls linearly with log *t* followed by a plateau of the potential at *ca.* 0.68 V, the equilibrium potential of the Fe reaction. Figure 5.11 shows a CV of a carbon-cloth electrode in a 1 M H_2SO_4 electrolyte containing 0.1 M $Fe^{2+/3+}$, and the equilibrium potential can be estimated by the halfway point between the anodic peak (*ca.* 0.82 V) and cathodic peak (*ca.* 0.53 V), approximately 0.68 V.

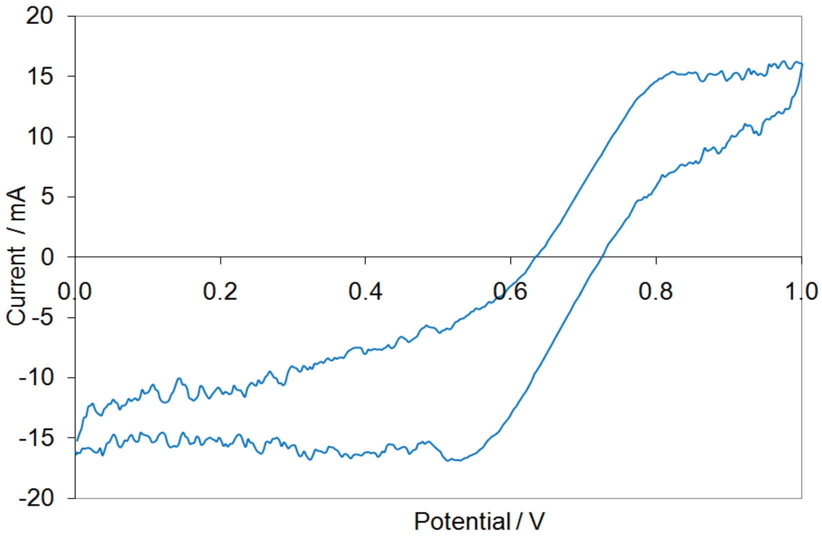

Figure 5.11: CV of a 11.5 mg Spectracarb 2225 carbon-cloth electrode at 1 mV s^{-1} in a 1 M H_2SO_4 electrolyte containing 0.1 M $Fe^{2+/3+}$.

The Conway model predicts that an activation-controlled discharge results in a linear decline in potential with log *t*, after some time, however, because the high concentration of Fe^{2+} present in the electrolyte discharges the electrode so quickly, the instrument is unable to collect data quickly enough during the first *ca.* 250 mV of potential loss on open circuit. For this reason the initial potential plateau expected in the self-discharge profile is not present.

Comparing the self-discharge profile of the carbon cloth in the presence of Fe ions to results obtained with the activation-controlled model on the hardware circuit, it might be expected to see multiple slopes in the self-discharge profile, relating to regions of activation-controlled discharge only, as well as regions where the activation-controlled discharge is combined with charge redistribution within the pores of the electrode. However, multiple slopes are not visible in the self-discharge profile of the carbon cloth in the presence of Fe ions. This is likely because the Fe ions are discharging the electrode very quickly, such that the electrode has reached the equilibrium potential after only *ca.* 100 s. Examining the self-discharge profile of Spectracarb 2225 carbon cloth in 1 M H_2SO_4 (Figure 5.9) revealed that charge redistribution may not begin until *ca.* 60 s as evidenced by the onset of Region II in the self-discharge profile. At *ca.* 60 s in the self-discharge profile in the presence of Fe ions the electrode is almost fully discharged, and is only *ca.* 100 mV above the equilibrium potential of the $Fe^{2+/3+}$ reaction. Therefore, a significant change in the slope is not apparent in the self-discharge profile.

To obtain a self-discharge profile which exhibits a region of both an activation-controlled discharge, as well as charge redistribution, which would enable comparison to the transmission line circuit model, either the activation controlled discharge would have to take place over a longer period of time, or charge redistribution would need to start earlier. In order to have a longer activation controlled discharge region, a reaction which has a lower equilibrium potential or tafel slope could be utilized. For charge redistribution to begin earlier a carbon which has a lower RC constant, and therefore different pore structure could be used. Due to time constraints, however, other carbons were not tested for this work.

5.3 Conclusions

A de Levie transmission line hardware circuit was used to model the self-discharge profile which occurs on a highly porous EC electrode in the presence of an activation-controlled Faradaic discharge reaction. The model showed that this situation results in three distinct regions in the self-discharge profile. The first region in the profile (Region I) corresponds to a purely activation-controlled profile. This is because charge redistribution, which is expected to occur on the porous electrode, requires some time to initiate, and has not yet begun to occur in this region. The presence and length of this first region depend on the incremental solution resistance in the pore and can be used to predict the solution resistance in real EC systems. Region II in the self-discharge profile has a shallower slope than expected for a purely activation-controlled self-discharge profile. This shallower slope is due to the charge redistribution in the circuit, where the capacitors down the circuit (or surface area deep in the pores) begin to feed charge back up to the first capacitor (pore mouth) where the activation-controlled discharge is occurring. The profile of the first capacitor does not, therefore, fall as quickly as would be expected if this recharging were not taking place. Increasing the resistances and capacitance in the model pore (akin to modeling narrower, longer pores or lower electrolyte conductivities) increased the length of Region II. Upon completion of the charge redistribution, the slope of the self-discharge profile again increases (Region III), providing a means to determine the duration of the charge redistribution in experimental systems.

When the self-discharge profile of a highly porous carbon electrode was examined in 1 M H_2SO_4, the predicted distinct regions were observed. A very short, nearly absent, Region I was seen, suggesting a very low incremental solution resistance, which correlates nicely with the high concentrations of protons in this electrolyte. Region II is very long for this experimental system. Again, this is consistent with expected results, as long narrow pores (such as those in the carbon examined) are predicted to have a very large RC time constant, as the cumulative resistance and surface area would be very high in these pores. From the self-discharge profile, it is suggested that charge redistribution requires at least 60 000 s (*ca.* 17 hours) to complete, which is much longer than had been previously predicted in the literature.[3]

Unfortunately running self-discharge experiments in a 1 M H_2SO_4 electrolyte containing 0.1 M $Fe^{2+/3+}$ did not result in a useful comparison to the transmission line model for an activation-controlled discharge in the presence of charge redistribution, due to the rapid discharge of the electrode in the presence of high concentrations of Fe.

Chapter 6

EFFECT OF PORE SHAPE ON SELF-DISCHARGE/CHARGE REDISTRIBUTION

Part of this work was published as *"Pore Shape Affects Spontaneous Charge Redistribution in Small Pores", Jennifer M. Black and Heather A. Andreas, J Phys. Chem. C, 114(27), 2010, 12030-12038.* All data presented have been previously published. Some changes have been made to the text.

6.1 Introduction

It is well known that the performance of the carbon-electrode-based EC greatly depends on the properties of the carbon, including, surface functional groups,[86, 87] surface wettability,[88, 89] pore size,[35, 90, 91] and pore size hierarchy[57, 88, 89]. With high surface-area carbons, the majority of the electrochemical surface resides in micropores, and is only accessible through the large cumulative solution resistance within these small pores. Since the majority of charge storage on the surface is therefore dependent on the movement of ions through the micropores, and the pore structure determines the pore solution resistance, the pore structure is an important factor for the device performance.[92, 93]

Similarly, the pore shape has a strong influence on the pore solution resistance, and thus, there have been multiple efforts to change pore shape using different synthetic methods, including: carbon activation (slit-shaped and ellipsoid-shaped pores[94-96]) and templating (cylindrical and spherical,[46, 97] as small as 2-3 nm[98]). The frequency response of various pore geometries has been evaluated using mathematical models and experimentally.[7, 47] The pore geometry was shown to have a significant effect on the electrochemical impedance profile. Therefore, it is expected that pore shape would have an effect on the charge and discharge characteristics of an EC and on the spontaneous movement of charge through the pore during charge redistribution.

Therefore, the research contained herein is important to the understanding of how pore shape influences charge redistribution, as a full understanding of charge redistribution is required to determine how it influences self-discharge of ECs and other systems based on the charging of porous electrodes.

This chapter examines for the first time the effect of pore geometry on the self-discharge profile of a model pore undergoing charge redistribution, using a hardware transmission line circuit based on de Levie's Transmission Line Model of a pore.[2] This hardware circuit allows for modeling charge redistribution in the pore and tracking of the potentials at various points down the model pore, which is difficult or impossible in real pores of the small sizes which experience charge redistribution. Additionally, this model removes any issue associated with unequal charge balancing due to inefficient packing of ions into the pores. Pores of very small diameter may not allow for efficient ion packing in the pore, as required to balance the charge. These pores may require the ion to distort or lose its solvation shell in order to enter the pore[35] or the ions may not have the room to properly align in very narrow parts of the pore[99] (*e.g.* the bottom of cone shaped pores or the sides of slit shaped pores). This provides a model which clearly delineates the effect of pore resistance due to pore shape. This is the first time that the effect of pore shape on the spontaneous movement of charge has been considered. The data from the transmission line model presented herein provide a good prediction of the charge redistribution in templated systems, or any systems where pores are uniform in shape and size. Further research will build on these data to model the charge redistribution of more complex systems (combinations of various pore shapes and sizes).

6.2 Results and Discussion

6.2.1 Effect of Pore Mouth Size and Pore Shape on Charge Redistribution

The self-discharge profiles for a number of different pore shapes (cylinders, cone, and inverted cone) are shown in Figure 6.1. All of the pore shapes have the same surface area, as this is governed by the capacitors in the circuit. For each of these pore geometries the self-discharge profile has three regions: first a potential plateau, followed by a linear decrease in potential with log *t*, and finally another plateau after charge redistribution is complete.

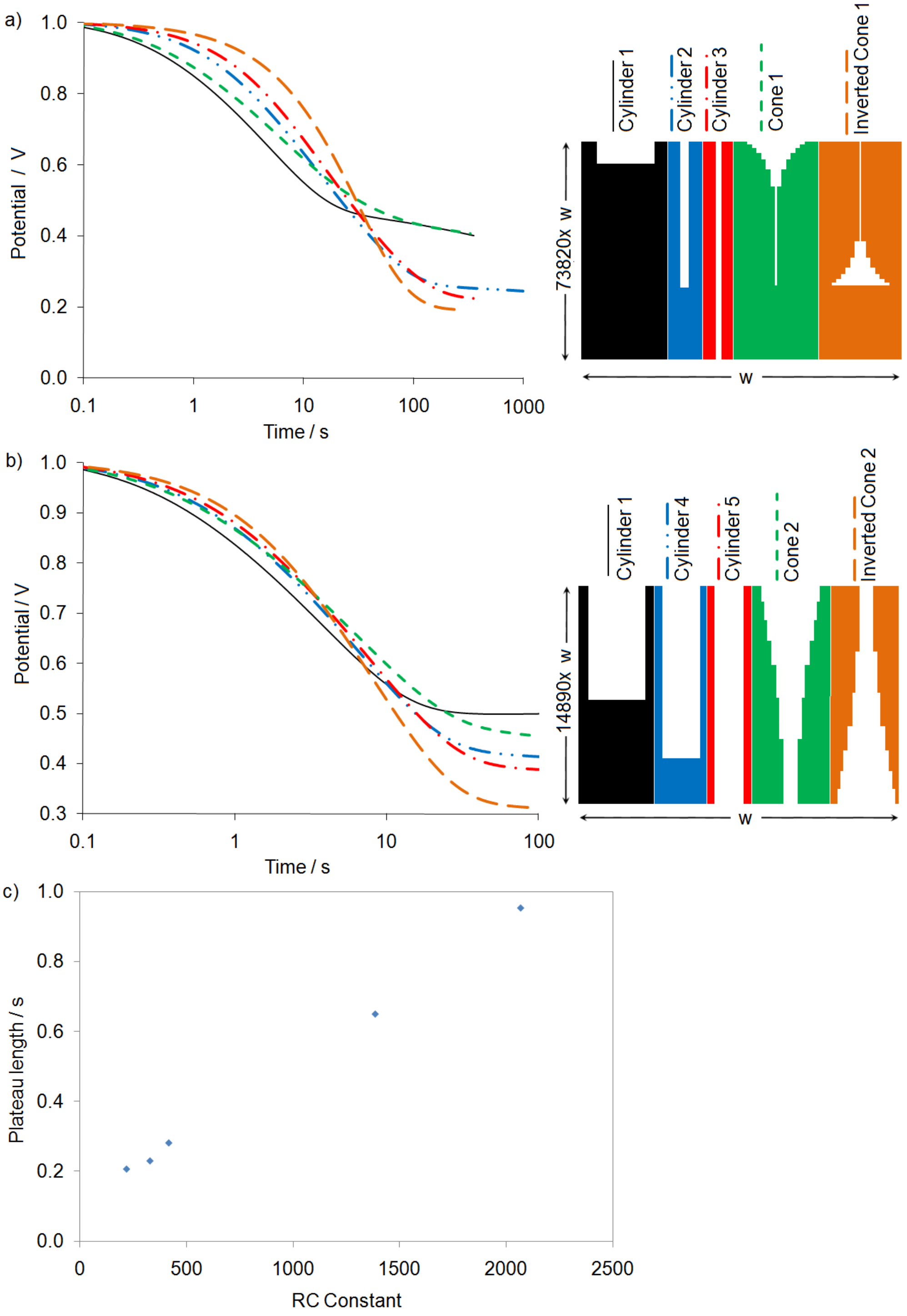

Figure 6.1: Self-discharge profile for different pore shapes. a) pore shapes with exaggerated high disparity in pore section sizes, b) more realistic pore shapes. c) Time required for charge redistribution curve to deviate away from plateau (defined as reaching a potential of 92.5 % of the full potential drop) for cylinders 1 - 5 which have an increasing RC constant in the order of cylinder 1,4,5,2, and 3.

The plateau length is dependent on the pore length/diameter. Three cylindrically shaped pores of the same surface area but different diameters (therefore different pore mouth sizes) are shown in Figure 6.1. Because of the requirement of a constant surface area, decreasing the size of the pore diameter necessitates an increase in the length of the pore. Cylinder 1, which has the largest diameter, has the shortest plateau, and cylinder 3 with the smallest diameter has the longest plateau of the cylinders. This can be seen in Figure 6.1c where the plateau length is plotted as a function of the RC constant (larger RC constant corresponds to smaller pore diameter and longer pore), and suggests that the pore diameter/length has a large impact on the plateau length. To determine whether it is the pore diameter (defined as the widest part of the pore) or the pore mouth size which is responsible for this increase in plateau length with a decrease in pore diameter, several other shapes with different pore mouth sizes were examined.

A comparison between the inverted cone, which has a very small pore mouth and a cone of the same pore length shows that the plateau length is significantly longer for the inverted cone with the small pore mouth, consistent with the plateau length being strongly influenced by the pore mouth (Figure 6.1a and b). Similarly, cylinder 1 and cone 1 geometries (Figure 6.1a) have the same pore mouth size and the plateau lengths for these pore geometries are very similar, even though these pores are very different in length, diameter and shape. This suggests that it is the pore mouth that has the dominant effect on the plateau length. The slightly longer plateau for cone 1 is due to this shape's longer length (higher total electrolyte pore resistance, since it has higher resistance values beyond the pore mouth) indicating that although the plateau length is predominantly controlled by the pore mouth size, there is some contribution from the pore length as well.

To examine pore geometries with the same size pore mouth and different total length, a series of diamond shaped pores with different aspect ratios was modeled. For the diamond shaped pores the plateau length remains essentially the same for geometries having the same pore mouth size (Figure 6.2), with slight increases in plateau length with increasing total pore length. This suggests that although the plateau length is predominantly controlled by the pore mouth size, there is some contribution from electrolyte resistance further down the pore.

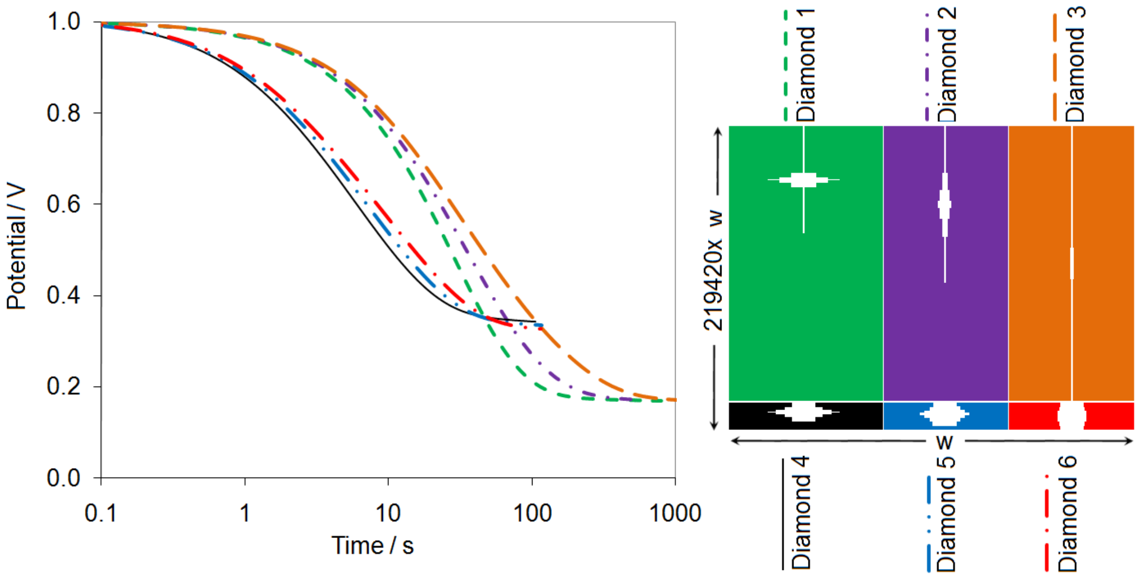

Figure 6.2: Self-discharge profiles for diamond shapes with different aspect ratios. The pore mouth size is the same for diamonds 1 - 3 and the same for diamonds 4 - 6.

Pore geometry also significantly affects the rate of potential decay during the region of linear potential drop with log *t* and the potential of the final plateau after completion of charge redistribution. Cylinder 2, cone 1, and inverted cone 1 have the same surface area and the same total pore resistance, yet the charge redistribution behaviour is very different (Figure 6.1a). For a cone shaped pore, which has the least resistance near the pore mouth (largest pore mouth) and the majority of the electrolyte resistance present near the pore base, the initial plateau is shortest, for the reasons discussed above, and the final potential after charge redistribution is highest (*ca.* 0.41 V), indicating the total amount of charge present in the pore is highest. The inverted cone geometry, on the other hand, has the smallest pore mouth (most electrolyte resistance near the pore mouth) and as a result the longest plateau, and the lowest final potential (*ca.* 0.19 V). The intermediate case, cylinder 2 has an initial plateau length and final potential (*ca.* 0.25 V) which lies between these geometries. The value of the final potential indicates how much charge is placed on these pore during charging, and, as expected, a smaller pore mouth causes less charge to be placed on the pore, given the same charging rate. Since the surface area in the pore is only accessible through the pore mouth, a small pore mouth (high electrolyte resistance) limits the current during charging and results in a smaller amount of charge passing into the pore during a given charging period than a large pore mouth (low electrolyte resistance at the pore mouth). Since the total surface areas of all of these pores are the same, a lower amount of charge results in a lower final potential after charge redistribution. Again, this highlights that for high power applications the pore mouth must be large and pore mouth interference (say from a deposited film or film damage due to electrode preparation) must be avoided.

For pores having the same pore mouth size, the rate of the linear potential decay in the region between the two plateaus decreases with increasing total pore length (see diamond shapes in Figure 6.2), as the charge moves through the pore more slowly with an increase in pore electrolyte resistance. With the diamond shaped pores, the pore mouth resistance is, again, playing a major role in determining the final potential after charge redistribution as the final potential remains essentially the same for diamonds 1-3 which have the same pore mouth resistance but very different total resistances. This is a direct result of the large pore mouth resistance in these models, since pores which have much lower pore mouth resistances relative to the overall resistance (diamonds 4-6) do not exhibit the same final potential. Instead, for a wide pore mouth the final potential decreases with increasing pore length. Diamonds 1-3 had an extremely small pore mouth (high pore mouth resistance) which represented a large portion of the total pore resistance, and for this reason the size of the pore mouth was a major influence on the final potential after charge redistribution, which was very similar for these shapes.

It is essential to consider the importance of the pore mouth in certain applications, for example, charging of electroactive polymers, which may undergo volume expansion during charging.[100] In a porous polymer the potential, after charging, is highest at the pore mouth, and therefore the pore tip swells preferentially, which may result in the pore mouth becoming very small. A very small pore mouth limits the total amount of charge placed on the pore, and results in a low potential after completion of charge redistribution. It is therefore important to design these materials to account for any volume expansion such that swelling in the polymer does not result in a closed-off pore mouth. For example, templating a polymer material with cone shaped would counter the effect of the polymer swelling at the pore mouth, and therefore, the swelling would not result in occlusion of the pore mouth but, rather, would result in a more cylindrically shaped pore.

To highlight (exaggerate) the effect of each pore region, high resistances were used in the pore models for Figure 6.1a, which resulted in very elongated regions of the pore. The self-discharge profiles of more realistic pore shapes are shown in Figure 6.1b. The same conclusions may be drawn from the comparison of these pore shapes as for those in Figure 6.1a, as the plateau length and the final potential are primarily controlled by the pore mouth size, however, differences in plateau lengths are less noticeable as the pore mouths have less variation for these shapes. These results are akin to those expected for pores of larger diameter. These results highlight that the charge redistribution and pore shape effects are most important for small pores.

Thus, making long pores (and therefore increasing surface area) is of no real use if the pore mouth of these pores is narrow or occluded. This must be considered when making electrodes using templated methods (*e.g.* using nanotubes) followed by a film deposition or pressing of the electrode against a membrane. In both cases, care must be taken that no narrowing of the pore mouth is caused, as this will render the surface area in the nanotubes only useful at very low current situations.

6.2.2 Effect of Pore Occlusion on Charging Characteristics of the Pore

For occluded pore geometries, where the pore mouth electrolyte resistance is high (*e.g.* inverted cone), essentially only the surface at the pore mouth (the first capacitor in the model) is charged with the charging rates used in this study (Figure 6.3a). Although the potential of capacitor 1 (RE1) is brought to 1.0 V (shown at $t = 0$ s) with each of these pore shapes, the potentials of the other capacitors in the circuit are at some value below 1.0 V, and depend on the circuit resistances. The pore geometry with a very occluded pore mouth (*e.g.* inverted cone, Figure 6.3a) results in very low potentials on capacitors 2-8, and the majority of the charge is present at the pore mouth with little charge present near the pore base. Non-occluded pores (*e.g.* cylinder, cone, Figure 6.3b and c, respectively) are able to accumulate a significant amount of charge on all capacitors in the circuit (*i.e.* over the whole surface of the model pore), and as a result the total amount of charge present in the pore after charging is higher for these pore shapes.

Figure 6.3 also shows that once the circuit has been placed in open-circuit configuration and charge is allowed to move spontaneously throughout the circuit, a different final potential is reached for each shape, based on the initial amount of charge present in the circuit after charging. The lower final potential for the more occluded inverted cone geometry is, again, due to the lower total charge that is placed on the circuit during charging (due to the high pore mouth resistance arising from the small pore mouth), therefore when the charge redistributes to be equal over all eight capacitors, each capacitor has a lower voltage than it would have if more charge had been in the circuit initially. These results are consistent with the differences in the final potential seen with all of the pore shapes studied in Section 6.2.2 and suggests, again, that small pore mouths and occluded pore shapes should be avoided.

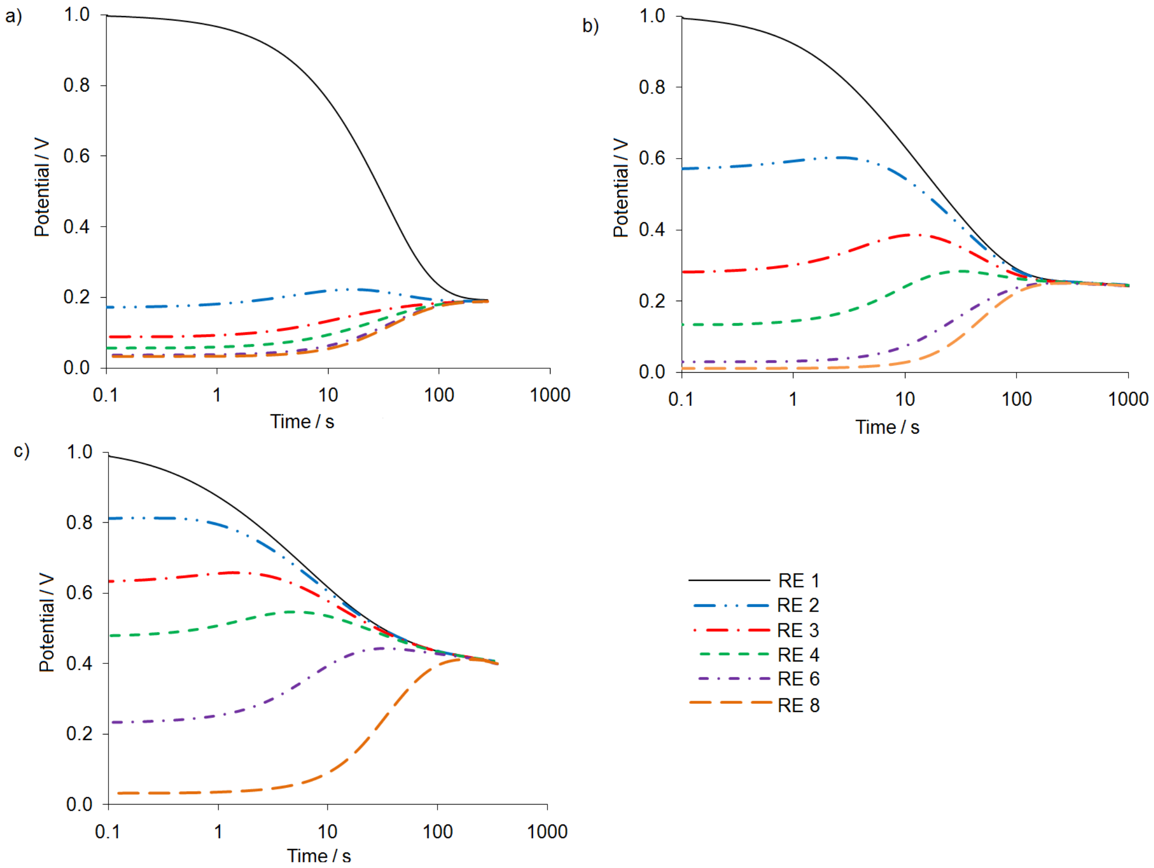

Figure 6.3: Potential recorded on RE1 - 4, RE6 and RE8, for three different pore shapes: a) inverted cone, b) cylinder and c) cone.

6.2.3 Effect of Pore Narrowing (Bottleneck)

The effect of pore narrowing was also examined using inverted diamond (ID) pore shapes and a number of cylindrical pores of varying radius, *r*, containing the same sized bottleneck (BN) midway down the pore, or in other words pores having varying $r_{mouth}/r_{bottleneck}$ ratios. Similar to what was shown in Section 6.2.1, the length of the plateau increases with a smaller pore mouth (Figure 6.4).

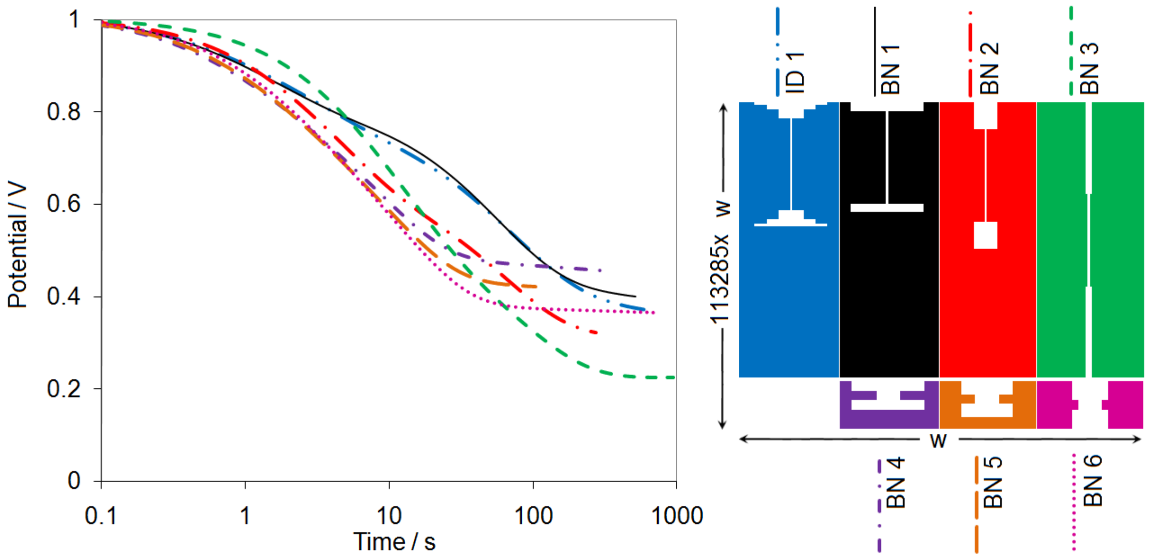

Figure 6.4: Self-discharge profiles for different pore $r_{mouth}/r_{bottleneck}$: with ratio of BN 1 > BN 2 > BN 3 = BN 4 > BN 5 > BN 6.

An inverted diamond shaped pore has a profile which contains a knee during the potential decline before charge redistribution completes (ID 1, Figure 6.4). A similar shape is observed in a cylindrical pore with the same pore mouth size and containing a bottleneck of the same size as the inverted diamond (BN 1, Figure 6.4). The similarity in the shape of these profiles highlights that the charge movement in a pore is dominated by the narrowest pore section (the bottleneck). Thus, any narrowing of the pore (*e.g.* narrowing due to template shape, electrode damage or film formation) must be avoided during electrode preparation.

Since the surface area is constant with all of these pores, the ID is slightly longer than BN1, and this extra length for the ID results in a slightly longer initial plateau and lower final potential when compared to BN 1. The emergence of the knee is most obvious for pore geometries where the pore mouth is large compared with the bottleneck (*e.g.* ID 1and BN 1) and least obvious for pores where the mouth and bottleneck are similar in size (*e.g.* BN 6), where the pore looks the most like a cylinder. The appearance of the knee in the profile can be rationalized as the bottleneck present within the pore breaks the pore into two regions, and the first slope is essentially due to charge redistribution within the upper region of the pore, above the bottleneck, and the second slope initiates at a longer time as the effective RC constant for the capacitors below the bottleneck is much larger due to the resistance through the bottleneck.

The separation of the charge redistribution in the different parts of the pore can be seen in Figure 6.5 which shows the potential of all eight capacitors during charge redistribution for BN 1 and BN 3. BN 3 has a smaller pore mouth than BN 1 and the potential of capacitors above the bottleneck (capacitors 1 - 4) range from 1.0 V to *ca.* 0.65 V for BN 1 and from 1V to *ca.* 0.1 V for BN 3. For BN 1 (Figure 6.5), the potential of capacitors 5-8 remain essentially constant until *ca.* 10 s while at *ca.* 1 s the potential of capacitors 3 and 4 begin to climb as charge from capacitors 1 and 2 is fed down the circuit. After *ca.* 10 s the charge redistributes throughout the entire pore, as seen by the increase in potential of capacitors 5-8 and the potential decrease of capacitors 1 - 4. As the capacitors in the lower half of the pore are at a much lower potential than capacitors above the bottleneck, there is a drastic increase in slope as the potential distribution between the capacitors taking part in charge redistribution has significantly increased, leading to an increased rate of potential loss on capacitor 1. Since there is a much larger disparity in potential down BN 3 (*cf.* BN 1), there is an increased potential distribution among the capacitors for BN 3, which leads to the steeper slope in the first linear region. For BN 3 the resistance of the bottleneck is comparable to the resistance throughout the rest of the pore, and the change in slope which leads to the knee seen in the profile for BN 1 is much less apparent in the profile for BN 3. This is reasonable, as this pore now looks more like a cylinder (very little difference in the incremental resistances down the pore) and the charge redistribution reflects this by being similar to that of a cylinder (Figure 6.1).

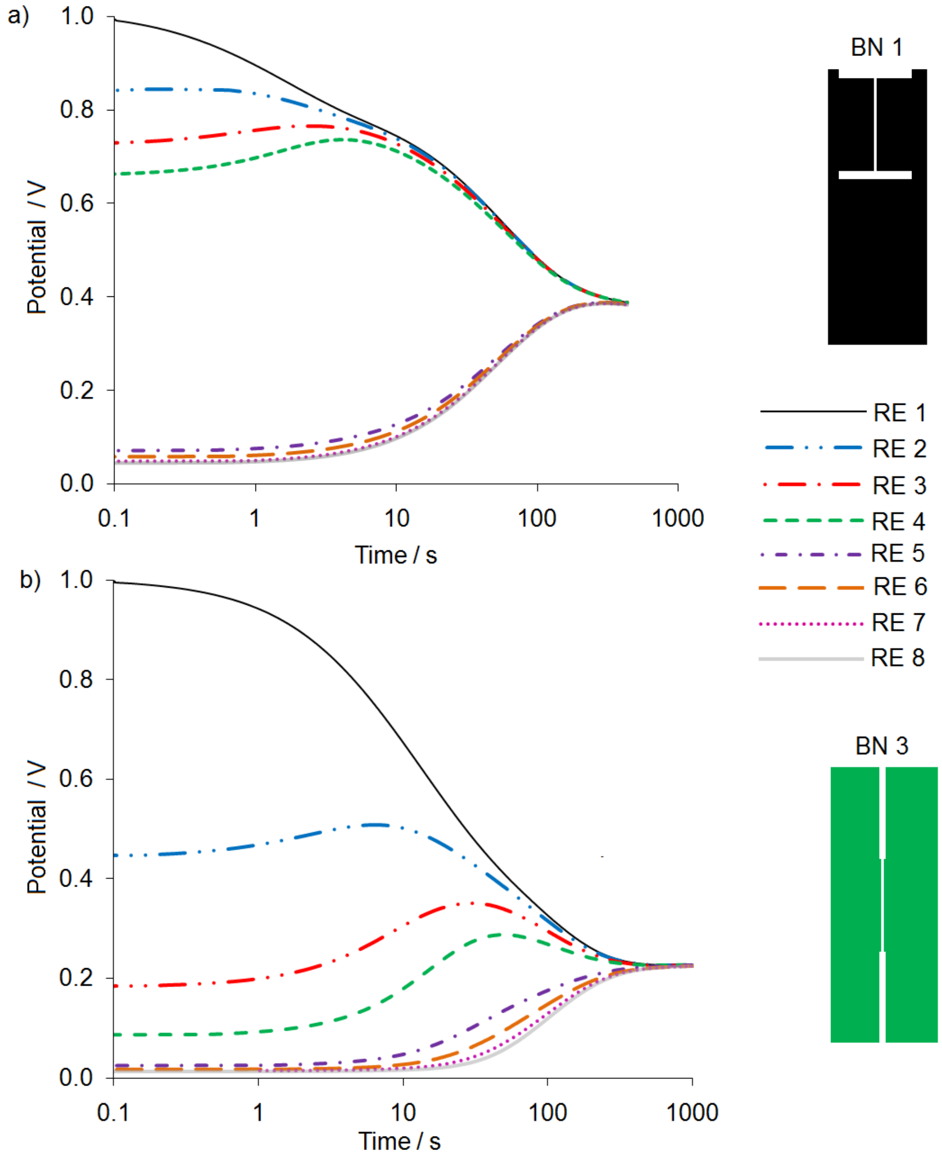

Figure 6.5: Potential recorded on capacitor 1 - 8 for a) BN1 and b) BN 3.

The pores modeled with less narrow bottlenecks (BN 4-6) show little variation in the plateau length in the self-discharge profile since the pore mouth sizes are similar;

however the plateau length does increase slightly with decreasing pore mouth radius. Similarly, the final potential is also shown to decrease as the pore mouth gets smaller. The presence of a knee in the self-discharge profile is not obvious for these bottlenecks. This again can be explained as these shapes are more similar to cylindrically shaped pores with small differences in the pore radius down the pore, and for this reason the self-discharge profile resembles that of a cylindrically shaped pore. To further understand the effect of bottlenecks on the charge redistribution a number of pore geometries containing bottlenecks were examined.

6.2.4 Effect of Length of Bottleneck at Pore Mouth

A series of pore geometries containing bottlenecks of different lengths positioned at the pore mouth were examined (Figure 6.6). Because the pore mouth size is the same for BN 7-9 and for BN 10-12, the length of the plateau in the self-discharge profile is approximately the same for BN 7-9 and for BN 10-12 (Figure 6.6), with a slight increase in plateau length with increasing bottleneck and pore length. Each of these pore geometries results in a self-discharge profile which is linear in log *t*, with a single slope in the potential decline region, dependent on the length of the bottleneck, with a longer bottleneck resulting in a decrease in slope.

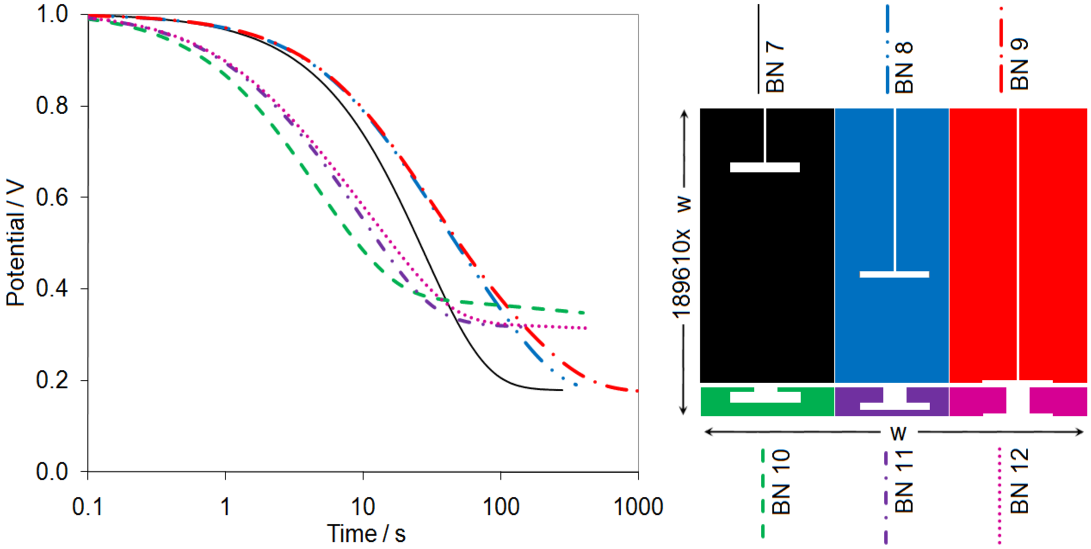

Figure 6.6: Self-discharge profile for different length bottlenecks of positioned at the pore mouth, with the bottleneck length increasing from BN 7-9 and BN 10-12.

6.2.5 Effect of Bottleneck Position in the Pore

Several pore geometries containing the same size bottleneck at different positions in the pore were also examined in order to examine the effect of moving a bottleneck deeper into a pore, and the results are shown in Figure 6.7. As mentioned above, a bottleneck present at the pore mouth leads to a self-discharge profile with a single slope for the potential decline region. However, a bottleneck partway down the pore results in a knee in the self-discharge profile, similar to that described in Section 6.2.4. A similar result is shown in Figure 6.7, where BN 7 and 10, which have the bottleneck at the pore mouth have only one slope in the potential decline region, while bottlenecks present at all other positions throughout the pore lead to a knee in the self-discharge profile. The presence of a knee in the profile is not obvious for BN 15 and 16 since there are small differences in incremental solution resistance down the pore resulting in a self-discharge profile which resembles that of a cylindrically shaped pore. The length of the plateau is related to the both the pore length as well as bottleneck position, with a long pore with a bottleneck at the pore mouth resulting in the longest plateau (BN 7), while a short pore with the bottleneck furthest from the pore mouth having the shortest plateau (BN 16).

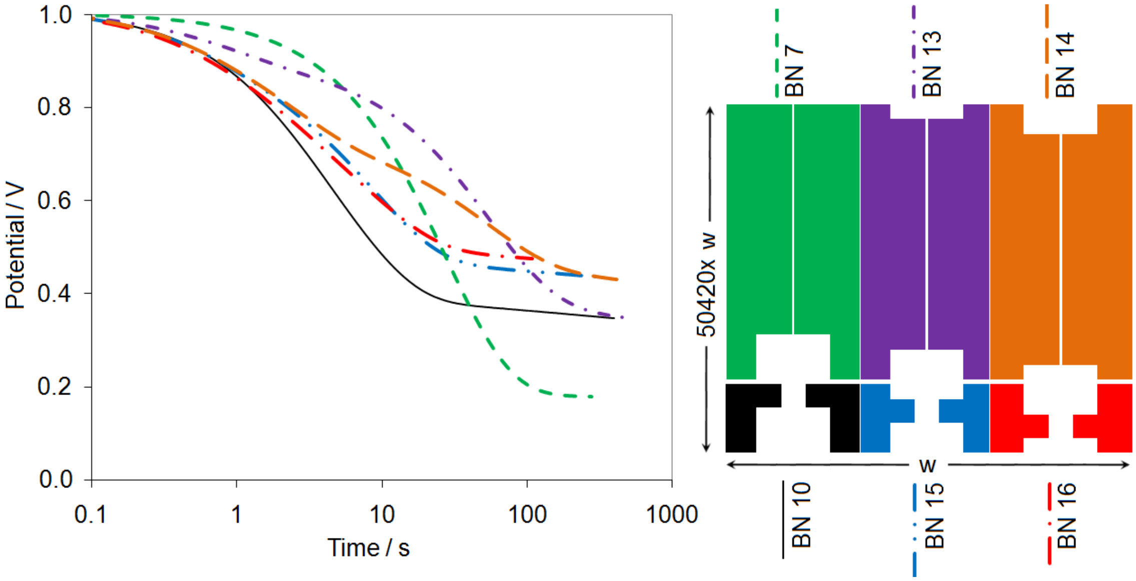

Figure 6.7: Self-discharge profile for bottlenecks positioned at different depths in the pore, with the depth increasing from BN 7-14 and BN 10-16.

The position of the bottleneck also affects the slopes of the potential decay during charge redistribution. The first slope of the self-discharge profile decreases as the bottleneck is moved closer to the pore mouth. BN 13, which has the bottleneck present right below the pore mouth, has the lowest first slope, while BN 14 whose bottleneck is farthest from the pore mouth has the steepest slope in this region. This first slope after the plateau in the self-discharge profile is related to the charge redistribution that results from the pore area above the bottleneck, and since BN 13 has the lowest number of capacitors (smallest surface area) above the bottleneck, the amount of potential distribution above the bottleneck is small, leading to a small rate of potential decrease during this region. BN 14 on the other hand has a greater number of capacitors (higher surface area) above the bottleneck for the group of BN 7 to 14, and as a result there is a greater potential distribution developed among these capacitors, leading to an increased rate of potential decline during this first slope. Conversely, BN 13 has a larger area below the bottleneck compared to BN 14, and the greatest potential distribution among capacitors below the bottleneck, so once the pore area below the bottleneck is able to participate in charge redistribution, at these longer times, the second slope (after the knee) is largest for BN 13, and smallest for BN 14.

The final potential after charge redistribution, and therefore the total amount of charge, increases as the bottleneck moves away from the pore mouth. This is not surprising as during charging only the capacitors (surface area) above the bottleneck are charged significantly, and increasing the number of capacitors (surface area) above the bottleneck increases the number of capacitors (surface area) participating in charging.

6.2.6 Effect of Having More Than One Bottleneck

A number of pore geometries containing more than one bottleneck were also examined. Similar to what was shown above, for pores having the smallest bottleneck at the pore mouth (BN 7,17,18,20,21, Figure 6.8) the self-discharge profile contains only 1 slope in the potential decline region, while pores which have the smallest bottleneck partway down the pore exhibit a knee in the profile (BN 19 and 22, Figure 6.8). The plateau length depends mainly on the bottleneck at the pore mouth (compare BN 7, 17 and 18, where the pore mouth is the same but the bottleneck down each pore is different).

There is very little difference between the self-discharge profiles for BN 7 and BN 18, indicating that the presence of the second, less restricting, bottleneck midway down the pore is not significantly affecting the self-discharge profile.

BN 17 has a slightly lower slope than BN 7 and 18, indicating that the presence of the second bottleneck of the same size midway down the pore results in a slower charge redistribution. BN 19, which has a wider bottleneck at the pore mouth, and narrower bottleneck midway down the pore, has a self-discharge profile containing knee, as the largest bottleneck is present partway down the pore, as opposed to the pore mouth. This is consistent with the smaller bottleneck dominating the self-discharge profile. Due to the large pore mouth, the initial plateau length is shorter for BN 19, followed by the first steeper slope, and a second shallower slope. The presence of the bottleneck at the pore mouth causes a significant potential distribution to develop between the capacitors above the second bottleneck, causing a fairly rapid drop in potential, during the first slope, in contrast to the diamond geometries discussed earlier.

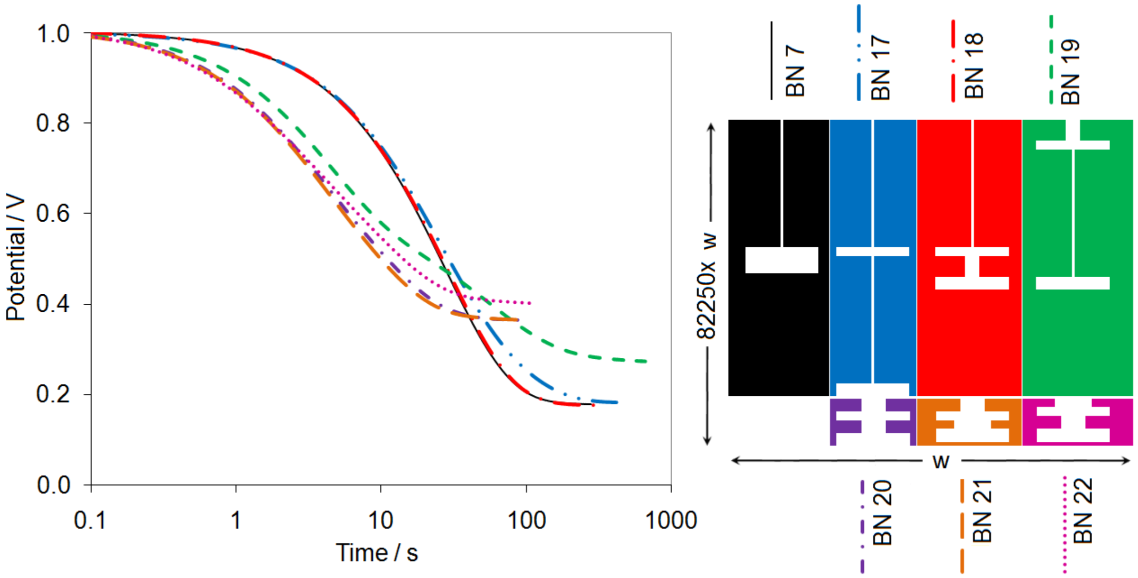

Figure 6.8: Self-discharge profile for pore geometries containing multiple bottlenecks of various positions and size.

6.3 Conclusions

Since the pore structure of electrodes, including pore size and pore shape, is a major factor determining the performance of devices using porous electrodes (such as ECs), it is important to have a good understanding of the effect of changes in pore shapes on electrode performance. Of particular concern here is how the shape of the pore affects the spontaneous movement of charge once the system has been placed on open circuit (immediately after electrode charging). This charge redistribution results in a lower than desired effective potential on the electrode surface, which may reduce the energy density for the system.

Modeling various pore shapes using a hardware transmission line circuit showed that cone, inverted cone and diamond shapes all resulted in self-discharge profiles akin to the self-discharge profiles obtained for cylindrically shaped pores, with an initial plateau, followed by a linear decrease in potential in log *t*, and finally another plateau as charge redistribution is complete. The length of the initial potential plateau is strongly influenced by the size of the pore mouth, with smaller pore mouths exhibiting longer plateaus. However, small pore mouths result in slower charging rates for these pores, and may lead to less charge available during capacitor use. The length of the pore plays a more minor role in the determination of the plateau length, with longer pores resulting in longer plateaus.

The results suggest that the damage or occlusion of the pore mouth must be avoided during templating of the electrode, film formation or cell preparation, as a small amount of pore occlusion can have a very important effect on the charging and charge redistribution characteristics of the electrode. Similarly, when using porous materials which undergo swelling during charging, (*e.g.* conducting polymers) it is important to design these materials to account for the volume change such that the swelling does not result in occlusion of the pore mouth (*e.g.* cone shaped pores).

Comparing cone, inverted cone, and cylindrically shaped pores having the same total resistance and capacitance illustrated that cone shaped pores were able to accumulate the most charge during the charging rates used in this study, as evidenced by the final potential on completion of charge redistribution. Comparisons between pores with the same pore mouth radius indicate that the pore mouth plays an important role in determining the amount of charge entering the pore during charging. Given that the pore mouth resistance was the same for these pore geometries, the length of the initial plateau was also very similar, with the cone shaped pore having a slightly longer plateau due to the increase in total pore resistance. However, the rate of potential loss at the pore mouth was lower for the cone shaped pore, due to the increased total resistance within the pore, and therefore slower movement of charge during charge redistribution.

Pore geometries containing bottlenecks at positions other than the pore mouth resulted in self-discharge profiles that have multiple slopes or rates of potential decline in log *t*, evidenced as a knee in the potential profile. The presence of a bottleneck essentially divides the pore into two separate regions, above and below the bottleneck, with the first slope being related to charge redistribution within the pore area above the bottleneck, and the second slope being related to charge redistribution throughout the entire pore surface, including the area below the bottleneck. During charging of a pore containing a bottleneck essentially only the pore area above the bottleneck participates in the charging process, with the pore area below the bottleneck accumulating only a small amount of charge during charging of the electrode, and this significantly decreases the overall amount of charge within a pore during charging. Predictably, for this reason, the presence of bottlenecks in the porous structure is undesirable.

Chapter 7

CAPACITANCE PROFILE OF VARIOUS PORE GEOMETRIES AND COMPARISON TO PROFILE OF SPECTRACARB 2225 CARBON CLOTH

7.1 Introduction

For porous carbons, it is useful to examine the dependence of the capacitance on the frequency of an applied alternating voltage. Due to increasing penetration depths with decreasing frequency, the measured capacitance of a porous carbon increases with decreasing frequency until a maximum capacitance is reached at very low frequencies. For high power performance, it is important that the capacitance is accessible at the highest possible frequencies (analogous to fast charge/discharge rates). This chapter examines the capacitance-frequency profile of various pore geometries using a transmission line model. Results are compared to the capacitance-frequency profiles of Spectracarb 2225 carbon cloth and graphite carbon powder to determine if the shape of the capacitance-frequency profile for Spectracarb 2225 carbon cloth reveals any information on the pore structure.

7.2 Results and Discussion

Figure 7.1 shows a plot of the series capacitance ($1/-\omega Z_{im}$) of Spectacarb 2225 carbon cloth and graphite carbon powder as a function of frequency, calculated from electrochemical impedance spectroscopy data. At high frequency the capacitance approaches zero for both samples, and as the frequency decreases, the capacitance increases. For graphite carbon powder, the capacitance plateaus at a frequency of *ca.* 0.1

Hz, presumably corresponding to the maximum electrode capacitance. The capacitance of the Spectracarb 2225 carbon cloth increases with decreasing frequency until a frequency of *ca.* 0.01 Hz, at which point the capacitance continues to increase, but at a slower rate, for all frequencies tested in this experiment (> 300 μHz), *i.e.*, a plateau corresponding to the maximum electrode capacitance is never truly reached.

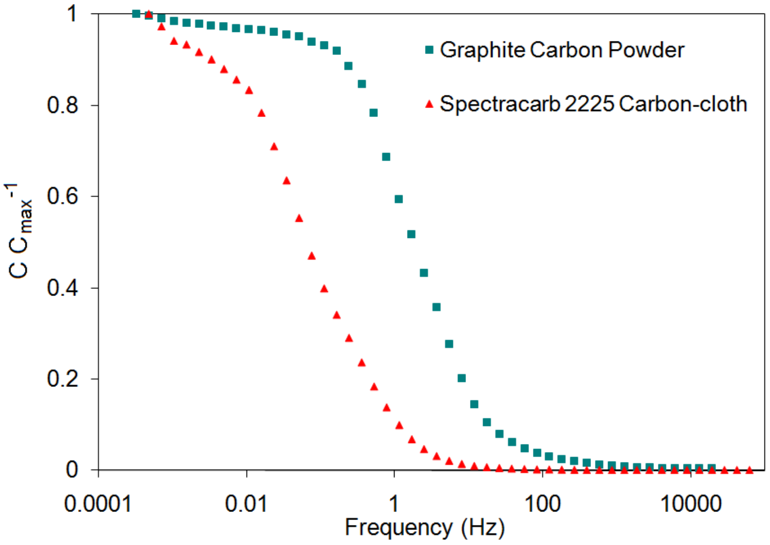

Figure 7.1: Plot of the capacitance of Spectracarb 2225 carbon cloth and graphite carbon powder in 1 M H_2SO_4, calculated from electrochemical impedance spectroscopy data at a potential of 0.75 V, as a function of frequency.

To examine whether the shape of the capacitance profile from electrochemical impedance spectroscopy data for Spectracarb 2225 carbon cloth revealed information regarding pore shapes, similar profiles were modeled with Z-Sim using various pore shapes. To ensure the Z-Sim modeling was working properly, impedance data were simulated for cylindrical, cone, and inverted cone geometries (Figure 7.2). The profiles were normalized for total resistance by dividing the real, Z_{Re}, and imaginary components,

Z_{Im}, of the impedance by the total circuit resistance. The limiting value of Z_{Re} for the cylindrical geometry is *ca.* 0.3 of the total pore resistance, which agrees well with previous results.[7, 47] The limiting value of Z_{Re} was found to decrease below 0.3 for pores which are narrowing, with the more narrowing geometries exhibiting lower limiting values, such as cone 1 which narrows more quickly than cone 2, and has a lower limiting value of Z_{Re} (0.08) than does cone 2 (0.20). Conversely, pores which broaden have limiting values of Z_{Re} greater than 0.33, and the more broadening the geometry, the larger the limiting value of Z_{Re}. Inverted cone 1 broadens more quickly than does inverted cone 2, and has a larger value of Z_{Re} (0.63) than does inverted cone 2 (0.44). These trends match those of Eloot *et al.*, and suggest that the model being used is adequate.[7]

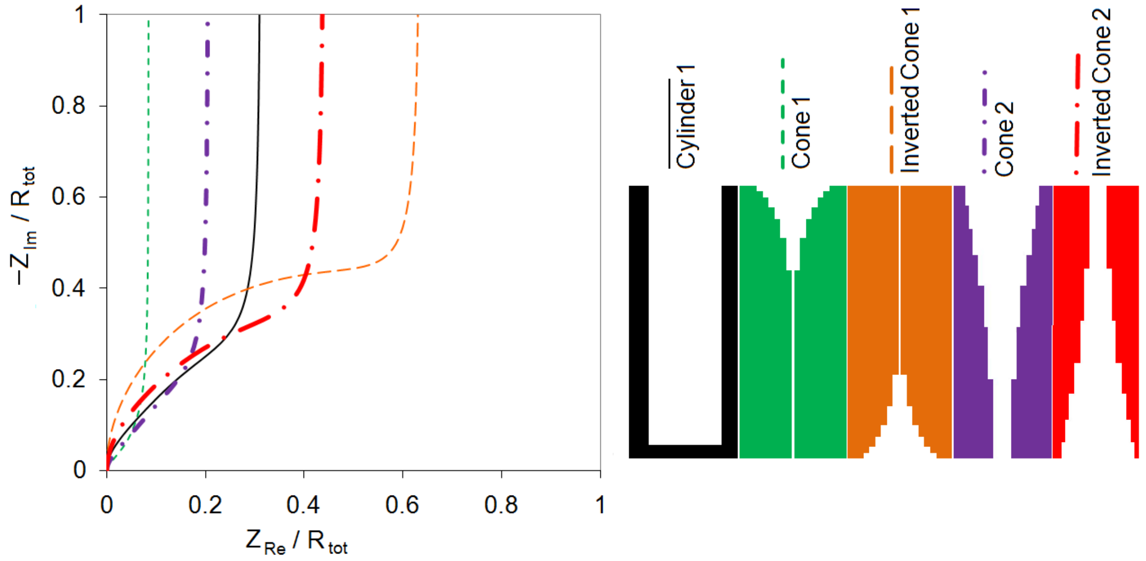

Figure 7.2: Simulated Nyquist plot for cylindrical cone and inverted cone geometries. Z_{Re} and Z_{Im} are normalized by dividing by the total resistance, R_{tot}.

The variation of capacitance as a function of frequency was modeled for numerous pore geometries. Figure 7.3 shows the capacitance-frequency profile for different pore shapes (cylinders, cone, and inverted cone) all of which have the same surface area (as the total capacitance for each is equal). However, as described in a paper by Eloot *et al.*, the impedance profile of a given pore geometry is significantly affected by the number of sections, *n*, which the pore is divided into, and as *n* approaches ∞ the impedance profile approaches the true analytical solution.[7] The capacitance profiles were calculated for various pore geometries based on a transmission line model where *n*, the number of capacitors, is 8 or 22, to examine the effect of n on the capacitance profile. For each pore geometry included in this figure the capacitance transitions from a minimum value at high frequencies to a maximum value at low frequencies. The minimum capacitance value at high frequencies approaches zero as n approaches ∞ and the incremental capacitances and resistances decrease (minimum capacitance is total capacitance divided by *n*). Otherwise, the capacitance profile calculated for *n* = 8 matches well to *n* = 22, and the overall shape remains the same.

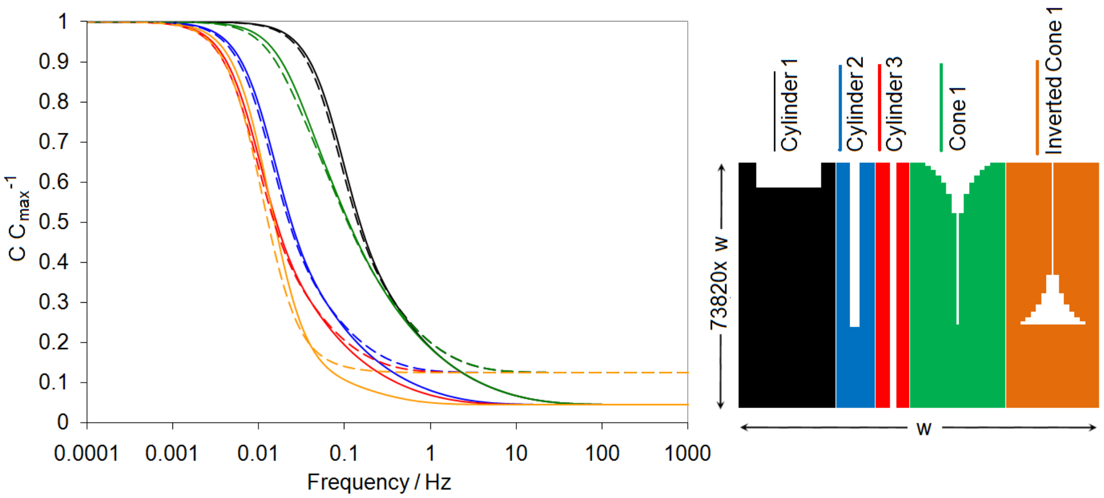

Figure 7.3: Plot of capacitance vs. frequency for various pore geometries, calculated with *n* = 8 (dashed) and 22 (solid).

For the cylinders, cone, and inverted cone geometries the capacitance profile contains two plateaus, and a region between them in which the capacitance varies linearly with log frequency. Cylinder 1 and cone 1 have the same pore mouth resistance, and the capacitance profiles for these pore geometries match very well at high frequencies. However, as the frequency decreases below *ca.* 0.2 Hz, the capacitance of cylinder 1 is higher than cone 1 until the maximum capacitance of cone 1 is reached at ca 0.01 Hz. This is not surprising as cylinder 1 models a shorter pore with a lower total resistance than cone 1. Cylinder 2 has the same pore length as cone 1, but shows a lower capacitance than cone 1 until very low frequencies (*ca.* 0.002 Hz). This highlights the advantage of cone shaped pores for high power applications as the same capacitance is accessible at higher frequencies, compared to a cylindrically shaped pore with the same surface area and length. The capacitance of cylinder 3 and inverted cone 1 geometries, which have a large pore mouth resistance, is not accessible until very low frequencies (< 0.1 Hz), illustrating the problems with having very restrictive pore mouths. These results agree well with conclusions drawn from self-discharge profiles of various pore geometries discussed in Chapter 6.

The capacitance-frequency profiles of a number of diamond shaped geometries are shown in Figure 7.4. The pore mouth resistance of diamonds 1 - 3 (300 kΩ) is much higher than the pore mouth resistance of diamonds 4 - 6 (30 kΩ), and as a result, the capacitance profile is shifted to much lower frequencies. Comparing diamond geometries with the same size pore mouth, the capacitance profiles match at high frequencies, but as the pore width decreases (and therefore pore length increases) the capacitance increases less quickly with diminishing frequency.

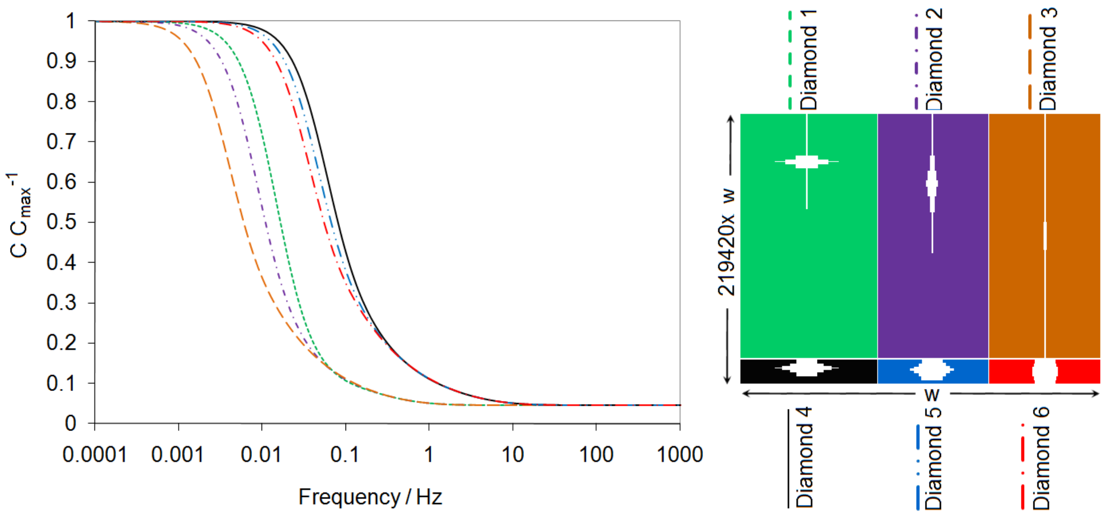

Figure 7.4: Plot of capacitance vs. frequency for various diamond shaped pore geometries, calculated with $n = 22$.

The capacitance-frequency profiles for various pore geometries containing bottlenecks are shown in Figure 7.5. A bottleneck present at the pore mouth (*e.g.* BN 7 and BN 10) results in a capacitance profile which falls linearly with increasing log frequency between the two capacitance plateaus. When a bottleneck is present midway through the pore (*e.g.* BN 13-16), there is no longer a simple linear increase in capacitance with decreasing log frequency between the two capacitance plateaus, and for very restrictive bottlenecks a knee appears in the capacitance-frequency profile (BN 13 and 14). Because the surface area above the bottleneck is lower in BN 13 compared to BN 14, the knee occurs at lower capacitance values.

The presence of bottlenecks can therefore alter the capacitance-frequency profile from the linear profile that is expected for all pore geometries that do not contain bottlenecks. The capacitance-frequency profile obtained for Spectracarb 2225 carbon cloth had a capacitance which increased linearly with log frequency between *ca.* 100 and 1 Hz, and continues to increase at frequencies lower than 1 Hz, but the increase is at a slower rate, never reaching a plateau in the range of frequencies tested. This capacitance profile may be a result of the presence of restrictive bottlenecks or very small pores which are only accessible at very low frequencies, and the absence of a plateau in the capacitance-frequency profile may suggest that the entire electrode capacitance is not accessed even at the lowest frequencies tested (300 μHz).

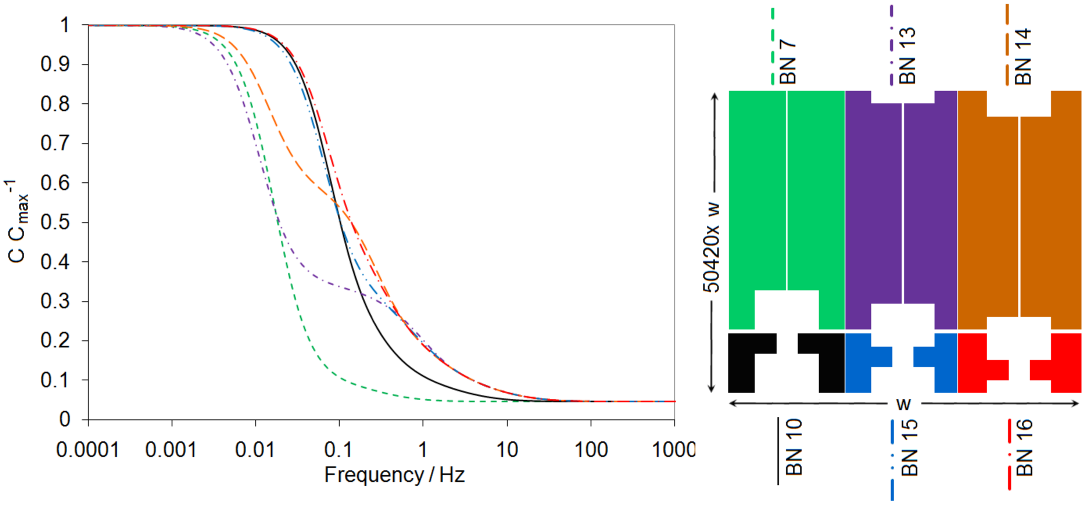

Figure 7.5: Plot of capacitance vs. frequency for various pore geometries containing bottlenecks, calculated with $n = 22$.

7.3 Conclusions

The capacitance-frequency profiles for various pore geometries highlighted the advantage of cone shaped pore over a cylindrical pore having the same surface area and length for high power applications. The disadvantages of restrictive bottlenecks or pore mouths were also demonstrated, as they reduce the power capability, evident by a shift in the capacitance profile to lower frequencies. The presence of bottlenecks partway through the pore resulted in a knee in the capacitance-frequency profile, different from the linear capacitance profile with log frequency obtained for all other geometries. This may help to explain the capacitance-frequency profile obtained for Spectracarb 2225 in which the capacitance does not simply increase linearly with log frequency, but rather contains two regions of different slope, suggesting the presence of very small pores or restrictive bottlenecks which are only accessible at very low frequency.

Chapter 8

EFFECT OF ELECTROLYTE ION ON SELF-DISCHARGE AND CHARGE REDISTRIBUTION

8.1 Introduction

In ECs, charge on the electrode surface is balanced by ions in the electrolyte, and charge redistribution in the pores of the material is coupled with a movement of electrolyte ions in the pores. This movement of ions within the pores is the limiting step during charge redistribution, as the resistance of the electrode which limits charge movement is very small in comparison to the resistance of the electrolyte within the pores which limits ion movement. For this reason, it is expected that a change in the electrolyte ions would significantly affect charge redistribution. This chapter examines the effect of different electrolyte ions on the self-discharge profile of porous carbon-cloth electrodes. Self-discharge experiments were also performed on a low surface-area carbon and results were compared to those of the high surface-area carbon cloth to gain insight on the role of charge redistribution in self-discharge of high surface-area carbons.

8.2 Results and Discussion

8.2.1 Spectracarb 2225 Carbon Cloth

Self-discharge experiments were performed on Spectracarb 2225 carbon cloth in various electrolytes (1 M aqueous solutions of H_2SO_4, HCl, NaCl, KCl, $MgCl_2$, and

$CaCl_2$) to examine the effect of electrolyte ion on the self-discharge and charge redistribution in porous carbons.

CVs were collected prior to and following each self-discharge experiment, and the first and last CV collected in each electrolyte are shown in Figure 8.1. In acids (H_2SO_4 and HCl, Figure 8.1a and b) peaks are observed at *ca.* 0.5 V, attributed to oxidation and reduction of quinone surface functionalities (Chapter 4). In neutral electrolytes (Figure 8.1c-f), this peak is absent. The potential of the quinone reaction is dependent on pH, and will be shifted by 60 mV for every unit change in pH. Since the pH of the 1 M NaCl electrolyte is close to 6, it would be expected that the potential of the quinone reaction would shift *ca.* 360 mV to lower potentials compared to the 1 M acid, with a pH of 0. This suggests that the quinone reaction in 1 M NaCl should occur at *ca.* 0.15 V, however this peak is not evident in the CV, and the reason why the peak is not present is unclear. As a result, the capacitance in acidic electrolytes is higher, as capacitance from the pseudocapacitive quinone reaction adds to the double-layer capacitance. In neutral electrolytes, the absence of pseudocapacitive reactions results in a CV with a more rectangular shape, associated with charging and discharging of the double-layer capacitance only. For easier comparison Figure 8.2 shows a CV in each electrolyte overlaid. The potential regions of interest for self-discharge from 1.0 V and 0.0 V have approximately constant capacitance with no large peaks, and it is therefore not expected to see any features in the self-discharge profile associated with changes in differential capacitance with potential.

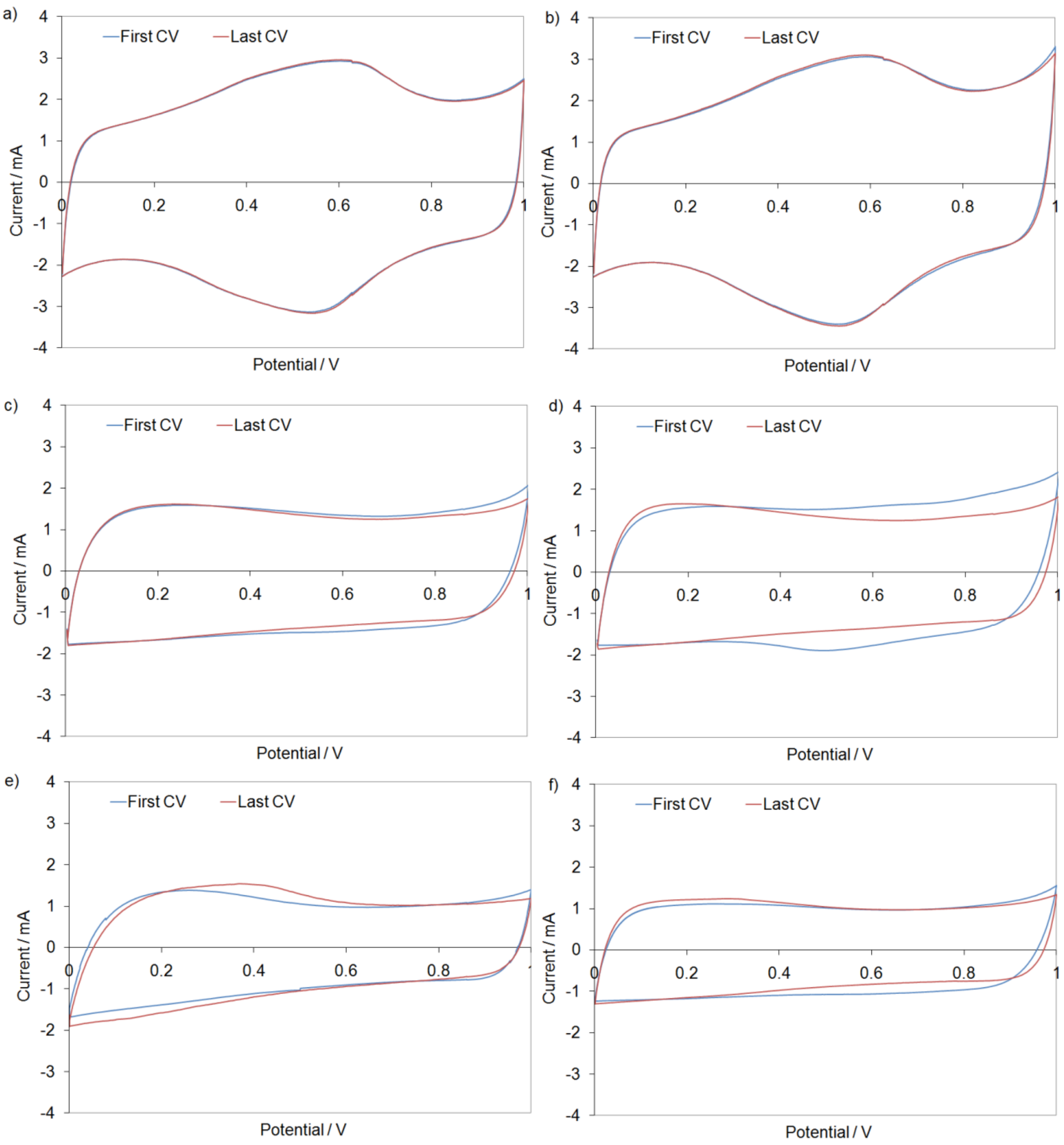

Figure 8.1: CV of Spectracarb 2225 carbon-cloth electrodes at 1 mV s^{-1} in a) H_2SO_4 (electrode mass - 9.0 mg), b) HCl (electrode mass - 8.9 mg), c) NaCl (electrode mass - 9.9 mg), d) KCl (electrode mass - 9.3 mg), e) $MgCl_2$ (electrode mass - 6.9 mg), and f) $CaCl_2$ (electrode mass - 7.2 mg).

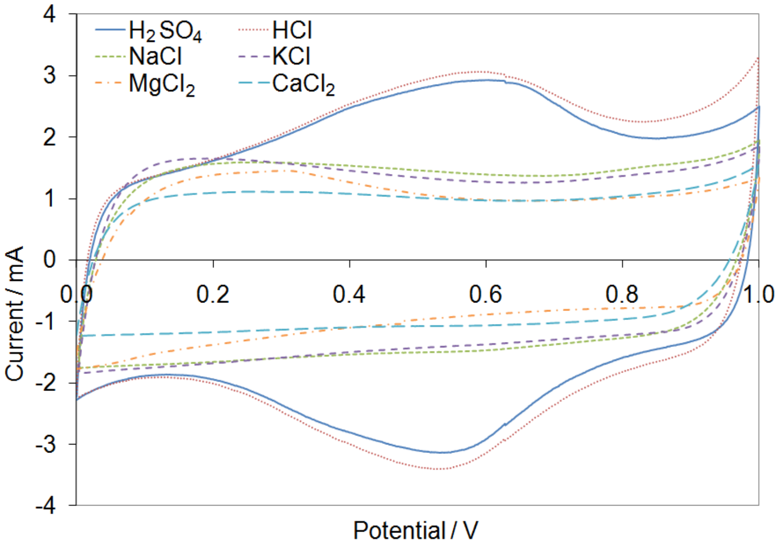

Figure 8.2: CV of Spectracarb 2225 carbon-cloth electrodes at 1 mV s^{-1} in 1 M H_2SO_4 (electrode mass - 9.0 mg), HCl (electrode mass - 8.9 mg), NaCl (electrode mass - 9.9 mg), KCl (electrode mass - 9.3 mg), $MgCl_2$ (electrode mass - 6.9 mg), and $CaCl_2$ (electrode mass - 7.2 mg).

Figure 8.3 shows the self-discharge profiles of Spectracarb 2225 carbon cloth in each electrolyte from an initial potential of 1.0 V plotted in log *t* (Figure 8.3a) and $t^{1/2}$ (Figure 8.3b). For the self-discharge profile in 1 M $CaCl_2$, the increase in potential seen at the end of the self-discharge profile is believed to be a result of a shift in the potential of the Ag/AgCl reference electrode. It is possible that if the reference electrode lead from the potentiostat was moved out of place it may have caused the reference electrode to be unintentionally pulled partially out of solution for some period of time. For this reason, this particular self-discharge profile was not included in this analysis.

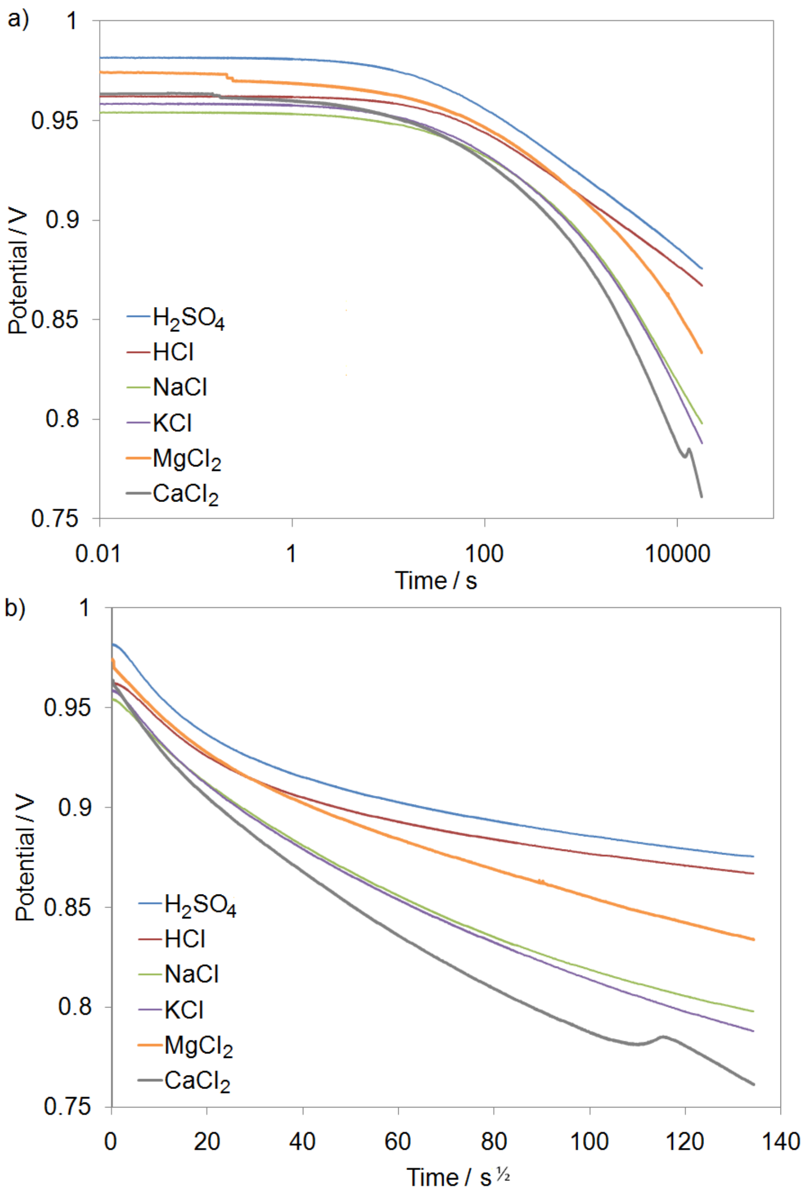

Figure 8.3: Self-discharge profiles of Spectracarb 2225 carbon-cloth electrodes in 1 M H_2SO_4 (electrode mass - 9.0 mg), HCl (electrode mass - 8.9 mg), NaCl (electrode mass - 9.9 mg), KCl (electrode mass - 9.3 mg), $MgCl_2$ (electrode mass - 6.9 mg), and $CaCl_{2,}$ (electrode mass - 7.2 mg) after charging from 0.5 V to 1.0 V at 1 mV s^{-1} in plotted in a) log *t* and b) $t^{\frac{1}{2}}$.

Self-discharge profiles from an initial potential of 1.0 V appear to contain a region of linear decrease in potential with log *t*. This is most apparent for acidic electrolytes, (H_2SO_4, and HCl). For the neutral electrolytes (NaCl, KCl, and $MgCl_2$), it was more difficult to determine whether the profile was more linear in log t or $t^{1/2}$ over times collected, and upon visual inspection it was decided that the profiles were more linear in log t than $t^{1/2}$. The reason that the linearity of the self-discharge profile is more apparent in acidic electrolytes may be because the plateau length in acidic electrolytes is shorter, and therefore the linear region is longer for times collected in this experiment. The charge redistribution plateau length is expected to increase with increasing electrolyte resistance, as the plateau length is related to the time required for charge redistribution to initiate, which increases with increasing resistance (Chapter 6). Therefore, a longer plateau for the neutral electrolytes is not unexpected, and is consistent with charge redistribution. For initial potentials of 0.6 – 0.9 V, similar results were obtained in that the self-discharge profiles were assessed as linear in log t, as opposed to $t^{1/2}$, and these results are included in Appendix A1.

Figure 8.4 shows the relationship between the initial potential (> 0.5 V) and slope of the linear region of the self-discharge profile in log t. Data for $CaCl_2$ are not included here as there was not a sufficient linear region over which to calculate the slope. The slope increases (becomes more negative) with increasing initial potential, consistent with charge redistribution (Chapter 4). For charge redistribution, it is expected that for lower electrolyte conductivity, and therefore higher electrolyte resistance, charge redistribution initiates more slowly and takes longer to complete (Chapter 5). However, a higher electrolyte resistance also results in a larger potential distribution within the pores after charging, and therefore a greater 'driving force' for charge redistribution. For this reason, the rate of charge redistribution may be faster, increasing the slope of the self-discharge profile in a less conductive electrolyte. This is analogous a larger concentration gradient increasing the rate of diffusion. For self-discharge profiles from 1.0 V the slope is negative, and the slope may be expected to increase, or become more negative, with an increase in electrolyte resistivity (decrease in electrolyte conductivity) due to a larger potential distribution created in the pores during charging. In contrast, the electrolyte conductivity, or the identity of the ionic species, is not expected to affect the slope of the self-discharge profile for an activation-controlled Faradaic mechanism, unless perhaps one of the ionic species under study was involved in the Faradaic reaction. These results then suggest that charge redistribution is contributing to the potential loss for an electrode charged to 1.0 V for all electrolytes tested.

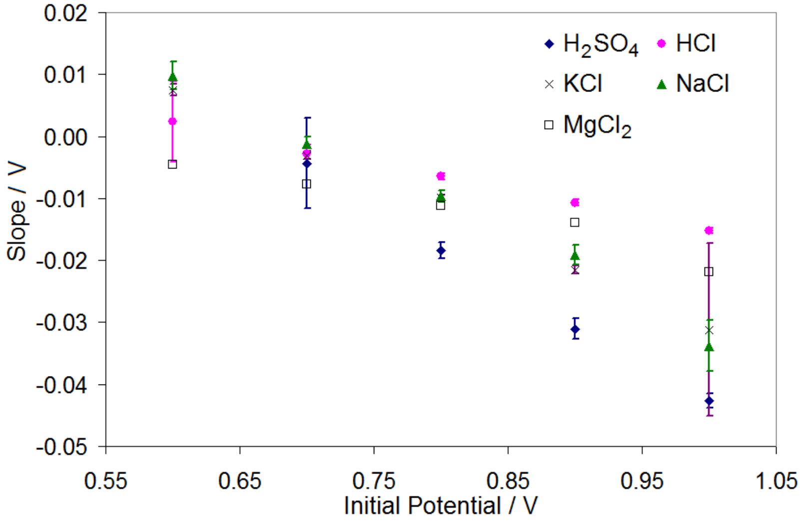

Figure 8.4: Relationship between initial charging potential (> 0.5 V) and slope of the linear region of the self-discharge profile when plotted in log *t* in s.*

Figure 8.5 shows the self-discharge profiles of Spectracarb 2225 carbon cloth in

---

*Error bars are one standard deviation for seven electrodes for H_2SO_4, five electrodes for HCl, and six electrodes for NaCl, and KCl. No error bars are shown for $MgCl_2$ since only one set of data was collected in this electrolyte. A number of error bars are not visible due to the large marker size for the data point and the small standard deviation. Data for all electrolytes are available in Appendix A1.

each electrolyte from an initial potential of 0.0 V plotted in log *t* and $t^{1/2}$. Self-discharge profiles from an initial potential of 0.0 V appear to contain a region in which the potential varies linearly with $t^{1/2}$. Similar results were obtained for initial potentials of 0.1 – 0.4 V and those results are included in Appendix A1.

That the self-discharge profile from high initial potentials is linear in log *t*, and from low initial potentials is linear in $t^{1/2}$ suggests different mechanisms of self-discharge for the two initial potentials. A linear decrease in potential with log *t* may be indicative of an activation-controlled Faradaic mechanism, or, may be a result of charge redistribution within the pores of the electrode, as discussed in Chapter 4. On the other hand, a linear decrease in potential with $t^{1/2}$ suggests that a diffusion-controlled Faradaic mechanism is responsible for the self-discharge. Results in Section 4.2.2 showed that the self-discharge from 0 V decreased with an increase in hold time, consistent with what is expected for charge redistribution. However, the linear profile in $t^{1/2}$ suggests a diffusion-controlled self-discharge mechanism. The self-discharge profile from 0 V is linear in $\mathrm{t}^{1/2}$ but only at times longer than *ca.* 1000 s. It is possible that both charge redistribution and a diffusion-controlled Faradaic reaction occur on an electrode charged to 0 V, with the self-discharge being under mixed control at short self-discharge times, and at longer self-discharge times the diffusion-controlled reaction discharges the electrode more quickly, and dominates the self-discharge profile.

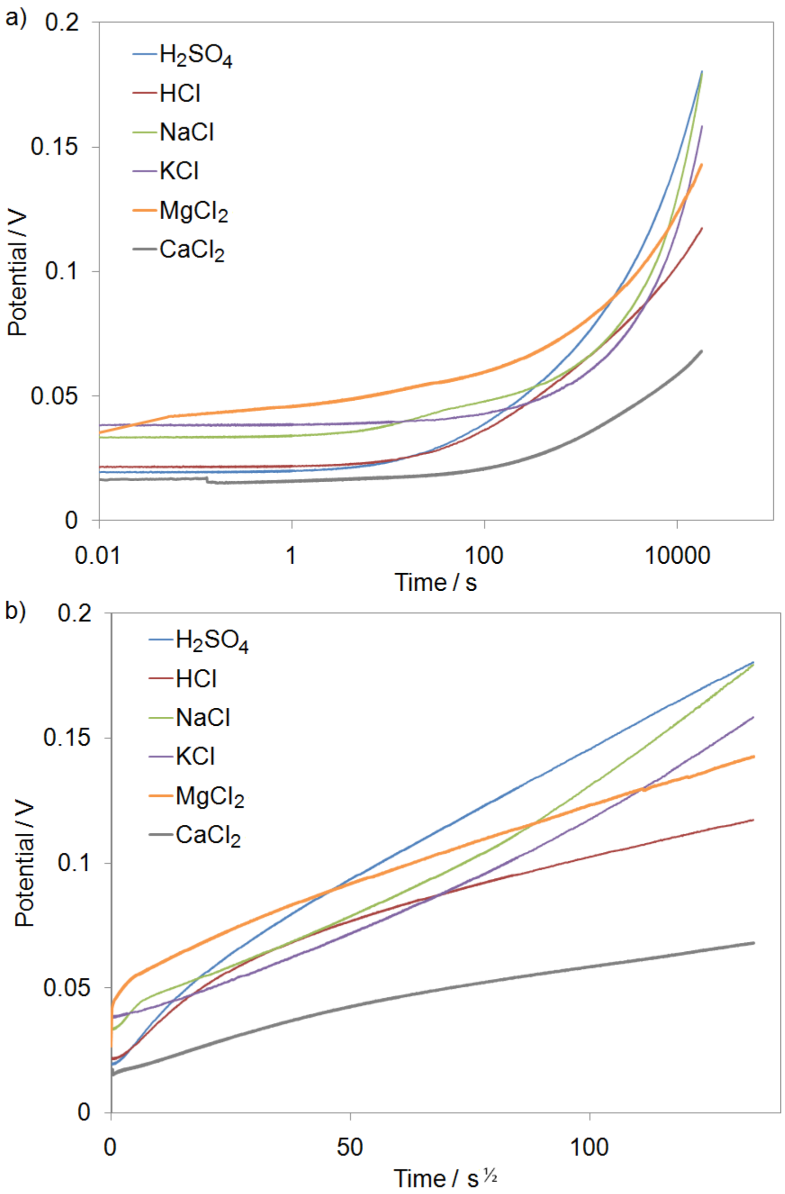

Figure 8.5: Self-discharge profiles of Spectracarb 2225 carbon-cloth electrodes in 1 M H_2SO_4 (electrode mass - 9.0 mg), HCl (electrode mass - 8.9 mg), NaCl (electrode mass - 9.9 mg), KCl (electrode mass - 9.3 mg), $MgCl_2$ (electrode mass - 6.9 mg), $CaCl_2$ (electrode mass - 7.2 mg) after charging from 0.5 V to 0.0 V at 1 mV s^{-1} plotted in a) log t and b) $t^{½}$.

Figure 8.6 shows the relationship between the initial potential (< 0.5 V) and the slope of the linear region of the self-discharge profile in $t^{½}$. The slope decreases with increasing initial potential. The linear relationship in $t^{½}$ suggests a diffusion-controlled

Faradaic self-discharge mechanism, however, the dependence of the rate of potential loss on the initial charging potential is unexpected for this type of reaction. If the self-discharge is due to reaction of electrolyte impurities at the electrode surface, it is not expected that the rate of potential loss to depend on the initial charging potential, as the electrode is discharged as quickly as the impurity can be brought to the electrode surface. In addition to this, the electrolytes used in this study were of high purity (up to 99.999%) and therefore the concentration of impurities in the electrolyte is expected to be low, and the electrolyte ions themselves should not do reactions at these potentials.

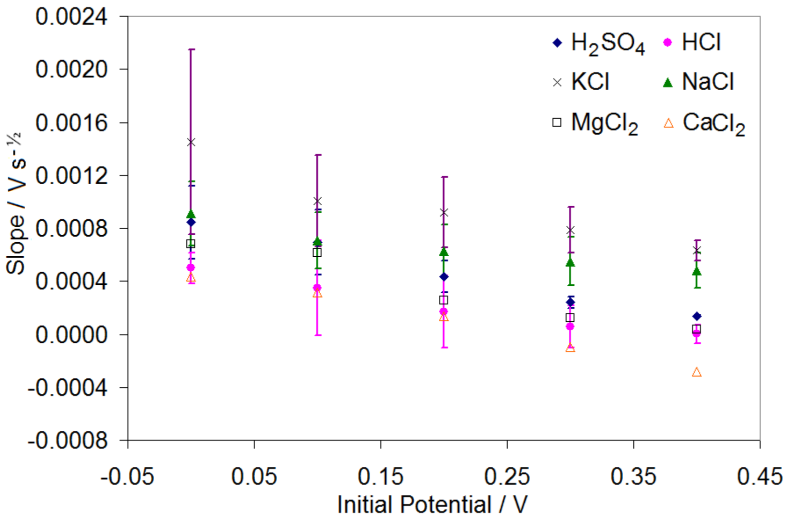

Figure 8.6: Relationship between initial charging potential (< 0.5 V) and slope of linear region of self-discharge profile in $t^{½}$.*

A diffusion-controlled self-discharge profile may also be limited by diffusion of a species away from the electrode surface; however the slope is not expected to depend on initial potential for this type of self-discharge mechanism. Unless, perhaps, the

---

[*] Error bars are one standard deviation for two electrodes for H_2SO_4, five electrodes for HCl, four electrodes for KCl, and six electrodes for NaCl. No error bars are shown for $MgCl_2$ or $CaCl_2$ since only one set of data was collected in these electrolytes. Data for all electrodes are shown in Appendix A1.

concentration of the species on the species on the electrode surface was somehow potential dependent. It may be speculated that charging to lower initial potentials results in an increased concentration of a species on the electrode surface, which increases the rate of diffusion of that species away from the surface, allowing more reaction to occur on the surface and so increasing the rate of self-discharge. However, results in Section 4.2.2 suggest that charge redistribution also occurs for an electrode charged to 0 V. It is therefore possible that the dependence of the slope of the self-discharge profile on the initial potential is related to charge redistribution effects.

If charge redistribution is responsible for part of the potential loss during self-discharge it is expected that the rate of potential loss would be affected by the electrolyte resistance, and therefore the electrolyte ion. Figure 8.7 shows the relationship between the slope of the self-discharge profile in log t for initial potentials > 0.5, and $t^{½}$ for initial potentials < 0.5 V, vs. the ionic conductivity of the cation (Figure 8.7a) and anion (Figure 8.7b) taken from reference 101. The slope of the self-discharge profile in log t from an initial potential of 1.0 V increases with increasing cation conductivity, with no correlation between the slope and anion conductivity. This is because for all of the electrolytes studied the cation is a larger contributor to the overall electrolyte conductivity than the anion, with conductivities about one order of magnitude higher than the anions. Therefore changing the cation has a larger effect on the electrolyte resistance. That the slope of the self-discharge profile from an initial potential of 1.0 V shows a dependence on the cation conductivity suggests that charge redistribution is occurring, and also that the cations are largely responsible for charge transport.

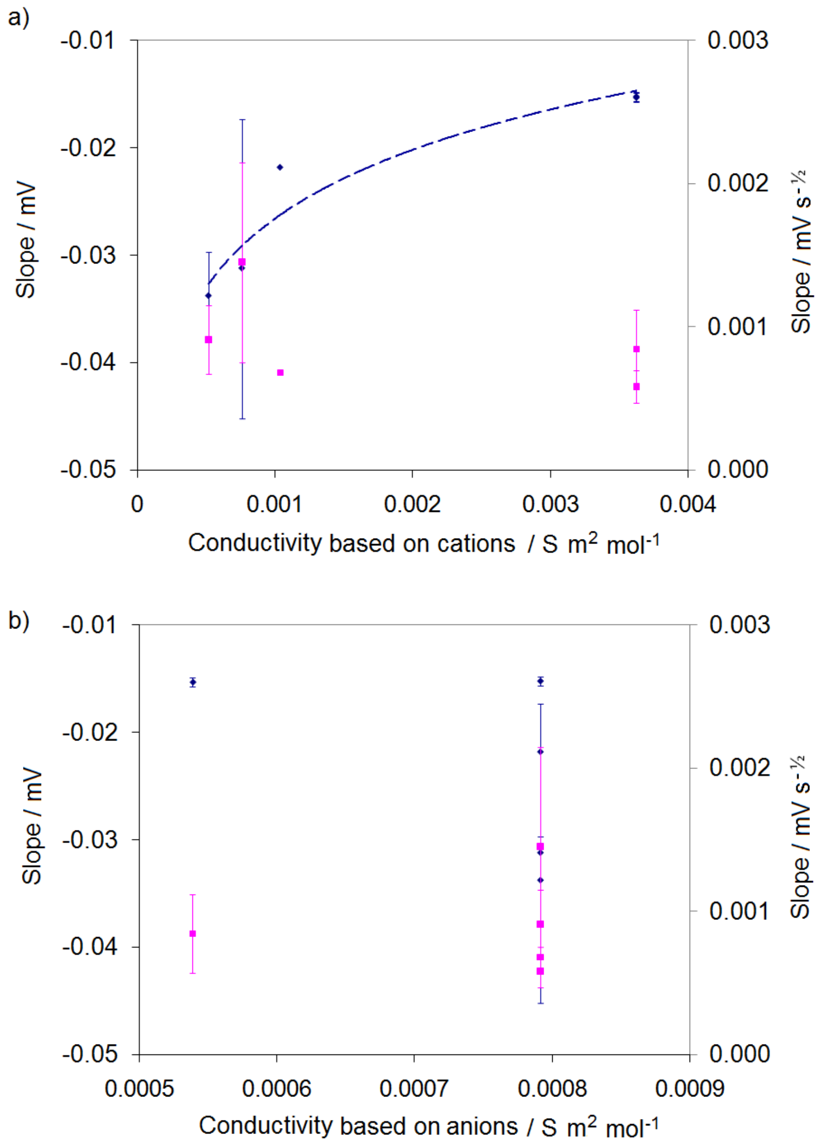

Figure 8.7: Slope of linear region of self-discharge profile for Spectracarb 2225 carbon-cloth electrodes when plotted in log *t* in s from an initial potential of 1.0 V (blue, left axis), and in $t^{\frac{1}{2}}$ from an initial potential of 0.0 V (pink, right axis) vs. a) the cation conductivity and b) the anion conductivity.[*]

---

[*] Error bars are for the 1.0 V self-discharge one standard deviation for seven electrodes for H_2SO_4, five electrodes for HCl, and six electrodes for NaCl, KCl and no error bars are shown for $MgCl_2$ since only one set of data were collected in these electrolytes. For the 0.0 V self-discharge one standard deviation for two electrodes for H_2SO_4, five electrodes for HCl, four electrodes for KCl, and six electrodes for NaCl and no error bars are shown for $MgCl_2$ or $CaCl_2$ since only one set of data was collected in these electrolytes. Data for all electrodes are shown in Appendix A1.

This means that although the electrode is thought to be positively charged at a potential of 1.0 V, and anions from solution balance the electrode charge, it is the mobility of the cations which limits charge redistribution because the cations used in this study are much more mobile than the anions. In other words, for a positively charged electrode surface, a surface excess of anions (Γ_-) is required to balance the charge. In order to provide the needed surface excess of anions, the cations (which are more mobile) will migrate away from the surface, leaving behind a surface excess of anions. Whether this migration of cations within the pores takes place axially or radially is unclear, and this could be the focus of further study. If the migration was radial, such that the cations migrated toward the center of the pore, an excess positive charge would build up in the center of the pore, which is energetically unfavourable, and would likely force axial diffusion of cations to minimize the build-up of charge in the middle of the pore.

The slope of the self-discharge profile in $t^{1/2}$ from an initial potential of 0.0 V displayed no dependence on the cation or anion conductivity. Results in Section 4.2.2 suggest that charge redistribution is occurring for an electrode charged to 0 V, and it may therefore be expected to see a dependence of the slope of the self-discharge profile on the conductivity of the electrolyte ions. However, the slopes of self-discharge profiles were calculated throughout the linear region in $t^{1/2}$, where it is believed that a diffusion-controlled Faradaic mechanism is controlling the self-discharge. For a diffusion-controlled Faradaic self-discharge mechanism the conductivity of the electrolyte ions would not be expected to affect the slope of the self-discharge profile (unless the electrolyte ions were involved in the self-discharge reaction). This result suggests that a diffusion-controlled Faradaic mechanism is responsible for the potential loss at long self-discharge times.

The self-discharge profile of Spectracarb 2225 carbon cloth in 1 M NaCl was also examined over long times, (Figure 8.8) to determine if an increased slope is present at long times, as seen in 1 M H_2SO_4 electrolyte (Figure 5.9). The increase in slope at long times was attributed to a completion of charge redistribution up the pores of the electrode, and was estimated at *ca.* 60 000 s (17 hours) in 1 M H_2SO_4 (Chapter 5). Results in Chapter 5 showed that the length of time required for charge redistribution is dependent on the solution resistance. Given the higher solution resistance of 1 M NaCl compared to 1 M H_2SO_4, it is expected that the increase in slope in 1 M NaCl would occur at later times, since charge redistribution requires more time to complete with a larger solution resistance. An increase in slope is in fact present in the self-discharge profile at *ca.* 120 000 s (33 hours). Since the change in slope occurs much later with a higher solution resistance, this is further data to support the completion of charge redistribution being responsible for the increased slope at long self-discharge times. Again, this highlights the importance of charge redistribution (which is often neglected) during the self-discharge of high surface-area carbons.

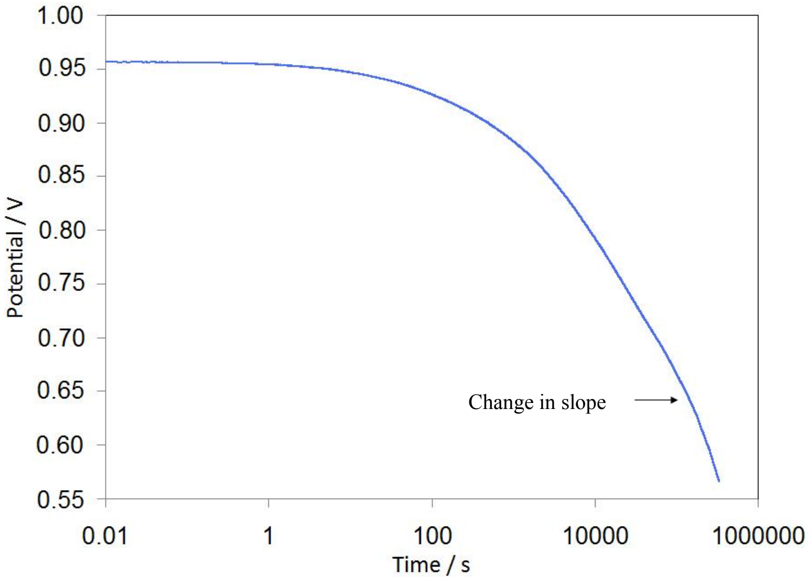

Figure 8.8: Self-discharge profile of a 6.7 mg Spectracarb 2225 carbon-cloth electrode in 1 M NaCl electrolyte after charging from 0.0 to 1.0 V at 1 mV s^{-1}.

Self-discharge profiles of Spectracarb 2225 carbon cloth in various electrolytes were examined after charging to an initial potential of 1.0 V at various ramp rates (0.5 – 10 mV s^{-1}) to determine the effect of ramp rate on the slope of the self-discharge profile. In Chapter 4 self-discharge profiles of Spectracarb 2225 carbon cloth after various ramp rates to 1.0 V were presented (Figure 4.18), and the relationship between the final potential and ramp rates was discussed. In this section, the slopes of self-discharge profiles after charging at various ramp rates, in various electrolytes are examined.

Figure 8.9 shows the relationship between the slope of the linear region of the self-discharge profile in log *t* and the ramp rate for each electrolyte. In each electrolyte, the slope becomes less negative with increasing ramp rate. The self-discharge profiles for each ramp rate and electrolyte are presented in Appendix A3. Upon closer examination, the relationship between the ramp rate and slope of the self-discharge profile appears to be an initial potential effect, as self-discharge profiles with higher ramp rates suffer from larger *IR* drops due to the increased current during the charging step, and as a result, when using higher ramp rates, the electrode is effectively reaching a lower initial potential (Section 4.2.5). Figure 8.9b shows a comparison of the slope of self-discharge profiles in 1 M H_2SO_4 and 1 M NaCl after charging to different initial potentials at 1 mV s^{-1}, and also after charging to 1.0 V at 0.5 – 10 mV s^{-1} where the initial potential is taken as the potential immediately after the *IR* drop. The slope of the self-discharge profiles after charging at various ramp rates follow a similar trend as the self-discharge slopes from various initial potentials, suggesting that the changes in slope seen for the ramp rates tested in this study are largely due to an initial potential effect. Therefore the self-discharge profiles performed after various charging rates did not provide additional information over self-discharge profiles from various initial potentials.

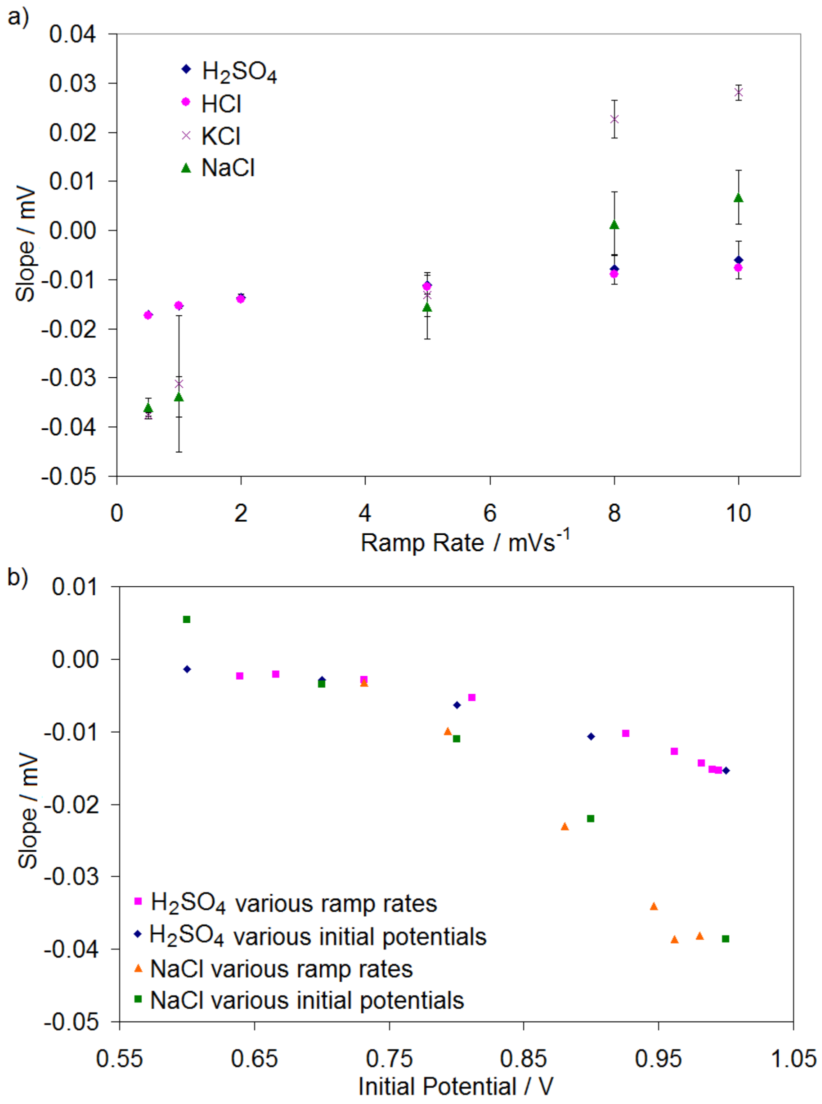

Figure 8.9: a) Relationship between ramp rate and slope of linear region of self-discharge profile when plotted in log *t* in s for Spectracarb 2225 carbon cloth in various electrolytes.[*]

---

[*] Error bars are one standard deviation for two electrodes for H_2SO_4, five electrodes for HCl, and six electrodes for NaCl and KCl. b) Relationship between slope of the linear region of the self-discharge profile in log *t* plotted in s and initial potential for Spectracarb 2225 carbon-cloth electrodes in 1 M H_2SO_4 and NaCl charged at 1 mV s^{-1} from 0.5 V to different initial potentials (0.6 - 1.0 V, H_2SO_4 (blue) and NaCl (green)) and different ramp rates (0.5 - 10 mV s^{-1}, H_2SO_4 (pink) and NaCl (orange)). For the different ramp rates data, the potential of the electrode immediately after the *IR* drop is considered the initial potential.

8.2.2 Graphite Carbon Powder

The self-discharge profiles of a low surface-area carbon, graphite carbon powder, were also studied in different electrolytes, to determine if results attributed to charge redistribution for Spectracarb 2225 carbon cloth occur in low surface-area carbons, where charge redistribution is not expected. Figure 8.10 shows a plot of the differentiated capacitance of graphite carbon powder obtained (by dividing the current by the sweep rate and mass) from CVs performed at various sweep rates. At high sweep rates the capacitance is greatly reduced, and at sweep rates below *ca.* 10 mV s^{-1} the capacitance remains approximately constant, indicating that the entire surface area is accessed. There is an increase in the oxidation peak present at potentials above *ca.* 1.0 V, and the reduction peak at a potential of *ca.* 0.6 V, with decreasing sweep rate. Since these peaks are a result of oxidation and reduction reactions at the electrode surface, a lower sweep rate allows more time for the reactions to take place, and therefore an increase in these peaks at low sweep rates is not unexpected. When charging the graphite carbon powder at a sweep rate of 1 mV s^{-1}, it is expected that the entire surface is charged, and therefore when the system is switched to open circuit, a loss in potential due to charge redistribution is not expected, making this a good candidate to compare to results of the high surface-area carbon where charge redistribution is expected.

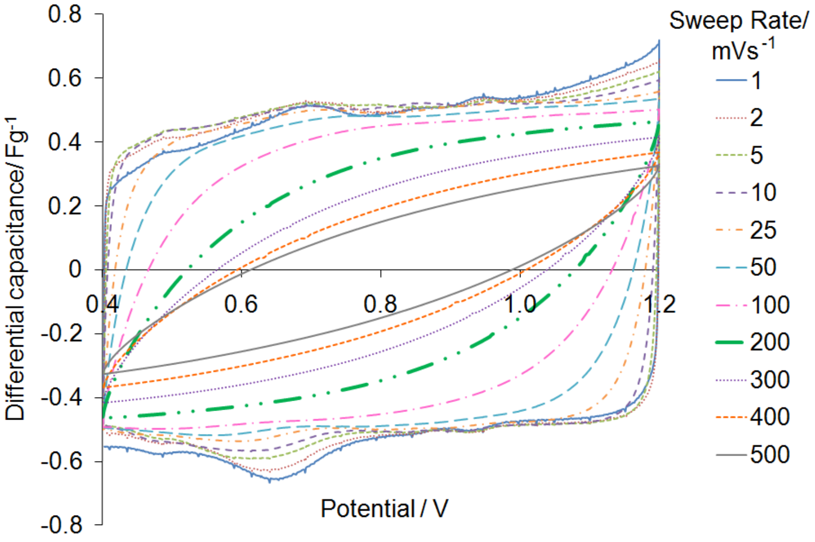

Figure 8.10: Differential capacitance plot of a 0.2472 g graphite carbon powder electrode in 1 M H_2SO_4 run with different sweep rates.

Self-discharge experiments were performed on graphite carbon powder, (BET surface area *ca*. 3 m^2 g^{-1}) in 1 M H_2SO_4, HCl, KCl, and NaCl electrolytes. Self-discharge experiments were performed from initial potentials of > 0.5 V only for the graphite carbon powder since at potentials lower than 0.4 V a large reduction wave is present in the CV (Figure 8.11). CVs of graphite carbon powder in various electrolytes are shown in Figure 8.12. In acidic electrolytes, oxidation and reduction peaks are present at *ca.* 0.65 V, attributed to oxidation and reduction of quinone groups. In neutral electrolytes, this peak disappears, as protons are no longer available to perform the oxidation and reduction reactions. In each of the electrolytes containing Cl^- ions (HCl, KCl, and NaCl) oxidation and reduction peaks are present at potentials above *ca.* 1.2 V, due to the oxidation and reduction of Cl^-/Cl_2.

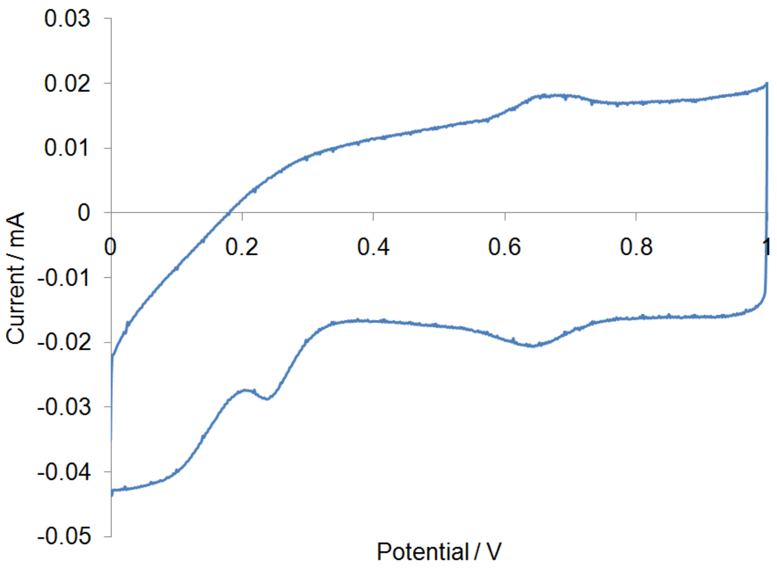

Figure 8.11: CV of *ca.* 100 mg graphite carbon powder electrode from 0.0 to 1.0 V at 1 mV s^{-1}.

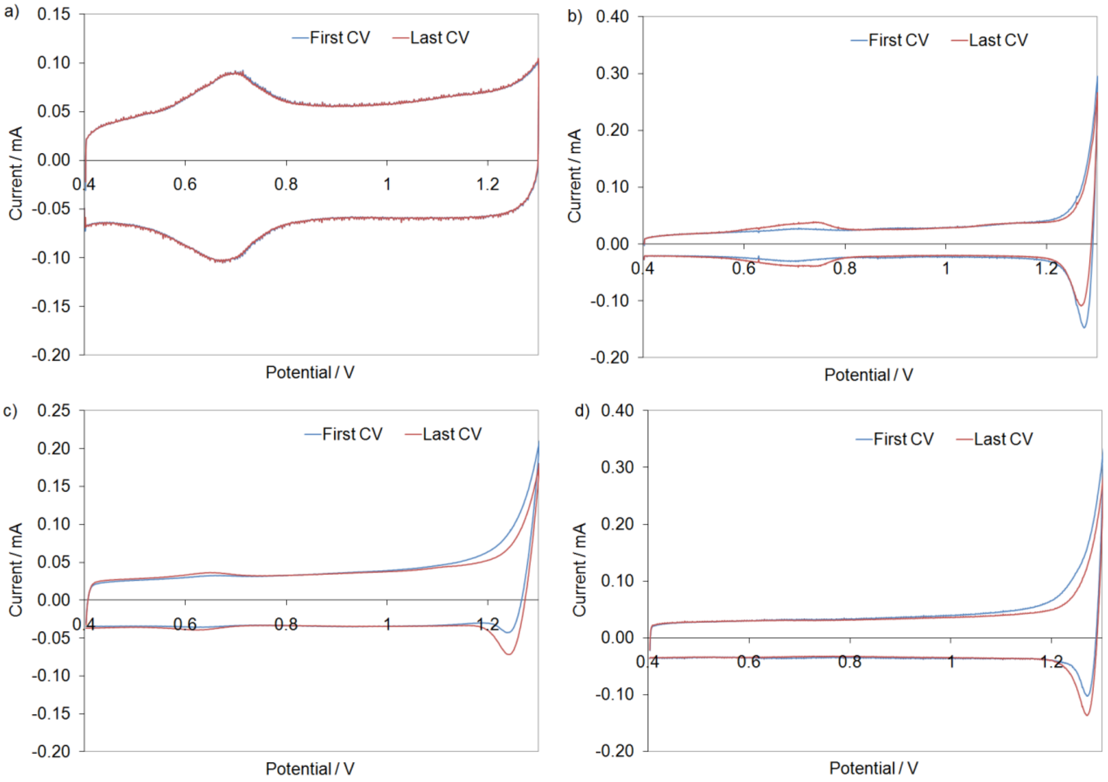

Figure 8.12: CVs of graphite carbon powder in a) 1 M H_2SO_4 (electrode mass - 0.1671 g), b) 1 M HCl (electrode mass - 0.1311 g), c) 1 M NaCl (electrode mass - 0.1360 g), and d) 1 M KCl (electrode mass - 0.1399 g).

The self-discharge profiles of graphite carbon powder in various electrolytes from an initial potential of 1 V are shown in Figure 8.13 plotted vs. log *t* (Figure 8.13a) and $t^{1/2}$ (Figure 8.13b). In HCl, KCl, and NaCl electrolytes the self-discharge profiles for the graphite carbon powder appear to be linear in $t^{1/2}$, and not log *t*. This is contrary to that for the self-discharge profiles of Spectracarb 2225 carbon cloth from high initial potentials. Similar results were obtained for these electrolytes at other initial potentials (0.6 – 0.9 V) and results are included in Appendix A2. In H_2SO_4 however, it is more difficult to determine whether the self-discharge profiles for the graphite carbon powder appear to be more linear in log *t* or $t^{1/2}$. It appears as though the self-discharge profile in this electrolyte follows a log *t* relationship, suggesting a different mechanism of self-discharge in H_2SO_4 electrolyte, compared to other electrolytes tested (HCl, KCl, and NaCl). A linear decline in potential with log *t* for H_2SO_4 suggests an activation-controlled Faradaic reaction or charge redistribution is responsible for self-discharge, but given the low surface area of this carbon charge redistribution is not expected. For the other electrolytes the linear decline in potential with $t^{1/2}$ suggests a diffusion-controlled Faradaic self-discharge mechanism.

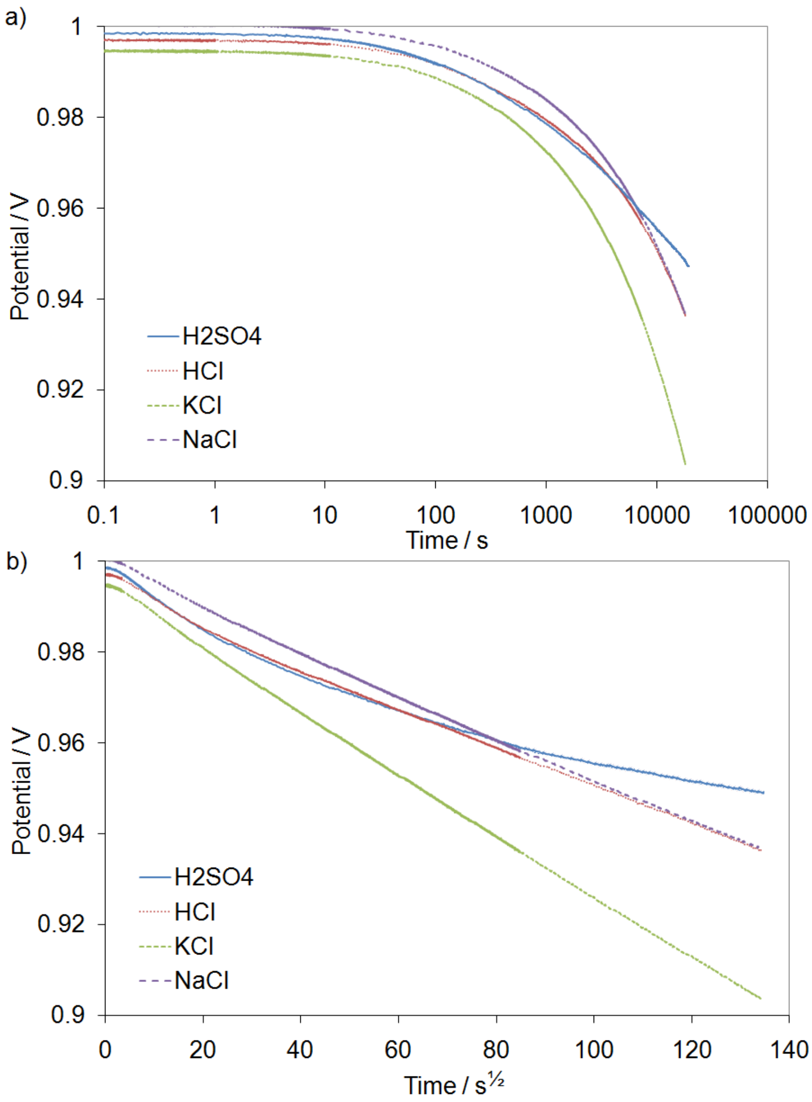

Figure 8.13: a) Self-discharge profiles graphite carbon powder electrodes in 1 M H_2SO_4 (0.1671 g), HCl (0.1311 g), KCl (0.1360 g), and NaCl (0.1399 g) after charging from 0.5 V to 1.0 V at 1 mV s^{-1} in different electrolytes plotted log t and b) $t^{½}$.

The relationship between the slope of the self-discharge profile in $t^{½}$ and the electrolyte conductivity is shown in Figure 8.14. There is no obvious trend between the rate of self-discharge and the cation or anion conductivity. If self-discharge is due to a diffusion-controlled Faradaic mechanism, as is suggested by the linear decline in potential with $t^{½}$ seen for most electrolytes, the rate of self-discharge is not expected to depend on the electrolyte resistivity, and rather the mobility and concentrations of the species involved in the Faradaic reaction.

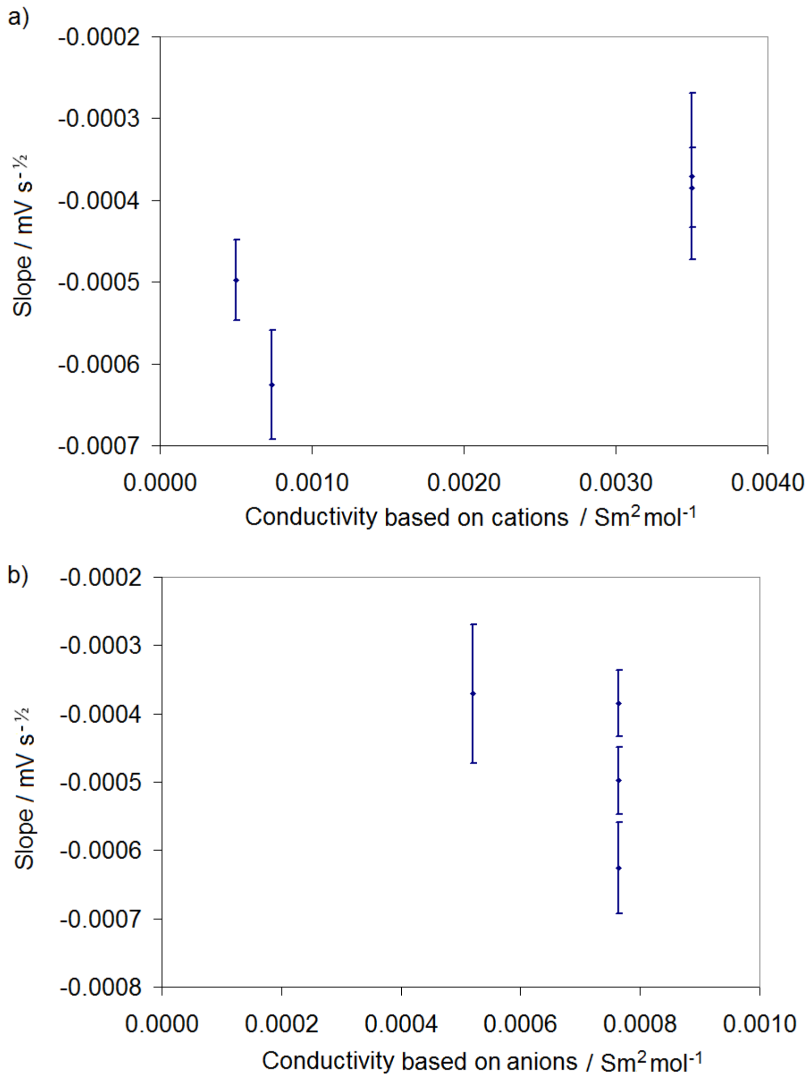

Figure 8.14: Slope of linear region of self-discharge profile in $t^{½}$ of graphite carbon powder electrodes in various electrolytes from an initial potential of 1.0 V vs. the conductivity due to the a) cation and b) anion.[*]

Figure 8.15 shows the relationship between the initial charging potential and the slope of the linear region of the self-discharge profile in $t^{½}$ for the graphite carbon powder

---

[*] Error bars are for three electrodes for HCl, NaCl, and KCl, and two electrodes for H_2SO_4.

in various electrolytes. Although the self-discharge profile of graphite carbon powder in H_2SO_4 seems more linear in log *t*, the slope in $t^{1/2}$ was calculated so that results can be compared to other electrolytes. In all electrolytes, the slope is dependent on initial potential, which is unexpected for a diffusion-controlled Faradaic mechanism, as described in Section 8.2.1. Again, it is possible that fitting the self-discharge profile to $t^{1/2}$ is not appropriate for the self-discharge mechanism, but further information is required to understand the dependence of the slope on the initial potential.

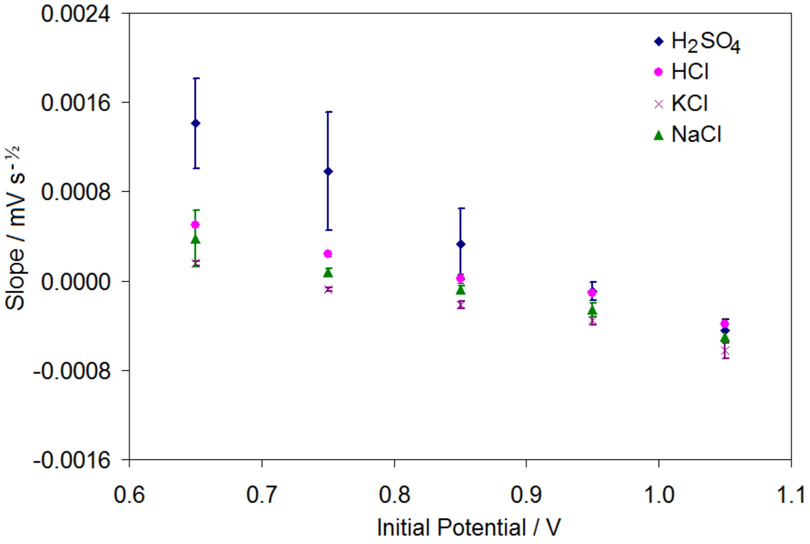

Figure 8.15: Relationship between initial charging potential and slope of linear region of self-discharge profile in $t^{1/2}$ for graphite carbon powder electrodes in various electrodes in various electrolytes after charging from 0.5 V to various initial potentials at 1 mV s^{-1}.*

8.3 Conclusions

Self-discharge profiles of Spectracarb 2225 carbon cloth examined in various electrolytes revealed a linear potential profile in log *t* from high initial potentials (> 0.5 V), suggesting self-discharge is related to either an activation-controlled Faradaic

---

*Error bars are one standard deviation for two electrodes for H_2SO_4, KCl, and NaCl, and three electrodes for HCl. Data are available in Appendix A2.

mechanism, or charge redistribution. However, the dependence of the slope of the self-discharge profile on initial potential and also on cation conductivity suggests that charge redistribution, and not an activation-controlled Faradaic reaction is responsible for the linear potential profile in log t.

Self-discharge profiles of Spectracarb 2225 carbon cloth from low initial potentials (< 0.5 V) showed a linear change in potential in $t^{1/2}$ at long self-discharge times, suggesting a diffusion-controlled Faradaic mechanism is controlling the self-discharge at long times. The slope of the self-discharge profile from 0.0 V showed no dependence on the ionic conductivity, consistent with a diffusion-controlled mechanism.

Self-discharge profiles for a low surface-area carbon, graphite carbon powder, exhibited linear potential profiles in $t^{1/2}$, suggesting a diffusion-controlled Faradaic mechanism is responsible for self-discharge. The slope of the self-discharge profiles of graphite carbon powder showed no correlation to the electrolyte conductivity, consistent with self-discharge being related to a diffusion-controlled Faradaic mechanism. The lack of evidence for charge redistribution in the low surface-area carbon, further supports that trends in the self-discharge profiles of Spectracarb 2225 carbon cloth are due to charge redistribution.

Chapter 9

DEVELOPMENT OF A THIN LAYER CELL AS A MODEL PORE TO STUDY CHARGE REDISTRIBUTION

9.1 Introduction

The aim of this research is to use a thin layer cell to model the electrochemical behaviour of a pore in order to study charge redistribution and to gain a better understanding of the processes that take place within a pore. In a thin layer cell the current flowing between the working electrode and the counter electrode travels through a thin solution layer, introducing Ohmic potential differences along the length of the cell, analogous to the potential differences developed within a pore of a porous electrode during charging/discharging. In this work, a thin layer cell was designed in which the one working electrode typically found in thin layer cells had the option to be replaced with a series of smaller working electrodes, positioned at various distances from the counter electrode. In this way, the potential can be monitored at each working electrode individually, akin to monitoring the potential at various depths down a pore within a porous electrode.

9.2 Results and Discussion

9.2.1 Electrolyte Leaking

The first objective was to test the thin layer cell setup, to make sure it was sealed properly, and all of the components worked. Due to initial difficulties in cutting the glassy carbon with appropriately flat and parallel sides on each electrode, initial experiments were conducted in this cell with a single longer working electrode (rather than the eight individual working electrodes). The cell was first setup with the eight current collectors atop the working electrode.

Figure 9.1a shows CVs of the single glassy carbon electrode in 1 M H_2SO_4 with a Pt mesh pseudo-reference, using eight aluminum current collectors and a 75 µm gasket. The current in the CV decreases over time, which may indicate a loss of electroactive area (area of contact between the electrode and electrolyte).

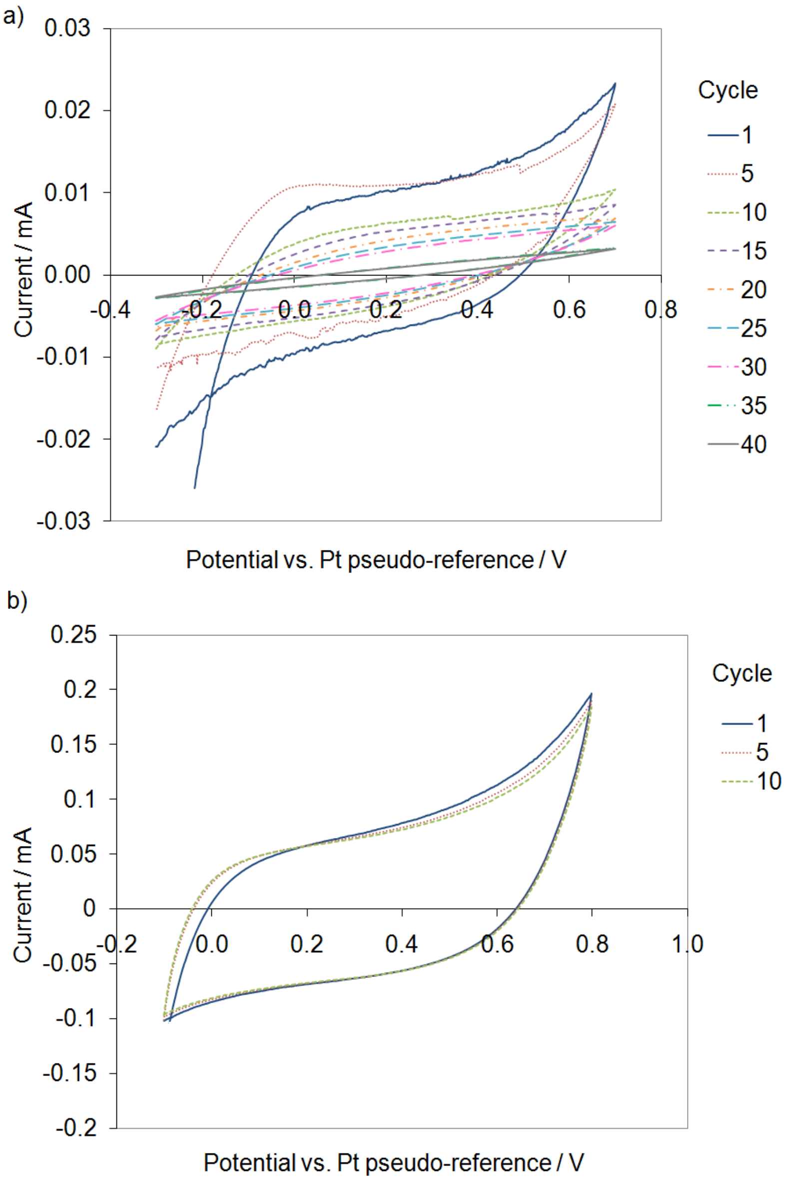

Figure 9.1: CVs of thin layer cell based on initial setup a)showing a loss in current as the electrolyte leaked from the cell and b) approximately constant current when electrolyte leak was resolved.

Many different gasket thicknesses (50 – 187.5 μm) were tested, however, the electrolyte leaked from the cell in each case, and it appeared that this leak originated between the glass slide and the Teflon gasket. This is not at all surprising considering that Teflon seals quite poorly to glass. Since Teflon was the desired gasket material, as it has the chemical stability to withstand all of the electrolytes that were expected to be used in this work, a number of methods were tested to try and prevent this leak from occurring. First candle wax was positioned along the gasket on the microscope slide in an attempt to avoid leakage between the glass slide and the gasket, but this did not prevent the leaking. Silicone caulking used in the same manner stopped the leak between the glass slide and the gasket; however the electrolyte then began to leak between the glassy carbon working electrode and the Teflon block (Block A and B, Figure 3.4). From here the electrolyte was able to travel along the current collectors on the back of the carbon, causing corrosion of the current collector blocks. The difficulty in maintaining a seal with this setup was probably due to small differences in the size of the current collectors, which made it difficult to apply an even pressure along the length of the cell. This uneven application of pressure resulted in places in the cell which were more vulnerable to leaks.

To prevent the pressure inequalities in the cell, the eight aluminum current collectors were replaced with a large, single aluminum current collector. With this setup the leaking issue was resolved. Figure 9.1 shows the CVs of the glassy carbon working electrode in 1 M H_2SO_4 with a Pt mesh pseudo-reference, using a 75 μm gasket, while the seal was maintained in the thin layer cell, and there were no problems with leaking of the electrolyte. The CV size remained constant over time, as subsequent CVs fall atop one another, as expected if the electrolyte seal is maintained.

9.2.2 Testing Potential Windows

Cyclic voltammetry experiments were run using the thin layer cell in 1 M H_2SO_4 using a large aluminum current collector and a 75 μm gasket. The CVs were first run between 0.0 and 1.0 V vs. the Pt mesh pseudo-reference electrode potential. The shape of the CV in Figure 9.2a suggests that the potential of the reference electrode is not 0 V vs. SHE. At the more positive end of the potential window the current increases significantly, and as the sweep direction is reversed the current falls closely along the same line before continuing on into its cathodic current. Also, during the experiment bubbles formed on the electrode surface, suggesting that the increased current was due to oxidation of the electrolyte, producing oxygen. The onset of this oxidation is expected at a potential of 1.23 V vs. SHE, and because it is seen at 0.8 – 0.9 V here, this suggests that the reference is shifted at least 0.3 V from SHE. The shift away from the SHE potential scale is not surprising since the reference electrode used acts only as a pseudo-reference. A pseudo-reference electrode refers to a reference electrode whose potential is not necessarily known, or stable, but is one which is used as if it were stable. A Pt mesh is being used as a pseudo-reference in the thin layer cell, and should act similarly to a SHE, as they are both based on the half-reaction: $2H^+ + 2e^- \leftrightarrows H_2$. However, in the SHE there is H_2 gas bubbled through to ensure the pressure of the hydrogen is at 1 atm, and this is not the case for the thin layer cell. Since no hydrogen is bubbled through the electrolyte, the concentration of hydrogen is likely not equal to that in an SHE, which would in turn cause a shift in the potential of this pseudo-reference.

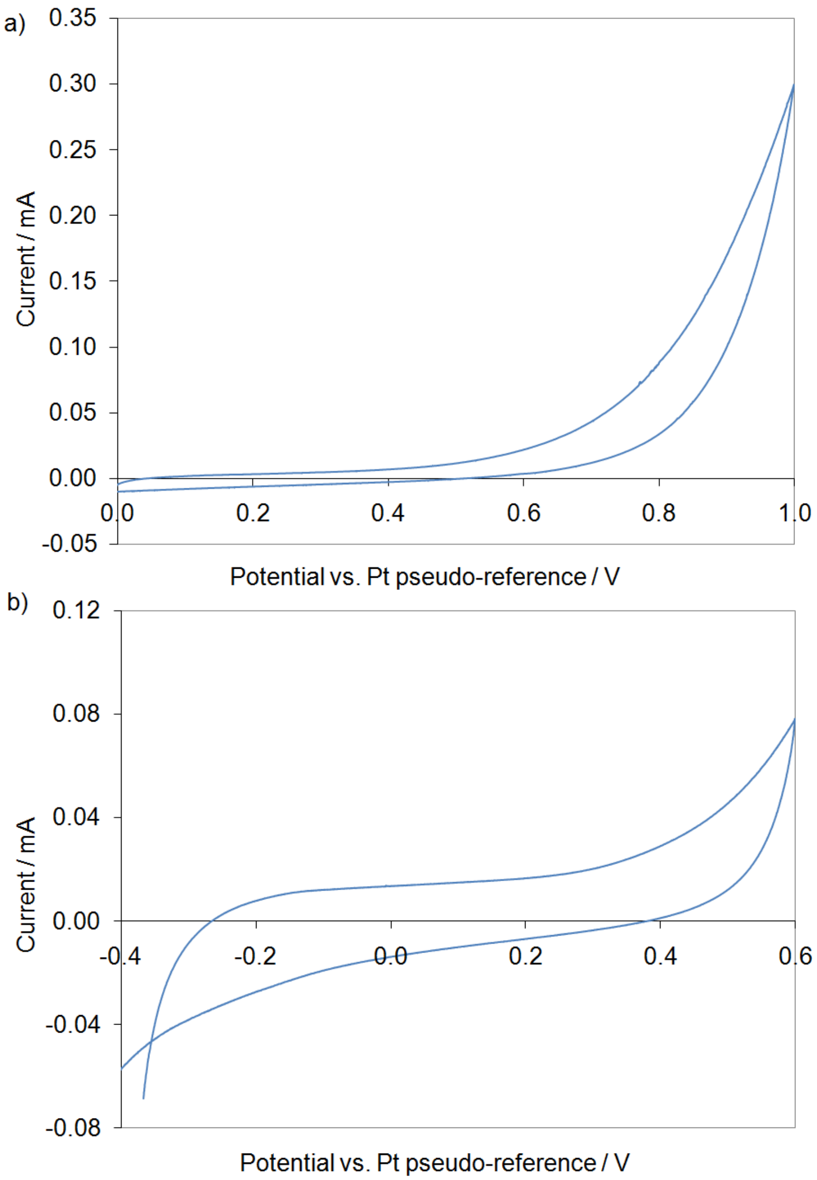

Figure 9.2: CV of glassy carbon in 1 M H_2SO_4 from 0.0 to 1.0 V vs. Pt pseudo-reference at 1 mV s^{-1} in thin layer cell with 75 μm gasket.

It is very undesirable to move outside the correct potential window when performing electrochemical experiments in the thin layer cell. Since at potentials above 1.23 V the electrolyte may be oxidized, producing oxygen, and this may form bubbles that can block some of the useable surface area of the working electrode(s). This can be significant when working in a cell of such small dimensions. Also the evolution of oxygen can cause increased pressure build up within the cell, and result in the electrolyte leaking. At the other end of the potential window, at potentials below 0 V vs. SHE (likely -0.3 V vs. Pt pseudo-reference), the electrolyte may be reduced to form hydrogen gas. Besides the similar issues due to gas formation, this can be extremely detrimental since there is a very small amount of electrolyte present, and if the H^+ ions are being used up to produce the hydrogen gas, the concentration of H^+ in the electrolyte will be significantly altered, which in turn changes the potential of the pseudo-reference electrode. So, for these reasons it is very important that the correct potential window is used during testing.

CVs were run with different potential windows in order to find the appropriate window for this setup. Figure 9.2b shows the CV for a potential window of -0.4 to 0.6 V vs. the Pt pseudo-reference, which was found to be the optimal potential window when using the Pt pseudo-reference, as the shape of the CV is closer to the desired shape, with the absence of any large oxidation or reduction waves.

For an ideal capacitor, the CV is a mirror image across the zero current axis, and has linear drops in the current at the switching potentials. The CV in Figure 9.2b differs from the CV expected for an ideal capacitor, as the CV is tilted slightly off axis, which is an indication that there is a resistance contribution in the cell causing an Ohmic drop. Resistance is not unexpected in this cell since the very thin layer of electrolyte solution through which the current must flow is designed to simulate the Ohmic resistance experienced in long, thin pores. Since resistance is inversely proportional to the cross-sectional area via Equation 5, a small cross section for the thin layer of electrolyte in the cell results in a large resistance, which is apparent in the tilting of the CV.

9.2.3 Self-discharge/Charge Redistribution Experiments

Due to problems with uneven pressure distribution created when using the eight aluminum current collectors, experiments with the working electrode assembly having eight separate glassy carbon working electrodes were not performed. In order to run self-discharge experiments the large glassy carbon working electrode was replaced by a series of five smaller glassy carbon working electrodes, sealed in an acid resistant epoxy resin, and the large aluminum current collector was replaced by a circuit board which provided separate electrical contact to each of the five working electrodes. This current board allowed for data to be collected individually from each working electrode, but has the added advantage of being one flat piece, which resolves the problem of having an uneven distribution of the pressure when using multiple current collectors.

The first self-discharge experiments were run with the thin layer cell filled with 1 M H_2SO_4, and using a Pt pseudo-reference. However, problems were encountered with this setup, as the acid leaked up between the circuit board and working electrodes and corroded the electrical contacts on the circuit board. For this reason the electrolyte was switched to 1 M NaCl, and the reference electrode was switched to a Ag/AgCl electrode. When using the Ag/AgCl reference electrode the potential is shifted *ca.* 0.23 V vs. SHE, and therefore the potential window for experiments when using a Ag/AgCl reference is shifted.

Initially self-discharge experiments were run where the circuit board provided electrical contact between all five working electrodes. The potential of working electrode 1 (closest to the counter electrode) was ramped at 1 mV s^{-1} from 0.0 to 1.0 V vs. Ag/AgCl, and then switched to open circuit, while the potential at all other working electrodes was monitored over time. Figure 9.3 shows self-discharge data (including ramp and open circuit steps) collected for each of the five working electrodes in the thin layer cell using a 1 M NaCl electrolyte. Throughout the entire experiment, the potential recorded at all working electrodes is equivalent. Originally, it was believed that no potential distribution was developed because the electrolyte resistance was not large enough to create significant Ohmic differences between working electrodes. For this reason, self-discharge experiments also were performed in electrolyte concentrations of 0.1 and 0.01 M NaCl to increase the electrolyte resistivity, however none resulted in potential distribution among the working electrodes during charging. After further consideration, it was concluded that the lack of a potential distribution being observed was due to the way in which data were collected, as explained below.

The potential measured at all five electrodes is the same because with all electrodes being electrically connected the potential is measured between the reference electrode and the working electrode closest to the reference electrode, because this is the point accessible through the least solution resistance. The potential measured for each of the five working electrodes then corresponds to the potential of the first working electrode, and the potential difference between the working electrodes created by the solution resistance in the cell is not seen.

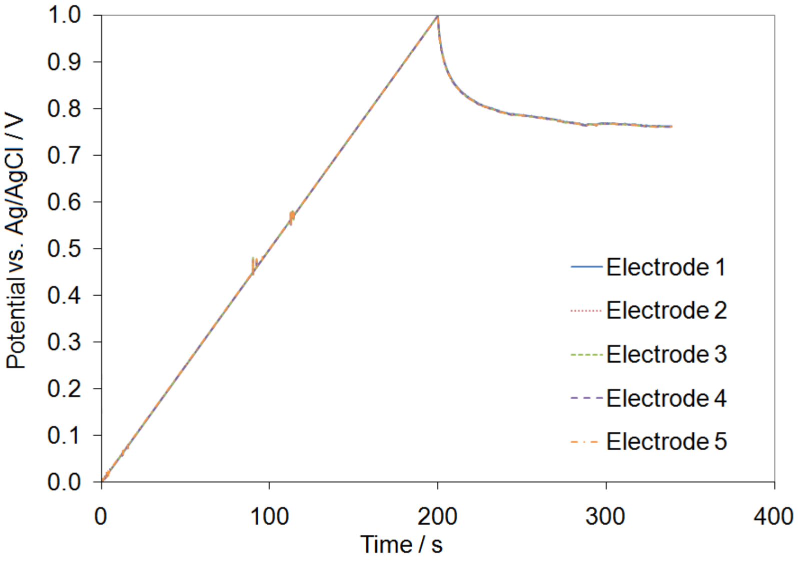

Figure 9.3: Ramp and open-circuit data for each electrode in the thin layer cell, with electrical connection between all working electrodes. The potential of electrode 1 was ramped from 0.0 to 1.0 V at 1 mV s^{-1} in 1 M NaCl.

The control box for the circuit board also provides the option of having each electrode electrically separate from one another, so self-discharge experiments were also performed in this configuration. Since there is no electrical connection between the electrodes, the potential measured for each working electrode should reflect the true potential felt at each electrode. In this configuration, during charging of one of the five electrodes the potential of the other electrodes is not expected to follow as there is no electrical connection between the electrodes. However, because the current may have to pass over some of the working electrodes in order to reach the electrode of interest, this can influence the measured potential.

Figure 9.4 shows charging and open-circuit data for the thin layer cell in which the potential of one of the working electrodes was ramped from 0.5 to 1.0 V, followed by an open-circuit step, while the potential at each working electrode was monitored over time. Figure 9.4a shows the data in which the potential of working electrode 1 (closest to the counter electrode) was ramped. Since the electrode being charged in this case is closest to the counter electrode, the current between the counter electrode and working electrode 1 does not have to pass over any other electrodes, thus it is not expected for the potential of working electrodes 2 - 5 to change significantly during the charging of working electrode 1. However, Figure 9.4a shows that the potential of working electrodes 2 and 4 seem to follow the potential of working electrode 1. The potential of working electrode 3 oscillated from very high to very low potentials throughout all experiments in which the working electrodes were electrically separated, and this is likely due to a bad connection between the working electrode and the circuit board. For this reason the data for electrode 3 is not presented in Figure 9.4. The potential of working electrode 5, on the other hand, remained at a potential of *ca.* 0.4 V throughout each experiment, and did not seem influenced by the development of potentials on the other working electrodes.

That the potential of working electrodes 2 and 4 seem to follow the potential of working electrode 1 is surprising, as there should be no electrical contact between the electrodes, and no reason for the potential of working electrodes 2 and 4 to increase. Instead, it is expected for the potential of these electrodes to remain relatively constant during the charging of working electrode 1, similar to what is seen for working electrode 5. These results may then suggest that working electrodes 1, 2, and 4 are somehow electrically connected to one another, although the circuit board was designed to prevent electrical connection between the working electrodes when used in this configuration. This may be due to a problem within the circuit board, the wires connecting the circuit board to the control box, or in the control box itself. In contrast, working electrode 5 appears to be electrically isolated from the other electrodes, as desired. When the potential of working electrode 2 (or 4) is ramped (Figure 9.4b and c), similar results are obtained in that the potential of electrodes 1 and 4 (1 and 2) follow the potential of the electrode being ramped. When the potential of working electrode 5 is ramped (Figure 9.4d) the potential of all working electrodes climb over time, although the potential of electrode 1 is very noisy due to some electrolyte leaking, causing electrode 1 to only be partially in solution.

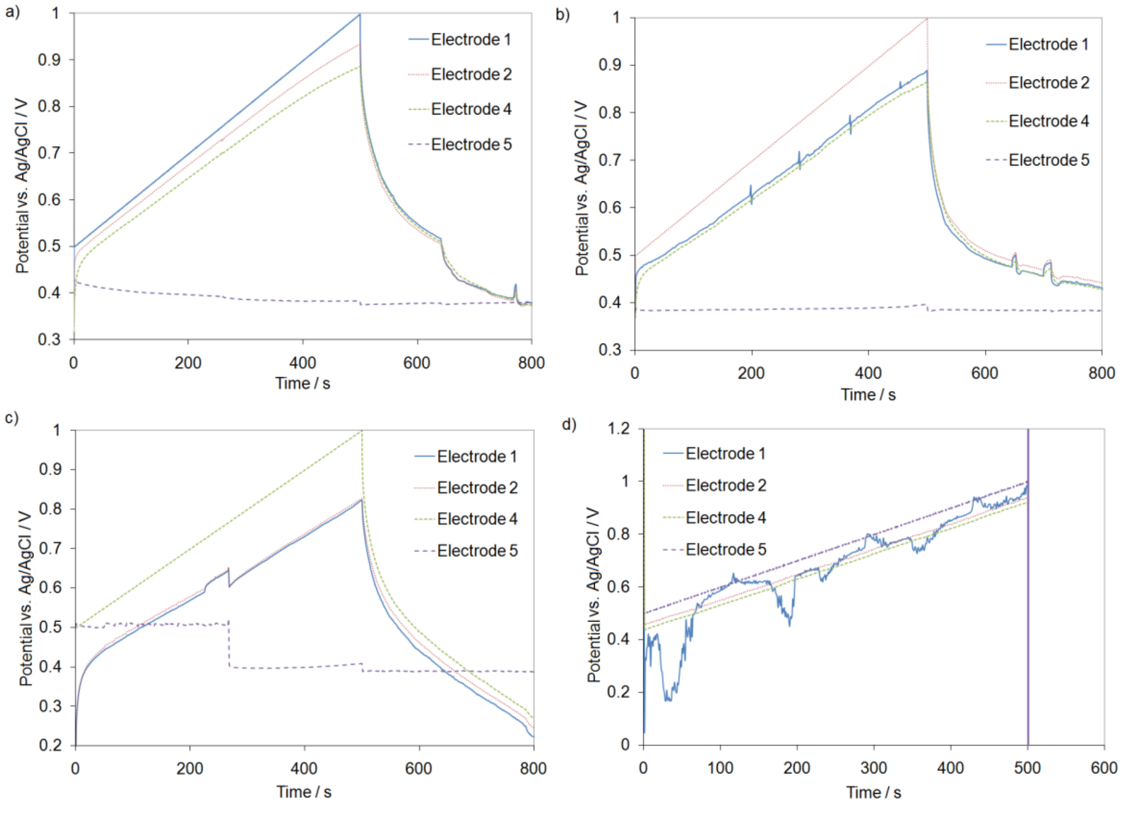

Figure 9.4: Charging and open-circuit data for thin layer cell after charging electrode 1, 2, 4 or 5 (a-d respectively) from 0.5 to 1.0 V at 1 mV s^{-1} followed by an open-circuit step, while recording potential of each working electrode.

In order to examine charge redistribution using the thin layer cell it is necessary to ramp the potential of working electrode 1 (nearest the counter electrode) to the desired potential while all working electrodes are electrically connected to one another. This allows charge also to pass down the cell to electrodes 2-5 during charging, similar to how charge moves down a pore during charging, where the pore tip is charged but the surface area deeper in the pore is charged as well. However, in order to see the potential difference developed among the different working electrodes the working electrodes must not be electrically connected to one another, or else the potential is measured between the reference electrode and the closest point on the working electrodes (the path of least resistance). This means that even when attempting to measure the potential of electrodes 2-5, the value measured is the potential of electrode 1. Thus, in order to measure the potential difference among the working electrodes, the electrical connection between the electrodes would need to be disconnected very briefly to allow for the potential at each electrode to be measured individually, without appreciably interrupting the flow of charge between the electrodes. This requirement is not achievable using the circuit board described here, where the electrodes can either be electrically connected, or separate, controlled by the user through a manual switch on the control box.

9.3 Conclusions

Testing various thin layer cell configurations revealed that a solid current collector was required to minimize leaking, as using separate current collectors (which are not identical in size) created an uneven pressure distribution, making the cell more vulnerable to electrolyte leaks. When using a Pt pseudo-reference electrode the true potential window vs. SHE was hard to determine, and maintaining a constant reference potential is difficult in thin layer cells since there is a very small amount of solution, and during charging the concentration of ions near the reference electrode may be depleted as ions are required to carry the current as well as balance the charge in the double-layer. Additionally, bubbles were sometimes formed on the working electrode surface during experiments, which is very problematic in this setup as the formation of bubbles results in a reduced electroactive area, as well as increased pressure within the cell.

Unfortunately, using the existing circuit board and control box it is not possible to examine the potential of each working electrode separately during charge redistribution. In order to model and study charge redistribution using a thin layer cell a new circuit board and control box would have to be designed, combined with proper interfacing with the commercial potentiostat. Getting the thin layer cell setup working would be a large project, and since the transmission line circuit allowed for similar experiments to be performed very rapidly and reproducibly, the thin layer cell was abandoned, and efforts were focused on the transmission line circuit.

Chapter 10

CONCLUSIONS

10.1 Thesis Summary

The aim of this research was to gain a better insight into the role of charge redistribution in the self-discharge of ECs. Self-discharge experiments were performed on five different carbon samples with a range of surface areas: Spectracarb 2225 carbon cloth (*ca.* 2100 $m^2 g^{-1}$), Black Pearls 2000 carbon powder (*ca.* 1500 $m^2 g^{-1}$), mesoporous carbon powder (*ca.* 300 $m^2 g^{-1}$), graphite carbon powder (*ca.* 3 $m^2 g^{-1}$), and glassy carbon powder (*ca.* 1 $m^2 g^{-1}$). Self-discharge experiments with various hold times and charging rates were conducted to determine how the charging rate, or addition of a hold step, affected the subsequent self-discharge profile. For high surface-area carbons (*i.e.* Spectracarb 2225 carbon cloth and Black Pearls 2000 carbon powder), the addition of a hold step significantly reduced the potential loss during self-discharge, and very long hold steps (*e.g.* > 50 hours for the Spectracarb 2225 carbon cloth) were required before no further decrease in self-discharge took place. These results suggest that in high surface-area carbons, charge redistribution is responsible, at least in part, for the potential loss during self-discharge. Similar self-discharge experiments performed on low surface-area carbons (*i.e.* glassy and graphite carbon powders), and a carbon with a larger pore size (*i.e.* mesoporous carbon powder) revealed that the addition of a hold step caused only minor reductions in the self-discharge, consistent with the expectation that charge redistribution is not a major component of self-discharge in non-porous carbons.

A hardware transmission line circuit, based on the de Levie transmission line model of a pore, was used to examine charge redistribution and the self-discharge profile created. Self-discharge experiments with various hold times and charging rates were performed on the hardware circuit, and results correlate well with those obtained for the high surface-area carbons. Similar results were obtained, with longer hold times and slower ramp rates resulting in decreased self-discharge. Data collected with the hardware circuit suggest that charge redistribution likely requires much more time than previously thought, as a system requiring a hold time of > 50 hours to remove the effects of charge redistribution likely requires hours, rather than seconds for charge redistribution to complete.

Using the hardware circuit, it was also shown that charge redistribution results in a self-discharge profile which is linear in log *t*. This was the first time charge redistribution was shown to have the same self-discharge profile that was predicted by Conway *et al.* for an activation-controlled Faradaic self-discharge mechanism. Therefore, when performing mechanistic studies, a linear self-discharge profile in log *t* is not necessarily indicative of an activation-controlled Faradaic reaction, and may instead be a result of charge redistribution. The self-discharge profile of Spectracarb 2225 carbon cloth when plotted as a function of log *t* contains a plateau, followed by a linear region of potential decline with log *t*, and this profile cannot necessarily be attributed to an activation-controlled Faradaic mechanism, as charge redistribution has the same predicted profile. This highlights the importance of minimizing charge redistribution effects when using the self-discharge profile to aid in the elucidation of the self-discharge mechanism.

Self-discharge experiments with Spectracarb 2225 carbon cloth were also performed at various initial charging potentials, and the slope of the self-discharge profile was found to depend on the initial potential to which the electrode was charged. This is contrary to the Conway model which does not predict a dependence of the slope on the initial charging potential. Similar data collected with the transmission line circuit also showed a dependence of the slope on the initial charging potential, and these results further suggest that charge redistribution is a major contributor to the potential loss during self-discharge in high surface-area carbons.

Since charge redistribution is not likely the only contributor to self-discharge, the hardware circuit was used to model the self-discharge profile that results for a combination of charge redistribution and an activation-controlled Faradaic reaction. The model predicted a self-discharge profile which contains three distinct regions. The first region in the profile (Region I) corresponds to a purely activation-controlled profile, as charge redistribution has not yet initiated, and the length of this region was found to depend on the electrolyte resistance in the pore, with higher resistance (smaller pore, lower electrolyte conductivity) resulting in a longer Region I. The second region (Region II) in the self-discharge profile has a shallower slope than is expected for a purely activation-controlled self-discharge profile. This is a result of the onset of charge redistribution where charge removed from the pore mouth as a result of the activation-controlled reaction is replenished by charge from deeper in the pore. The length of Region II was shown to increase as the resistance and capacitance in the model pore increases (which models longer or narrower pores, or lower electrolyte conductivities). Finally, in the third region (Region III) there is an increase in slope as charge redistribution essentially completes. The change in slope in the self-discharge profile could therefore provide a way to estimate the duration of the charge redistribution in experimental systems.

The self-discharge profile of Spectracarb 2225 carbon cloth in 1 M H_2SO_4 was examined over long times, and the three regions predicted by the model combining charge redistribution and an activation-controlled Faradaic reaction were observed. Region I was short, indicating a low incremental solution resistance, consistent with the high electrolyte conductivity. The change in slope between Region II and Region III occurred at *ca.* 60 000 s, suggesting that charge redistribution requires *ca.* 60 000 s (17 hours) to complete, much longer than the seconds or minutes previously suggested in the literature.

Self-discharge profiles of Spectracarb 2225 carbon cloth were also examined in the presence of high concentrations of Fe to compare to the self-discharge profile predicted by the activation-controlled Faradaic reaction and charge redistribution model. Unfortunately the self-discharge profiles observed did not contain the regions predicted by the model, as the high concentrations of Fe caused the electrode to discharge very quickly.

The hardware circuit was also used to model various pore geometries, and to determine the effect of pore shape on the self-discharge profile. A number of pore geometries were modeled, including cylindrical, cone, inverted cone, and diamond shaped pores. In addition, a number of pores containing bottlenecks of various sizes and in various positions in the pore were examined. Cone, inverted cone, and diamond shapes each produced a self-discharge profile similar to the self-discharge profile for a cylindrically shaped pore. The first region of the self-discharge profile is an initial potential plateau, the length of which depends strongly on the pore mouth size, and less strongly on the pore length (with a decrease in pore mouth size or an increase in pore length causing an increase in plateau length). The initial plateau is then followed by a linear decrease in potential in log *t*, and finally another plateau as charge redistribution completes.

A cone shaped pore, when compared to an inverted cone or cylindrically shaped pore having the same total resistance and capacitance demonstrated that the cone shaped pore was able to accumulate the most charge, highlighting the advantage of cone shaped pores for high power applications. The pore mouth resistance was shown to have a large effect on the amount of charge entering the pore, which emphasizes the importance of avoiding occlusion of the pore mouth.

For pore shapes which contain a bottleneck midway down the pore, the self-discharge profile becomes more complex, and contains multiple slopes. This is attributed to the bottleneck essentially dividing the pore into two separate regions, above and below the bottleneck. Initially charge redistribution within the area above the bottleneck takes place, as the presence of the restrictive bottleneck delays the participation of the surface below the bottleneck. Eventually, the surface area below the bottleneck begins to participate in charge redistribution, causing a change in slope. During charging of a pore containing a restrictive bottleneck, essentially only the pore area above the bottleneck participates in charging, resulting in a large loss in potential after charge redistribution, stressing the disadvantage of restrictive bottlenecks.

The advantage of cone shaped pores for high power applications was also evident by examination of the capacitance-frequency profiles obtained from electrochemical impedance spectroscopy. Similarly, the capacitance frequency profiles also highlighted the disadvantages of restrictive pore mouths for high power performance. The capacitance-frequency profile of pores containing bottlenecks partway through the pore resulted in a knee in the capacitance-frequency profile, as opposed to the more simple linear variation of capacitance with log frequency obtained for all other geometries.

The capacitance-frequency profile obtained for Spectracarb 2225 carbon cloth showed multiple slopes, where the capacitance initially increased fairly quickly with decreasing frequency, followed by a region in which the capacitance decreases less quickly with decreasing frequency. This suggests the presence of very small pores or restrictive bottlenecks which are only accessed at very low frequencies.

The effect of electrolyte ion on the self-discharge profile of Spectracarb 2225 carbon cloth and graphite carbon powder was tested by performing self-discharge experiments in various electrolytes (H_2SO_4, HCl, NaCl, KCl, $MgCl_2$, and $CaCl_2$). Self-discharge profiles of Spectracarb 2225 carbon cloth from high initial potentials were linear in log t, and linear in $t^{½}$ from low initial potentials. This suggests a different mechanism of self-discharge for an electrode charged to a high initial potential (> 0.5 V) than one charged to a lower initial potential (< 0.5 V).

The slope of the self-discharge profile from high initial potentials was dependent on both the initial charging potential and the electrolyte conductivity, specifically the conductivity of the cation. This is because the cation contributes most to the overall conductivity of the electrolyte, and highlights that although the electrode charge may be balanced by anions, cations are responsible for charge transport during charge redistribution. The dependence of the slope on the initial charging potential and conductivity of the electrolyte suggest that charge redistribution is responsible for the loss in potential during self-discharge, since the electrolyte ion is not expected to have a large effect for other self-discharge mechanisms (unless the electrolyte ions themselves are involved in self-discharge).

A linear self-discharge profile in $t^{1/2}$ at long self-discharge times obtained for Spectracarb 2225 carbon cloth from low initial potentials (< 0.5 V) suggests a diffusion-controlled Faradaic mechanism is responsible for self-discharge. The slope of the self-discharge profile from low initial potentials did not correlate with the ionic conductivities, consistent with what is expected for a diffusion-controlled Faradaic self-discharge mechanism. However, the slope of the self-discharge profile from low initial potentials did show a dependence on the initial charging potential, which is not expected for a diffusion-controlled Faradaic mechanism. Self-discharge experiments performed with various hold times suggest that charge redistribution is also occurring for an electrode charged to 0 V, and it is possible that the dependence of the slope of the self-discharge profile on initial potential is a charge redistribution effect.

Self-discharge profiles of graphite carbon powder were also linear in $t^{1/2}$, again suggesting a diffusion-controlled Faradaic mechanism is responsible for self-discharge. This agrees well with charge redistribution not being expected in this low surface-area carbon, and further supports that the linear profile in log *t* for Spectracarb 2225 carbon cloth from high initial potentials is due to charge redistribution. The slope of the self-discharge profile of graphite carbon powder showed no dependence on the ionic conductivity, consistent with self-discharge being related to a diffusion-controlled Faradaic mechanism. As with the self-discharge profiles for Spectracarb 2225 carbon cloth from low initial potentials, the slope of the self-discharge profile for graphite carbon powder was shown to depend on initial charging potential, which is an unexpected result.

Finally, a thin layer cell was designed and fabricated to act as a model pore for the purpose of examining charge redistribution. However, due to problems realised when testing the cell, and the complicated circuitry required to properly examine charge redistribution using this setup, further work is required before meaningful results can be obtained.

10.2 Future Work

In order to more accurately model a porous electrode, the transmission line model used in this work could be improved in a number of ways. The model could be made to include a larger number of sections (*i.e.* larger n) which would improve the modeling capability. Also, the current model is only capable of modeling a single pore, and it could be expanded to include combinations of pores of various shapes or sizes, as well as larger pores with several smaller pores protruding from the pore wall, to better model the fractal nature of porous carbons.

Mathematical modeling could also be used to examine the effects of charge redistribution on self-discharge. Using mathematical modeling would make it easier to model complex systems with numerous pores of various shapes and sizes would allow for a more accurate depiction of the effect of charge redistribution on the self-discharge profile in a real porous system.

So far, when modeling an activation-controlled Faradaic reaction in the presence of charge redistribution the activation-controlled discharge was set to take place at the pore mouth (capacitor 1), and this model could be expanded by setting the activation controlled discharge to take place at multiple positions in the pore. Also, the profile of an activation-controlled Faradaic reaction with charge redistribution was only examined for pores which are cylindrically shaped, and this could be expanded to include pores of various geometries.

In order to compare the activation-control and charge redistribution model to experimental results, a carbon with very narrow pores combined with a larger redox species (larger than the carbon pore size) could be examined, to ensure the activation-controlled discharge occurs at the external surface area only. In this way, the self-discharge profile of an electrode undergoing both charge redistribution and an activation-controlled Faradaic discharge at the pore mouth could be examined, and contrasted to profiles predicted by the model.

For the thin layer cell project much work is required before the thin layer cell can be used to examine charge redistribution. Establishing the proper electronic circuitry and method of data collection is vital, and will likely involve a large amount of effort. Once this is worked out, the thin layer cell could be used to explore charge redistribution in a number of different ways. This includes an examination of the effects of hold times, charging rates, and initial potentials which could then be compared to experimental results obtained for various carbons, as well as results obtained from the transmission line model. In addition, by utilizing various gasket geometries, various pore shapes can be modeled and compared to results obtained with the transmission line model.

REFERENCES

(1) Conway, B. E. *Electrochemical Supercapacitors: Scientific Fundamentals and Technological Applications;* Plenum Publishers: New York, 1999 pp 11-31.

(2) de Levie, R. *Electrochim. Acta* **1963**, *8*, 751-780.

(3) Pell, W. G.; Conway, B. E.; Adams, W. A.; de Oliveira, J. *J. Power Sources* **1999**, *80*, 134-141.

(4) Niu, J.; Conway, B. E.; Pell, W. G. *J. Power Sources* **2004**, *135*, 332-343.

(5) Conway, B. E.; Pell, W. G.; Liu, T. *J. Power Sources* **1997**, *65*, 53-59.

(6) Blake, M. B.; Lund, H. *Sustainable Development of Energy, Water and Environment Systems, Volume III, Proceedings of the Dubrovnik Conference, 3rd, Dubronik, Croatia, June 5-10, 2005* **2007**, 69-78.

(7) Eloot, K.; Debuyck, F.; Moors, M.; Van Peteghem, A. P. *J. Appl. Electrochem.* **1995**, *25*, 326-333.

(8) Barker, J. R. *Am. J. Phys.* **1999**, *67*, 1216-1226.

(9) Winter, M.; Brodd, R. J. *Chem. Rev.* **2004**, *104*, 4245-4269.

(10) Tashima, D.; Kurosawatsu, K.; Uota, M.; Karashima, T.; Otsubo, M.; Honda, C.; Sung, Y. M. *Thin Solid Films* **2007**, *515*, 4234-4239.

(11) Kotz, R.; Carlen, M. *Electrochim. Acta* **2000**, *45*, 2483-2498.

(12) Niu, J.; Pell, W. G.; Conway, B. E. *J. Power Sources* **2006**, *156*, 725-740.

(13) Conway, B. E.; Pell, W. G. *J. Solid State Electrohem.* **2003**, *7*, 637-644.

(14) Xing, W.; Qiao, S. Z.; Ding, R. G.; Li, F.; Lu, G. Q.; Yan, Z. F.; Cheng, H. M. *Carbon* **2005**, *44*, 216-224.

(15) Hadjipaschalis, I.; Poullikkas, A.; Efthimiou, V. *Renew. Sustain. Energy Rev.* **2009**, *13*, 1513-1522.

(16) Lu, W.; Qu, L.; Henry, K.; Dai, L. *J. Power Sources* **2009,** 189, 1270-1277.

(17) Kowal, J.; Avaroglu, E.; Chamekh, F.; Šenfelds, A.; Thien, T.; Wijaya, D.; Sauer, D. U. *J. Power Sources* **2011**, *196*, 573-579.

(18) Liu, P.; Verbrugge, M.; Soukiazian, S. *J. Power Sources* **2006**, *156*, 712-718.

(19) Chu, A.; Braatz, P. *J. Power Sources* **2002**, *112*, 236-246.

(20) Vol'fkovich, Y. M.; Serdyuk, T. M. *Russ. J. Electrochem.* **2002**, *38*, 935-959.

(21) Kim, K.; Hur, J.; Jung, S.; Kang, A. *Electrochim. Acta* **2004**, *50*, 863-872.

(22) Kibi, Y.; Saito, T.; Kurata, M.; Tabuchi, J.; Ochi, A. *J. Power Sources* **1996**, *60*, 219-224.

(23) Wee, J. *Renew. Sustain. Energy Rev.* **2007**, *11*, 1720-1738.

(24) Erdinc, O.; Uzunoglu, M. *Renew. Sustain. Energy Rev.* **2010**, *14*, 2874-2884.

(25) Qu, D. *J. Power Sources* **2002**, *109*, 403-411.

(26) Becker, H. I. New York/USA Patent 2800616, 1957.

(27) Jaenes, A.; Kurig, H.; Lust, E. *Carbon* **2007**, *45*, 1226-1233.

(28) Sevilla, M.; Alvarez, S.; Centeno, T. A.; Fuertes, A. B.; Stoeckli, F. *Electrochim. Acta* **2007**, *52*, 3207-3215.

(29) Song, H.; Jung, Y.; Lee, K.; Dao, L. H. *Electrochim. Acta* **1999**, *44*, 3513-3519.

(30) Sharma, P.; Bhatti, T. S. *Energy Convers. Manage.* **2010**, *51*, 2901-2912.

(31) Raymundo-Pinero, E.; Kierzek, K.; Machnikowski, J.; Beguin, F. *Carbon* **2006**, *44*, 2498-2507.

(32) Miller, J. R.; Burke, A. F. *Electrochem. Soc. Interface* **2008**, *17*, 53-57.

(33) Jurewicz, K.; Vix-Guterl, C.; Frackowiak, E.; Saadallah, S.; Reda, M.; Parmentier, J.; Patarin, J.; Beguin, F. *J. Phys. and Chem. Solids* **2004**, *65*, 287-293.

(34) Ruetschi, P. *J. Power Sources* **2004**, *127*, 33-44.

(35) Chmiola, J.; Yushin, G.; Gogotsi, Y.; Portet, C.; Simon, P.; Taberna, P. L. *Science* **2006**, *313*, 1760-1763.

(36) Frackowiak, E. *Phys. Chem. Chem. Phys.* **2007**, *9*, 1774-1785.

(37) Bleda-Martinez, M. J.; Morallon, E.; Cazorla-Amoros, D. *Electrochim. Acta* **2007**, *52*, 4962-4968.

(38) Sullivan, M. G.; Schnyder, B.; Bartsch, M.; Alliata, D.; Barbero, C.; Imhof, R.; Kotz, R. *J. Electrochem. Soc.* **2000**, *147*, 2636-2643.

(39) Conway, B. E. *J. Electrochem. Soc.* **1991**, *138*, 1539-1548.

(40) Aworn, A.; Thiravetyan, P.; Nakbanpote, W. *J. Anal. Appl. Pyrolysis* **2008**, *82*, 279-285.

(41) Inagaki, M.; Konno, H.; Tanaike, O. *J. Power Sources* **2010**, *195*, 7880-7903.

(42) Brown, A. P.; Fleischmann, M.; Pletcher, D. *J. Electroanal. Chem. Interfacial Electrochem.* **1974**, *50*, 65-72.

(43) Bjoernbom, P. *Electrochem. Commun.* **2007**, *9*, 211-215.

(44) Fuertes, A. B.; Pico, F.; Rojo, J. M. *J. Power Sources* **2004**, *133*, 329-336.

(45) Soneda, Y.; Toyoda, M.; Tani, Y.; Yamashita, J.; Kodama, M.; Hatori, H.; Inagaki, M. *J. Phys. Chem. Solids* **2004**, *65*, 219-222.

(46) Liang, C.; Li, Z.; Dai, S. *Angew. Chem, Int. Ed.* **2008**, *47*, 3696-3717.

(47) Keiser, H.; Beccu, K. D.; Gutjahr, M. A. *Electrochim. Acta* **1976**, *21*, 539-543.

(48) Hitz, C.; Lasia, A. *J. Electroanal. Chem.* **2001**, *500*, 213-222.

(49) Fievet, P.; Mullet, M.; Pagetti, J. *J. Membr. Sci.* **1998**, *149*, 143-150.

(50) Candy, J. P.; Fouilloux, P.; Keddam, M.; Takenouti, H. *Electrochim. Acta* **1981**, *26*, 1029-1034.

(51) Keddam, M.; Rakotomavo, C.; Takenouti, H. *J. Appl. Electrochem.* **1984**, *14*, 437-448.

(52) Moriguchi, I.; Nakahara, F.; Furukawa, H.; Yamada, H.; Kudo, T. *Electrochem. Solid-State Lett.* **2004**, *7*, A221-A223.

(53) Zhao, Y.; Zheng, M.; Cao, J.; Ke, X.; Liu, J.; Chen, Y.; Tao, J. *Mater. Lett.* **2008**, *62*, 548-551.

(54) Zhao, X.; Tian, H.; Zhu, M.; Tian, K.; Wang, J. J.; Kang, F.; Outlaw, R. A. *J. Power Sources* **2009**, *194*, 1208-1212.

(55) Zhang, L. L.; Zhou, R.; Zhao, X. S. *J. Mater. Chem.* **2010**, *20*, 5983-5992.

(56) Geim, A. K.; Novoselov, K. S. *Nat. Mater.* **2007**, *6*, 183-191.

(57) Zhang, Y.; Feng, H.; Wu, X.; Wang, L.; Zhang, A.; Xia, T.; Dong, H.; Li, X.; Zhang, L. *Int. J. Hydrogen Energy* **2009**, *34*, 4889-4899.

(58) Snook, G. A.; Kao, P.; Best, A. S. *J. Power Sources* **2011**, *196*, 1-12.

(59) Boehm, H. P. *Carbon* **1994**, *32*, 759-769.

(60) Montes-Moran, M. A.; Suarez, D.; Menendez, J. A.; Fuente, E. *Carbon* **2004**, *42*, 1219-1225.

(61) Barton, S. S.; Evans, M. J. B.; Halliop, E.; Macdonald, J. A. F. *Carbon* **1997**, *35*, 1361-1366.

(62) Kawaguchi, M.; Yamanaka, T.; Hayashi, Y.; Oda, H. *J. Electrochem. Soc.* **2010**, *157*, A35-A40.

(63) Frackowiak, E. *J. Braz. Chem. Soc.* **2006**, *17*, 1074-1082.

(64) Bentley, P.; Stone, D. A.; Schofield, N. *J. Power Sources* **2005**, *147*, 288-294.

(65) Hallum, J. V.; Drushel, H. V. *J. Phys. Chem.* **1958**, *62*, 110-117.

(66) Maeshima, H.; Shiromi, C., Osaka EP1746612, 2007.

(67) Hofstetter, C.; Pochapsky, T. C. *Magn. Reson. Chem.* **2000**, *38*, 90-94.

(68) Ing, H. R.; Wright, W. M. *Proc. Roy. Soc.(London)* **1933**, *B114*, 48-63.

(69) Barisci, J. N.; Wallace, G. G.; MacFarlane, D. R.; Baughman, R. H. *Electrochem, Commun.* **2004**, *6*, 22-27.

(70) Ania, C. O.; Pernak, J.; Stefaniak, F.; Raymundo-Pinero, E.; Beguin, F. *Carbon* **2006**, *44*, 3126-3130.

(71) Kazaryan, S. A.; Kharisov, G. G.; Litvinenko, S. V.; Kogan, V. I. *J. Electrochem. Soc.* **2007**, *154*, A751-A759.

(72) Tom, G. M.; Hubbard, A. T. *Anal. Chem.* **1971**, *43*, 671-674.

(73) Yaniv, M.; Soffer, A. *J. Electrochem. Soc.* **1976**, *123*, 506-511.

(74) Hinman, A. S.; Pons, S.; Cassidy, J. *Electrochim. Acta* **1985**, *30*, 89-94.

(75) Posey, F. A.; Morozumi, T. *J. Electrochem. Soc.* **1966**, *113*, 176-184.

(76) Conway, B. E.; Pell, W. G. *J. Power Sources* **2002**, *105*, 169-181.

(77) Bard, A. J.; Faulkner, L. R. *Electrochemical Instrumentation; Electrochemical Methods: Fundamentals and Applications*. John Wiley & Sons: United States, 2001; Vol. 7, pp 632-658.

(78) Hamnett, A.; Hamann, C. H.; Vielstich, W. *Methods for the study of the electrode/electrolyte interface; Electrochemistry*; John Wiley and Sons: New York, 1997; 251-339.

(79) Bockris, J. O.; Reddy, A. K. N.; Gamboa-Aldeco, M. E.; Editors *Electrodics; Modern Electrochemistry 2A, Second Edition: Fundamentals of Electrodics.* Kluwer Academic / Plenum Publishers: New York, 2001; pp 1035-1400.

(80) Bard, A. J.; Faulkner, L. R. *Techniques Based on Concepts of Impedance; Electrochemical Methods: Fundamentals and Applications.* John Wiley & Sons, Inc.: United States, 2001; Vol. 7, pp 368-416.

(81) Beydokhti, N. *Minimization of nonuniform potential distribution in thin-layer electrochemical cells*. Master's Thesis. Department of Chemistry, University of Calgary. **2000**.

(82) Garten, V. A.; Weiss, D. E. *Aust. J. Chem.* **1955**, *8*, 68-95.

(83) Lefevre, M.; Dodelet, J. *Electrochim. Acta* **2008**, *53*, 8269-8276.

(84) Wissler, M. *J. Power Sources* **2006**, *156*, 142-150.

(85) Andreas, H. A.; Lussier, K.; Oickle, A. M. *J. Power Sources* **2009**, *187*, 275-283.

(86) Seredych, M.; Hulicova-Jurcakova, D.; Lu, G. Q.; Bandosz, T. J. *Carbon* **2008**, *46*, 1475-1488.

(87) Hulicova-Jurcakova, D.; Kodama, M.; Shiraishi, S.; Hatori, H.; Zhu, Z. H.; Lu, G. Q. *Adv. Funct. Mater.* **2009**, *19*, 1800-1809.

(88) Nishihara, H.; Itoi, H.; Kogure, T.; Hou, P.; Touhara, H.; Okino, F.; Kyotani, T. *Chem. Eur. J.* **2009**, *15*, 5355-5363.

(89) Bleda-Martinez, M. J.; Macia-Agullo, J. A.; Lozano-Castello, D.; Morallon, E.; Cazorla-Amoros, D.; Linares-Solano, A. *Carbon* **2005**, *43*, 2677-2684.

(90) Largeot, C.; Portet, C.; Chmiola, J.; Taberna, P.; Gogotsi, Y.; Simon, P. *J. Am. Chem. Soc.* **2008**, *130*, 2730-2731.

(91) Chmiola, J.; Largeot, C.; Taberna, P.; Simon, P.; Gogotsi, Y. *Angew. Chem. Int. Ed.* **2008**, *47*, 3392-3395.

(92) Lin, C.; Popov, B. N.; Ploehn, H. J. *J. Electrochem. Soc.* **2002**, *149*, A167-A175.

(93) Lee, G.; Pyun, S.; Rhee, C. *Microporous Mesoporous Mater.* **2006**, *93*, 217-225.

(94) Daley, M. A.; Tandon, D.; Economy, J.; Hippo, E. J. *Carbon* **1996**, *34*, 1191-1200.

(95) Paredes, J. I.; Martinez-Alonso, A.; Tascon, J. M. D. *Langmuir* **2001**, *17*, 474-480.

(96) Purewal, J. J.; Kabbour, H.; Vajo, J. J.; Ahn, C. C.; Fultz, B. *Nanotechnology* **2009**, *20*, 204012/1-204012/6.

(97) Xia, Y.; Mokaya, R. *Adv. Mater.* **2004**, *16*, 886-891.

(98) Lee, J.; Joo, S. H.; Ryoo, R. *J. Am. Chem. Soc.* **2002**, *124*, 1156-1157.

(99) Woermann, D. *Phys. Chem. Chem. Phys.* **2003**, *5*, 1853-1858.

(100) Otero, T. F.; Bengoechea, M. *Langmuir* **1999**, *15*, 1323-1327.

(101) Weast, R. C. (Ed.), *CRC Handbook of Chemistry and Physics, 1st Student Edition,* CRC Press: United States, 1987; pp D-105.

APPENDIX A

CARBON SELF-DISCHARGE DATA

A.1 Self-discharge profiles of Spectracarb 2225 carbon cloth from various initial charging potentials

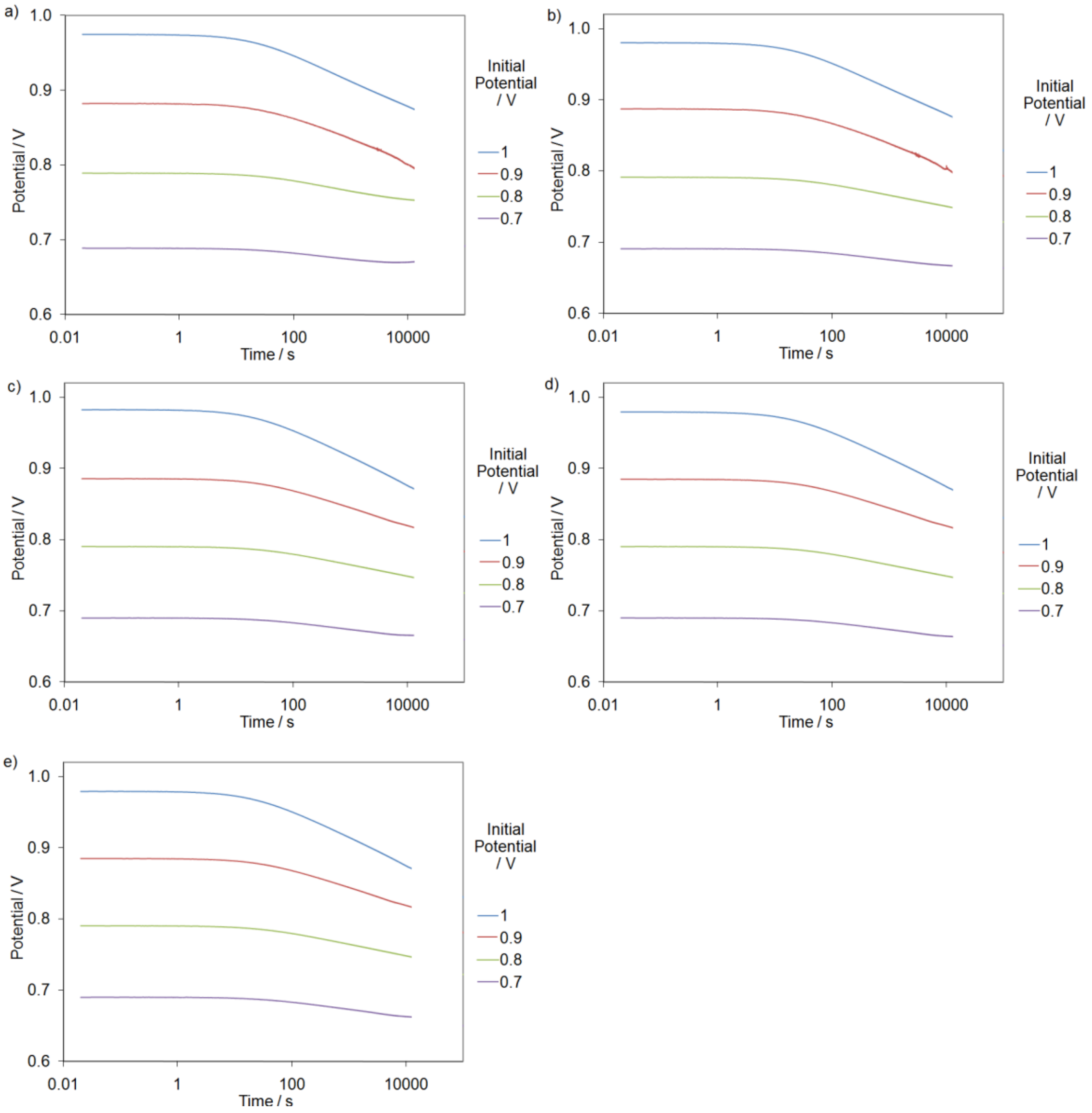

Figure A.1: Self-discharge profile for a Spectacarb 2225 carbon-cloth electrode in 1 M H_2SO_4 plotted as a function of log *t* after charging at 1 mV s^{-1} to various initial charging potentials (0.6 – 1.0 V). Electrode masses were a) 9.4 mg, b) 9.0 mg, c) 9.1 mg, d) 9.1 mg and e) 9.4 mg

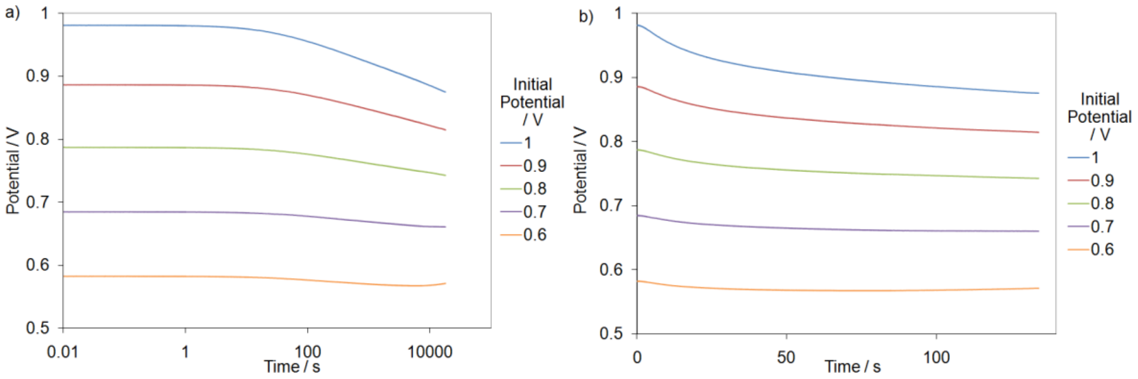

Figure A.2: Self-discharge profiles of a 9.0 mg Spectracarb 2225 carbon-cloth electrode in 1 M H_2SO_4 after charging from 0.5 V to various initial charging potentials (0.6 – 1.0 V) at 1 mV s^{-1} plotted in a) log *t* and b) $t^{½}$.

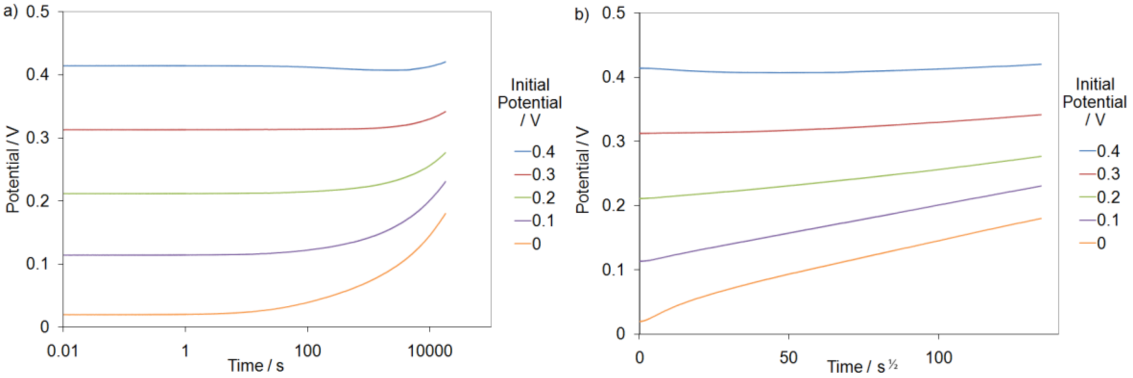

Figure A.3: Self-discharge profiles of a 9.0 mg Spectracarb 2225 carbon-cloth electrode in 1 M H_2SO_4 after charging from 0.5 V to various initial charging potentials (0.0 – 0.4 V) at 1 mV s^{-1} plotted in a) log *t* and b) $t^{½}$.

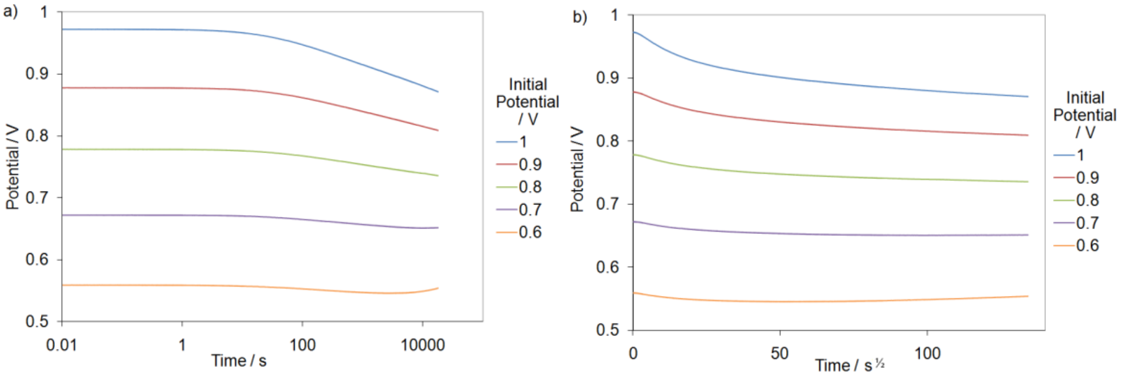

Figure A.4: Self-discharge profiles of a 9.2 mg Spectracarb 2225 carbon-cloth electrode in 1 M H_2SO_4 after charging from 0.5 V to various initial charging potentials (0.6 – 1.0 V) at 1 mV s^{-1} plotted in a) log *t* and b) $t^{½}$.

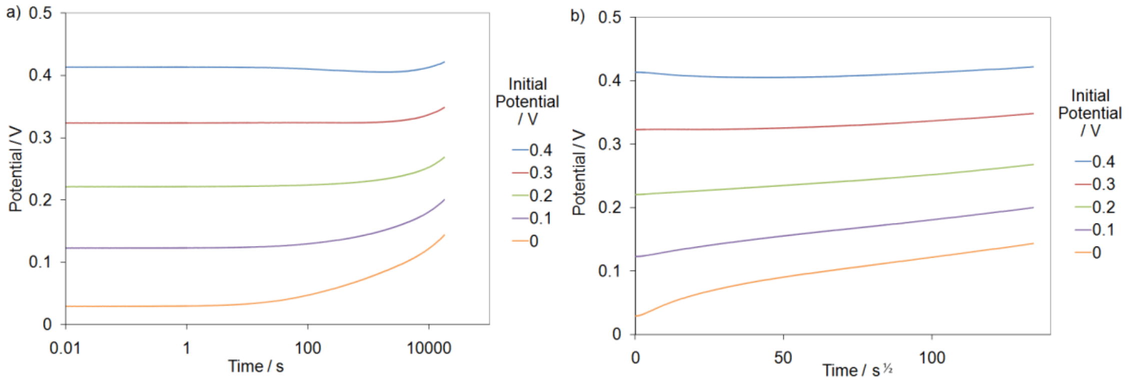

Figure A.5: Self-discharge profiles of a 9.2 mg Spectracarb 2225 carbon-cloth electrode in 1 M H_2SO_4 after charging from 0.5 V to various initial charging potentials (0.0 – 0.4 V) at 1 mV s^{-1} plotted in a) log t and b) $t^{½}$.

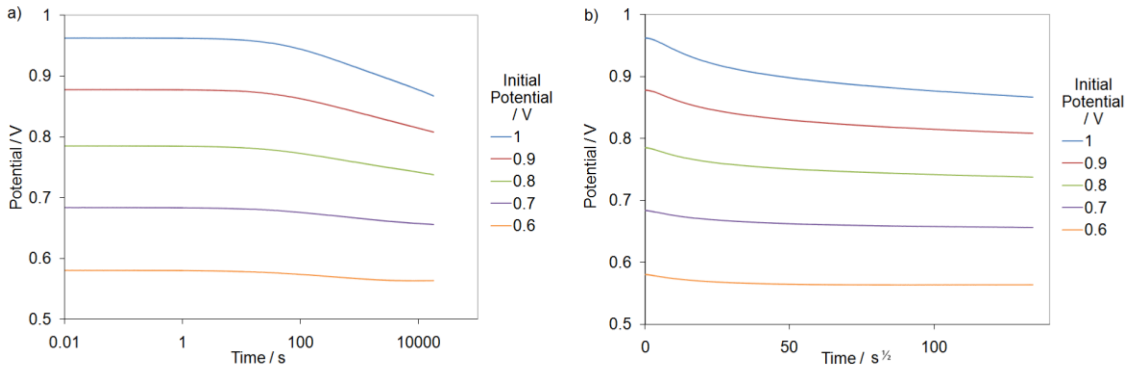

Figure A.6: Self-discharge profiles of a 8.9 mg Spectracarb 2225 carbon-cloth electrode in 1 M HCl after charging from 0.5 V to various initial charging potentials (0.6 – 1.0 V) at 1 mV s^{-1} plotted in a) log t and b) $t^{½}$.

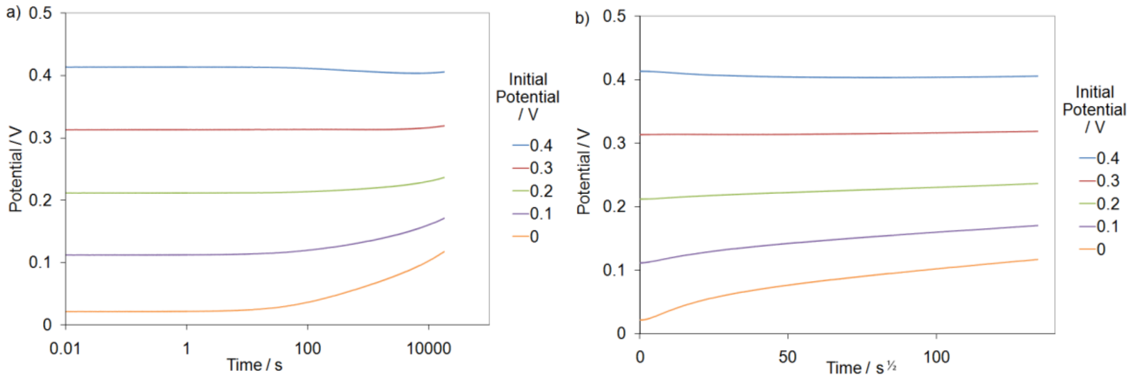

Figure A.7: Self-discharge profiles of a 8.9 mg Spectracarb 2225 carbon-cloth electrode in 1 M HCl after charging from 0.5 V to various initial charging potentials (0.0 – 0.4 V) at 1 mV s^{-1} plotted in a) log t and b) $t^{½}$.

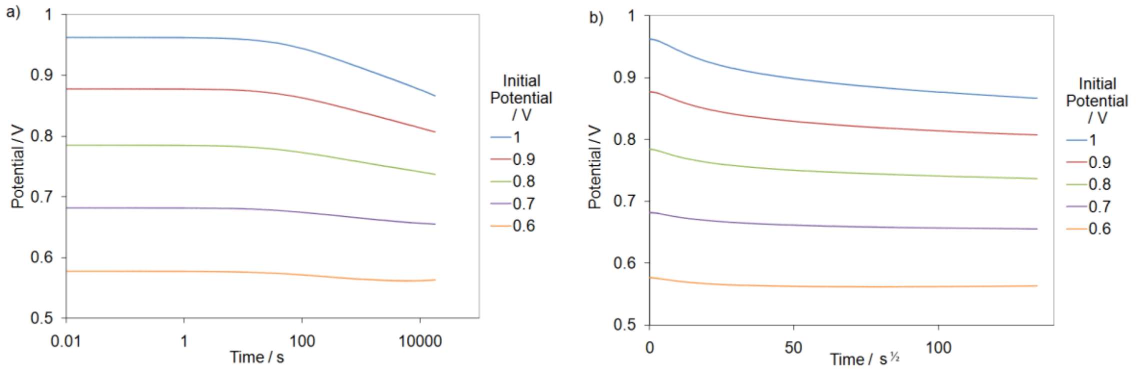

Figure A.8: Self-discharge profiles of a 8.6 mg Spectracarb 2225 carbon-cloth electrode in 1 M HCl after charging from 0.5 V to various initial charging potentials (0.6 – 1.0 V) at 1 mV s^{-1} plotted in a) log *t* and b) $t^{½}$.

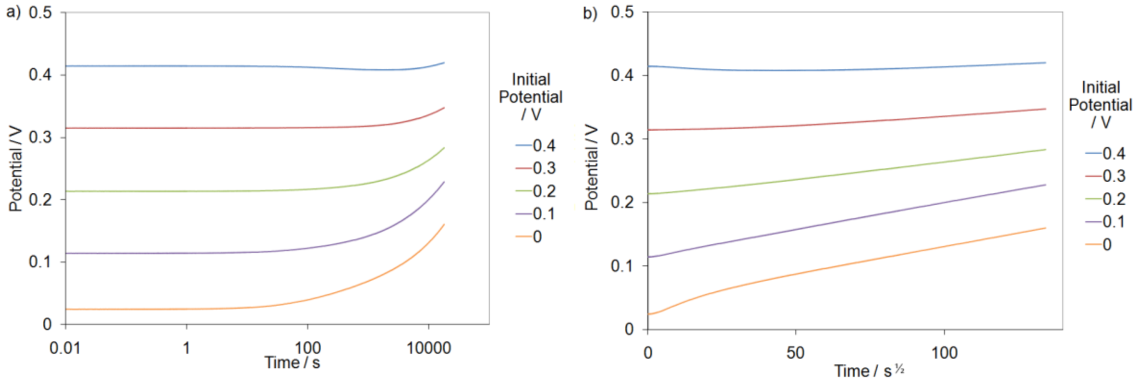

Figure A.9: Self-discharge profiles of a 8.6 mg Spectracarb 2225 carbon-cloth electrode in 1 M HCl after charging from 0.5 V to various initial charging potentials (0.0 – 0.4 V) at 1 mV s^{-1} plotted in a) log *t* and b) $t^{½}$.

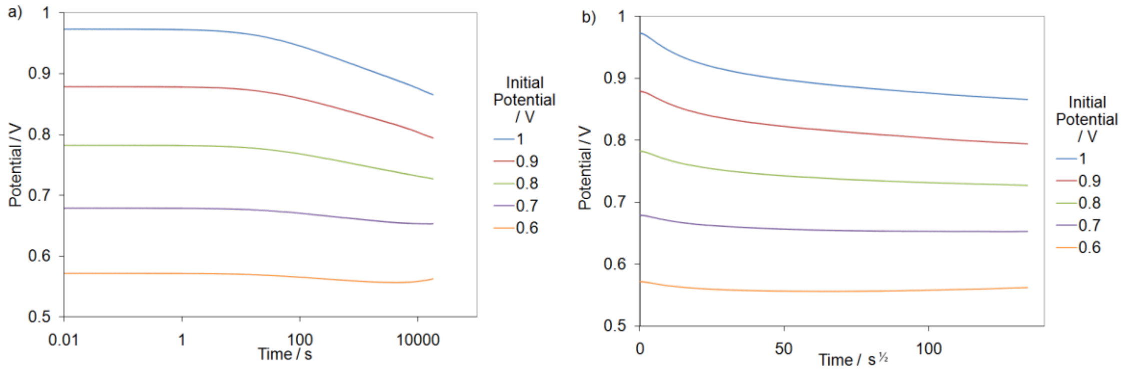

Figure A.10: Self-discharge profiles of a 9.6 mg Spectracarb 2225 carbon-cloth electrode in 1 M HCl after charging from 0.5 V to various initial charging potentials (0.6 – 1.0 V) at 1 mV s^{-1} plotted in a) log *t* and b) $t^{½}$.

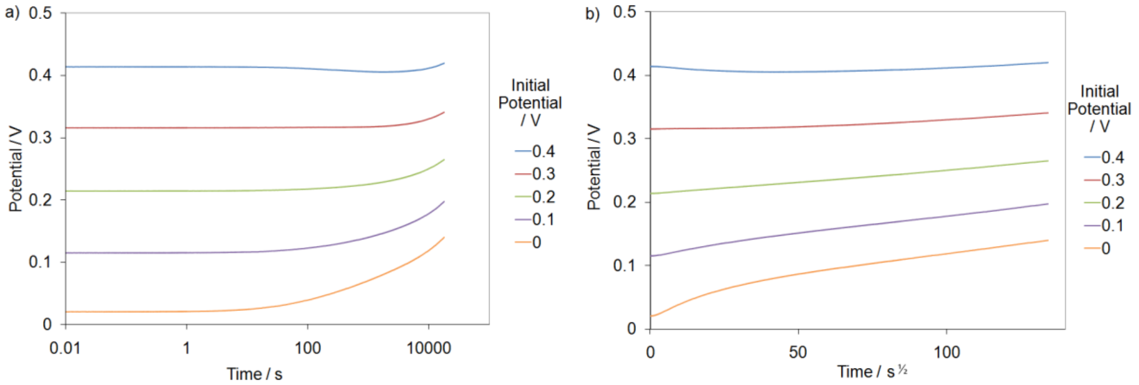

Figure A.11: Self-discharge profiles of a 9.6 mg Spectracarb 2225 carbon-cloth electrode in 1 M HCl after charging from 0.5 V to various initial charging potentials (0.0 – 0.4 V) at 1 mV s^{-1} plotted in a) log *t* and b) $t^{½}$.

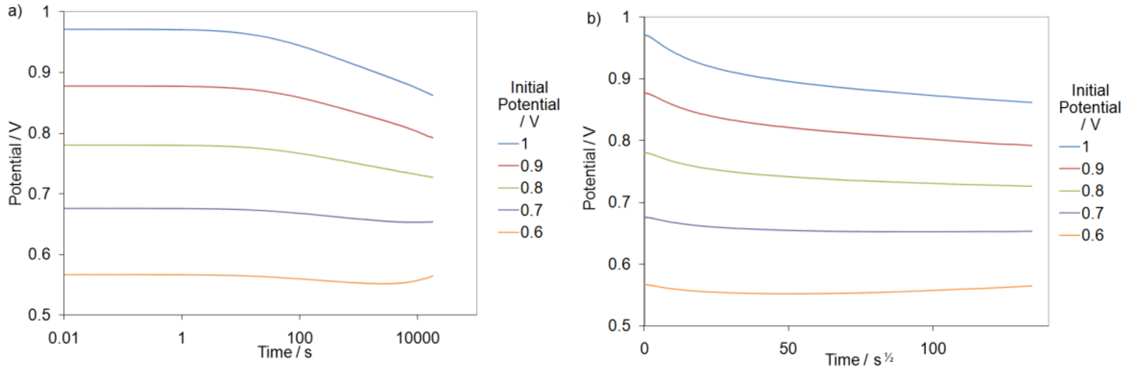

Figure A.12: Self-discharge profiles of a 9.2 mg Spectracarb 2225 carbon-cloth electrode in 1 M HCl after charging from 0.5 V to various initial charging potentials (0.6 – 1.0 V) at 1 mV s^{-1} plotted in a) log *t* and b) $t^{½}$.

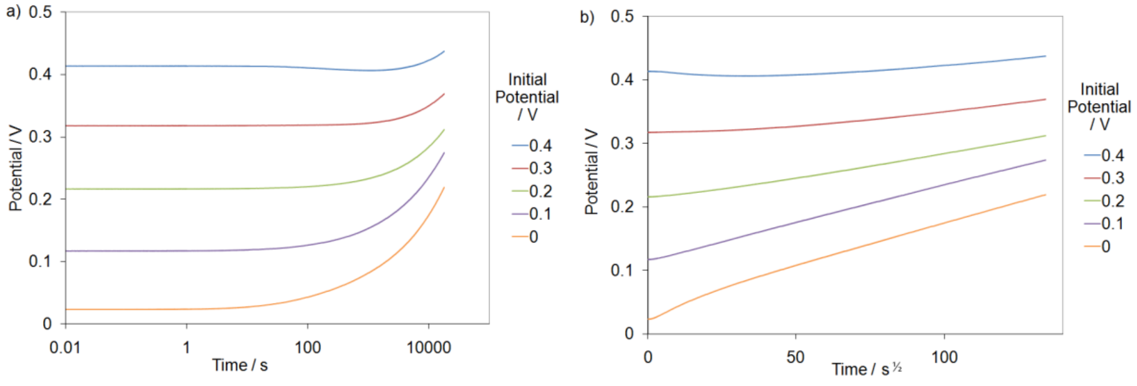

Figure A.13: Self-discharge profiles of a 9.2 mg Spectracarb 2225 carbon-cloth electrode in 1 M HCl after charging from 0.5 V to various initial charging potentials (0.0 – 0.4 V) at 1 mV s^{-1} plotted in a) log *t* and b) $t^{½}$.

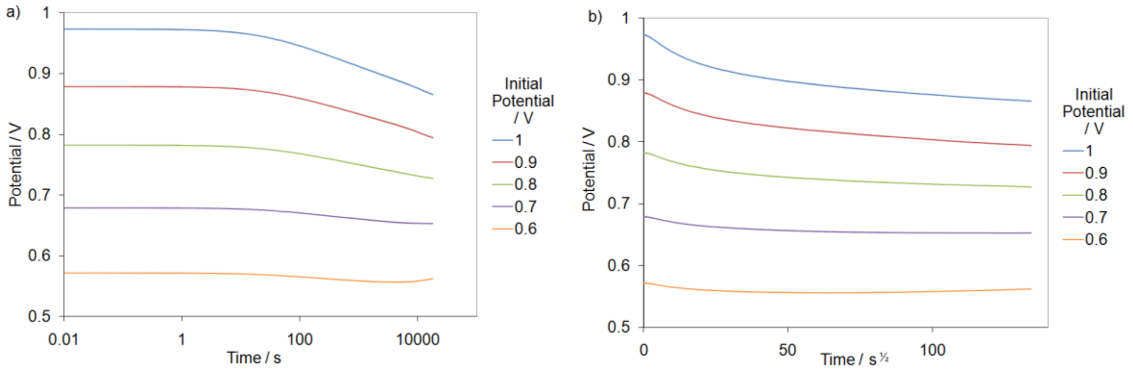

Figure A.14: Self-discharge profiles of a 8.4 mg Spectracarb 2225 carbon-cloth electrode in 1 M HCl after charging from 0.5 V to various initial charging potentials (0.6 – 1.0 V) at 1 mV s^{-1} plotted in a) log t and b) $t^{½}$.

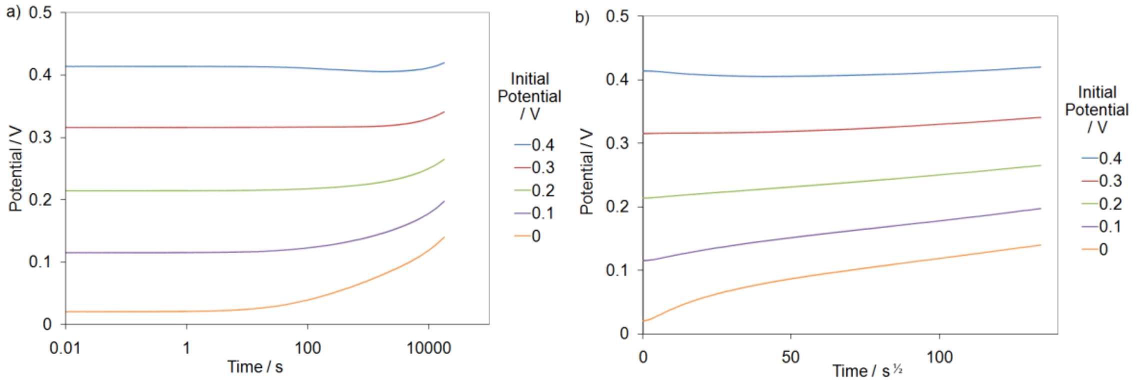

Figure A.15: Self-discharge profiles of a 8.4 mg Spectracarb 2225 carbon-cloth electrode in 1 M HCl after charging from 0.5 V to various initial charging potentials (0.0 – 0.4 V) at 1 mV s^{-1} plotted in a) log t and b) $t^{½}$.

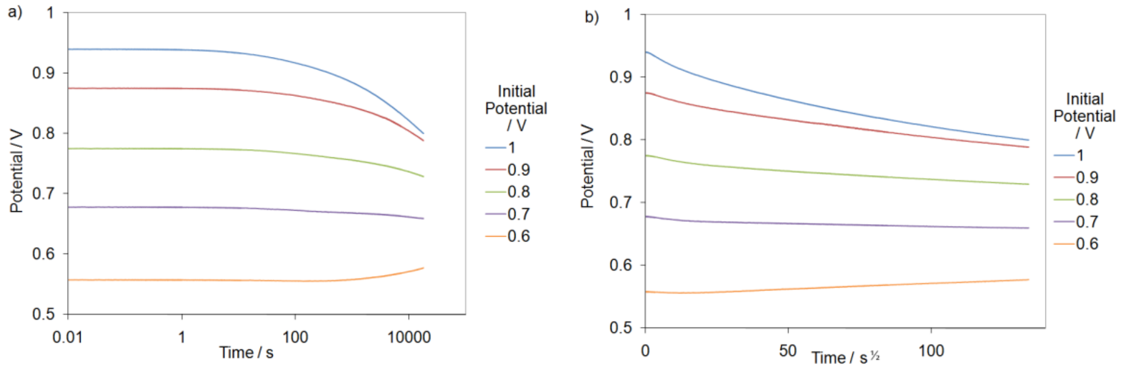

Figure A.16: Self-discharge profiles of a 9.2 mg Spectracarb 2225 carbon-cloth electrode in 1 M KCl after charging from 0.5 V to various initial charging potentials (0.6 – 1.0 V) at 1 mV s^{-1} plotted in a) log t and b) $t^{½}$.

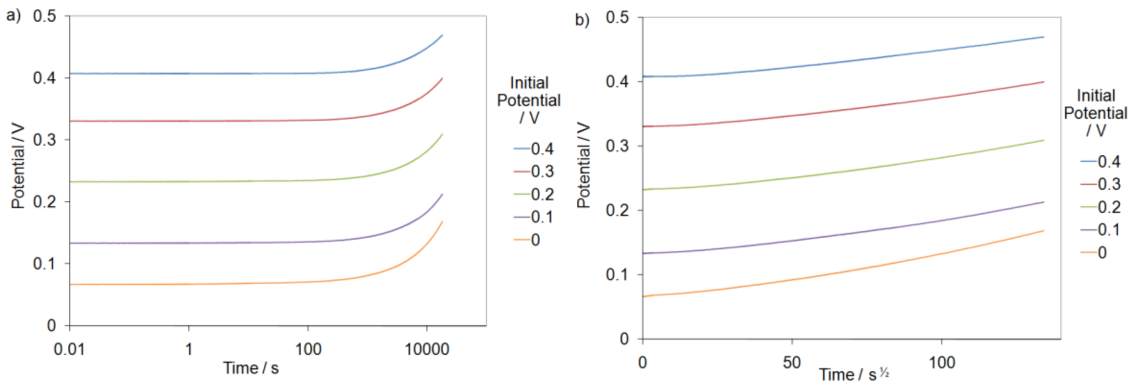

Figure A.17: Self-discharge profiles of a 9.2 mg Spectracarb 2225 carbon-cloth electrode in 1 M KCl after charging from 0.5 V to various initial charging potentials (0.0 – 0.4 V) at 1 mV s^{-1} plotted in a) log *t* and b) $t^{½}$.

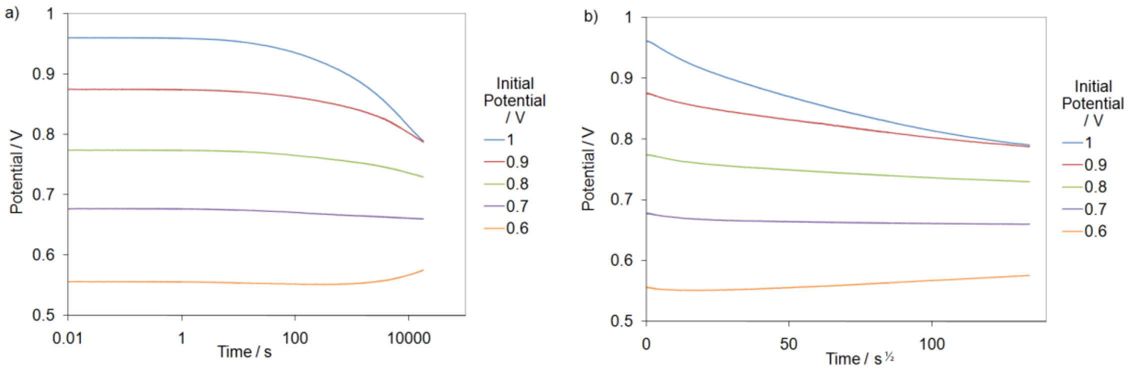

Figure A.18: Self-discharge profiles of a 9.1 mg Spectracarb 2225 carbon-cloth electrode in 1 M KCl after charging from 0.5 V to various initial charging potentials (0.6 – 1.0 V) at 1 mV s^{-1} plotted in a) log *t* and b) $t^{½}$.

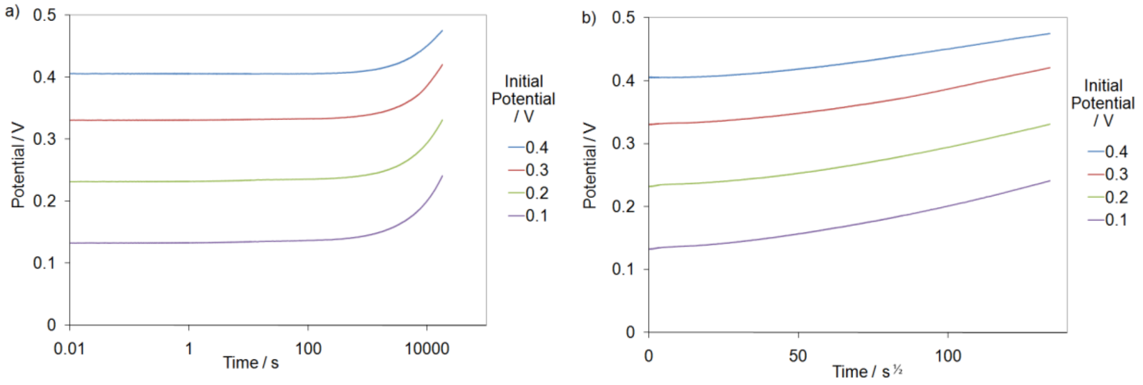

Figure A.19: Self-discharge profiles of a 9.1 mg Spectracarb 2225 carbon-cloth electrode in 1 M KCl after charging from 0.5 V to various initial charging potentials (0.0 – 0.4 V) at 1 mV s^{-1} plotted in a) log *t* and b) $t^{½}$.

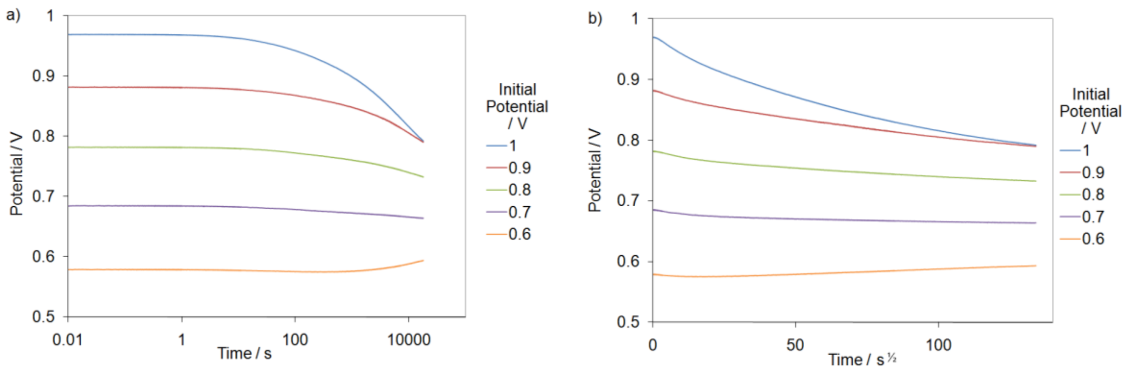

Figure A.20: Self-discharge profiles of a 9.3 mg Spectracarb 2225 carbon-cloth electrode in 1 M KCl after charging from 0.5 V to various initial charging potentials (0.6 – 1.0 V) at 1 mV s^{-1} plotted in a) log t and b) $t^{½}$.

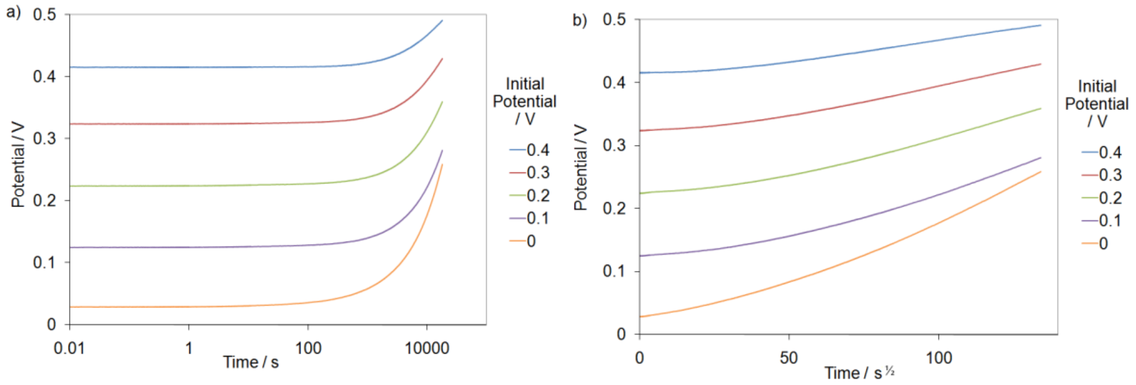

Figure A.21: Self-discharge profiles of a 9.3 mg Spectracarb 2225 carbon-cloth electrode in 1 M KCl after charging from 0.5 V to various initial charging potentials (0.0 – 0.4 V) at 1 mV s^{-1} plotted in a) log t and b) $t^{½}$.

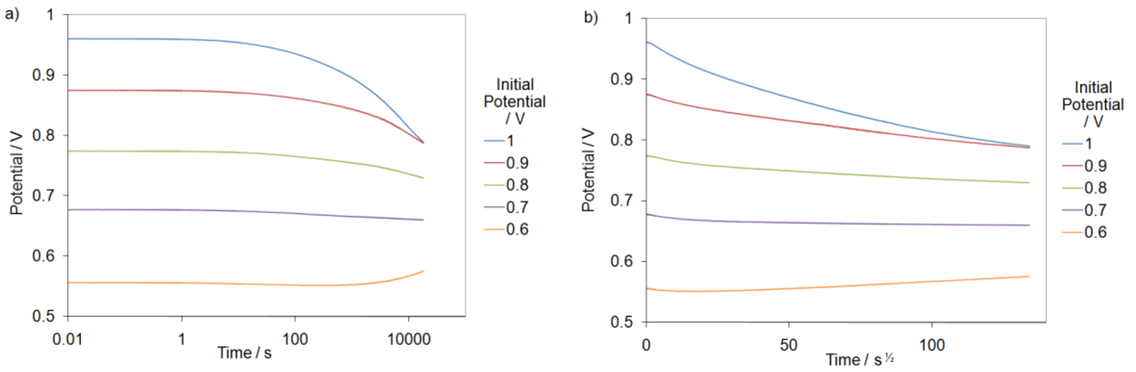

Figure A.22: Self-discharge profiles of a 9.1 mg Spectracarb 2225 carbon-cloth electrode in 1 M KCl after charging from 0.5 V to various initial charging potentials (0.6 – 1.0 V) at 1 mV s^{-1} plotted in a) log t and b) $t^{½}$.

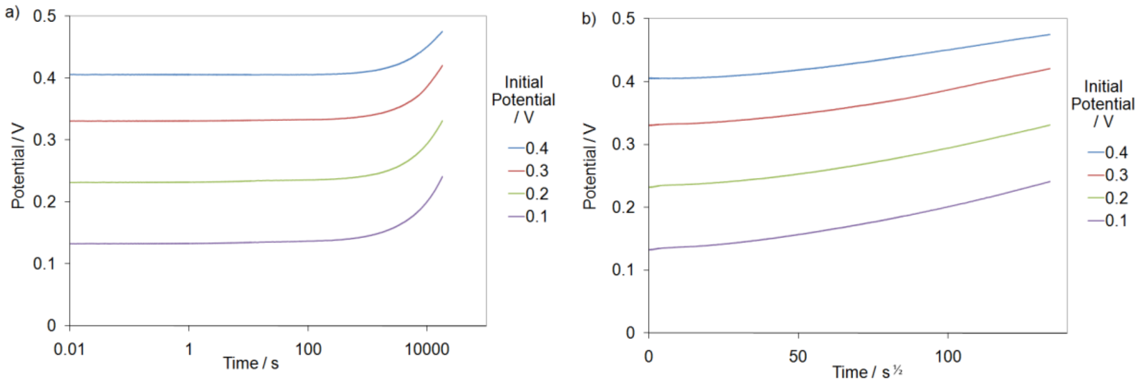

Figure A.23: Self-discharge profiles of a 9.1 mg Spectracarb 2225 carbon-cloth electrode in 1 M KCl after charging from 0.5 V to various initial charging potentials (0.0 – 0.4 V) at 1 mV s^{-1} plotted in a) log *t* and b) $t^{½}$.

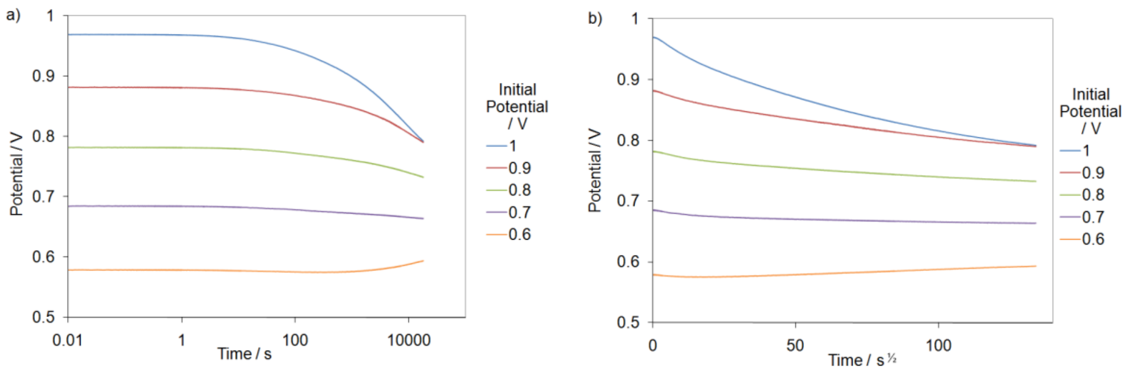

Figure A.24: Self-discharge profiles of a 9.3 mg Spectracarb 2225 carbon-cloth electrode in 1 M KCl after charging from 0.5 V to various initial charging potentials (0.6 – 1.0 V) at 1 mV s^{-1} plotted in a) log *t* and b) $t^{½}$.

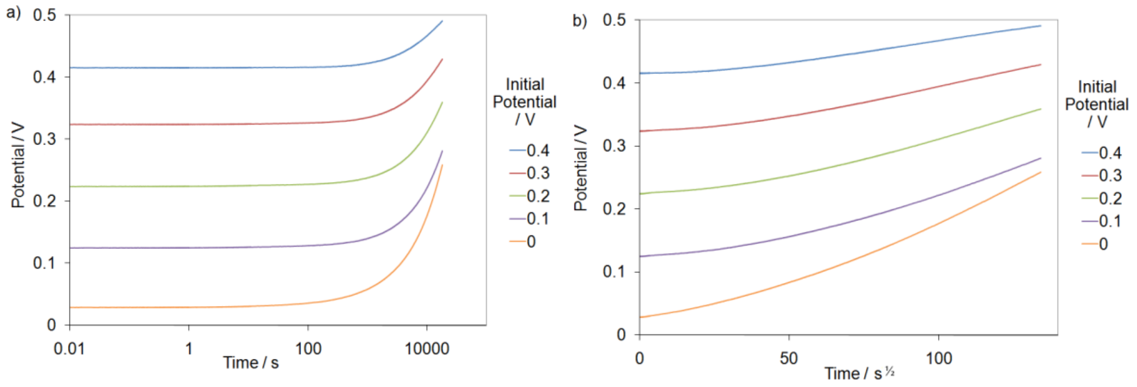

Figure A.25: Self-discharge profiles of a 9.3 mg Spectracarb 2225 carbon-cloth electrode in 1 M KCl after charging from 0.5 V to various initial charging potentials (0.0 – 0.4 V) at 1 mV s^{-1} plotted in a) log *t* and b) $t^{½}$.

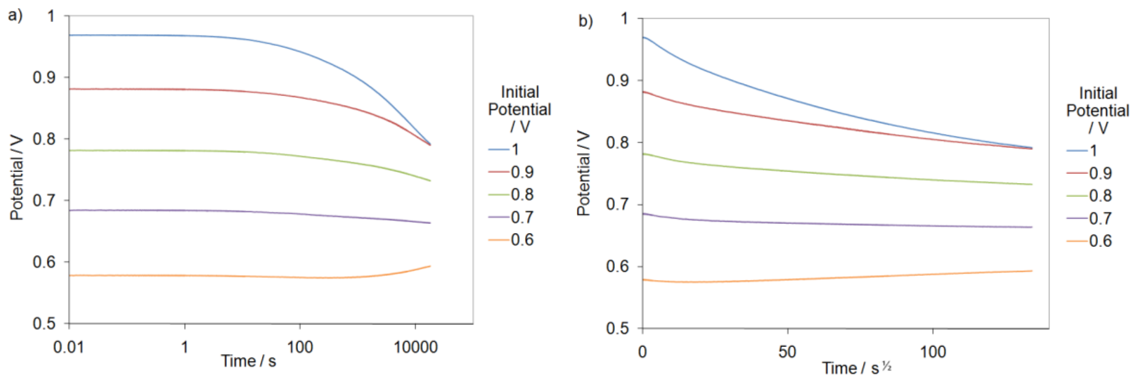

Figure A.26: Self-discharge profiles of a 8.9 mg Spectracarb 2225 carbon-cloth electrode in 1 M KCl after charging from 0.5 V to various initial charging potentials (0.6 – 1.0 V) at 1 mV s^{-1} plotted in a) log *t* and b) $t^{½}$.

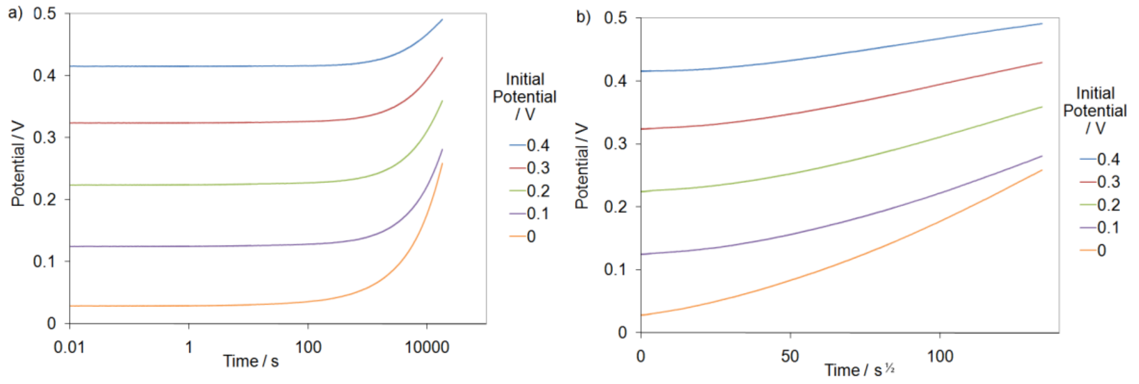

Figure A.27: Self-discharge profiles of a 8.9 mg Spectracarb 2225 carbon-cloth electrode in 1 M KCl after charging from 0.5 V to various initial charging potentials (0.0 – 0.4 V) at 1 mV s^{-1} plotted in a) log *t* and b) $t^{½}$.

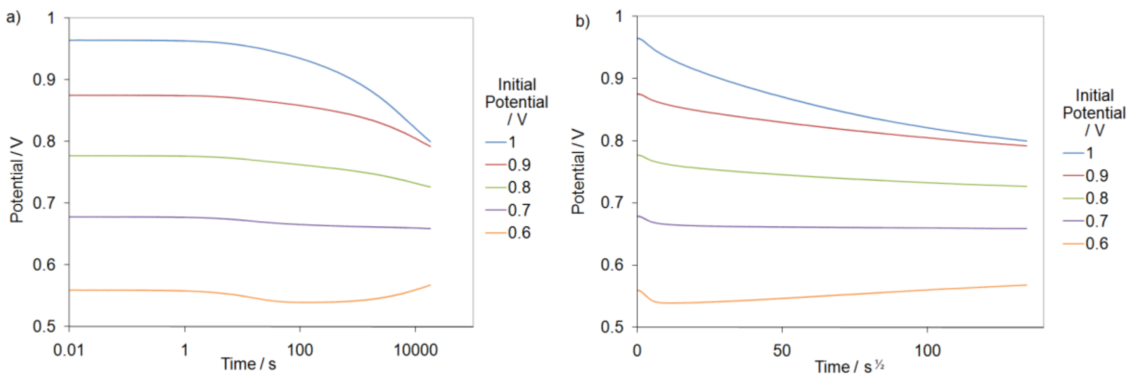

Figure A.28: Self-discharge profiles of a 9.7 mg Spectracarb 2225 carbon-cloth electrode in 1 M NaCl after charging from 0.5 V to various initial charging potentials (0.6 – 1.0 V) at 1 mV s^{-1} plotted in a) log *t* and b) $t^{½}$.

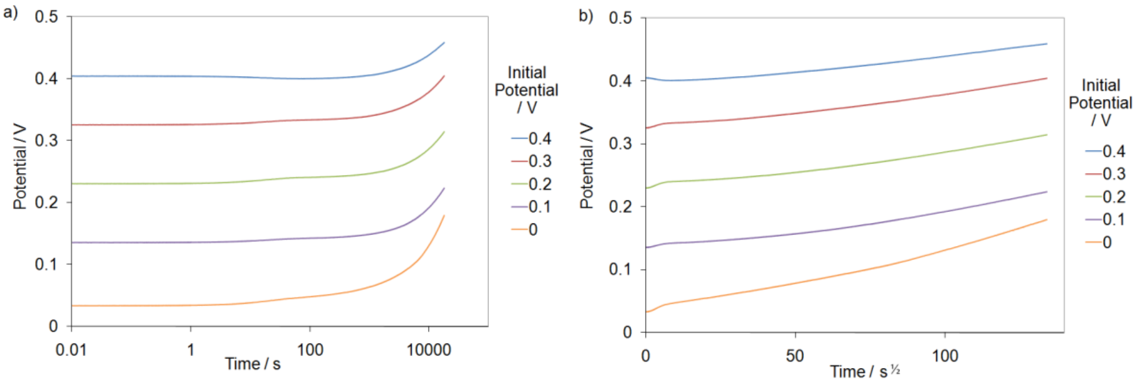

Figure A.29: Self-discharge profiles of a 9.7 mg Spectracarb 2225 carbon-cloth electrode in 1 M NaCl after charging from 0.5 V to various initial charging potentials (0.0 – 0.4 V) at 1 mV s^{-1} plotted in a) log *t* and b) $t^{½}$.

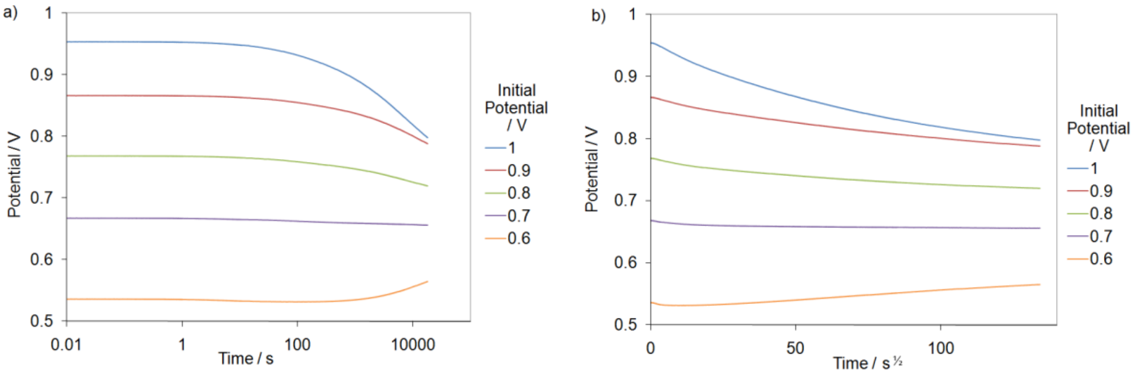

Figure A.30: Self-discharge profiles of a 9.5 mg Spectracarb 2225 carbon-cloth electrode in 1 M NaCl after charging from 0.5 V to various initial charging potentials (0.6 – 1.0 V) at 1 mV s^{-1} plotted in a) log *t* and b) $t^{½}$.

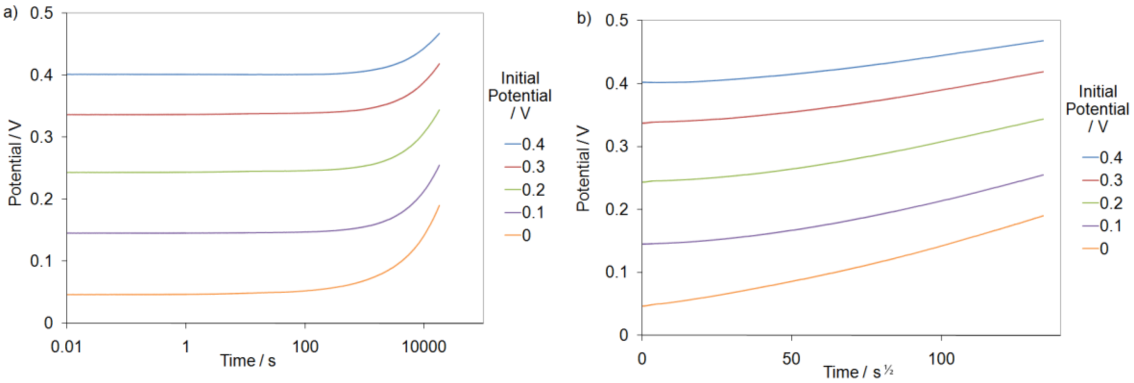

Figure A.31: Self-discharge profiles of a 9.5 mg Spectracarb 2225 carbon-cloth electrode in 1 M NaCl after charging from 0.5 V to various initial charging potentials (0.0 – 0.4 V) at 1 mV s^{-1} plotted in a) log *t* and b) $t^{½}$.

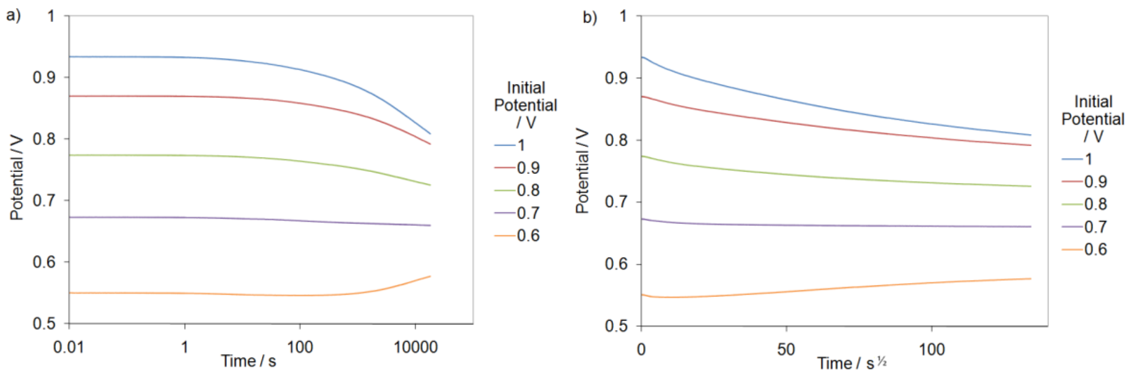

Figure A.32: Self-discharge profiles of a 9.1 mg Spectracarb 2225 carbon-cloth electrode in 1 M NaCl after charging from 0.5 V to various initial charging potentials (0.6 – 1.0 V) at 1 mV s^{-1} plotted in a) log *t* and b) $t^{½}$.

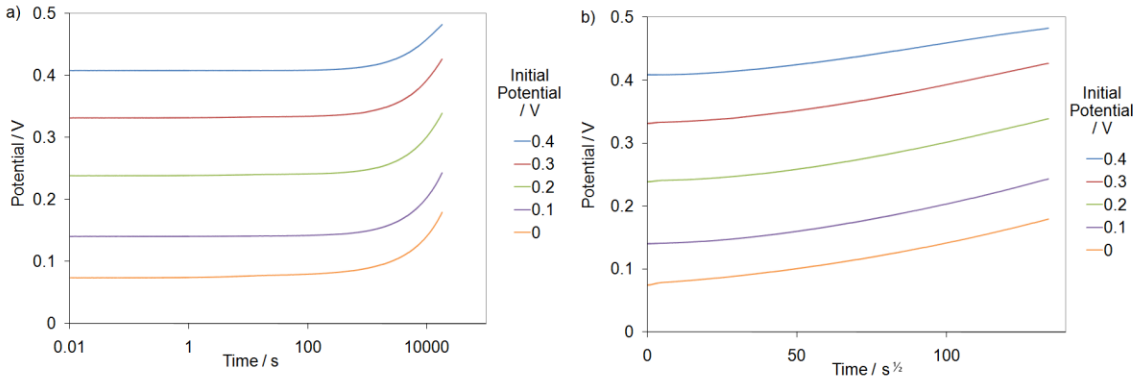

Figure A.33: Self-discharge profiles of a 9.1 mg Spectracarb 2225 carbon-cloth electrode in 1 M NaCl after charging from 0.5 V to various initial charging potentials (0.0 – 0.4 V) at 1 mV s^{-1} plotted in a) log *t* and b) $t^{½}$.

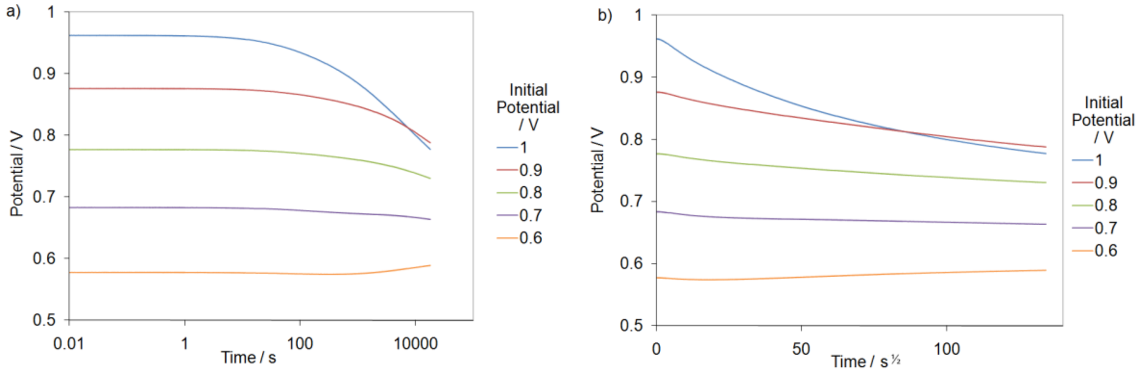

Figure A.34: Self-discharge profiles of a 9.1 mg Spectracarb 2225 carbon-cloth electrode in 1 M NaCl after charging from 0.5 V to various initial charging potentials (0.6 – 1.0 V) at 1 mV s^{-1} plotted in a) log *t* and b) $t^{½}$.

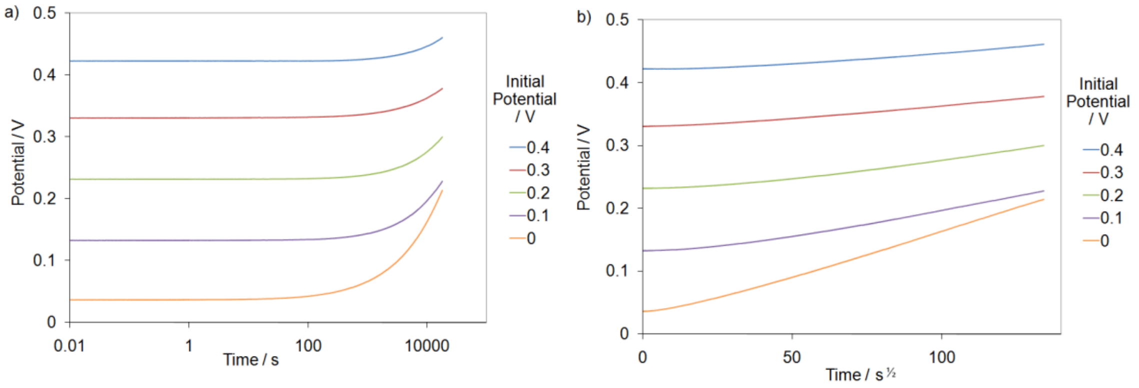

Figure A.35: Self-discharge profiles of a 9.1 mg Spectracarb 2225 carbon-cloth electrode in 1 M NaCl after charging from 0.5 V to various initial charging potentials (0.0 – 0.4 V) at 1 mV s^{-1} plotted in a) log *t* and b) $t^{½}$.

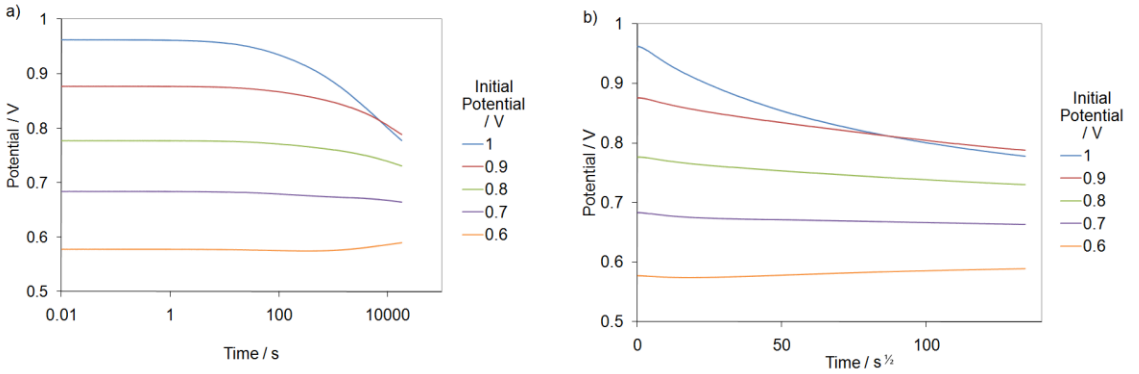

Figure A.36: Self-discharge profiles of a 9.7 mg Spectracarb 2225 carbon-cloth electrode in 1 M NaCl after charging from 0.5 V to various initial charging potentials (0.5 – 1.0 V) at 1 mV s^{-1} plotted in a) log *t* and b) $t^{½}$.

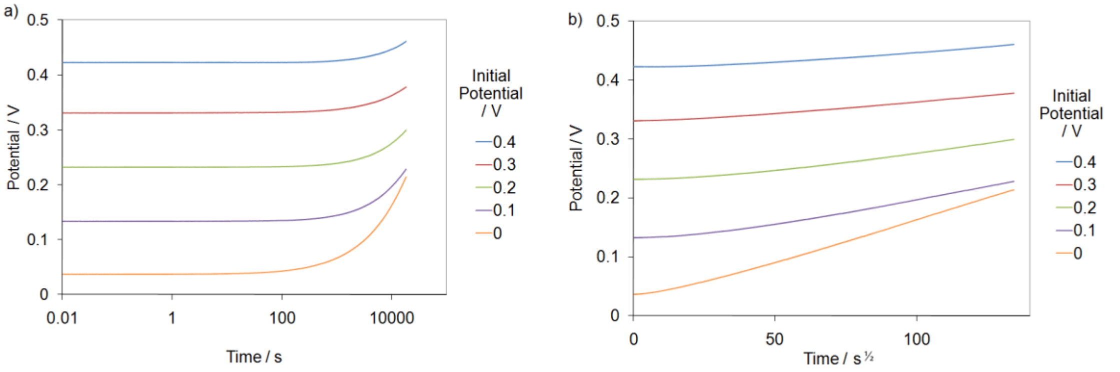

Figure A.37: Self-discharge profiles of a 9.7 mg Spectracarb 2225 carbon-cloth electrode in 1 M NaCl after charging from 0.5 V to various initial charging potentials (0.0 – 0.4 V) at 1 mV s^{-1} plotted in a) log t and b) $t^{½}$.

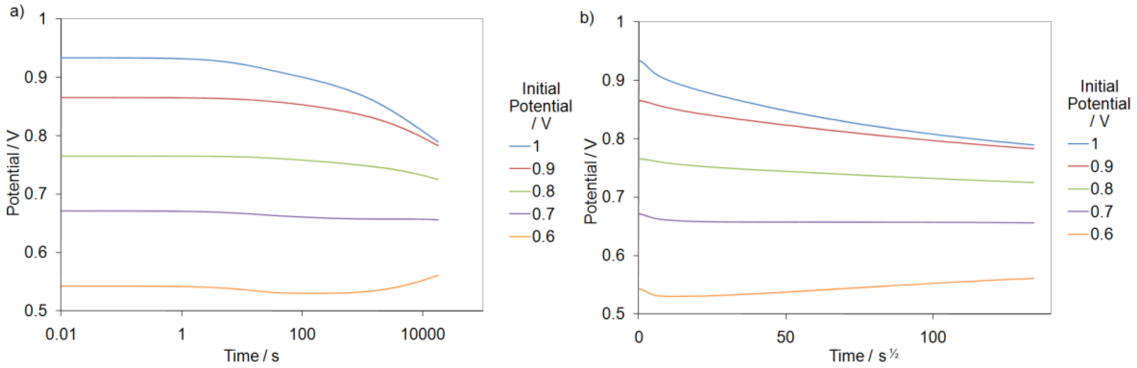

Figure A.38: Self-discharge profiles of a 9.7 mg Spectracarb 2225 carbon-cloth electrode in 1 M NaCl after charging from 0.5 V to various initial charging potentials (0.5 – 1.0 V) at 1 mV s^{-1} plotted in a) log t and b) $t^{½}$.

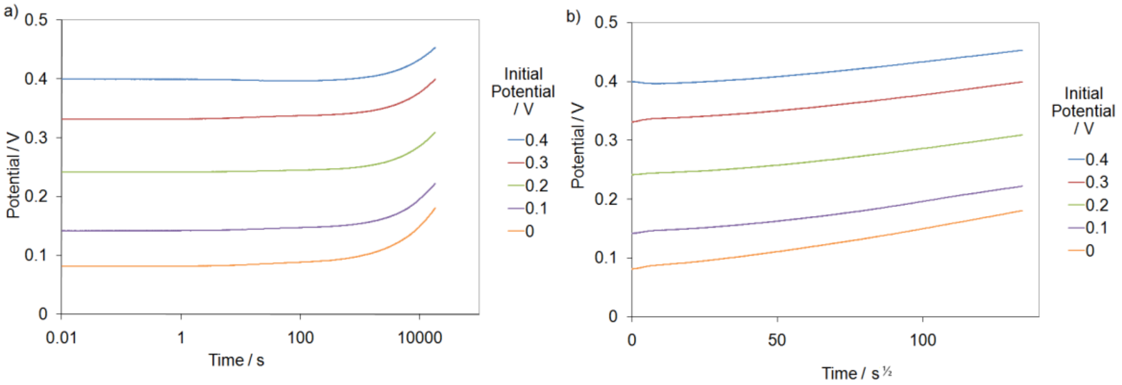

Figure A.39: Self-discharge profiles of a 9.7 mg Spectracarb 2225 carbon-cloth electrode in 1 M NaCl after charging from 0.5 V to various initial charging potentials (0.0 – 0.4 V) at 1 mV s^{-1} plotted in a) log t and b) $t^{½}$.

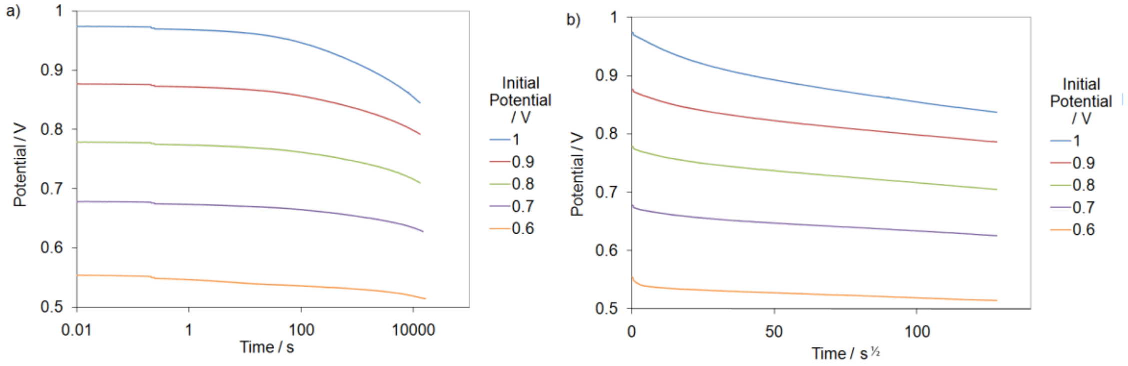

Figure A.40: Self-discharge profiles of a 6.92 Spectracarb 2225 carbon-cloth electrode in 1 M $MgCl_2$ after charging from 0.5 V to various initial charging potentials (0.6 – 1.0 V) at 1 mV s^{-1} plotted in a) log t and b) $t^{½}$.

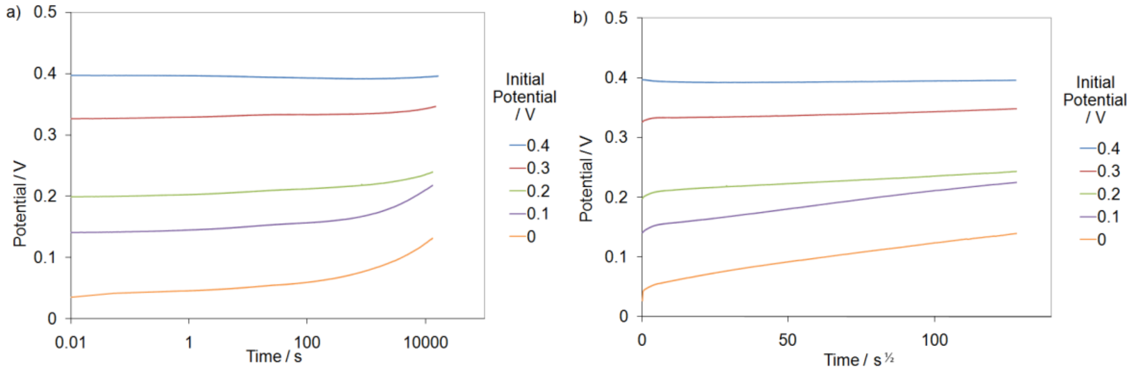

Figure A.41: Self-discharge profiles of a 6.9 mg Spectracarb 2225 carbon-cloth electrode in 1 M $MgCl_2$ after charging from 0.5 V to various initial charging potentials (0.0 – 0.4 V) at 1 mV s^{-1} plotted in a) log t and b) $t^{½}$.

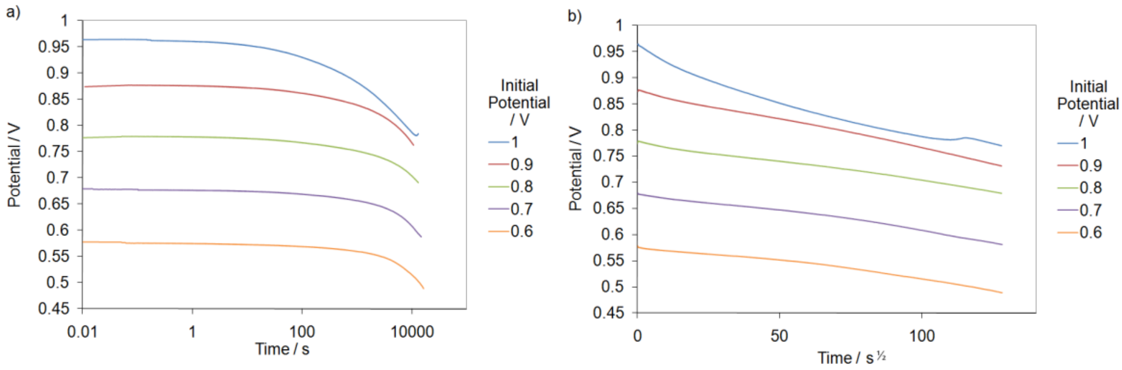

Figure A.42: Self-discharge profiles of a 7.2 mg Spectracarb 2225 carbon-cloth electrode in 1 M $CaCl_2$ after charging from 0.5 V to various initial charging potentials (0.6 – 1.0 V) at 1 mV s^{-1} plotted in a) log t and b) $t^{½}$.

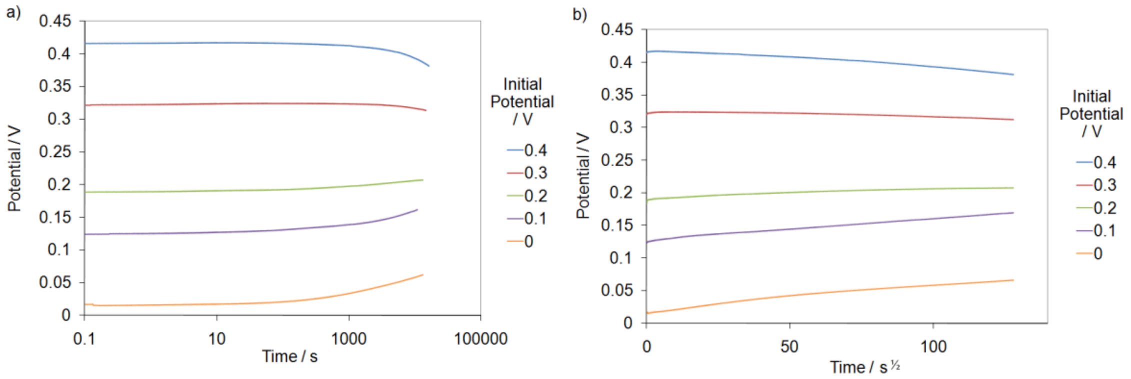

Figure A.43: Self-discharge profiles of a 7.2 mg Spectracarb 2225 carbon-cloth electrode in 1 M $CaCl_2$ after charging from 0.5 V to various initial charging potentials (0.0 – 0.4 V) at 1 mV s^{-1} plotted in a) log t and b) $t^{½}$.

A.2 Self-discharge profiles of graphite carbon powder from various initial charging potentials

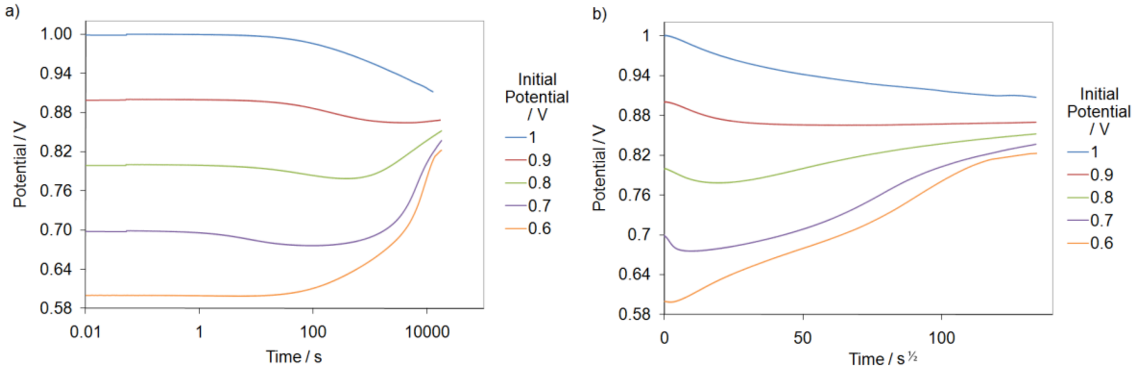

Figure A.44: Self-discharge profiles of a 0.1671 g Graphite carbon powder electrode in 1 M H_2SO_4 after charging from 0.5 V to various initial charging potentials (0.6 – 1.0 V) at 1 mV s^{-1} plotted in a) log *t* and b) $t^{½}$.

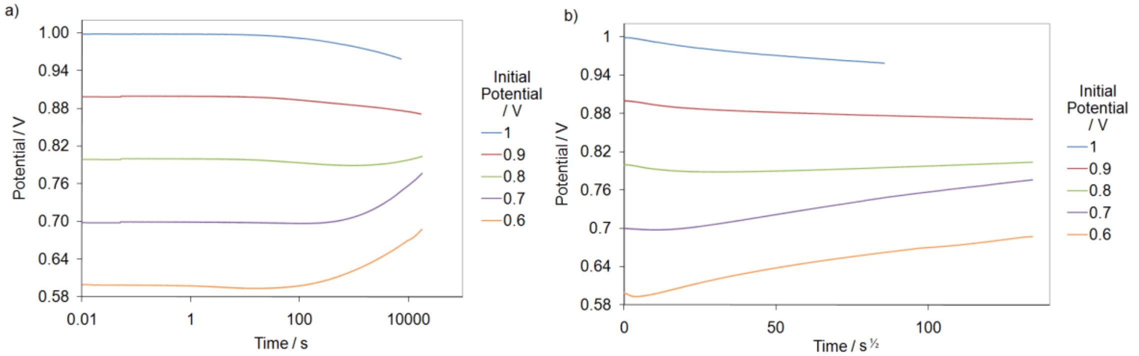

Figure A.45: Self-discharge profiles of a 0.2038 g Graphite carbon powder electrode in 1 M H_2SO_4 after charging from 0.5 V to various initial charging potentials (0.6 – 1.0 V) at 1 mV s^{-1} plotted in a) log *t* and b) $t^{½}$.

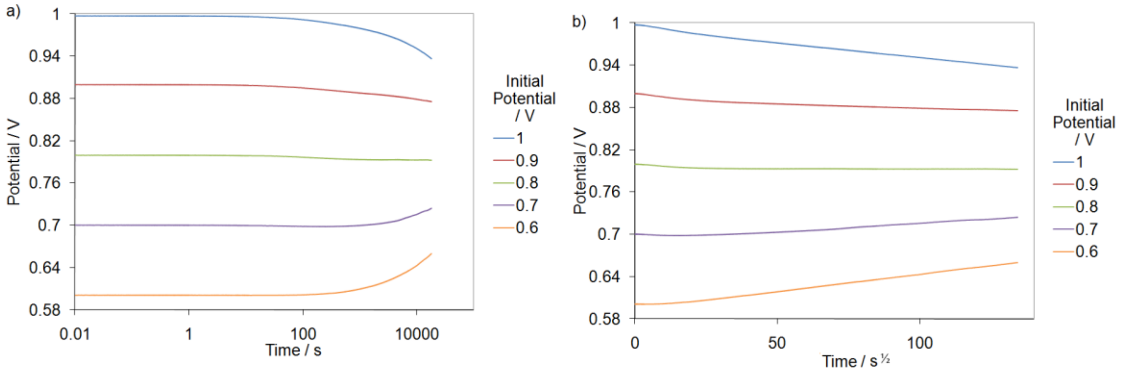

Figure A.46: Self-discharge profiles of a 0.1131 g Graphite carbon powder electrode in 1 M HCl after charging from 0.5 V to various initial charging potentials (0.6 – 1.0 V) at 1 mV s^{-1} plotted in a) log *t* and b) $t^{½}$.

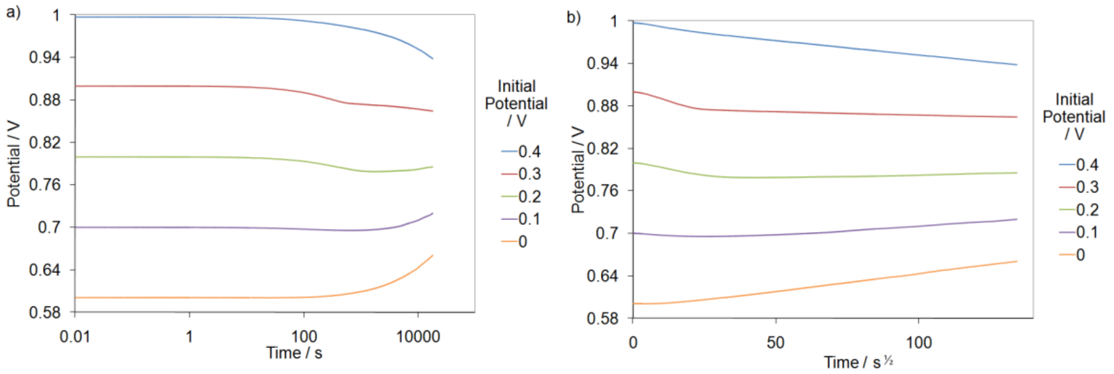

Figure A.47: Self-discharge profiles of a 0.1349 g Graphite carbon powder electrode in 1 M HCl after charging from 0.5 V to various initial charging potentials (0.6 – 1.0 V) at 1 mV s^{-1} plotted in a) log *t* and b) $t^{½}$.

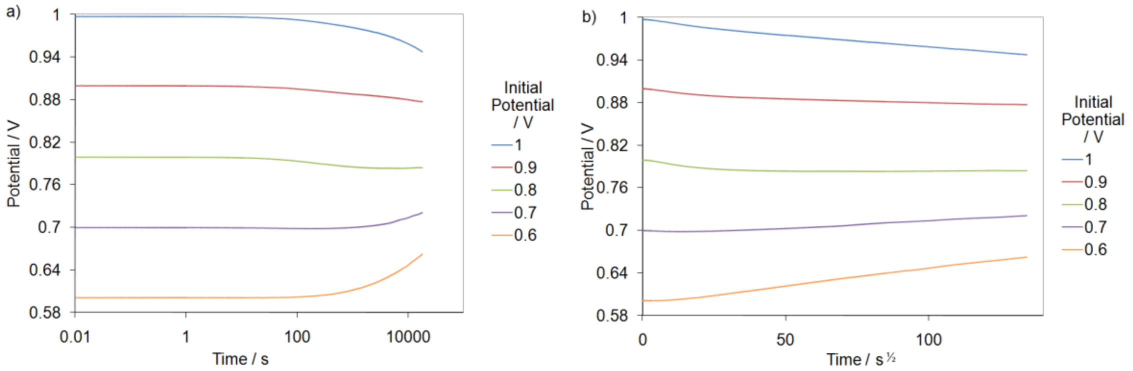

Figure A.48:Self-discharge profiles of a 0.1942 g Graphite carbon powder electrode in 1 M HCl after charging from 0.5 V to various initial charging potentials (0.6 – 1.0 V) at 1 mV s^{-1} plotted in a) log *t* and b) $t^{½}$.

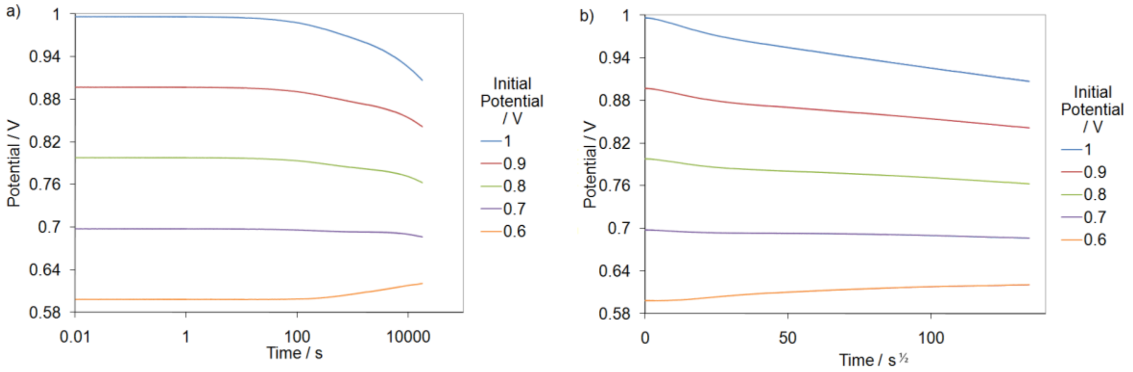

Figure A.49: Self-discharge profiles of a 0.1397 g Graphite carbon powder electrode in 1 M KCl after charging from 0.5 V to various initial charging potentials (0.6 – 1.0 V) at 1 mV s^{-1} plotted in a) log *t* and b) $t^{½}$.

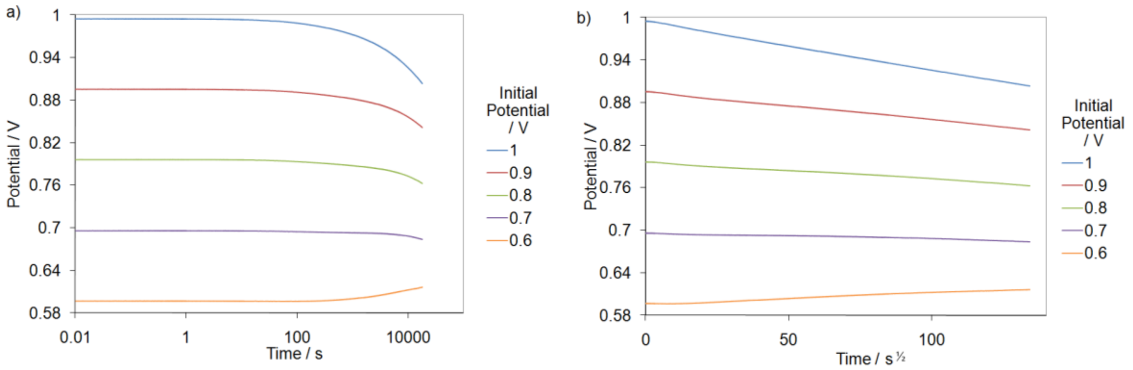

Figure A.50: Self-discharge profiles of a 0.1360 g Graphite carbon powder electrode in 1 M KCl after charging from 0.5 V to various initial charging potentials (0.6 – 1.0 V) at 1 mV s^{-1} plotted in a) log *t* and b) $t^{½}$.

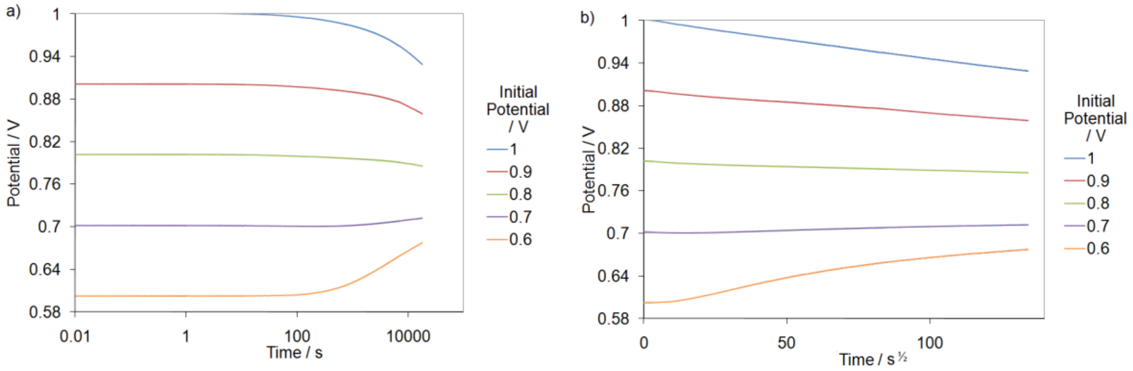

Figure A.51: Self-discharge profiles of a 0.1276 g Graphite carbon powder electrode in 1 M NaCl after charging from 0.5 V to various initial charging potentials (0.6 – 1.0 V) at 1 mV s^{-1} plotted in a) log *t* and b) $t^{½}$.

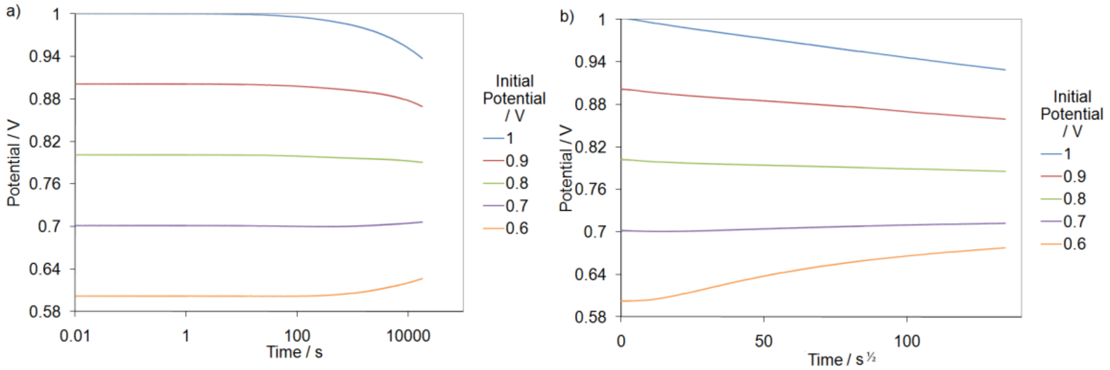

Figure A.52: Self-discharge profiles of a 0.1399 g Graphite carbon powder electrode in 1 M NaCl after charging from 0.5 V to various initial charging potentials (0.6 – 1.0 V) at 1 mV s^{-1} plotted in a) log *t* and b) $t^{½}$.

A.3 Self-discharge profiles of Spectracarb 2225 carbon cloth after charging to 1.0 V at various ramp rates

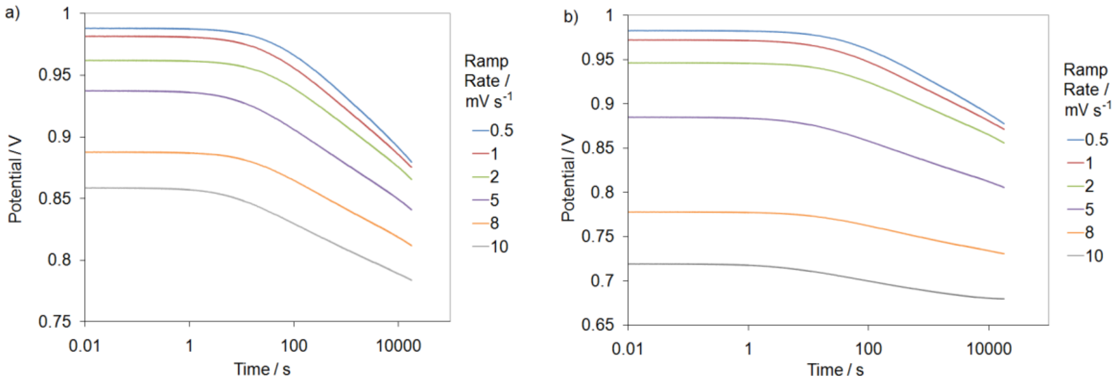

Figure A.53: Self-discharge profiles of 9.2 mg Spectracarb 2225 carbon-cloth electrodes in 1 M H_2SO_4 after charging from 0.5 V to 1.0 V at various ramp rates (0.5 - 10 mV s^{-1}). Electrode masses were a) 9.0 mg and b) 9.2 mg.

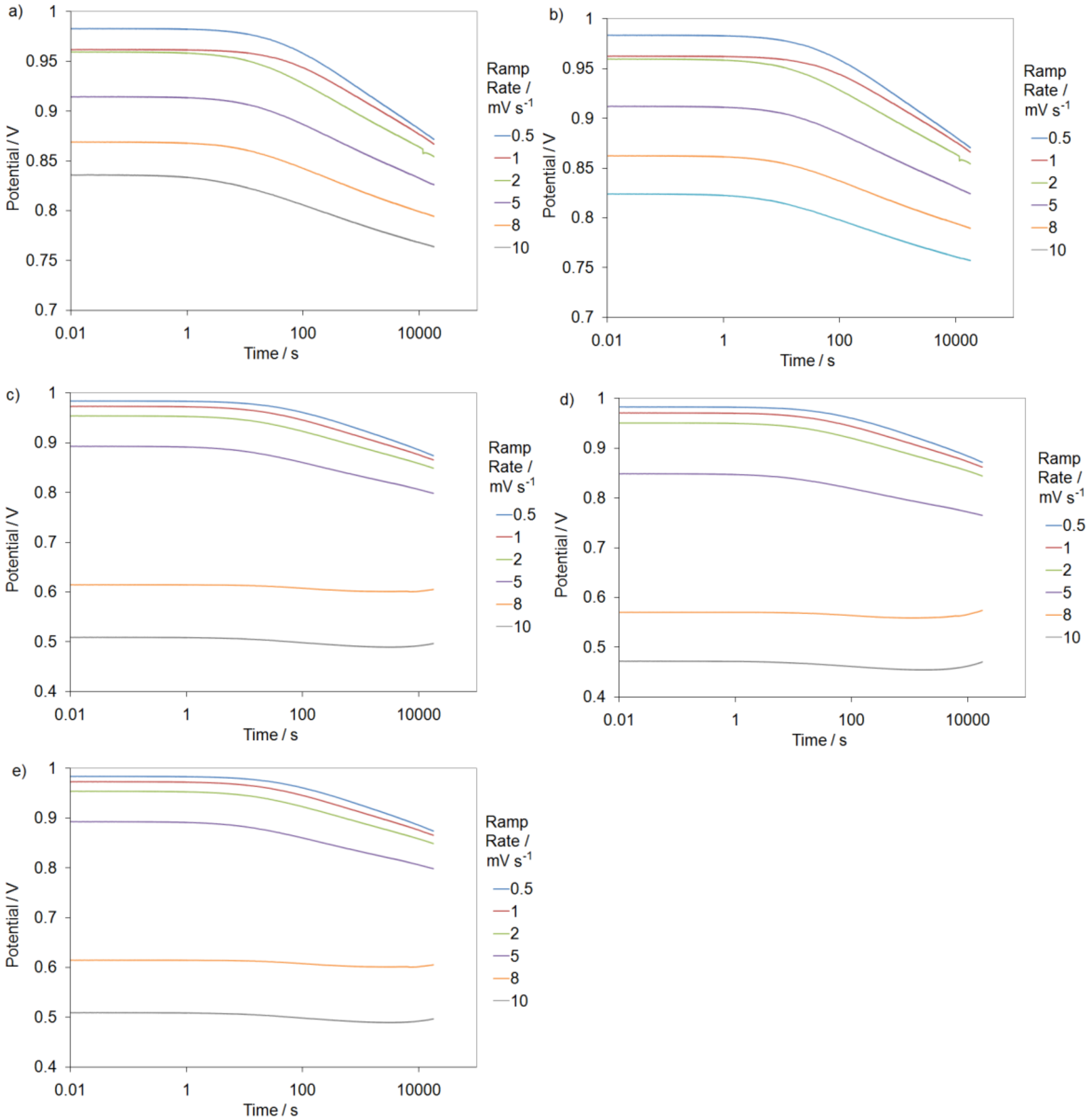

Figure A.54: Self-discharge profiles of Spectracarb 2225 carbon-cloth electrode in 1 M HCl after charging from 0.5 V to 1.0 V at various ramp rates (0.5 - 10 mV s^{-1}). Electrode masses were a) 8.9 mg, b) 8.6 mg, c) 9.6 mg, d) 9.2 mg, and e) 8.4 mg

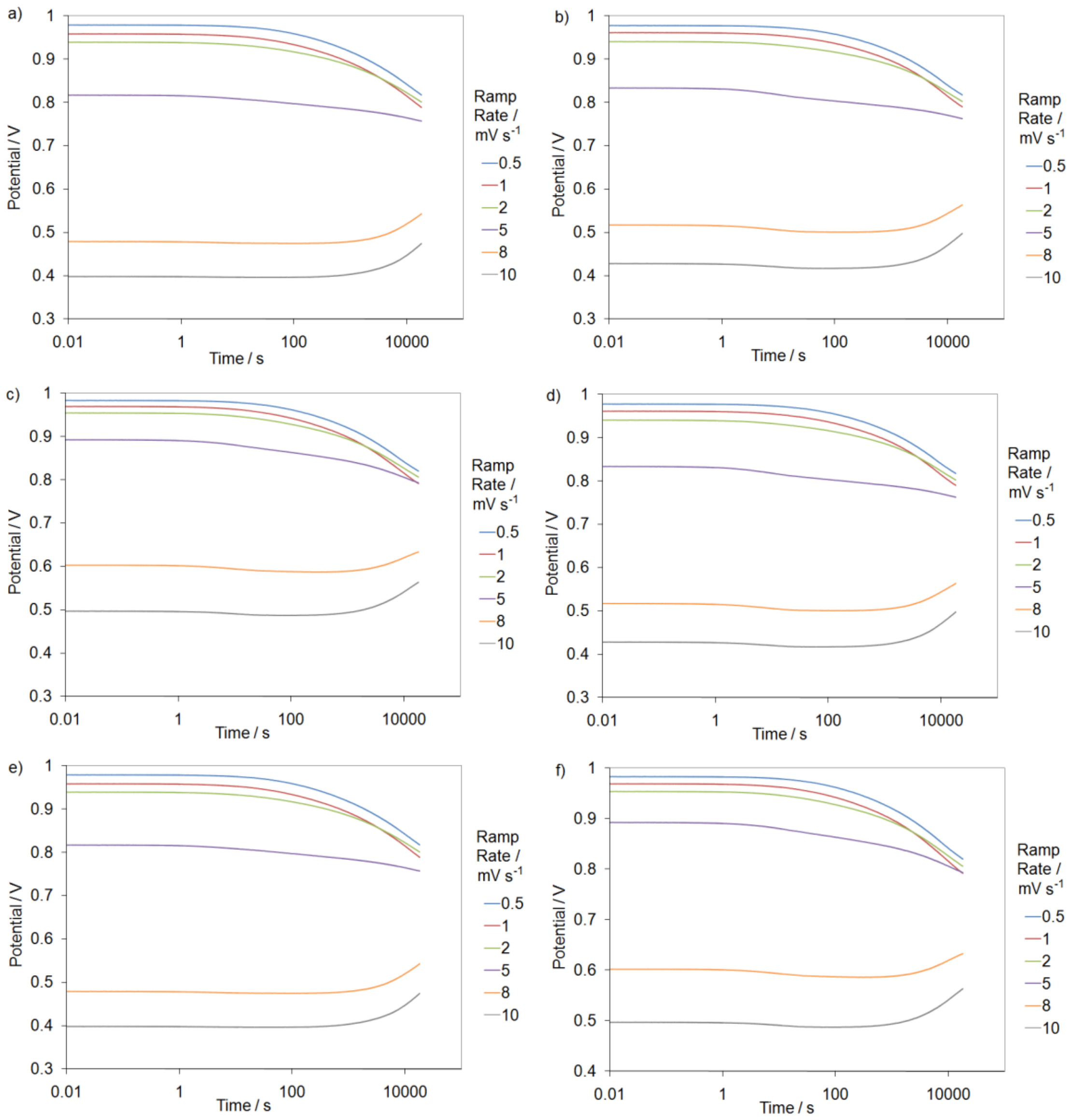

Figure A.55: Self-discharge profiles of Spectracarb 2225 carbon-cloth electrodes in 1 M KCl plotted vs. log *t* after charging from 0.5 V to 1.0 V at various ramp rates (0.5 - 10 mV s^{-1}). Electrode masses used were a) 9.2 mg, b) 9.1 mg, c) 9.3 mg, d) 9.1 mg, e) 9.3 mg, and f) 8.9 mg.

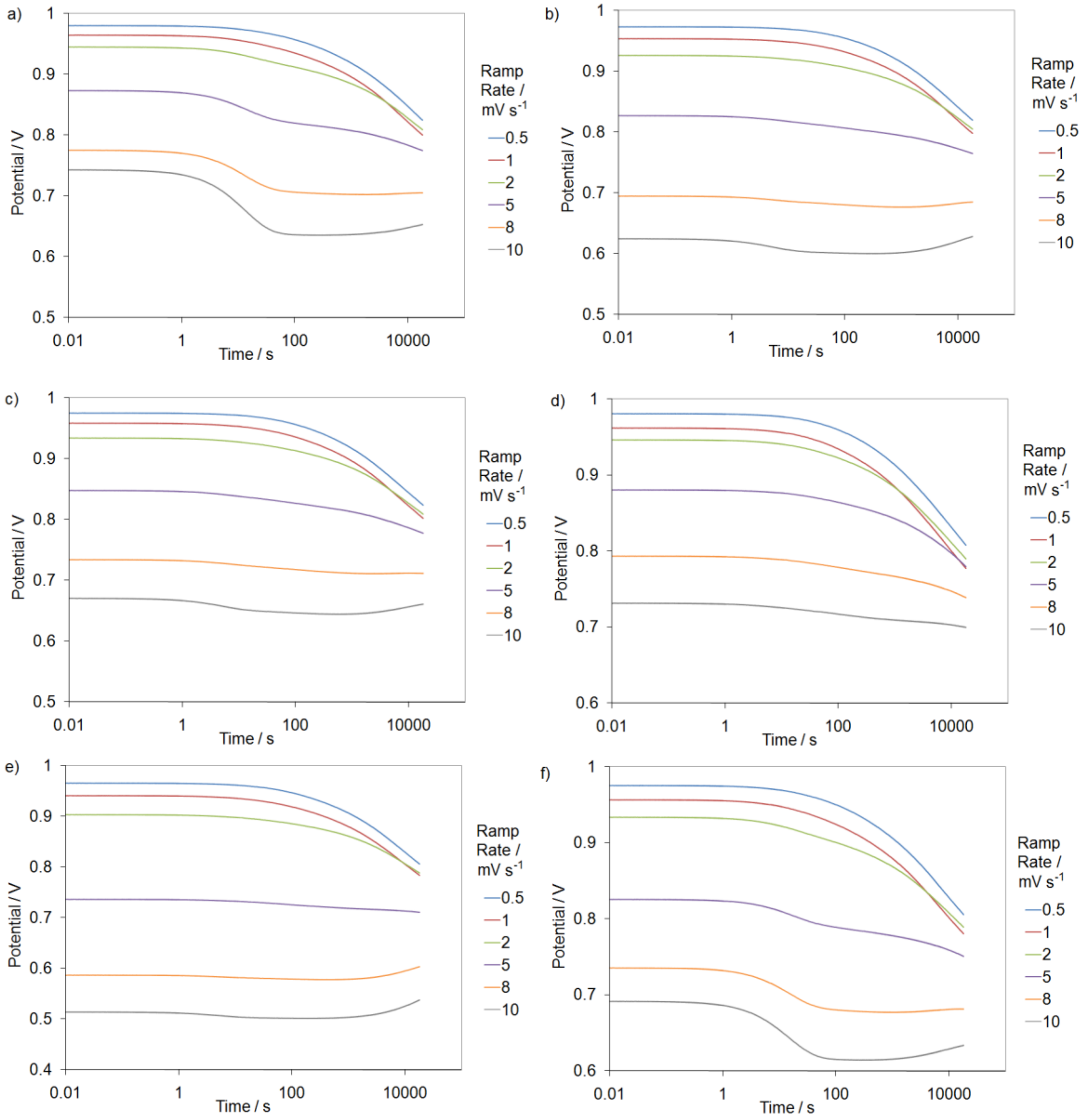

Figure A.56: Self-discharge profiles of Spectracarb 2225 carbon-cloth electrodes in 1 M NaCl plotted vs. log *t* after charging from 0.5 V to 1.0 V at various ramp rates (0.5 - 10 mV s^{-1}). Electrode masses were a) 9.7 mg, b) 9.5 mg, c) 9.1 mg, d) 9.1 mg, e) 9.7 mg, and f) 9.7 mg.

APPENDIX B

HARDWARE TRANSMISSION LINE CIRCUIT DATA

B.1 Self-discharge data for hardware transmission line circuit after charging capacitor to 1.0 V at 50 mV s^{-1} with no hold, and hold time required for all capacitors to reach 1.0 V.

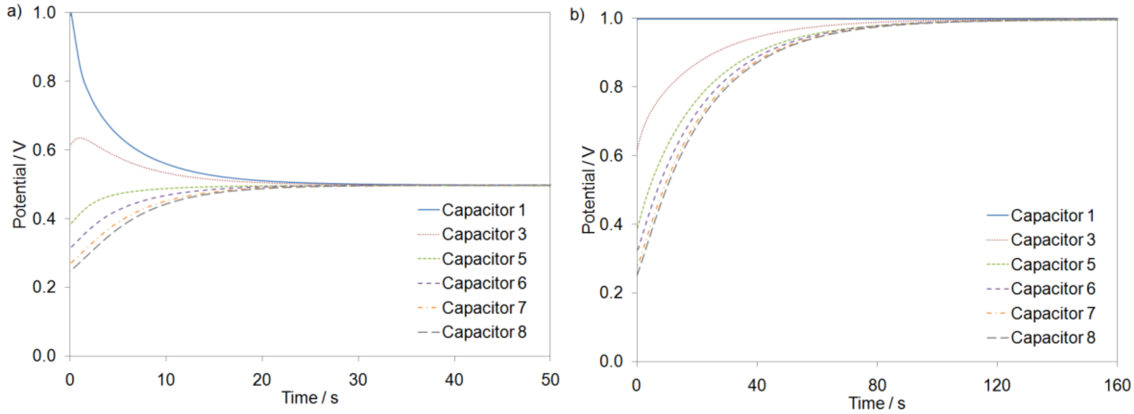

Figure B.1: Data taken at various positions down the transmission line circuit during a) self-discharge with no hold, and b) during hold step. The resistances were set to 10 kΩ and the voltage of the first capacitor was ramped from 0.0 V to 1.0 V at 50 mV s^{-1}.

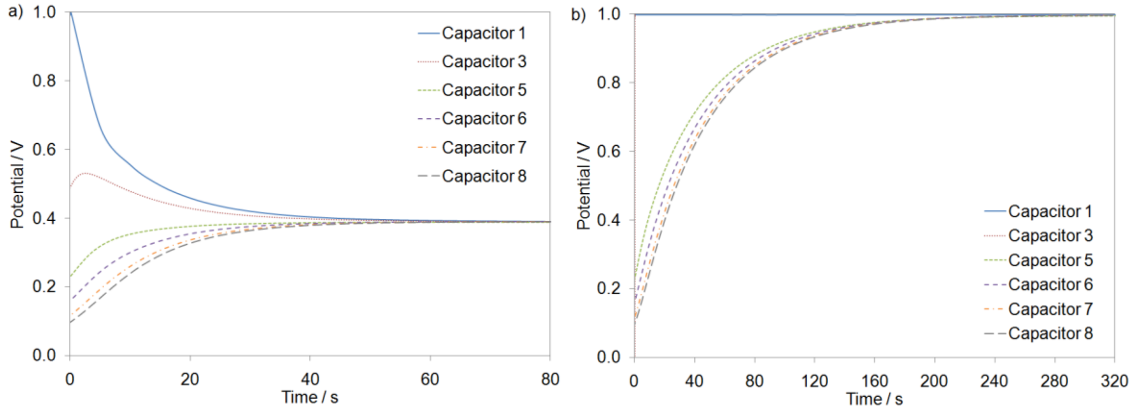

Figure B.2: Data taken at various positions down the transmission line circuit during a) self-discharge with no hold, and b) during hold step. The resistances were set to 20 kΩ and the voltage of the first capacitor was ramped from 0.0 V to 1.0 V at 50 mV s^{-1}.

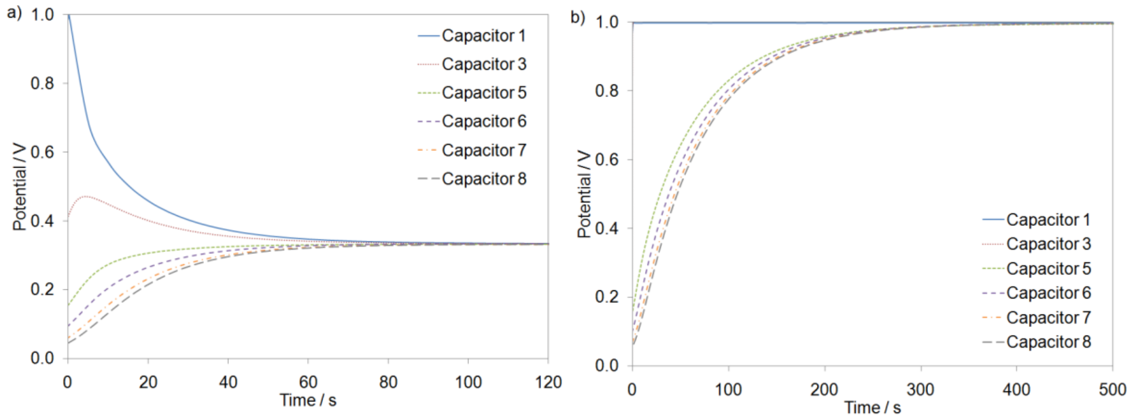

Figure B.3: Data taken at various positions down the transmission line circuit during a) self-discharge with no hold, and b) during hold step. The resistances were set to 30 kΩ and the voltage of the first capacitor was ramped from 0.0 V to 1.0 V at 50 mV s^{-1}.

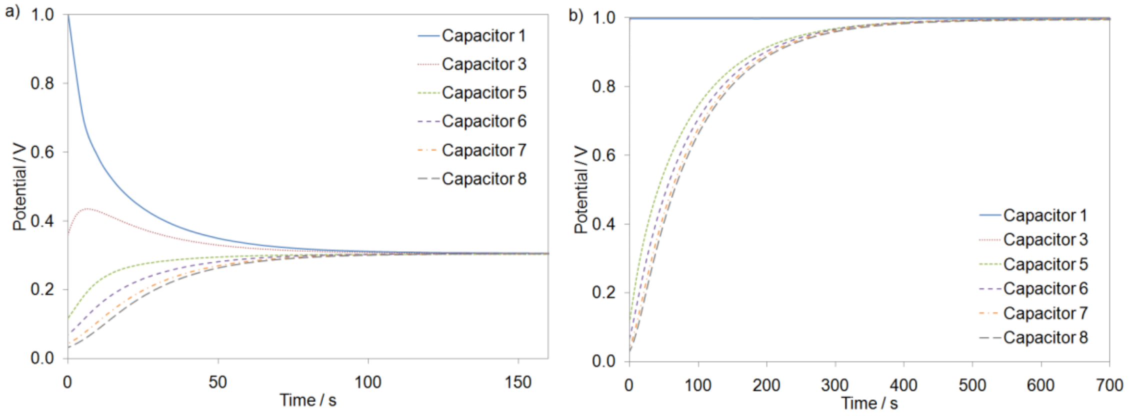

Figure B.4: Data taken at various positions down the transmission line circuit during a) self-discharge with no hold, and b) during hold step. The resistances were set to 40 kΩ and the voltage of the first capacitor was ramped from 0.0 V to 1.0 V at 50 mV s^{-1}.

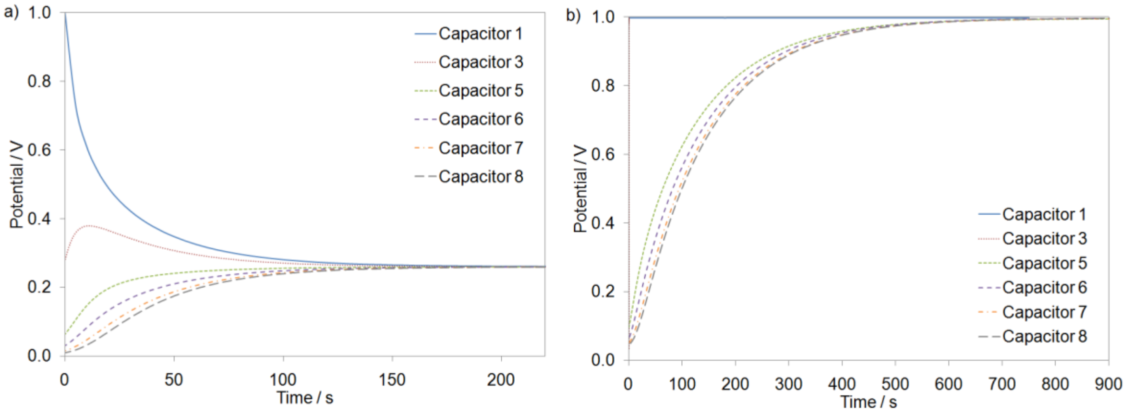

Figure B.5: Data taken at various positions down the transmission line circuit during a) self-discharge with no hold, and b) during hold step. The resistances were set to 60 kΩ and the voltage of the first capacitor was ramped from 0.0 V to 1.0 V at 50 mV s^{-1}.

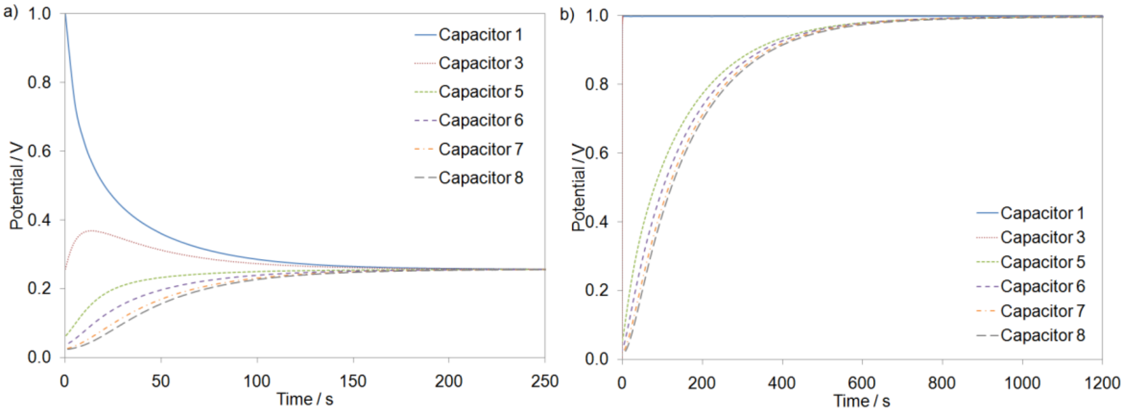

Figure B.6: Data taken at various positions down the transmission line circuit during a) self-discharge with no hold, and b) during hold step. The resistances were set to 70 kΩ and the voltage of the first capacitor was ramped from 0.0 V to 1.0 V at 50 mV s^{-1}.

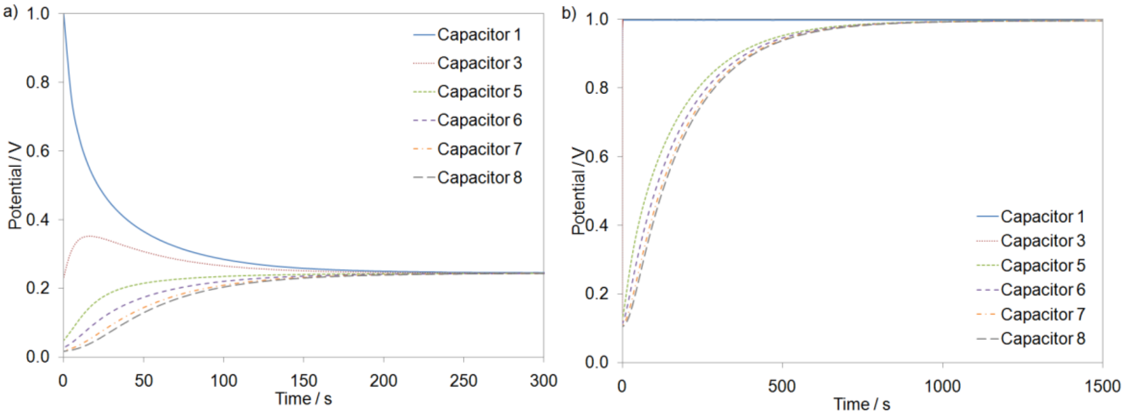

Figure B.7: Data taken at various positions down the transmission line circuit during a) self-discharge with no hold, and b) during hold step. The resistances were set to 80 kΩ and the voltage of the first capacitor was ramped from 0.0 V to 1.0 V at 50 mV s^{-1}.

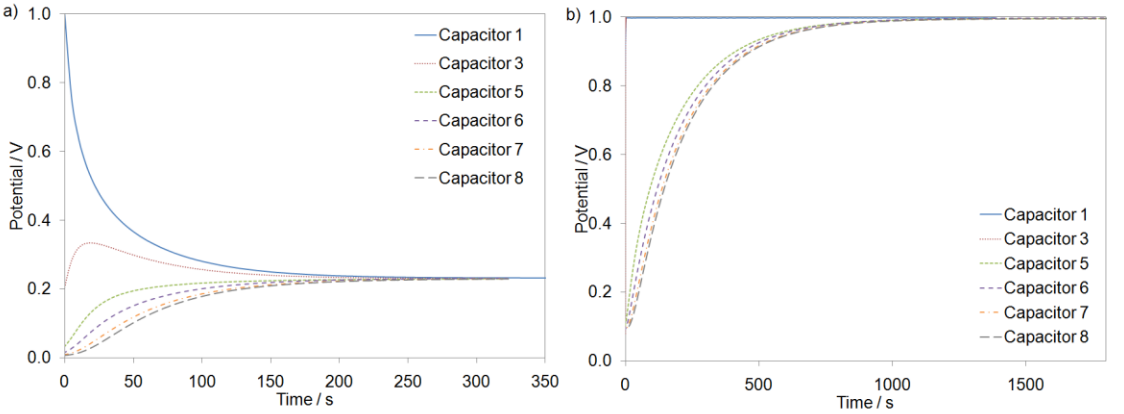

Figure B.8: Data taken at various positions down the transmission line circuit during a) self-discharge with no hold, and b) during hold step. The resistances were set to 90 kΩ and the voltage of the first capacitor was ramped from 0.0 V to 1.0 V at 50 mV s^{-1}.

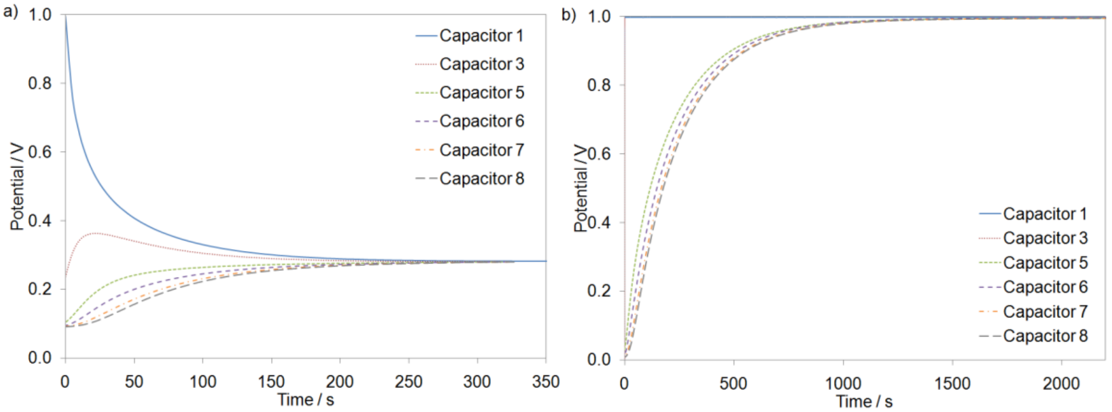

Figure B.9: Data taken at various positions down the transmission line circuit during a) self-discharge with no hold, and b) during hold step. The resistances were set to 100 kΩ and the voltage of the first capacitor was ramped from 0.0 V to 1.0 V at 50 mV s^{-1}.

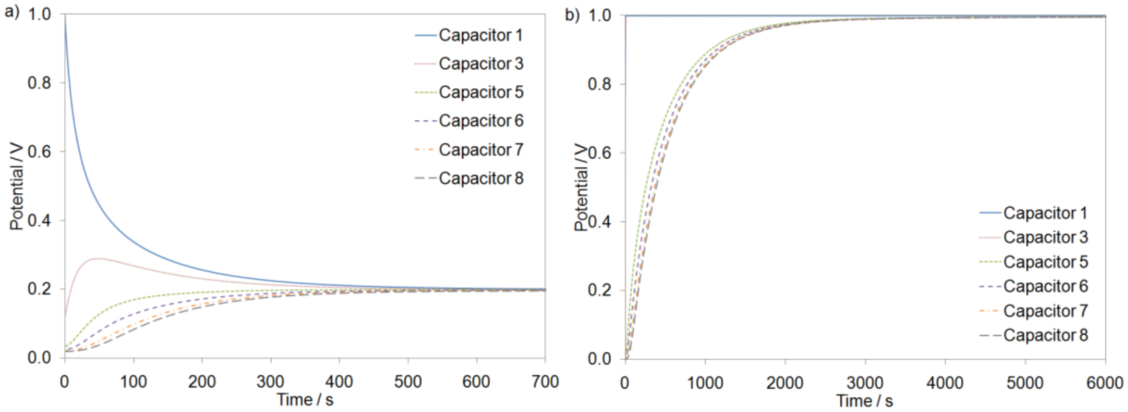

Figure B.10: Data taken at various positions down the transmission line circuit during a) self-discharge with no hold, and b) during hold step. The resistances were set to 200 kΩ and the voltage of the first capacitor was ramped from 0.0 V to 1.0 V at 50 mV s^{-1}.

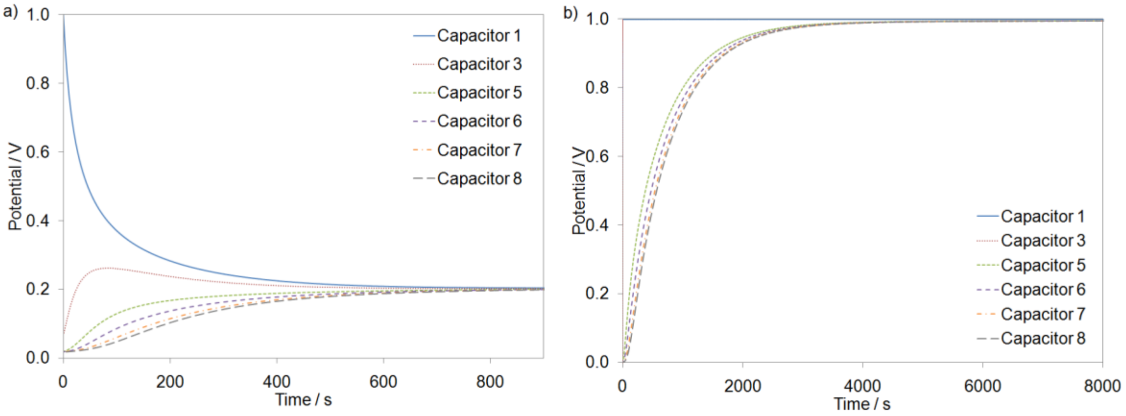

Figure B.11: Data taken at various positions down the transmission line circuit during a) self-discharge with no hold, and b) during hold step. The resistances were set to 10 kΩ and the voltage of the first capacitor was ramped from 0.0 V to 1.0 V at 50 mV s^{-1}.

B.2 Activation-controlled discharge and charge redistribution up the pore ($AC+CR_{up}$)

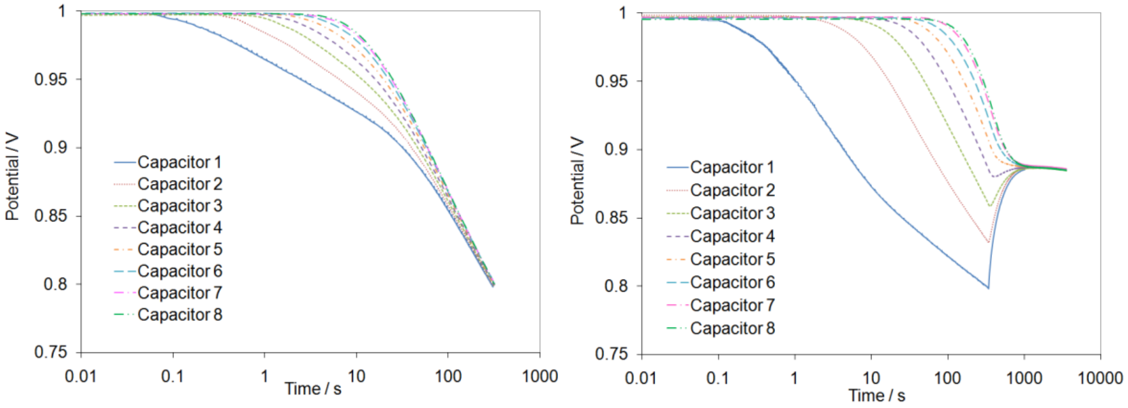

Figure B.12: Potential of all eight capacitors of transmission line circuit during activation-controlled discharge on capacitor 1 and CR_{up}. Prior to this discharge, all capacitors were brought to 1.0 V using a ramp rate of 1 mV s^{-1}, followed by a 15 min hold time. Resistors R2-R8 in the circuit were set to a)10 kΩ, and b) 300 kΩ, and in each case R_s was set to 0.

B.3 Activation-controlled discharge and charge redistribution up and down the pore (AC + CR_{up} + CR_{down})

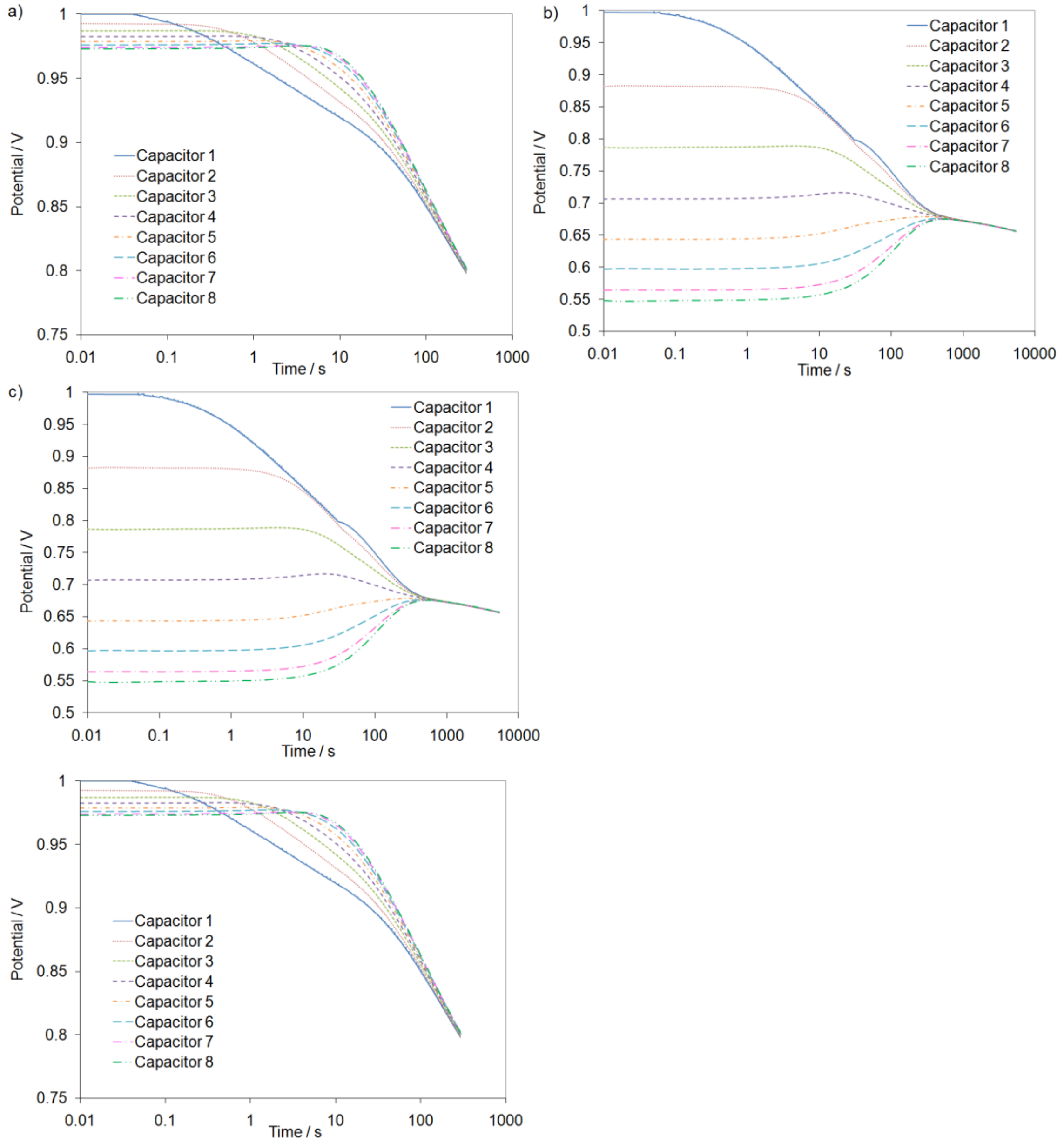

Figure B.13: Potential profiles of each capacitor in transmission line circuit using after charging capacitor 1 at 1 mV s^{-1} to 1.0 V, no hold time. Resistors R2-R8 in the circuit were set to a)10 kΩ, b) 200 kΩ, and c) 300 kΩ resistances, and in each case R_s was set to 0.

B.4 Resistances used to calculate pore shapes

Table 3: Resistances used to model various pore shapes for $n = 8$. The pore length listed is the ratio of pore length/pore diameter.

	Cylinder 1	Cylinder 2	Cylinder 3	Cylinder 4	Cylinder 5	cone 1	cone 2	Inverted cone 1	Inverted cone 2	Diamond 1	Diamond 2	Diamond 3	Diamond 4
Resistor 1	10	63	94	15	19	10	10	300	40	300	300	300	30
Resistor 2	10	63	94	15	19	12	11	51.5	25	28	112.5	257	18.75
Resistor 3	10	63	94	15	19	14.8	12.5	28.2	20	15	69	225	13
Resistor 4	10	63	94	15	19	19.5	15	19.5	15	10	50	200	10
Resistor 5	10	63	94	15	19	28.2	20	14.8	12.5	15	69	225	13
Resistor 6	10	63	94	15	19	51.5	25	12	11	28	112.5	257	18.75
Resistor 7	10	63	94	15	19	300	40	10	10	300	300	300	30
Total	70	441	658	105	133	436	133.5	436	133.5	696	1013	1764	133.5
Length (x1000)	43	1731	4134	97	155	269	82	269	82	429	3182	18473	82

	Diamond 5	Diamond 6	Inverted Diamond 1	BN 1	BN 2	BN 3	BN 4	BN 5	BN 6	BN 7	BN 8	BN 9	BN 10
Resistor 1	30	30	10	10	30	100	10	14	20	300	300	300	30
Resistor 2	24	28	15	10	30	100	10	14	20	10	300	300	10
Resistor 3	18	25.5	28	10	30	100	10	14	20	10	300	300	10
Resistor 4	15	25	300	300	300	300	30	30	30	10	10	300	10
Resistor 5	18	25.5	28	10	30	100	10	14	20	10	10	300	10
Resistor 6	24	28	15	10	30	100	10	14	20	10	10	10	10
Resistor 7	30	30	10	10	30	100	10	14	20	10	10	10	10
Total	159	192	406	360	480	900	90	114	150	360	940	1520	90
Length (x1000)	147	302	250	222	887	5654	55	99	188	222	579	936	55

	BN 11	BN 12	BN 13	BN 14	BN 15	BN 16	BN 17	BN 18	BN 19	BN 20	BN 21	BN 22
Resistor 1	30	30	10	10	10	10	300	300	50	30	30	20
Resistor 2	30	30	10	10	10	10	10	10	10	10	10	10
Resistor 3	30	30	300	10	30	10	10	10	10	10	10	10
Resistor 4	10	30	10	10	10	10	300	50	300	30	20	30
Resistor 5	10	30	10	300	10	30	10	10	10	10	10	10
Resistor 6	10	10	10	10	10	10	10	10	10	10	10	10
Resistor 7	10	10	10	10	10	10	10	10	10	10	10	10
Total	130	170	360	360	90	90	650	400	400	110	100	100
Length (x1000)	80	105	222	222	55	55	400	246	246	68	62	62

Table 4: Resistances used to model pore shapes for *n* = 22. The pore length listed is the ratio of pore length/pore diameter.

	Cylinder 1	Cylinder 2	Cylinder 3	cone 1	Inverted cone 1	Diamond 1	Diamond 2	Diamond 3	Diamond 4	Diamond 5	Diamond 6
Resistor 1	3.3	21.0	31.3	3.3	100.0	100.0	100.0	100.0	10.0	10.0	10.0
Resistor 2	3.3	21.0	31.3	3.3	100.0	100.0	100.0	100.0	10.0	10.0	10.0
Resistor 3	3.3	21.0	31.3	3.3	100.0	100.0	100.0	100.0	10.0	10.0	10.0
Resistor 4	3.3	21.0	31.3	4.0	17.2	9.3	37.5	85.7	6.3	8.0	9.3
Resistor 5	3.3	21.0	31.3	4.0	17.2	9.3	37.5	85.7	6.3	8.0	9.3
Resistor 6	3.3	21.0	31.3	4.0	17.2	9.3	37.5	85.7	6.3	8.0	9.3
Resistor 7	3.3	21.0	31.3	4.9	9.4	5.0	23.0	75.0	4.3	6.0	8.5
Resistor 8	3.3	21.0	31.3	4.9	9.4	5.0	23.0	75.0	4.3	6.0	8.5
Resistor 9	3.3	21.0	31.3	4.9	9.4	5.0	23.0	75.0	4.3	6.0	8.5
Resistor 10	3.3	21.0	31.3	6.5	6.5	3.3	16.7	66.7	3.3	5.0	8.3
Resistor 11	3.3	21.0	31.3	6.5	6.5	3.3	16.7	66.7	3.3	5.0	8.3
Resistor 12	3.3	21.0	31.3	6.5	6.5	3.3	16.7	66.7	3.3	5.0	8.3
Resistor 13	3.3	21.0	31.3	9.4	4.9	5.0	23.0	75.0	4.3	6.0	8.5
Resistor 14	3.3	21.0	31.3	9.4	4.9	5.0	23.0	75.0	4.3	6.0	8.5
Resistor 15	3.3	21.0	31.3	9.4	4.9	5.0	23.0	75.0	4.3	6.0	8.5
Resistor 16	3.3	21.0	31.3	17.2	4.0	9.3	37.5	85.7	6.3	8.0	9.3
Resistor 17	3.3	21.0	31.3	17.2	4.0	9.3	37.5	85.7	6.3	8.0	9.3
Resistor 18	3.3	21.0	31.3	17.2	4.0	9.3	37.5	85.7	6.3	8.0	9.3
Resistor 19	3.3	21.0	31.3	100.0	3.3	100.0	100.0	100.0	10.0	10.0	10.0
Resistor 20	3.3	21.0	31.3	100.0	3.3	100.0	100.0	100.0	10.0	10.0	10.0
Resistor 21	3.3	21.0	31.3	100.0	3.3	100.0	100.0	100.0	10.0	10.0	10.0
Total	70	441	658	436	436	696	1013	1764	133.5	159	192
Length (x1000)	43	1731	4134	269	269	429	3182	18473	82	147	302

	BN 10	BN 13	BN 14	BN 15	BN 16
Resistor 1	10.0	3.3	3.3	3.3	3.3
Resistor 2	10.0	3.3	3.3	3.3	3.3
Resistor 3	10.0	3.3	3.3	3.3	3.3
Resistor 4	3.3	3.3	3.3	3.3	3.3
Resistor 5	3.3	3.3	3.3	3.3	3.3
Resistor 6	3.3	3.3	3.3	3.3	3.3
Resistor 7	3.3	100.0	3.3	10.0	3.3
Resistor 8	3.3	100.0	3.3	10.0	3.3
Resistor 9	3.3	100.0	3.3	10.0	3.3
Resistor 10	3.3	3.3	3.3	3.3	3.3
Resistor 11	3.3	3.3	3.3	3.3	3.3
Resistor 12	3.3	3.3	3.3	3.3	3.3
Resistor 13	3.3	3.3	100.0	3.3	10.0
Resistor 14	3.3	3.3	100.0	3.3	10.0
Resistor 15	3.3	3.3	100.0	3.3	10.0
Resistor 16	3.3	3.3	3.3	3.3	3.3
Resistor 17	3.3	3.3	3.3	3.3	3.3
Resistor 18	3.3	3.3	3.3	3.3	3.3
Resistor 19	3.3	3.3	3.3	3.3	3.3
Resistor 20	3.3	3.3	3.3	3.3	3.3
Resistor 21	3.3	3.3	3.3	3.3	3.3
Total	90	360	360	90	90
Length (x1000)	55	222	222	55	55